NATIONAL INSTITUTE FOR FUSION SCIENCE

Evolution of Pulse Power and its Peripheral Technology

Edited by Keiichi Kamada and Tetsuo Ozaki

(Received - May 25, 2017)

NIFS-PROC-106

Nov. 01, 2017

Evolution of Pulse Power and its Peripheral Technology

Edited by Keiichi Kamada and Tetsuo Ozaki

January 8-9, 2015
National Institute for Fusion Science
Toki, Gifu, Japan

Abstract

In this proceedings, the papers presented at the symposium on "Evolution of pulse power and its peripheral technology" held at National Institute for Fusion Science on January 8-9, 2015 are collected. The papers reflect the present status and recent progress in the experimental and theoretical works on plasma science using pulsed power technology.

Keywords: high energy density plasma, warm dense matter, microwave, EUV, laser, plasma focus, z-pinch, high power ion beam, material processing, micro plasma.

Editor's Preface

The symposium on "Evolution of Pulse Power and its Peripheral Technology" was held at National Institute for Fusion Science on January 8-9, 2015 at National Institute for Fusion Science (NIFS), Toki. This symposium was organized as a part of the General Collaborative Research of NIFS. Over 56 researchers and students from universities, institutes and companies joined in the symposium. The number of oral presentations was 34. Twenty-two papers presented at the symposium are included in this proceeding.

The main topics of this symposium were developments and applications of the pulse power technology. Scientists presented their results at many other symposia or meetings of their own fields. In this symposium, scientists from various fields related to the pulse power technology presented their latest studies. The topics covered recent developments on pulsed power technology and experimental and theoretical studies on physics, accelerator, biology, electromagnetic wave source, inertial fusion, etc. using pulsed power technology. Scientists engaged in fruitful discussions from various points of view. It is our pleasure if this symposium contributes to the progress in the science and technology using pulsed power technology.

We would like to acknowledge the contribution of all the participants and staff of NIFS.

Keiichi Kamada
Kanazawa University

Tetsuo Ozaki
National Institute for Fusion Science

Contents

List of Participants

N. Yugami	Utsunomiya Univercity
T. Honmyo	Utsunomiya Univercity
H. Mori	Iwate Univercity
T. Tomite	Iwate Univercity
K. Takayama	High Energy Accelerator Research Organization
H.Kobayashi	Tokyo City Univercity
G. Imada	Niigata Institue of Technology
H.nakao	Niigata Institue of Technology
J. Weihua	Nagaoka University of Technology
T.Sugai	Nagaoka University of Technology
K. Kobayashi	Nagaoka University of Technology
R. Sato	Nagaoka University of Technology
Le Xu	Nagaoka University of Technology
K. Monma	Nagaoka University of Technology
T. Kawamura	Tokyo Institute of Technology
J. Hasegawa	Tokyo Institute of Technology
Y. Ishikawa	Tokyo Institute of Technology
A.Takada	Tokyo Institute of Technology
H. Hirade	Tokyo Institute of Technology
E. Baba	Tokyo Institute of Technology
E., Hotta	Tokyo Institute of Technology
Y.Takahashi	Tokyo Institute of Technology
K. Horioka	Tokyo Institute of Technology
K.Kawaguchi	Tokyo Institute of Technology
T.Kawasaki	Tokyo Institute of Technology
Y.Syo	Tokyo Institute of Technology
D.Nishii	Tokyo Institute of Technology
H.Ito	University of Toyama
H.Ohashi	University of Toyama
S.Shinokawa	University of Toyama
K.Okajima	University of Toyama
K.Oyama	University of Toyama
T.Nakamura	University of Toyama
S.Katsuki	Kumamoto University

T.Namihira	Kumamoto University
N.Takamura	Kumamoto University
S.Lim	Kumamoto University
A.Tokuchi	Pulsed Power Japan laboratory ltd
T.Kikuchi	Nagaoka University of Technology
T.Sato	Nagaoka University of Technology
Y.Haraguchi	Nagaoka University of Technology
T.Kudo	Nagaoka University of Technology
T.Tazima	National Institute for Fusion Science
T.Ozaki	National Institute for Fusion Science
K.Kamada	Kanazawa University
R.Ando	Kanazawa University
Y.Soga	Kanazawa University
Y.Paku	Kanazawa University
T.Asami	Kanazawa University
Y.Mihara	Kanazawa University
T.Yamaguchi	Kanazawa University
M.Katsuoka	Kanazawa University
R.Kiyomoto	Kanazawa University
M.Takeda	Kanazawa University
D.Takagi	Kanazawa University
M.Honda	Kanazawa University
S.Nakada	Kanazawa University

Recent Technology trends of Pulsed-power Generator

Akira Tokuchi

Pulsed Power Japn Laboratory Ltd.

ABSTRACT

Many industrial applications require high performances of high voltage pulsed power generators such as high reliability, high repetition, long life and easy adjustment of high voltage output waveform. In order to achieve these requirements, we are developing many kind of high voltage pulsed power supplies using semiconductor switches as output switches. In this paper, we introduce recent technology trends of pulsed-power generators .

Keywords

Pulsed-power Generator, Semi-conductor Switch, LTD, SOS diode.

1. Introduction

Recently a pulsed-power technology is evolving rapidly with developing of each technology namely a power conversion technology, a pulse compression technology and a pulse conversion technology.

In a power conversion technology, old devices such as IVR and the SCR have been replaced by MOS-FETs or IGBTs. By using combination with such high-speed devices, high power conversion has become possible with high stability, high speed and high efficiency. In near future, these devices may be replaced by SiC with higher performances.

In a pulse compression technology, old devices such as gap switches or thyratrons have been replaced by also MOS-FETs, IGBTs. Furthermore, SI thyristors or the SOS diodes are used as new pulsed power devices. Of course the SiC devices are expected as next-generation devices, too.

In a pulse conversion technology, semi-conductor MARX circuits, semi-conductor LTD circuits, induction voltage adders and unitized pulsed transformer are greatly improves the flexibility of the high-voltage pulsed power generator, it has become possible to adjust easily the very short pulsed high-voltage waveform.

By these remarkable improvements of pulsed power generator, many industrial applications using pulsed power technology are rapidly expected.

2. Expected Industrial Applications

Figure 1 shows examples of expected industrial applications. In particular, since the degree of freedom of the high voltage waveform is increased, innovative good results in applications of the engine combustion promotion, wastewater treatment and EUV generation is expected.

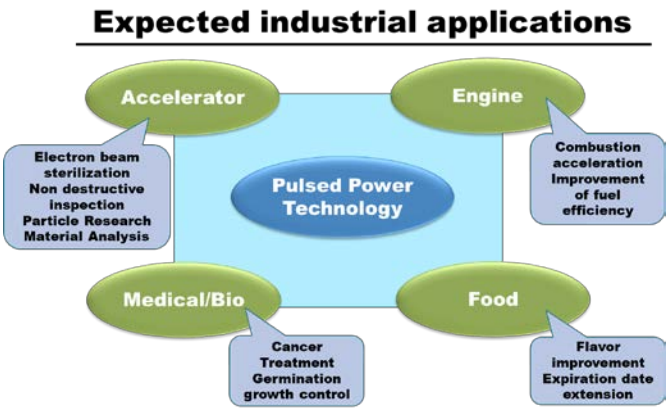

Fig. 1 Expected industrial applications using pulsed power technology

Recent requirements from new industrial applications for pulsed power generators are as follows,

- High voltage < several 10kVp
- Short pulse < several 10ns
- Fast rise time < 10ns
- High repetition kHz ～ MHz
- Portable(compact, lightweight, battery powered)

- Adjustable waveform
- Long life
- Maintenance free
- Digital control (microcomputer, FPGA, DSP)

3. Specific application examples

3.1 Wastewater treatment

Purification of industrial wastewater by the streamer discharge is expected as industrial applications of pulse power. Figure 2 shows a circuit diagram of the pulsed power generator for the streamer discharge.

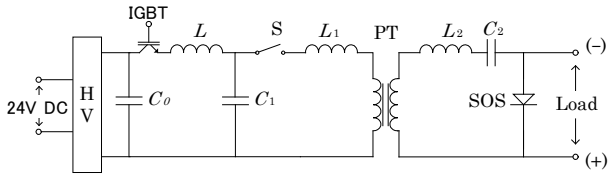

Fig. 2 A circuit diagram of the pulsed power generator for the streamer discharge

By using a SOS diode, this generator is very compact and a weight of just 16.5kg is very light. Furthermore it is portable because of a battery drive. After confirming the effect of the wastewater treatment by using this power supply, we are planning a higher performance of the pulsed power supplies for the streamer discharge in accordance with the developing roadmap shown in figure 3.

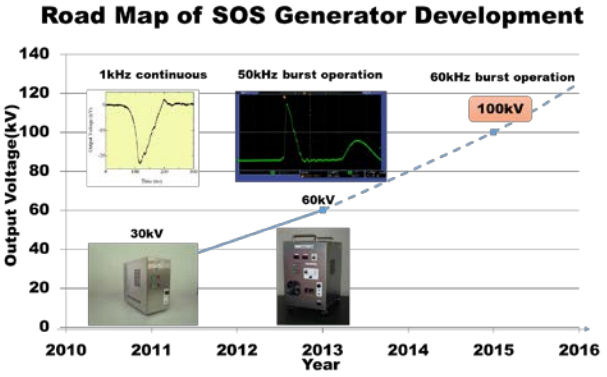

Fig. 3 A developing roadmap of the pulsed power generator for the streamer discharge

In the latest power supply, we can operate it at 50kHz of repetition frequency in burst and 60kV of an output voltage. Furthermore an output voltage height of each pulse during the burst operation can be changed easily by a digital control. Figure 4 shows the output voltage waveforms at an example pattern.

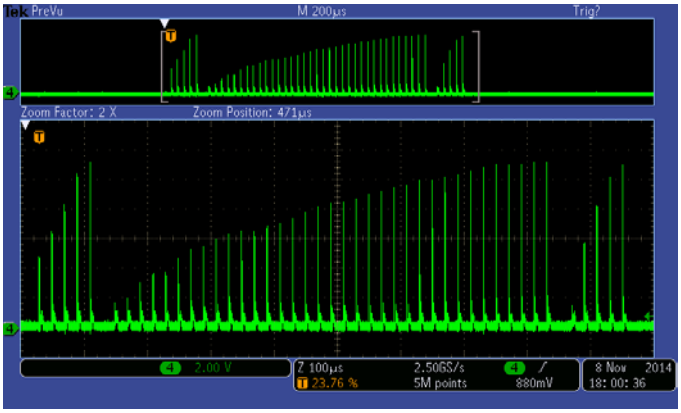

Fig. 4 The output voltage waveforms at an example pattern. 10kV/div and 10us/div

By changing the time duration of conduction time on IGBT shown in figure 2 pulse to pulse, we can change the output voltage height in burst operation. This enables a more precise control of a streamer plasma, and the higher efficiency of wastewater treatment can be expected.

3.2 Klystron modulator for the ILC (International Linear Collider)

ILC are planned by international cooperation as an accelerator of the next generation. ILC will use many number more than 500 of the high voltage pulsed power generators for RF source. Since it is necessary to install in a narrow tunnels, a small size and a high efficiency power supply is required. TABLE 1 shows a requirement parameter of the klystron modulator for ILC.

TABLE 1. REQUIREMENT OF ILC KYLSTRON MODULATOR

Requirement of ILC KLYSTRON MODULATOR	
Parameter	***Requirement value***
Output voltage	-120V
Output current	140A
Pulse width	1.7ms
Pulse repetition frequency	5Hz
Ripple Ratio	<±0.5%

In order to achieve the requirements mentioned above, we chose a new circuit using semiconductor

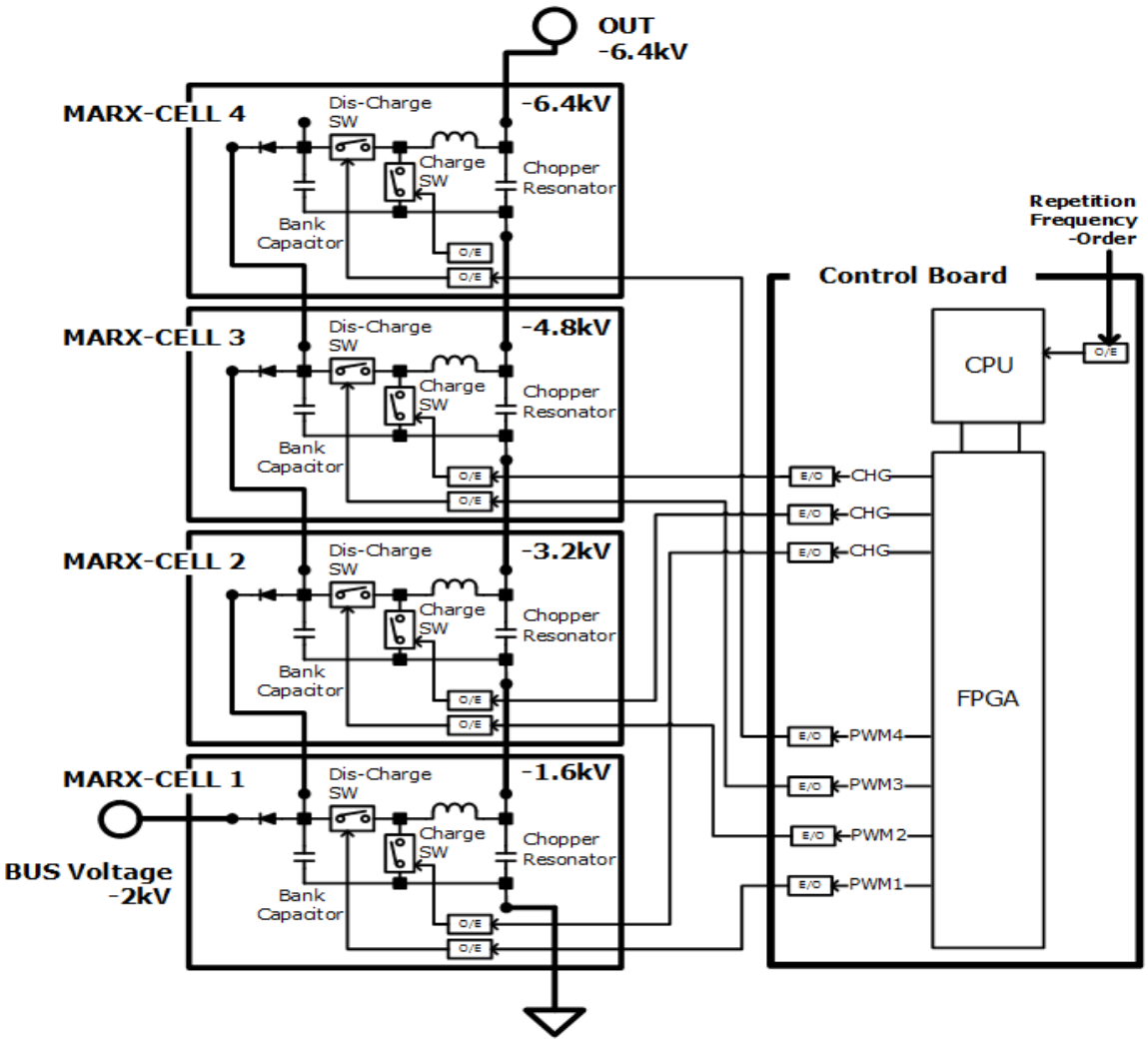

Fig. 5 A circuit diagram of a MARX unit of the klystron modulator for ILC

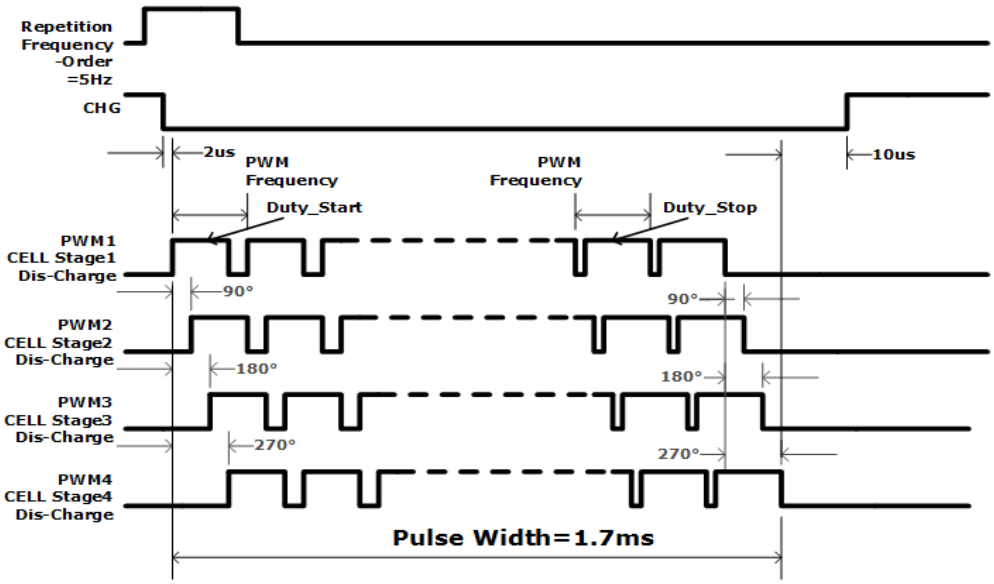

Fig. 6 A timing chart of the chopper operation

MARX circuit with a chopper modulation. Figure 5 shows the circuit diagram of a MARX unit of the modulator. This MARX unit uses four MARX cells and each MARX cell generate 1.6kV of an output voltage. Thus this unit can generate 6.4kV of an output voltage by using 4-MARX cells. Using 20 number of the MARX units, 120kV of an output voltage may be generated. Each MARX cell has chopper switch using SiC-MOS-FETs to get a good flatness of long pulse of output voltage. This chopper frequency is 50kHz and by changing the phase of the chopper frequency for each MARX cells, the ripple of the output voltage is effectively reduced. Figure 6 shows a timing chart of the chopper operation.

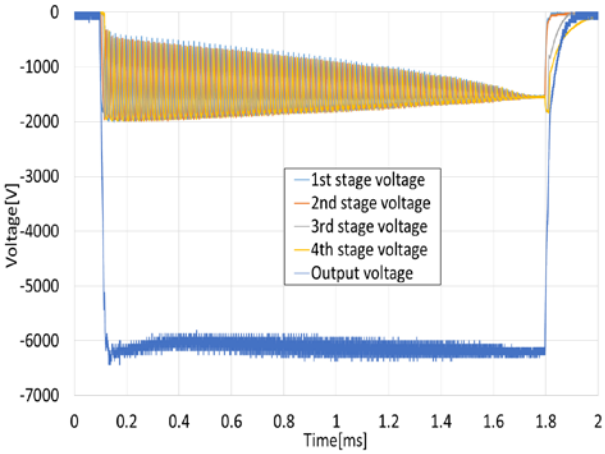

Fig. 7 An output voltage waveform of the MARX unit

Figure 7 shows an output voltage waveform of the MARX unit with the output voltage waveforms on each MARX cells. It is difficult to distinguish all waveforms because all waveforms are piled up, but most of each wave pattern are the same wave patterns, and only the phase of the wave patterns are different. The output voltage waveforms on each MARX cells are Ripple of output voltage on each MARX cell is very large more than ±40%, but a ripple of the output voltage of MARX unit using four MARX cells is effectively reduced about ±4%. Furthermore by using 20 MARX units, good flatness less than ± 0.5% of the output voltage may be obtained.

3.3 Muon beam kicker for J-PARC

Materials and Life Science Facility (MLF) of J-PARC generates world's highest intensity of neutron beam and muon beam by pulsed proton beam. In order to supply double pulse structured muon beam to each experimental area efficiently, beam kicker is installed at a branch to beam line legs of muon beam line in MLF experimental hall. The purpose of beam kicker is to distribute double pulse structured muon beam to each experimental area efficiently. Figure 8 shows beam kicker position, beam kicker is installed at a branch to beam line legs of muon beam line in MLF experimental hall.

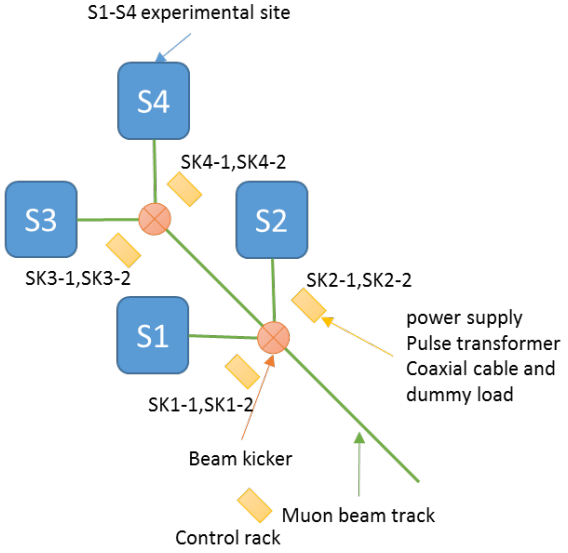

Fig. 8 Planned experimental site for muon beam line at MLF, J-PARC

As pulsed power supply using in beam kicker, requirement is defined Table 2 shown in below.

TABLE 2. REQUIREMENT OF PULSED POWER SUPPLY FOR MUON BEAM KICKER

Requirement of pulsed power supply for Muon beam kicker	
Parameter	***Requirement value***
Rated output voltage	+54kV and -54kV (bipolar)
Output pulse width	300ns (+54kV), 300ns (-54kV)
Output impedance	50Ω
Discharge voltage wave form	square wave
Output pulse rise time	50nsec
Reputation frequency	25Hz

In order to achieve the requirements mentioned above, we chose a new circuit using semiconductor MARX circuits and inductive voltage adders with a high-voltage and a high-response.

Figure 9 shows a block diagram of the pulsed power supply for the muon kicker.

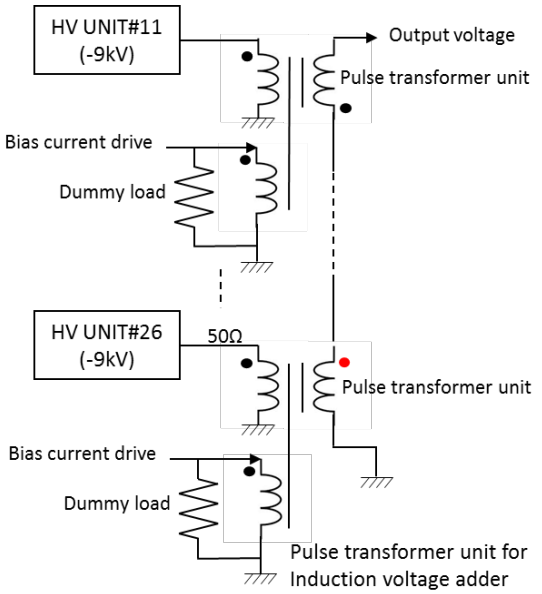

Fig. 9 HV pulsed power supply unit and Pulse transformer unit for Induction voltage adder

Each HV unit generate 9kV, 300ns of an output pulse voltage by using 16-stage MOS-FET based MARX circuit. And using 6 HV units, 54kV, 300nsec of an output voltage pulse is generated. By using two different types of polarity pulse transformer in series, we succeeded to obtain a high voltage bipolar pulse. Figure 10 shows an output voltage waveform of the pulse transformer.

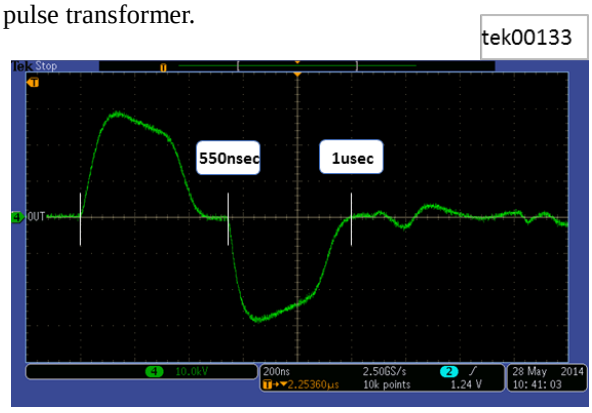

Fig. 10 Output waveform of the pulse transformer 20kV/div, 200ns/div

It is succeeded that a pair of bipolar high voltage pulse of +54kV and -54kV of each peak voltage is obtained during a short time interval of one microsecond.

Since HV units is constituted by MARX circuit, it is possible to change the waveform of the output voltage by changing the inserting the trigger. In the near future, it is expected to greatly assist in the precise control of the muon beam.

4. Conclusions

Some attracting attention as a recent trend of pulsed power technology were introduced in this paper. By a progress of replacement to semiconductor devices as high voltage switches of high-voltage pulsed power supplies, it will be expected that industrial applications using them to be progressed. We hope to promote further development of the pulsed power technology to assist a progress of new industrial applications of the pulsed power.

Implementation of Magnetic Pulse Compression Circuit in Inductive Energy Storage Pulsed Power Generator

Yuki Takahashi, Takuya Uyama, Masato Watanabe, Eiki Hotta

Tokyo Institute of Technology, 4259 Nagatsuta, Midori-ku, Yokohama, 226-8502, Japan

ABSTRACT

Magnetic pulse compression circuit was added to an inductive energy storage pulsed power generator, in order to shorten the pulse width and consequently achieve high voltage rise rate. As a result, we got the pulsed voltage of 15.6 kV with a full width at half maximum of 51.5 ns. The voltage rise rate was 408 kV/μs, which was approximately two times higher than that obtained without a magnetic pulse compression circuit. The energy transfer efficiency was about 20%.

Keywords

Pulsed power generator, inductive energy storage, magnetic pulse compression, magnetic switch

1. Introduction

Currently, depletion of energy resources and environmental pollution by the exhaust gases from factories and automobiles, etc. have become a problem on a global scale. Therefore, the development of combustion with high efficiency and low pollution is required for the internal combustion engine. The examples are lean burn technology and waste recycling technology in the spark ignition engine [1]. In recent years, plasma-assisted combustion using a non-thermal plasma has drawn attention. This is intended to facilitate the fuel ignition and combustion in the internal combustion engine by generating reactive species such as radicals. By utilizing it for a spark ignition engine, higher efficiency and lower emission can be expected. Ignition using non-thermal plasma for spark ignition engine are studied by many researchers [2-5]. In the previous report, for examples, Tanoue et al. reported that the reduction of ignition delay time and the extension of flammability limit was observed by applying the repetitive nanosecond pulse discharge to the ignition systems [2].

As described above, plasma-assisted combustion with non-thermal plasma is intended to enhance the fuel ignition and combustion of the engine by the reactive species such as radicals. Therefore, it is important to produce a large amount of the active species. In general, it was reported that energy efficiency of the active species generation using pulse discharge is very high [6-8]. Here, we consider shortening the pulse width of pulse voltage waveform. The voltage rise rate dV/dt increases by shortening the pulse. From a v-t curve, generally the breakdown voltage in the air gap increases as dV/dt of applied voltage becomes larger. When the discharge voltage is high, it can be expected that the number of high energy electrons increases. They contribute the excitation, ionization and dissociation of neutral particles, which leads to the formation of active species. Therefore, increase of an amount of active species can be expected if the number of high energy electrons increased.

In view of the above mentioned concept, in this study, we attempt to shorten the pulse width of pulsed power generator in order to achieve higher voltage rise rate dV/dt.

2. Experimental Setup

2.1. Pulsed power generator

The schematic of the pulsed power generator used in this study is shown in Fig. 1. The pulsed power generator is an inductive energy storage (IES) system. IES system stores energy in the inductor as magnetic

energy, and outputs a pulse voltage by interrupting the flow of current by using opening switch. The IES system has about 1 - 2 order higher energy storage density per unit volume, as compared to capacitive energy storage system [9]. For this reason, downsizing the power supply is easy. In other words, it is advantageous in the viewpoint of attachment to the vehicle body. Furthermore, IES system is capable of operating at low voltage, which means that restriction of the dc power supply is little.

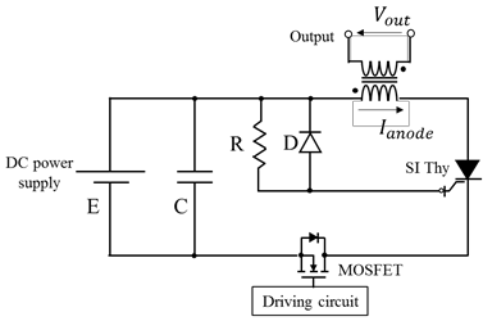

Fig.1. Schematic diagram of IES pulsed power generator

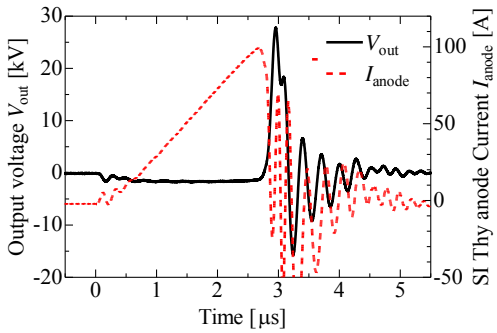

Fig.2 Typical waveforms of output voltage and SI Thy anode current

In Fig. 1, the primary winding of transformer works as an inductor for storing energy. The inductance L was about 5 μH. MOSFET and Static Induction Thyristor (SI Thy) connected in series to the transformer act as the opening switch. The peak value of output voltage is expressed as $nLI_a/\Delta t$, where n is the turn ratio of the transformer, I_a is the peak anode current of the SI Thy at the end of the energy storage period and Δt is the interruption time of the current. For more information on this circuit and operation principle, refer to [10].

Figure 2 shows typical waveforms of the output voltage and the SI Thy anode current. The peak value of the SI Thy anode current at the end of the energy storage period, I_a, was 100 A for no-load. Full width at half maximum (FWHM) of the output voltage was 243 ns. The voltage rise rate, dV/dt, was 245 kV/μs. In this study, it is noted that dV/dt was defined as the slope of a straight line connecting 90% and 30% of the peak voltage.

2.2. Magnetic pulse compression circuit

In this study, we used a magnetic pulse compression (MPC) circuit as a method for shortening the output pulse width. MPC circuit is one for compressing the pulse width of current using a magnetic switch (MS) [9,11]. Figure 3 (a) and (b) show the circuit diagram of MPC and the waveforms of voltage and current.

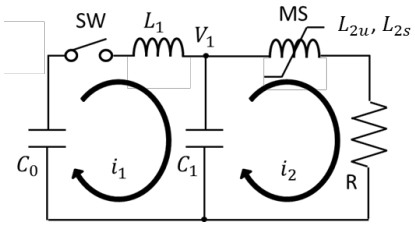

(a) The circuit diagram

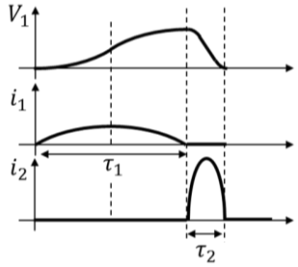

(b) Waveforms of voltage and current

Fig.3. Schematic of basic MPC circuit

Table 1 Specification of MP3210VF3T Hitachi Metals, Ltd

Outer diameter [mm]	35
Internal diameter [mm]	19.9
Height [mm]	11.5
Mean magnetic path length [mm]	85.8
Effective cross section [mm^2]	40.7
Total flux $2\emptyset_s$ [Wb]	97.4

For MS, the saturated inductance, L_{2s}, should be much less than the unsaturated inductance, L_{2u}, that is $L_{2s} \ll L_1 \ll L_{2u}$. Suppose that, the initial charged voltage of C_0 is V_0 and MS is unsaturated initially.

When the switch SW turns on at $t = 0$, a current i_1 flows to C_1 from C_0 through L_1. During this phase where $L_1 \ll L_{2u}$, the current i_1 does not flow to the resistor R. Therefore,

$$i_1 = V_0 \sqrt{\frac{C_{01}}{L_1}} \sin\omega t \quad (1)$$

$$V_1 = \frac{1}{C_1}\int i_1 dt = V_0 \frac{C_0}{C_0 + C_1}[1 - \cos\omega t] \quad (2)$$

where

$$C_{01} = \frac{C_0 C_1}{C_0 + C_1}, \quad \omega = \frac{1}{\sqrt{L_1 C_{01}}} \quad (3)$$

The half cycle τ_1 of i_1, i.e. pulse width before compression is given by

$$\tau_1 = \pi\sqrt{L_1 C_{01}} \quad (4)$$

When $t = \tau_1$, the energy transfer from C_0 to C_1 is completed, and the voltage of C_1, V_1 takes a peak value. If MS is designed to saturate at this moment, the pulse compression process begins. Now, the inductance of MS is L_{2s}. Because $L_{2s} \ll L_1$, almost no current flows in the circuit on the left side of C_1. The current i_2 flowing through R is given by

$$i_2 = \frac{2V_0 C_{01}}{\sqrt{L_{2s} C_1}} \sin\omega' t \quad (5)$$

where

$$\omega' = \frac{1}{\sqrt{L_{2s} C_1}} \quad (6)$$

The half cycle τ_2 of i_2, i.e. pulse width after compression is

$$\tau_2 = \pi\sqrt{L_{2s} C_1} \quad (7)$$

The ratio of τ_2 to τ_1, i.e. the compression ratio of pulse is

$$\frac{\tau_2}{\tau_1} = \frac{\pi\sqrt{L_{2s} C_1}}{\pi\sqrt{L_1 C_{01}}} = \sqrt{\frac{L_{2s}}{L_1}\frac{C_1}{C_{01}}} \ll 1 \quad (8)$$

In practice, to shorten the pulse width of the IES system using the MPC circuit, we replaced C_0 with the IES system. In general, voltage of 10~20 kV is required in the spark ignition engine. Therefore, in this study, the target voltage value was set to be $10 - 30$ kV. In the previous report [5], measurement of amount of OH generated by using a pulsed power supply with a pulse width of $111 - 310$ ns was performed. To enable the investigation in a shorter pulse width region, the target pulse width was set to be less than 100 ns.

2.3. Magnetic switch

For designing the MPC circuit, what is important is the timing at which MS turns on. In other words, the time τ for which MS holds the unsaturated state is important. The relationship between the time τ and the voltage V applied to MS can be given by the following equation (9). The equation (9) is called the voltage-time product.

$$\int_0^\tau V dt = N\int_A BdS = NA\Delta B = N \cdot 2\phi_s \quad (9)$$

where N is the number of turns, A is the cross section of the magnetic core. $2\phi_s$ is the available amount of the magnetic flux, and the value is determined by the magnetic properties of the magnetic material [9]. In this study, we used FINEMET core MP3210VF3T made by Hitachi Metals Ltd., as the magnetic material of MS. The specifications of the MP3210VF3T is shown in table 1. When actually manufacturing MS, silicone rubber insulated wire was wound around the core.

3. Results and Discussion

3.1 Selection of capacitance

First, we determined the value of the capacitance C. When $I_a = 100\ A$, the energy stored in the primary winding of the transformer per pulse is

$$\frac{1}{2}LI_a{}^2 = 25 \text{ mJ} \quad (10)$$

In the IES system, since the energy transfer efficiency of the transformer is approximately $40 - 50\%$, the resulted energy E stored in the capacitor C is

$$E = \frac{1}{2}CV^2 = 25 \times 0.4 = 10 \text{ mJ} \quad (11)$$

Setting 25 kV as the charged voltage of C, the capacitance is calculated as

$$C = \frac{2E}{V^2} = \frac{2 \times 10 \times 10^{-3}}{(25 \times 10^3)^2} = 24 \text{ pF} \qquad (12)$$

We used a coaxial cable (RG-8A/u) with capacitance of 97 pF/m as a capacitor and obtained C of 23.7 pF by adjusting its length. The capacitor C was used as C_1 in Fig. 3-(a).

3.2. Fabrication of magnetic switch

Next, magnetic switch was designed. In order to obtain the required voltage-time product, the voltage V_c of C was measured by using the circuit shown in Fig. 4. The results are shown in Fig. 5.

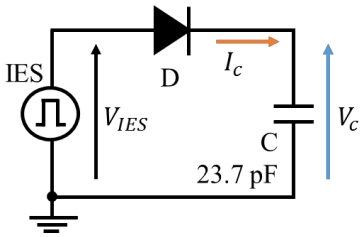

Fig.4 Circuit diagram to measure V_c

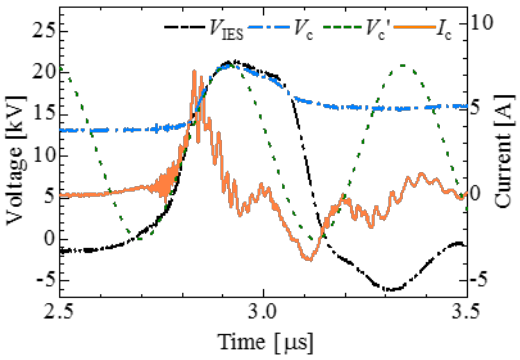

Fig. 5 Waveforms of the voltage of each part

In Fig. 5, the dashed-dotted line shows the voltage V_c of C and the thin solid line shows the current I_c flowing from the IES system. The half cycle τ of I_c is about 215 ns which corresponds to τ_1 in eq. (4). Then, the voltage-time product concerning V_c was calculated. V_c in Fig. 5 corresponds to eq. (2). Therefore, the fitting was conducted on V_c shown in Fig. 5 using the following eq. (13), which was obtained by substituting $C_0 = C_1 = 23.7$ pF in eq. (2).

$$V_c' = \frac{V_p}{2}[1 - \cos\omega t] \qquad (13)$$

where V_p is the peak value of V_c and the angular frequency ω was obtained from $\omega\tau = \pi$. The waveform of V_c' is shown by the broken line in Fig. 5. By replacing V_c' with V in eq. (9), the voltage-time product can be calculated. Here, the integration time was $\tau = 215$ ns. The result is shown in eq. (14).

$$N \cdot 2\phi_s = \int_0^{\tau} V dt = 2.30 \text{ mWb} \qquad (14)$$

From eq. (14) and the value in table 1, 24 was obtained as the number of turns of MS. The unsaturated inductance of MS L_{2u} was 10.3 mH and saturated inductance L_{2s} was 343 nH. From eq. (7), the theoretically obtained pulse width after compression was 8.96 ns.

3.3. Operation of the fabricated MPC circuit

MPC circuit was made by using C which selected in section 3.1 and MS fabricated in section 3.2. Figure 6 shows the circuit diagram. In Fig. 6, the output is the voltage across R of 2 kΩ. Figure 7 shows the typical waveforms of voltage and current of each part. In Fig. 7-(a), the dashed-dotted line and the solid line show the voltage V_c of C and the output voltage V_{MPC}, respectively. In Fig. 7-(b), the broken line, the dashed-dotted line and the solid line show the current I_{IES} flowing from IES system, the current I_c flowing into C and the current I_R flowing through R, respectively. From Fig. 7-(a), it can be seen that the pulsed voltage V_{MPC} with the peak value of 11.6 kV and the FWHM of 100 ns is obtained. The voltage rise rate dV/dt of V_{MPC} is 64.5 kV/μs. In comparison with the case without MPC circuit, the pulse width is shorter, however, dV/dt becomes smaller.

From Fig. 7-(a), at the time around 0.25 μs, it can be confirmed that V_{MPC} rises rapidly. This suggests that MS turns on at this moment. In earlier time before 0.25 μs, it can be seen that V_{MPC} is gradually increasing. This is probably caused by the leakage current flowing through MS during the charging period of C. By the effect of the leakage current, it may be considered that dV/dt of V_{MPC} becomes smaller than that obtained in the case without the MPC circuit. In order to reduce the leakage current, it is

necessary to increase the unsaturated inductance of MS.

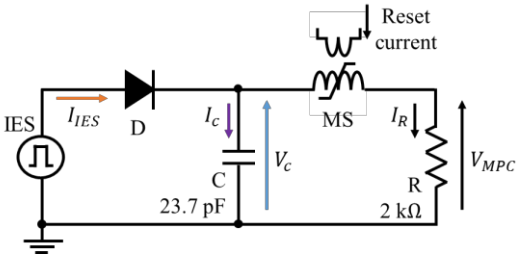

Fig.6. Schematic diagram of MPC circuit with IES.

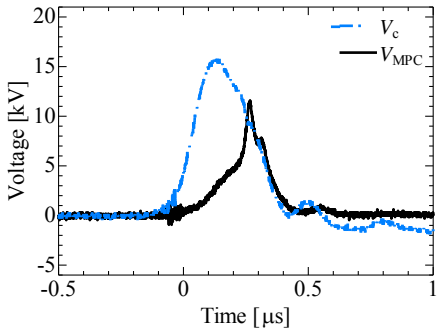

(a) Voltage waveforms

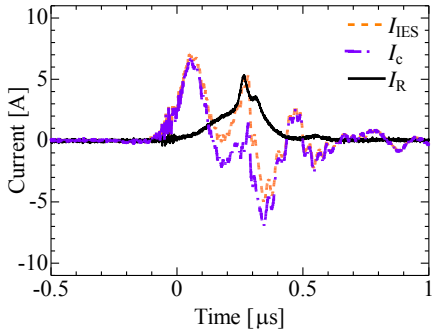

(b) Current waveforms

Fig. 7. Waveforms of voltage and current of each part

3.4. Re-design of magnetic switch

In the previous section, it was confirmed that the leakage current flowed before the MS turned on. It can be expected to decrease the leakage current by increasing the inductance of the MS. Therefore, it was tried to increase the inductance of the MS by increasing the number of turns. This also means that the on-timing of the MS is delayed. The integration period of the voltage-time product was lengthened to 315 ns from 215 ns. The voltage –time product is

$$N \cdot 2\phi_s = \int_0^{\tau'} Vdt = 4.08\ \text{mWb} \qquad (15)$$

From eq. (15) and the value in table 1, 42 was obtained as the number of turns of MS. The unsaturated inductance of the MS L_{2u} became 31.5 mH and saturated inductance L_{2s} became 1.05 nH. From eq. (7), the theoretical pulse width after compression became 15.9 ns. The new MS replaced the previous MS having the number of turns of 24. Figure 8 shows the typical waveforms of voltage and current of each part in MPC circuit in which the MS was replaced. In Fig. 8-(a), the dashed-dotted line and the solid line show the voltage V_c of C and the output voltage V_{MPC}, respectively. In Fig. 8-(b), the broken line, the dashed-dotted line and the solid line show the current I_{IES} flowing from IES, the current I_c flowing into C and the current I_R flowing through R, respectively.

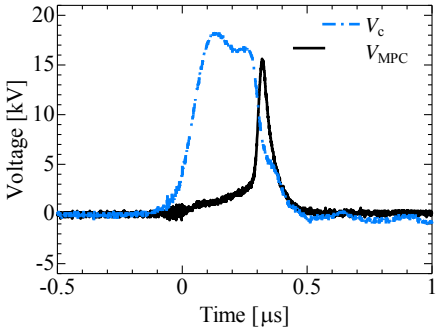

(a) Voltage waveforms

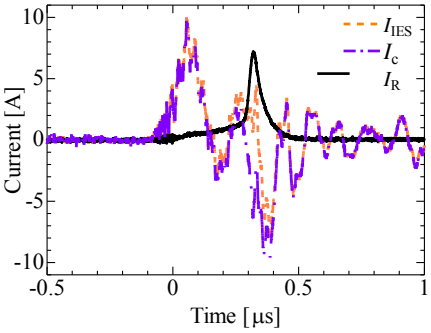

(b) Current waveforms

Fig. 8. Waveforms of voltage and current of each part

From Fig. 8-(a), at the time around 0.3 μs, it can be confirmed that V_{MPC} rises rapidly. Therefore, it is considered that MS turns on at that time. In an earlier

period before 0.3 μs, it is confirmed that the slope of V_{MPC} is smaller than that shown in Fig. 7-(a). It is conceivable that the leakage current decreases by increasing the inductance of MS. The pulse width of V_{MPC} obtained by use of redesigned MS was 51.5 ns. The dV/dt was 408 kV/μs and the peak value was 15.6 kV. The energy consumed by R was about 5 mJ per pulse. Therefore, the obtained efficiency of the IES pulsed power supply with the supplementary MPC circuit was approximately 20%.

4. Conclusions

In order to achieve higher voltage rise rate dV/dt, we attempted to shorten the output pulse width of IES system by connecting MPC circuit. As a result, we obtained the pulse voltage of 15.6 kV with FWHM of 51.5 ns and dV/dt of 408 kV/μs. The obtained efficiency of the IES pulsed power supply system with supplementary MPC circuit was approximately 20%.

References

[1] J.B. Heywood: "Internal Combustion Engine Fundamentals", McGraw-Hill, (1988).

[2] K. Tanoue, E. Hotta, and Y. Moriyoshi: "Enhancement of ignition characteristics of lean premixed hydrocarbon-air mixtures by repetitive pulse discharges", *Int. J. Engine Res.*, Vol. 10, pp.399–407 (2009).

[3] I. N. Kosarev, S.V. Kindysheva, H. L. Aleksandrov, A.Yu. Starikovskiy: "Ignition of ethanol-containing mixtures excited by nanosecond discharge above self-ignition threshold", *Combustion and Flame*, 162, pp.50–59 (2015).

[4] T. Shiraishi, T. Urushihara, M. Gundersen: "A trial of ignition innovation of gasoline engine by nanosecond pulsed low temperature plasma ignition", *Journal of Physics D: Applied Physics*, 42, pp.1-12 (2009).

[5] M. Watanabe, E. Hotta, K. Tanoue, K. Ushimaru, T. Kuboyama, Y. Moriyoshi: "Radical Measurements and Ignition Characteristics of Repetitive Nano-Pulse Discharges Plasma", *Journal of Plasma and Fusion Research*, 89, 4, pp.229-233 (2013).

[6] T. Namihira, S. Tsukamoto, D. Wang, H. Hori, S. Katsuki, R. Hackam, H. Akiyama, M. Shimizu and K. Yokoyama: "Influence of Gas Flow Rate and Reactor Length on NO Removal Using Pulsed Power", *IEEE Trans. Plasma Sci.*, 29, 4, pp.592-598 (2001).

[7] Y. Kim, W. Kang, J. Myung, S. Hong, Y. Song and S. Kim: "Experimental and Numerical Analysis of Streamers in Pulsed Corona and Dielectric Barrier Discharge", *IEEE Trans. Plasma Sci.*, 32, 1, pp.18-24 (2004).

[8] D. Wang, S. Okada, T. Matsumoto, T. Namihira and H. Akiyama: "Pulsed Discharge Induced by Nanosecond Pulsed Power in Atmospheric Air", *IEEE Trans. Plasma Sci.*, 38, 10, pp.2746-2751 (2010).

[9] M. Hara, H. Akiyama: "High-voltage Pulsed Power Engineering", Morikita publishing Co., Ltd. (1991).

[10] N. Shimizh, T. Sekiya, K. Iida, Y. Imanishi, M. Kimura, J. Nishizawa: "Over 55 kV/μs, dv/dt turn-off characteristics of 4 kV-Static Induction Thyristor for Pulsed Power Applications", Proc. 2004 Int. Symp. on *Power Semiconductor Devices & ICs*, pp.281-284 (2004).

[11] 行村建: "放電プラズマ工学", 株式会社オーム社 (2008).

Evaluation of Electron Beam Energy for Flyer Acceleration by using Intense Pulsed Power Generator

Takahiro Kudo*, Fumihiro Tamura*, Ryota Hayashi*, Naoto Takakura*, Tomoaki Ito*, Kazumasa Takahashi*, Toru Sasaki*, Takashi Kikuchi*, Nob. Harada*, Weihua Jiang*, Kenji Kashine**, Akira Tokuchi*,***, Shinsuke Fujioka****

*Nagaoka University of Technology
**National Institute of Technology, Kagoshima College
***Pulsed Power Japan Laboratory Ltd.
****Osaka University

ABSTRACT

In this study, to generate warm dense diamond-like carbon, we investigate a dependence of output energy of electron beam on the structure of electron beam diode in intense pulsed power generator "ETIGO-II." The results indicated that the fluctuation of output energy of electron beam for #10 mesh anode was higher than that for #20 mesh anode. The electron beam generated by using the curved blade with mesh anode concentrates around the center of the acrylic plate in comparison with that for the curved blade anode. These results indicate that the output energy of electron beam depends on uniformity of the electric field between the cathode and the anode. The energy fluence and the irradiation energy are evaluated by using a calorimeter with an aperture.

Keywords

Inertial Confinement Fusion, Pulsed Power, Warm Dense Matter, Thermonuclear Fusion Energy, Fast Ignition, Diamond-Like Carbon (DLC)

1 Introduction

Thermonuclear fusion energy is expected as a solution of energy problems [1]. In fast ignition of inertial confinement fusion [2], the fuel target which is compressed high density by implosion laser is satisfied ignition conditions by irradiating additional heating laser. When irradiate additional heating laser, the fuel target of fast ignition is used the guiding-cone to not affected by the ablation plasma. Diamond-Like Carbon (DLC) is one of candidates as the guiding-cone material due to the improvement of conversion efficiency because low-Z material decreases a divergence angle of the fast electron and radiation loss [3,4]. The guiding-cone becomes warm dense matter by irradiating an additional heating laser. However, physical properties of warm dense DLC, which affects the conversion efficiency in the ignition target, are unclear. We consider measuring the physical properties of warm dense DLC.

To generate warm dense DLC with well-defined state, we proposed a flyer impact method generated by intense electron beams. A flyer is accelerated by the reaction force from the expanding ablation plasma, which is generated by irradiation of the electron beams formed with the intense pulsed power generator "ETIGO-II" [5]. The ETIGO-II consists of a Marx generator, an energy-storage capacitor, a main gap switch, a pulse-forming line, an output gap switch, a pulse-transmission line, and an electron beam diode. Flyer acceleration with intense proton beam by using the ETIGO-II has been demonstrated [6]. The flyer impact method

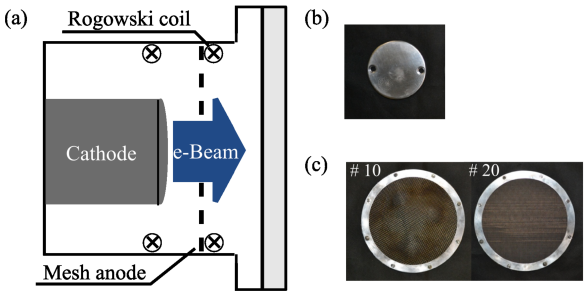

Figure 1: Configuration of electron beam diode for measurement of output energy of the electron beam for (a) electron beam diode, (b) disk cathode, and (c) mesh anode.

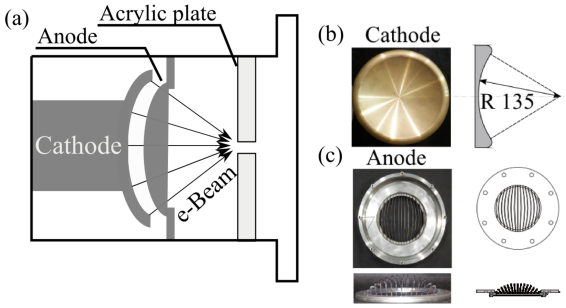

Figure 2: Configuration of electron beam diode to focus electron beam for (a) electron beam diode, (b) curved shape cathode, and (c) curved shape blade anode.

has advantages such as well-defined plasma parameters and measurable state of matter with Rankine-Hugoniot relation [7].

The flyer impact method to generate the reproducible warm dense DLC requires stable and intense electron beams. The size of the flyer and DLC being considered are tens of mm. To obtain the stable and intense electron beam, the output energy of electron beam should be evaluated. In this study, to generate the warm dense DLC by using the flyer impact with the ETIGO-II, the electron beam characteristics with the structure of the electron beam diode in the ETIGO-II is evaluated.

2 Experimental setup

Figure 1 shows a configuration of the electron beam diode for measuring the output energy of electron beam. The electron beam diode is set on the terminal of pulse transmission line (PTL) in ETIGO-II. The electron beam diode consists of a disk cathode and a mesh anode. The electron beam is emitted at the cathode surface, and passes through the mesh anode. The cathode current and the electron beam current are measured by using Rogowski coils. A gap distance between the anode and the cathode in the electron beam diode is set as 13 mm.

Figures 1(b) and (c) show the disk cathode of 210 mm diameter and the mesh anode of 300 mm diameter, respectively. The material of disk cathode and mesh anode is used for stainless steel. To investigate the dependence of output energy of electron beam on the mesh structure, the mesh anode is changed for #10 mesh (the thickness of wire is 0.4 mm) and for #20 mesh (the thickness of wires is 0.3 mm). "#10 mesh" means "10 meshes per 1 inch."

Figure 2 shows a configuration of the electron beam diode for focusing electron beam. Figures 2 (b) and (c) are photographs of the curved cathode and the curved blade anode. The material of cathode and anode were used for brass and stainless steel, respectively. To focus the generated electron beam, the electrodes are used with the curving shape having 135 mm of the curvature radius. The acrylic plate is set on 135 mm from the cathode surface. The gap distance between the anode and the cathode in the electron beam diode is 10 mm. To confirm the geometrical effect, the anode is set as the curved blade and/or the curved blade with mesh structures. The curved blade with mesh anode is made by the blade anode pasted the mesh. The focused electron beam is irradiated to the acrylic plate, which is placed to observe Lichtenberg patterns.

3 Experimental result

Figure 3 shows the typical output waveforms of ETIGO-II. The output voltages were measured in the pulse-transmission line of ETIGO-II using a capacitive voltage divider. The output energy E of electron beam was evaluated using electron beam current and the voltage of the PTL waveforms,

$$E = \int_0^{\tau_P} I_b \, V_{PTL} \, dt \qquad (1)$$

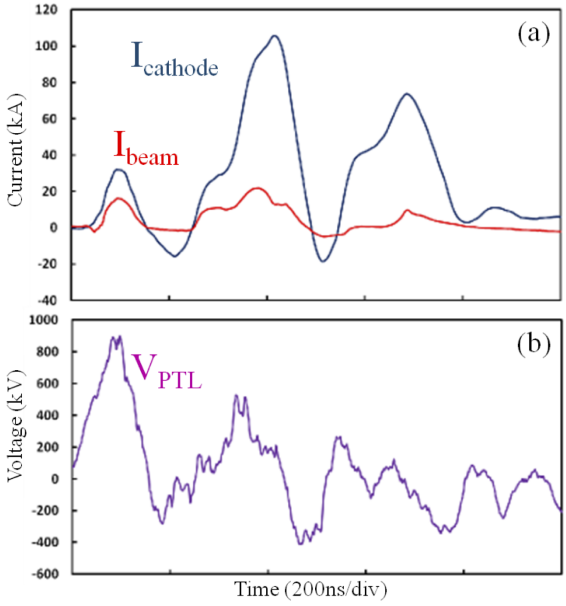

Figure 3: Typical output waveforms of ETIGO-II for (a) cathode current and electron beam current, (b) voltage of PTL.

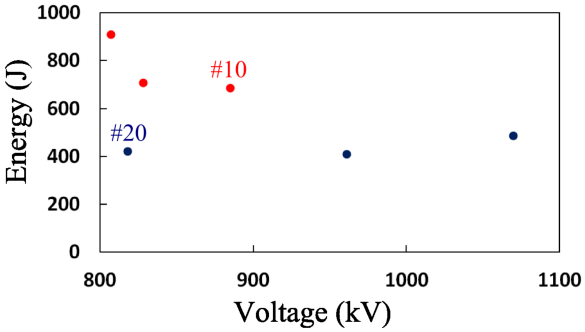

Figure 4: Output energy of electron beam at each mesh anode structure.

where, τ_p is the pulse duration of the electron beam, $I_b \equiv I_b(t)$ and $V_{PTL} \equiv V_{PTL}(t)$ are the electron beam current and the voltage of the PTL, respectively. In this case, the pulse duration of the electron beam is assumed by $\tau_p = 1\mu s$.

Figure 4 shows the evaluated output energy of electron beam on the mesh anode. The horizontal axis is used as the maximum value of the PTL voltage, because of the value fluctuates for each experiment. The output energy of electron beam for #10 mesh was higher than that for #20 mesh. However, fluctuation of output energy of electron beam for #10 mesh was larger than that for #20 mesh. It indicates that the fluctuation of

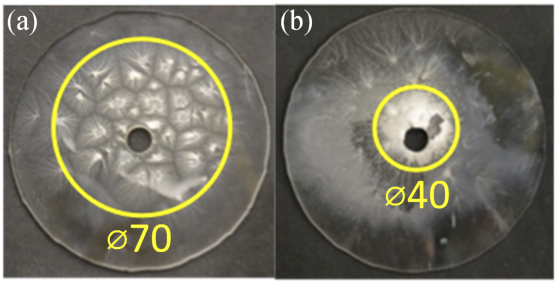

Figure 5: Acrylic plates after irradiation of electron beam, (a) for blade anode and (b) for blade and mesh anode.

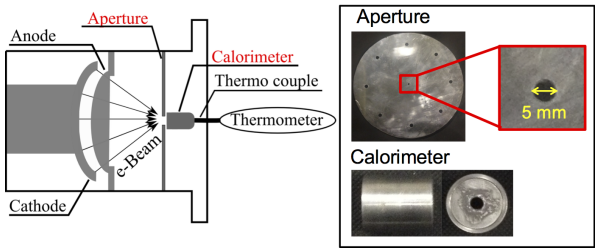

Figure 6: Setup of energy fluence measurement using calorimeter with aperture.

output energy of electron beam depends on uniformity of the electric field between the anode and the cathode. To understand the dependence of focusing the electron beam on the anode structure using curved electrodes, Lichtenberg patterns of the acrylic plate after irradiation of the electron beam were observed.

Figure 5 shows photographs of the acrylic plate after irradiation of the electron beam (a) for the "curved blade" anode and (b) for the "curved blade with mesh" anode. The electron beam for the curved blade with mesh anode concentrates around the center of the acrylic plate in comparison to that for the curved blade anode. It is found that the curved blade with mesh anode generates uniform electric field in comparison with the curved blade anode.

Figure 6 shows the output energy measurement by using a calorimeter with an aperture. The aperture diameter is 5 mm. The calorimeter is stainless steel, and has 0.5 J/gK of the specific heat c_v. The mass m of calorimeter is 79.8 g.

A part of electron beam passages through the aperture, and the calorimeter is heated up by the

electron beam irradiation. By measuring the temperature increase of the calorimeter, the input energy fluence Ψ is evaluated by

$$\Psi = \frac{c_{\mathrm{v}} m \Delta T}{S} \tag{2}$$

where ΔT is the temperature increase and $S = 19.6$ mm^2 is the area of the aperture.

The experimental result showed the temperature increase of 1.1 K. By using the above equation, the energy fluence of the electron beam is evaluated by 2.2 MJ/m^2. And then, the beam focal size is assumed by 20 mm of diameter estimated with the irradiation spot. For this reason, the irradiation energy is evaluated by about 690 J.

4 Conclusion

To generate the warm dense DLC by using flyer impact method with the intense pulsed power generator "ETIGO-II", the output energy of electron beam on the structure of the electron beam diode in ETIGO-II was investigated. The results showed that the output energy of electron beam depended on the anode structure. The fluctuation of output energy of electron beam was higher for #10 mesh than that for #20 mesh. It indicates that the output energy of electron beam stabilizes in uniformly electric field. The electron beam with the curved mesh anode was focused around the center of acrylic plate compared to that with the curved blade anode. It indicates that the curved mesh anode can generate the uniform electric field compared with the curved blade anode.

The energy fluence was evaluated by using the calorimeter with the aperture, and was estimated by 2.2 MJ/m^2. The irradiation energy was evaluated by about 690 J with from the viewpoint of the trace around the aperture.

From these results, to obtain stable and intense output energy of the electron beam, uniform electric field between the cathode and the anode is required.

Acknowledgment

This work was supported from the Grant-in-Aid for Scientific Research from the Ministry of Education, Science, Sports, Culture and Technology, Japan, and by Program for High Reliable Materials Design and Manufacturing in Nagaoka University of Technology.

References

[1] J.D. LINDL, P. AMENDT, R.L. BERGER, S.G. GLENDINNING, S.H. GLENZER, S.W. HAAN, R.L. KAUFFMAN, O.L. LANDEN and L.J. SUTER, *Phys. Plasmas*, **11**, pp.339-479 (2004).

[2] R. KODAMA, P.A. NORREYS, K. MIMA, A.E. DANGOR, R.G. EVANS, H. FUJITA, Y. KITAGAWA, K. KRUSHELNICK, T. MIYAKOSHI, N. MIYANAGA, T. NORIMATSU, S.J. ROSE, T. SHOZAKI, K. SHIGEMORI, A. SUNAHARA, M. TAMPO, K. A. TANAKA, Y. TOYAMA, T. YAMANAKA and M. ZEPF, *Nature*, **412**, pp.798-802 (2001).

[3] S. FUJIOKA, Z. ZHANG, N. YAMAMOTO, S. OHIRA, Y. FUJII, K. ISHIHARA, T. JOZAKI, A. SUNAHARA, Y. ARIKAWA, K. SHIGEMORI, Y. HIRONAKA, Y. SAKAWA, Y. NAKATA, J. KAWANAKA, H. NAGATOMO, H. SHIRAGA, N. MIYANAGA, T. NORIMATSU, H. NISHIMURA and H. AZECHI, *Plasma Phys. Control. Fusion*, **54**, 124042 (2012).

[4] P. MCKENNA, A.P.L. ROBINSON, D. NEELY, M.P. DESJARLAIS, D.C. CARROLL, M.N. QUINN, X.H. YUAN, C.M. BRENNER, M. BURZA, M. COURY, P. GALLEGOS, R.J. GRAY, K.L. LANCASTER, Y.T. LI, X.X. LIN, O. TRESCA and C.-G. WAHLSTROM, *Phys. Rev. Lett.*, **106**, 185004 (2011).

[5] W. JIANG, T. SAKAGAMI, K. MASUGATA and K. YATSUI, *Jpn. J. Appl. Phys.*, **32**, pp.L752-L754 (1993).

[6] K. KASHINE, M. YAZAWA, Nob. HARADA, W. JIANG and K. YATSUI, *Jpn. J. Appl. Phys.*, **41**, pp.4014-4018 (2002).

[7] N. OZAKI, T. SANO, M. IKOMA, K. SHIGEMORI, T. KIMURA, K. MIYANISHI, T. VINCI, F. H. REE, H. AZECHI, T. ENDO, Y. HIRONAKA, Y. HORI, A. IWAMOTO, T. KADONO, H. NAGAMOTO, M. NAKAI, T. NORIMATSU, T. OKUCHI, K. OTANI, T. SAKAIYA, K. SHIMIZU, A. SHIROSHITA, A. SUNAHARA, H. TAKAHASHI and R. KODAMA, *Phys. Plasmas*, **16**, 062702 (2009).

Radical production in Corona discharge reactor driven by SOS pulsed power generator

Hiroaki Mori, Katsuyuki Takahashi and Koichi Takaki

Department of Electrical Engineering and Computer Science, Iwate University, Morioka, Iwate 020-8551, Japan

ABSTRACT

Energy efficiency for radical production in a corona discharge reactor driven by inductive energy storage pulsed power generator using a semiconductor opening switch and an arrester. The experiment was conducted on ozone generation and NO removal to estimate O and N radical densities in the corona reactor, respectively. A coaxial reactor consisted of center rod wined with spirally-twisted tungsten wire and outer electrode was employed. The O_2 gas and N_2/NO mixed gases were injected to the reactor for ozone generation and NO removal, respectively. O and N radical densities in the plasma were ranged from 0.2 to 1.1×10^{20} m^{-3} and 1.8 to 8.0×10^{18} m^{-3} with the arrester, respectively. The energy efficiency for O radical production with the arrester was ranged from 84 to 88 g/kWh, which was about 1.6 times higher than that without the arrester. The energy efficiency for N radical production with the arrester was ranged from 24 to 52 g/kWh, which was about 9.4 times higher than that without the arrester.

Keywords

pulsed power generator, fast recovery diodes, arrester, energy efficiencies for radical productions

1. Introduction

A pulse discharge is one of the promising candidates for high-efficiency ozone (O_3) generation and nitric oxide (NO) reduction[1]-[4]. The pulse discharge develops basically in two phases; streamer corona discharge propagation phase and glow-like discharge phase[5],[6]. When a positive high voltage is applied to a center electrode (i.e., anode), a small luminous zone called a streamer head develops from the center electrode to the outer electrode (i.e., cathode). The streamer head reaches the cathode and generates an ionized filament that bridges the gap between the anode and cathode. This initial phase of the streamer propagation is called a “primary streamer”. After the arrival of primary streamer at the cathode, a subsequent streamer develops from the anode toward the cathode. That is called a “secondary streamer” or a “glow-like discharge”. The characteristics of the primary and secondary streamers are quite different. The primary streamer includes a relatively large number of high-energy electrons to dissociate molecules such as oxygen and nitrogen. Additionally, the continuous energy input during the secondary streamer phase reduces the energy efficiency for radical production owing to a decrement of the high-energy electrons[7]. Moreover, the duration time of secondary streamer phase is longer as the pulse width increases[8]. Therefore, shortening the pulse width of voltage applied to the corona reactor, to suppress the secondary streamer phase contribute to improve energy efficiency for radical production.

We developed an inductive energy storage (IES) system using semiconductor opening switch (SOS) for interruption of an inductor current within 100 ns[1],[9],[10]. The output voltage of the pulsed power generator using the SOS diodes can be changed easily by changing values of the circuit parameters[1],[11],[12]. The waveform of the voltage applied to the corona reactor can also be

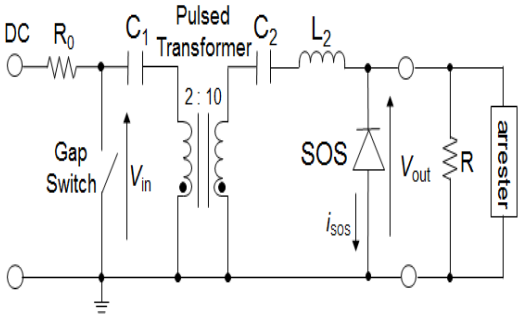

Fig. 1 Schematic diagram of the pulsed power generator using the SOS diode and the arrester.

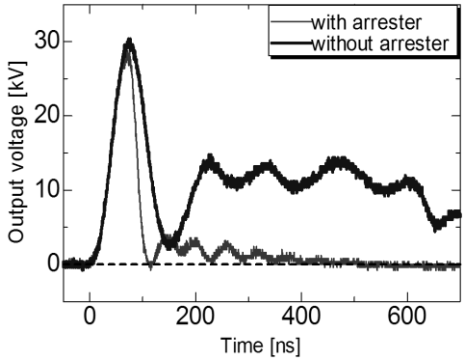

Fig. 2 Typical waveform of the output voltage without the corona reactor.

changed with the arrester connected in parallel to the reactor because the arrester can be used for diverting the short circuit to exceed the threshold voltage. In other words, the arrester is a suitable component for evaluating effect of the pulse width on radical production efficiency.

In this paper, the energy efficiencies for O radical and N radical productions in the corona reactor are evaluated at various pulse widths of the applied voltage. The pulsed voltage is generated by pulsed power generator using SOS diode with the arrester. The radical densities are estimated with O_3 generation and NO removal.

2. Experimental Setup

2.1 SOS pulsed power generator

Figure 1 shows the schematic diagram of the pulsed power generator using the SOS diode. The pulsed power generator consists of a gap switch, a primary capacitor C_1, a pulsed transformer (Hitachi

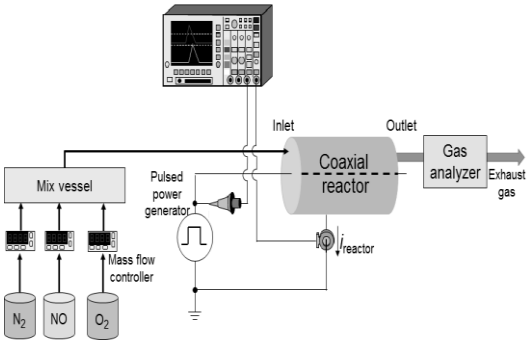

Fig. 3 Schematic diagram of the experimental setup for radical production.

Metals, Ltd., FT-3H), a secondary capacitor C_2, a secondary inductor L_2, the SOS diode, a resistor R and the arrester. The SOS diode consists of four serially and three parallelly connected fast recovery diodes (Voltage multipliers Inc., K100UF, 10kV/100A, reverse recovery time 100 ns). The arrester consists of seven serially connected surge-absorbers (Mitsubishi Materials, DSA-362MA). The capacitance of C_1 and C_2 are 20 and 4.0 nF, respectively. The inductance of L_2 is 20 μH. The turn ratio of pulsed transformer is 2:10. The resistance of R is 20 kΩ. The C_1 is charged by a DC voltage power supply. After closing the gap switch, the charge stored in C_1 flows through the pulse transformer to the SOS diode in forward direction. After the pulsed transformer saturates magnetically, the charge stored in C_2 flows through the SOS diode in reverse direction. Then the current in the SOS diode is rapidly interrupted. As a result, a pulse voltage is generated by an induced electromotive effect.

Figure 2 shows typical waveform of output voltage when the corona reactor is not connected. The full width at half maximum (FWHM) of pulse width is 47 ns with the arrester and is 70 ns without the arrester. The output voltage duration time is significantly reduced with connecting the arrester.

2.2 Radical production

Figure 3 shows a schematic diagram of the experimental setup for radical production. The coaxial corona discharge reactor consists of 2 mm

stainless wire of the center electrode and 28 mm inner diameter stainless cylinder with the 300 mm in length. The center rod electrode is wrapped with a spirally twisted tungsten wire of 0.2 mm diameter with 5 mm intervals to reduce the corona onset voltage[13]. The experiment was conducted on O_3 generation and NO removal to estimate O and N radical densities, respectively. In the case of O_3 generation, the oxygen gas is fed into the reactor at gas flow rate of 2 L/min. The ozone concentration is measured using an O_3 monitor (Ebara Jitsugyo, EG-2001B). In the case of NO removal, the NO gas is diluted with nitrogen (N_2) and is fed into the reactor at gas flow rate of 5 L/min. The NO initial concentration is set to be 200 ppm. The concentration of NO is measured using a gas analyzer (BEST Sokii, BCL-511) at the outlet of the reactor. The voltage applied to the corona reactor and the current in the corona reactor are measured using a high-voltage probe (Tektronix, P6015A) and a current transformer (Bergoz, CT-D1.0-B), respectively. Digital oscilloscope (Tektronix, DPO-4104B) is used to record the voltage and the current signals. The pulse repetition rate is changed from 5 to 80 pps. The energy consumption in the corona reactor U per one pulse is calculated by integrating the electric power obtained by the applied voltage and the current in the corona reactor. The input energy density w [J/L] is expressed as

$$w = \frac{60 \cdot U \cdot f}{q} \text{[J/L]} \quad \cdots\cdots\cdots\cdots (1),$$

where U [J] is the energy consumption per one pulse in the corona reactor, f [pps] is pulse repetition rate and q [L/min] is gas flow rate. The NO removal efficiency NO_{removal} is expressed as

$$NO_{removal} = \frac{NO_{initial} - NO_{treatment}}{NO_{initial}} \times 100 [\%] \quad \cdots\cdots (2),$$

where NO_{initial} [ppm] is the NO initial concentration (200 ppm), $NO_{\text{treatment}}$ [ppm] is the NO concentration after discharge treatment. O and N radicals are estimated under the assumption that O_3 generation and NO removal reactions are dominant reactions in the plasma at O_3 generation concentration in the range from 0 to 500 ppm and at NO removal efficiency in the range of 0 to 20%, respectively. Energy efficiency for radical production η [g/kWh] is expressed as

$$\eta = \frac{60 \cdot q \cdot [\text{A}] \cdot M}{N \cdot P} \times 10^{-3} \text{ [g/kWh]} \quad \cdots\cdots (3),$$

where q [L/min] is gas flow rate, [A] [ppm] is concentration of O and N radicals, M is molecular weight of O and N radicals, and P [W] is the power consumed in the reactor.

Table. 1 Reactions and rate coefficient of main reactions in the case of O_3 production.

NO.	Reaction	Rate coefficient
R1	$O+O_2+M \rightarrow O_3+M$	$6.2*10^{-34}(T/300)^{-2}$
R2	$O+O+M \rightarrow O_2+M$	$1.3*10^{-32}(T/300)^{-1}$ exp(-170/T)
R3	$O_3+O \rightarrow 2O_2$	$8.4*10^{-12}$exp(-2060/T)

Table. 2 Reactions and rate coefficient of main reactions in the case of the NO removal.

NO.	Reaction	Rate coefficient
R4	$NO+N \rightarrow N_2+O$	$3.4*10^{-11}$exp(-24/T)
R5	$NO+O+M \rightarrow NO_2+M$	$1.0*10^{-31}(T/300)^{-1.8}$
R6	$N+N+M \rightarrow N_2+M$	$1.78*10^{-33}$exp(485/T)
R7	$N+O+M \rightarrow NO+M$	$5.46*10^{-33}$exp(155/T)
R8	$O+O_2+M \rightarrow O_3+M$	$5.7*10^{-34}$ $(T/300)^{-2}$
R9	$NO+O_3 \rightarrow NO_2+O_2$	$1.4*10^{-12}$exp(-1310/T)
R10	$NO_2+O+M \rightarrow NO_3+M$	$9.02*10^{-32}$exp(T/298)$^{-2}$
R11	$NO_2+O \rightarrow NO+O_2$	$6.5*10^{-12}$exp(120/T)
R12	$NO_2+O_3 \rightarrow NO_3+O_2$	$1.2*10^{-13}$exp(-2450/T)
R13	$2NO_2+M \rightarrow N_2O_4+M$	$1.4*10^{-33}$ $(T/300)^{-3.8}$
R14	$NO_3+NO_2+M \rightarrow N_2O_5+M$	$2.7*10^{-30}$ $(T/300)^{-3.4}$
R15	$NO_3+NO \rightarrow 2NO_2$	$1.6*10^{-11}$exp(150/T)
R16	$N_2O_4+M \rightarrow 2NO_2+M$	$1.3*10^{-5}(T/300)^{-3.8}$ exp(-6400/T)
R17	$N_2O_5+M \rightarrow NO_2+NO_3+M$	$1.3*10^{-3}(T/300)^{-3.5}$ exp(-11000/T)

2.3 Radical derivation process

Table 1 and 2 show the reactions and rate coefficient of main reactions in the case of O_3 production and the NO removal[14]-[21]. M is the third collision partner; it takes part in energy absorption, but does not react chemically, and T is gas temperature. The dominant reactions concerned

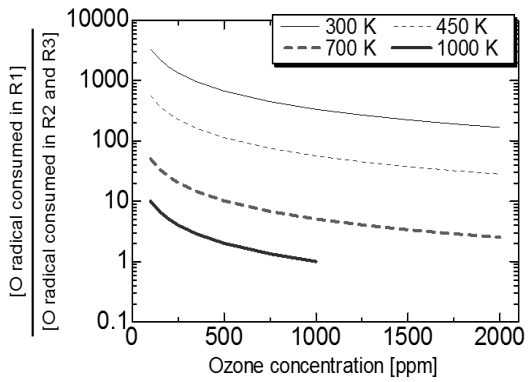

Fig. 4 The ratio of O radical consumed in the reaction (R1) to that in reactions (R2) and (R3) calculated as a function of ozone concentration.

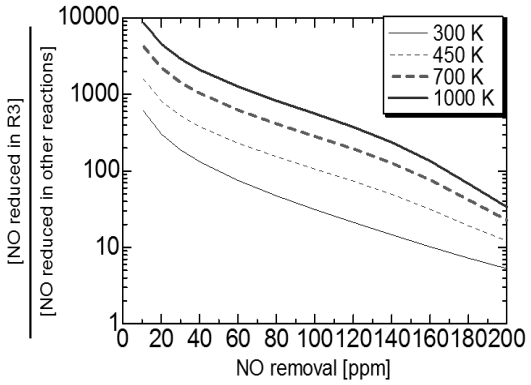

Fig. 5 The ratio of NO reduced in the reaction (R4) to that in other reactions calculated as a function of NO removal.

with O_3 production process in the plasma are O_3 production reaction (R1) and decomposition reaction of O_3 (R3). Since the rate constant of (R1) decreases and the rate constant of (R3) increases with increases with increasing T, the ozone production decreases with increasing gas temperature. Figure 4 shows the ratio of O radical consumed in the reaction (R1) to that in reactions (R2) and (R3) calculated as a function of the O_3 concentration under various gas temperatures. The ratio decreases with increasing the O_3 concentration and the gas temperature. In the glow-like discharge, the gas temperature increases with the lapse of time, which reaches up to about 450 K at 100 ns in sustained time of the discharge[8]. When the gas temperature and O_3 concentration are less than 450 K and 500 ppm, respectively, number of O radical consumed in (R1) is at least 100 times higher than that in (R2) and (R3). In this condition, since the O radical generated by the discharge is mostly consumed in the reaction (R1), the reactions (R2) and (R3) can be assumed negligible. Therefore, the production rate of O_3 and O radical can be obtained as

$$\begin{cases} \mathrm{d[O_3]}/\mathrm{d}t = k_1[\mathrm{O_2}][\mathrm{O}][\mathrm{M}] \\ -\mathrm{d[O]}/\mathrm{d}t = k_1[\mathrm{O_2}][\mathrm{O}][\mathrm{M}] \end{cases} \cdots\cdots\cdots (4),$$

where k_1 is the rate constant of reaction (R1). Thus, O radical density can be estimated by O_3 concentration.

In the gas mixture of N_2 and NO, NO is mainly reduced through the decomposition by N radical through the reaction (R4). Some species such as O and O_3 produced in the NO removal process contribute to the NO reduction and NO_2 oxidization as shown in table2. Figure 5 shows the ratio of NO reduced by N radical in the reaction (R4) to that in other reactions calculated as a function of the NO concentration under various gas temperatures. The ratio decreases with increasing the NO removal and the gas temperature. When the gas temperature and NO removal are less than 450 K and 40 ppm, respectively, number of NO reduced in (R4) is at least 100 times higher than that in other reactions. In this condition, since the NO is mostly reduced in the reaction (R4), the other reactions can be assumed negligible. Therefore, the decomposition rate of NO and N radical can be obtained as

$$\begin{cases} -\mathrm{d[NO]}/\mathrm{d}t = k_4[\mathrm{NO}][\mathrm{N}] \\ -\mathrm{d[N]}/\mathrm{d}t = k_4[\mathrm{NO}][\mathrm{N}] \end{cases} \cdots\cdots\cdots (5),$$

where k_4 is the rate constant of reaction (R4). Thus, N radical density can be estimated by NO removal.

3. Results

3.1 O radical production

Figure 6 shows the ozone concentration as a function of the input energy density. The ozone concentration increases with increasing the input energy density. Figure 7 shows the O radical number

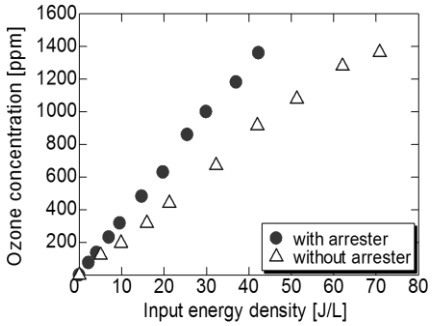

Fig. 6 Ozone concentration as a function of input energy density with and without the arrester.

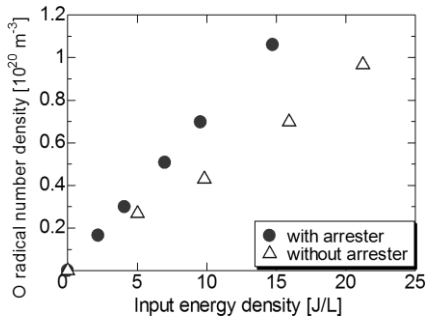

Fig. 7 O radical number density as a function of input energy density with and without the arrester.

density as a function of the input energy density. The O radical density is ranged from 0.2×10^{20} to 1.1×10^{20} m^{-3} with the arrester. Figure 8 shows the energy efficiency for O radical production as a function of the O radical number density. The energy efficiency for O radical production is ranged from 84 to 88 g/kWh with the arrester and from 51 to 63 g/kWh without the arrester. The energy efficiency with the arrester is approximately 1.6 times higher than that without the arrester.

3.2 N radical production

Figure 9 shows the NO removal efficiency as a function of the input energy density. The NO removal efficiency increases with increasing input energy density. Figure 10 shows the N radical number density as a function of the input energy density. The N radical number density is ranged from 1.8×10^{18} to 8.0×10^{18} m^{-3} with the arrester. Figure 11 shows the energy efficiency for N radical

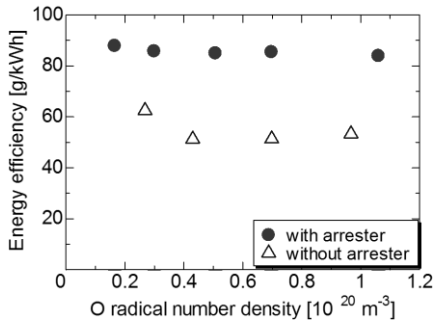

Fig. 8 Energy efficiency for O radical production as a function of O radical number density with and without the arrester.

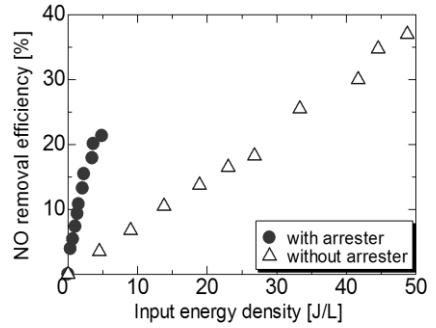

Fig. 9 NO removal efficiency as a function of input energy density with and without the arrester.

production as a function for the N radical number density. The energy efficiency of N radical production is ranged from 24 to 52 g/kWh with the arrester and from 3.3 to 3.5 g/kWh without the arrester. The energy efficiency with the arrester is approximately 9.4 times higher than that without the arrester.

3.3 Electrical property

Figure 12 shows typical waveforms of the applied voltage, discharge current, energy consumption, and the impedance between the electrodes with and without the arrester in the case of oxygen injection. The discharge current is obtained by subtracting the displacement current (i_c) from the total current in the corona reactor, calculated by following equations[22];

$$i_C = C_e \frac{dV}{dt}\text{[A]} \quad \cdots\cdots\cdots\cdots\cdots\cdots \quad (6),$$

$$i_d = (i_0 - i_c) = i_0 - C_e \frac{dv}{dt}\text{[A]} \quad \cdots\cdots\cdots\cdots \quad (7),$$

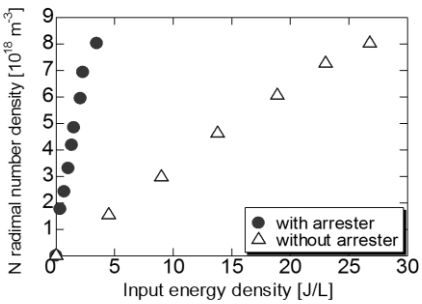

Fig. 10 N radical number density as a function of input energy density with and without the arrester.

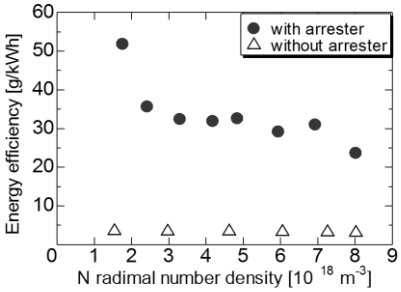

Fig. 11 Energy efficiency for N radical production as a function of N radical number density with and without the arrester.

where v is the applied voltage at the center electrode of the corona reactor, C_e is the capacitance of the corona reactor of 9.0 pF, i_d is discharge current, and i_0 is the total current in the corona reactor. The impedance between the electrodes is calculated by dividing the applied voltage at the center electrode by the discharge current. The pulse width is 32 ns with the arrester and is 103 ns without the arrester. The energy consumption in a pulse is 6.1 mJ with the arrester and is 30 mJ without the arrester. The energy consumption with the arrester is 5 times lower than that without arrester in the case of oxygen injection. The impedance decreases below several kΩ gradually, which indicates that the discharge phase transformed to the glow-like discharge[8]. By the shortening pulse width with the arrester, the decrease of the impedance is inhibited and the duration of the glow-like phase is reduced[8]. The energy into the reactor with the glow-like discharge is consumed to heat the plasma

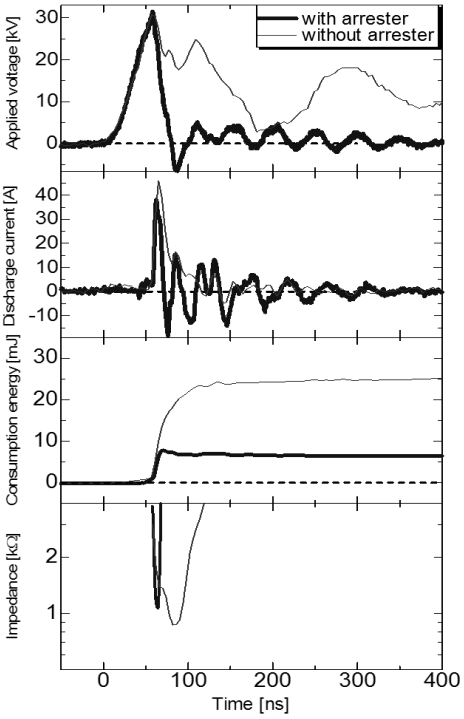

Fig. 12 Typical waveforms of the applied voltage, discharge current and energy consumption for ozone generation.

through a Joule heating process because of low impedance compared with the streamer discharge[8]. Therefore, the shortening pulse width of the applied voltage contributes to improve the energy efficiency for O radical production.

Figure 13 shows typical waveforms of the applied voltage, discharge current, energy consumption, and the impedance between the electrodes with and without the arrester in the case of N_2 and NO mixed gases injection. The FWHM of pulse width is 34 ns with the arrester and is 47 ns without the arrester. The energy consumption is 6.6 mJ with the arrester and is 70 mJ without the arrester. The energy consumption with the arrester is 10.6 times lower than that without the arrester. The impedance is kept low value during the output voltage is maintained without the arrester, which indicates that the glow-like discharge is sustained. The duration of the glow-like phase is approximately 600 ns without the arrester and is significantly reduced with the arrester. In the case of O_2 containing gas, the conductance

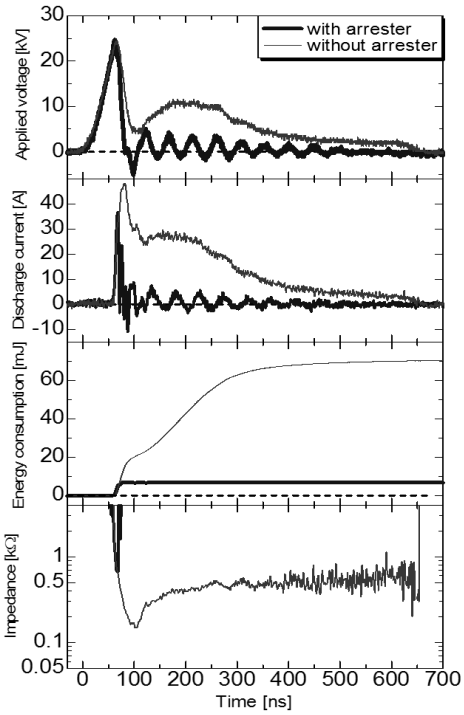

Fig. 13 Typical waveforms of the applied voltage, discharge current and energy consumption for NO removal.

and sustained time of the discharge decrease with increasing O_2 concentration due to electron attachment of O_2[7]. Therefore, in comparison with O radical production with O_2 gas infection, the shortening the pulse width of the applied voltage is particularly effective for the improvement of the energy efficiency for N radical production with N_2/NO mixed gas infection.

4. Conclusions

The energy efficiencies of O radical and N radical productions in the corona reactor are evaluated at various pulse widths of the applied voltage. The energy efficiency for O radical production is ranged from 84 to 88 g/kWh with the arrester, which is approximately 1.6 times higher than that without the arrester. The energy efficiency for N radical production is ranged from 24 to 52 g/kWh with the arrester, which is approximately 9.4 times higher than that without the arrester.

Acknowledgments

The author would like to thank Dr. S. Mukaigawa at Iwate University for their valuable comments and discussions. The author would also like to thank Mr. Shida at Iwate University technical staff. This work was supported by a Grant-In-Aid of Science Research from Japan Ministry of Education, Science and Culture (JSPS Fellowship NO. 21246047).

References

[1] K.Takaki et al., “Influence of Circuit Parameter on Ozone Synthesis Using Inductive Energy Storage System Pulsed Power Generator”, IEEE Trans. Dielectr. Insul., **18**, 5, pp.1752-1758(2011).

[2] T. Namihira et al., “Improvement of NO_x removal efficiency using short-width pulsed power”, IEEE Trans. Plasma Sci., **28**, 2, pp.434-422(2000).

[3] D. Wang et al., “Development of higher yield ozonier based on Nano-seconds pulsed disharge”, J. Adv. Oxid. Technol., **13**, 1, pp. 71-78(2010).

[4] T. Matsumoto et al., “Energy Efficiency Improvement of Nitric Oxide Treatment Using Nanosecond Pulsed Discharge”, IEEE Trans. Plasma Sci., **38**, 10, pp.2639-2643(2010).

[5] R. Ono et al., “Formation and structure of primary and secondary streamers in positive pulsed corona discharge – effect of oxygen concentration and applied voltage”, J. Phys. D: Appl. Phys., **36**, 16, pp. 1952-1958(2003).

[6] D. Wang et al, “Positive- and Negative-Pulsed Streamer Discharges Generated by a 100-ns Pulsed-Power in Atmospheric Air”, IEEE Trans. Plasma Sci., **35**, 4, pp. 1098-1103(2007).

[7] R. Ono et al., “Effect of pulse width on the production of radicals and excited species in a pulsed positive corona discharge”, J. Phys.D : Appl. Phys., **44**, 48, 485201(2011).

[8] T. Namihira et al, “Introduction of Nanoseconds Pulsed Dscharge Plasma and its Applications”, IEEF Trans. FM, **129**, 1, pp. 7-14(2009).

[9] I. Yagi et al., “Effect of Pulse Width on Ozone Yield using Inductive Energy Storage System Pulsed Power Generator”, IEEF Trans. FM, **130**, 6, pp. 549-544(2010).

[10] S.N.Rukin, ”High-Power Nanosecond Pulse Generator Based on Semiconductor Opening Switch(Review)”, Instruments and experiment Techniques, **42**, 4, pp.439-467(1999).

[11] I. Yagi et al., “Streamer Propagation of Nanosecond Pulse Discharge With Various Rise Times”, IEEE Trans. Plasma Sci., **39**, 11, pp. 2232-2233(2011).

[12] T. Sugai et al., “Influence of a Circuit Parameter for Plasma Water Treatment by an Inductive Energy Storage Circuit Using Semiconductor Opening Switch”, IEEE Trans. Plasma Sci., **41**, 4, pp. 967-974(2013).

[13] T. Kakuta et al., “Development of nanosecond-pulse generator using fast recovery diodes and its application for ozone yield improvement using arresters”, JIEED Japan, **56**, 2, pp. 7-12(2013).

[14] B.Eliasson et al., “Ozone synthesis from oxygen in dielectric barrier discharge”, J. Phys.D : Appl. Phys., **20**, 11, pp.1421-1437(1987).

[15] N.Tabata, “Ozone Generation and Generation Efficieny”, J. Plasma and Fusion Res., **74**, 10, pp.1119-1126(1998).

[16] R. Atkinson et al., “Evaluated Kinetic and Photochemical Data for Atmospheric Chemistry; Supplement III”, J. Phys. Chem, Ref. Data, **18**, 2, pp.881-1097(1989).

[17] R. Atkinson et al., “Evaluated kinetic and photochemical data for atmospheric chemistry: Volume 1-gas phase reaction of Ox,HOx,Nox and SOx species”, Atmos. Chem. Phys, **4**, pp.1461-1738(2004).

[18] Clyne, M.A.A, et al., “Rate of recombination of nitrogen atoms”, J. Phys. Chem, **71**, pp.3071-3073(1967).

[19] I.M.Campbell, et al., “Rate constants for $O^{(3P)}$ recombination and association with $N^{(4S)}$”, Chem. Phy. Lett, **18**, 4, pp.607-609(1973).

[20] R. Atkinson, et al., “Evaluated kinetic and photochemical data for atmospheric chemistry: supplement VI. IUPAC subcommittee on gas kinetic data evaluation for atmospheric chemistry”, J. Phys. Chem. Ref. Data, **26**, pp.1329-1499(1997).

[21] P. Norrell, et al., “Falloff curve and specific rate constants for the reaction nitrogen dioxide+ nitrogen dioxide .dblarw. nitrogen oxide (N2O4)”, J. Phys. Chem, **92**, 15, pp.4377-4384(1988).

[22] R. Ono et al., “Measurement of OH Radical in Pulsed Corona and Pulsed Dielectric Barrier Discharge”, IEEJ Trans. FM, **123**, 9, pp. 920-925(2003).

Development of Counter-facing Discharge Device for Extreme Ultraviolet Source

～Control of Current Waveform and Its Effects on the Plasma Dynamics～

Tomoaki Kawasaki, Kouki Kanou, Daisuke Nishii*, Tatsuya Sodekoda**, Hajime Kuwabara**, Mitsuo Nakajima, Kazuhiko Horioka

Department of Energy Sciences, Tokyo Institute of Technology
Nagatsuta 4259, Midori-ku, Yokohama, 226-8502, Japan

**Department of Mechano-Aerospace Engineering, Tokyo Institute of Technology*
Nagatsuta 4259, Midori-ku, Yokohama, 226-8503, Japan

***Advanced Applied Department, IHI Corporation,*
1 Shin-nakaharacho, Isogo-ku, Yokohama, Kanagawa, 235-8501, Japan

ABSTRACT

We studied the effect of rise time of discharge current on the EUV output from the Li plasma in counter-facing discharge device and investigated the plasma dynamics in the device. Results indicated the waveform can control the plasma dynamics and improve the conversion efficiency. The EUV output depended on the shot number in a successive operation mode. The results indicated that changes of Li surface condition during the successive operation affect the plasma dynamics.

Keywords

Key Words : EUV light source, Plasma focus, High energy density plasma, Pulsed current waveform

1. Introduction

The miniaturization of integrated circuits (ICs) has contributed to the technological progress of modern societies because the smaller the IC is, the more efficient electronic devices become. Photolithography in the microfabrication processes uses a light source to transfer a circuit pattern from a mask to a light-sensitive chemical photoresist on a semiconductor wafer [1]. Therefore, it is important to develop a shorter wavelength light source for the miniaturization of ICs.

Recently, plasma-based extreme ultraviolet (EUV) light sources have been developed for the next generation lithography. EUV is a wavelength region corresponding to a range of 0.2 – 100 nm [2] in which the photons are easily absorbed by various substances. A multilayer mirror using Mo/Si, which has reflectivity of about 70% at the wavelength of 13.5 nm [3,4], was developed to accommodate the optical system of lithography.

The EUV light is contained in a radiation from a high energy density plasma (T_e=10~30eV, n_e=10^{18}~10^{19} cm^{-3}) [5]. There are mainly three ways to produce the EUV photons at the wavelength of 13.5 nm. They are a synchrotron radiation, radiation from a Laser Produced Plasma (LPP), and a Discharge Produced Plasma (DPP). As the synchrotron radiation source is extremely expensive, it is not appropriate for the industrial use. The plasma-based radiation sources are more practical compared to the synchrotron radiation. In the case of LPP, the EUV plasma is produced by focusing a

pulsed laser on a target, while DPP utilizes a hot and dense plasma produced by a pulsed discharge [6,7]. Although LPP is a simple scheme to produce the EUV emission, the laser efficiency is a bottleneck of the application because it extremely degrades the plug-in efficiency and increases the operating costs. In contrast to the LPP sources, DPP is much more practical scheme because the electrical energy is directly converted to EUV plasma [7].

In order to realize an efficient EUV light source, we have developed a counter-facing plasma focus system [7]. From the proof-of-principle study so far, we assured that the pulse output of EUV light was typically 100mJ per shot. The next step is to demonstrate an average power exceeding 200W or more at 13.5nm (2% bandwidth) [8]. Therefore, the final goal of our research is to operate the device continuously with repetition of 1kHz – 10kHz.

However, there are some problems. One is electrodes damage when the device operates repetitively. One of the causes of the damage is considered to be joule heating by the pulsed current. Although the problem may be solved by reducing the drive current, the output of EUV tends to decrease. We need to optimize the waveform of pulsed current in order to prevent the decline of output of EUV. In addition, the optimization can lead to the improvement of the plug-in efficiency.

It is expected that it takes time until the discharge plasma starts to move by the Lorentz force because the rising time of the pulsed current is limited by the circuit parameter. The Li vapor proceeds to evaporate and expand while the current is still low level. If the rising rate of current is low at the initial phase of operation, the quantity of plasma which moves to the place of EUV radiation may be too much and the acceleration of plasma is not enough to come up to a hot-dense plasma which emits the EUV light.

In this paper, we discuss the effect of current rise rate on the plasma dynamics, in which we tried to increase the output of EUV with a fast rising current made by additional capacitors.

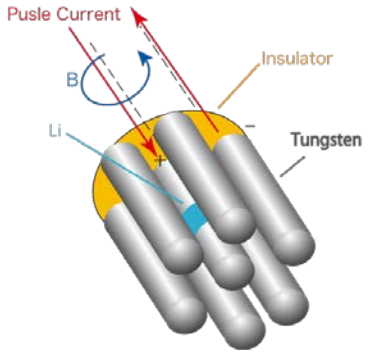

Fig.1. Electrode geometry of counter-facing plasma focus device.

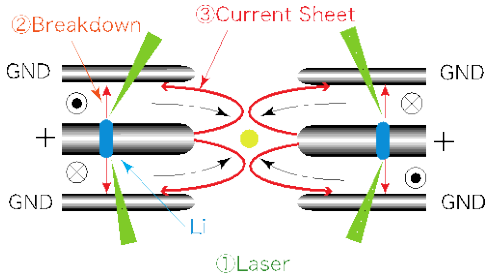

Fig.2.Schematic illustration of counter-facing plasma focus device.

2. Experimental Setup

2.1 Counter-facing Plasma Guns for EUV Light Sourse

Figure 1 shows a component of the plasma focus devices which consists of seven electrodes; a center electrode with a positive voltage and six outer ones with ground potential. For the plasma source, a target (Li) is set up in the middle of the center electrode.

A couple of the focus electrodes are facing each other and the operation procedure is shown schematically in Fig. 2. At first, capacitors connected between the center electrode and the outer electrodes are charged to ～ 7 kV and a Laser (Nd : YAG – 2 ω) irradiates the Li sources at the middle of two center electrodes. Then, the pulsed currents are induced through the plasma by the laser ablation. The plasma is accelerated to the center of the counter-facing electrodes by the Lorentz force. The plasmas which move from the counter-facing electrodes collide and thermalize at the center of electrodes. Then a high energy density plasma is

generated through the thermalization of the plasma. We designed the time-constant of discharge current to be more than μsec. Therefore, we can expect that the plasma is confined at the place and emits an EUV light during an order of μsec.

2.2 Relation between rising time of the pulsed current and the EUV output

The plasma is accelerated by the Lorentz force as schematically shown in Fig. 2. However, the pulsed currents hardly flow through the plasma right after the laser ablation because the breakdown process depends on the particle distribution between the electrodes. The evaporation and the expansion of Li last during the operation time. Then, the mass of plasma is expected to depend on the breakdown time from the laser irradiation. As has been discussed in the introduction, if the mass is too much compared with an appropriate quantity, the output of EUV decreases because the energy to be distributed to the electrons decrease. That is, the electron temperature does not rise sufficiently when they collide and thermalize at the center of electrodes.

In this experiment, we added a peaking capacitor to drive an additional current in the conventional RC circuit and modified the current waveform as shown in Fig. 3. Then, we compared the output of EUV light with and without the additional current.

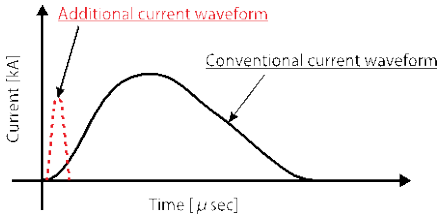

Fig. 3. Modification of current waveform.

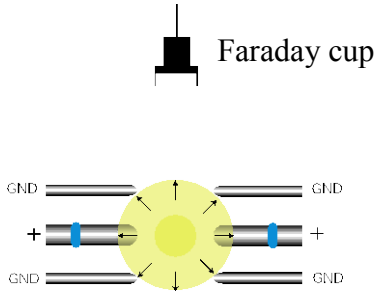

Fig. 4. Schematic of the ion flux measurements.

2.3 Observation of the ion flux after the formation of high energy density plasma

We set up a Faraday-cup 34cm above the center of counter-facing electrodes to investigate the plasma dynamics in the device. A schematic of the configuration is shown in Fig. 4. We can expect to observe the ion flux after time-of-flight of the EUV plasma, namely several μsec from the laser ablation, if the plasma is accelerated, thermalized, and confined in the place during the order of ~μsec.

3. Results and Discussion

3.1 Evaluation of the effect of additional circuits

Figure 5 shows a comparison of current waveforms driven by (a) the conventional circuit and (b) the modified one. As shown in the figure, the first peak made by the additional circuit corresponded to roughly 30% of the maximum peak. The rise time to reach 30% of the maximum peak from the laser breakdown was 70 nsec in the case of (a), while it reduced to 60 nsec in the case of (b). Therefore, we know that the additional circuit slightly increased the rising rate of the current.

3.2 The output of EUV light

Figure 6 compares typical EUV signals obtained from the plasma driven by the currents (a) without and (b) with additional circuit. Although similar waveforms of EUV shown in (b) was observed in the case of the conventional current waveform too, the higher peak signal (≧ 6 V) tended to appear in the case of (b). We observed that the peak of the EUV output tended to increase by the waveform modification.

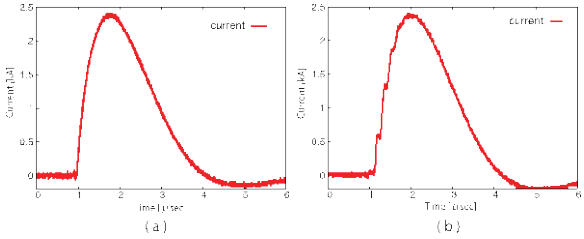

Fig. 5. Comparision of current waveforms driven by (a) conventional circuit and (b) modified one.

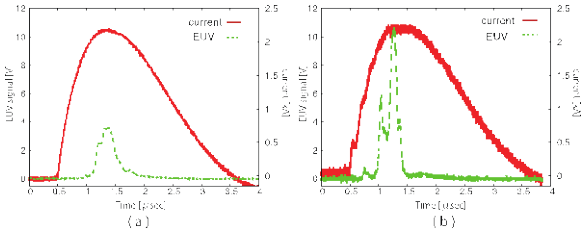

Fig. 6. EUV waveforms (a) without and (b) with additional capacitors.

3.3 Two characteristic EUV waveforms in the case of the modified current waveform

We observed that the EUV waveforms have two modes in the case of the modified current waveform. The EUV waveform shown in Fig. 7 (a) was observed frequently right after starting the experiment, while the one shown in Fig. 7 (b) was observed after successive operation of about 20 times. We think two modes of EUV waveforms are caused by the imprint of Li surface due to the laser ablation. A schematic of the ablation from smooth (a) and the imprinted surface (b) is shown in Fig. 8.

It is expected that the plasma made by the laser ablation expands spherically as shown in Fig.8 (a) if the Li surface is smooth, while it should expand with oval shape if the surface is imprinted by the successive laser irradiations as shown in Fig. 8 (b). The results indicate that the plasma formation process depends on the condition of Li surface. In other words, the value of the plasma quantity moving to the center depends on the Li surface condition in the case of solid plasma source.

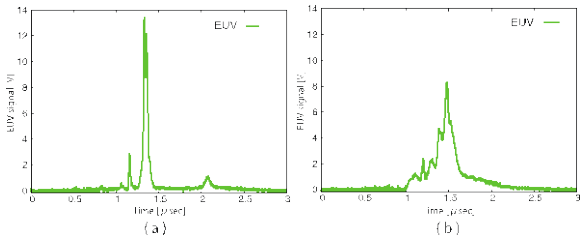

Fig. 7. Typical EUV waveforms;
(a) with narrow peak and (b) broad peak.

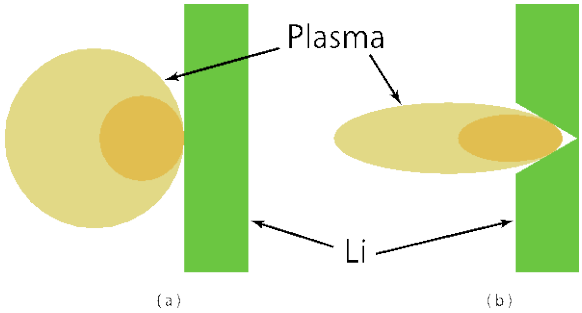

Fig. 8. Ablation of the plasma from (a) smooth and (b) imprinted surfaces.

3.4 Plasma dynamics after plasma thermalization

After the thermalization, the plasma is expected to be confined during the current pulse. After that, the plasma should expand isotropically when the EUV plasma is confined properly. To confirm the behavior, we placed a Faraday-cup 34 cm above the plasma. We can expect an ion flux waveform which has a peak after several μsec from the laser ablation if the plasma is properly confined during several μsec.

Figure 9 shows typical ion flux waveforms. There were two kinds of EUV waveforms as shown in the figure. The first peaks of about 2 μsec duration shown in both figures are considered to be the signal by a photoelectric effect. The peak at 6 ~ 8 μsec did not appeared in the case of (a), while the one appeared in the case of (b). This peak was expected to be the signal of the ion flux originated from the confined plasma.

Therefore, we know that the cause of the narrow EUV waveform in the case of (a). That is, in the case (a), the plasma temperature reaches the appropriate value for irradiating EUV light in a moment, it can not keep the state for several μsec, probably due to the non-uniformity of current sheet. Then, the current sheet can not keep the EUV plasma for the time duration. The arrival times of the current sheets seem to be different due to jitters of the discharge channels. Consequently, the plasma cannot keep a quasi-stable state in the case shown in Fig. 9 (a).

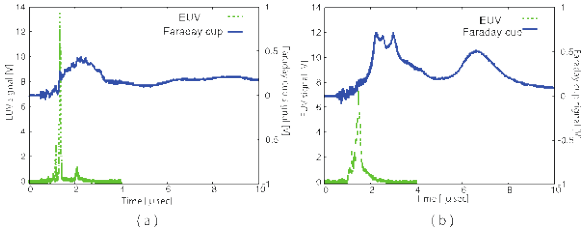

Fig. 9. Correlation of ion flux and EUV waveforms (a) with narrow peaks and (b) broad peaks.

4. Conclusions

We investigated the effect of current waveform on EUV-signals by placing additional capacitors in the discharge circuit. A highly peaked signal (≧ 6 V) appeared in the operation driven by the modified circuit. In addition, there were two modes in the EUV waveforms with the additional circuit; the narrow peaked and the broad ones.

We set up a Faraday-cup (to observe the ion flux) above the center of the counter-facing electrodes to examine whether the plasma is confined in the right place for several μsec. The EUV waveform had a broad peak width when the plasma was observed after 6 ~ 8 μsec from the laser ablation. Therefore, we could interpret that the plasma was confined as expected, if the EUV waveform had the broad peak.

Results also showed that waveform can control the plasma dynamics. Decreasing the rising time of pulsed current is likely to lead the output increase of EUV light. That is, the waveform control has a possibility not only to prevent the electrode damage but improve the plug-in efficiently also.

References

[1] W. Christian and et al., “EUV LITHOGRAPHY Lithography gets extreme”, *NATURE PHOTONICS*, **4**, 1, pp.24-26 (2010).

[2] D.Attwood, “SOFT X-RAYS AND EXTREME ULTRAVIOLET RADIATION : Principles and Applications”, Cambridge University Press, pp.1-2(1999).

[3] N. Benoit et al., “Radiation stability of EUV Mo/Si multilayer mirrors”, *PHYSICA B-CONDENSED MATTER*, **357**, 1-2, pp.222–226 (2005).

[4] S. Yulin et al., “EUV/soft x-ray multilayer optics”, *SPIE*, **5645**, pp.289–298 (2005).

[5] Majid Masnavi et al., “Estimation of optimum density and temperature for maximum efficiency of tin ions in Z discharge extreme ultraviolet sources”, *Journal of Applied Physics,* Vol.101, No.3, pp. 033 306 1-9 (2007).

[6] V. Banine et al., “Plasma sources for EUV lithography exposure tools”, *JOURNAL OF PHYSICS D-APPLIED PHYSICS,* **37**, 23, pp.3207-3212 (2004).

[7] T. Sodekoda, et al., “Repetitive operation of counter-facing plasma focus device : toward a practical light source for EUV lithography”, *Proc. SPIE*, **9048**, Extreme Ultraviolet Lithography V, 904824 (2014).

[8] A. Hassanein et al., “Multidimensional simulation and optimization of hybrid laser and discharge plasma devices for EUV lithography - art. no. 692113”, *SPIE*, **6921**, 1-2, 92113 (2008).

Development of Counter-facing Discharge Device for Extreme Ultraviolet Source
~ Evaluation of Electrode Damages for Stationary Operation ~

Daisuke Nishii, Kouki Kanou*, Tomoaki Kawasaki*, Tatsuya Sodekoda**, Hajime Kuwabara**, Mitsuo Nakajima*, Kazuhiko Horioka*

Department of Mechano-Aerospace Engineering, Tokyo Institute of Technology
2-12-1 Ookayama, Meguro-ku, Tokyo, 152-8550, Japan

**Department of Energy Sciences, Tokyo Institute of Technology*
4259 Nagatsuta-cho, Midori-ku, Yokohama, Kanagawa, 226-8503, Japan

***Advanced Applied Department, IHI Corporation*
1 Shin-nakahara-cho, Isogo-ku, Yokohama, Kanagawa, 235-8501, Japan

ABSTRACT

Center electrode damages of couter-facing discharge device for Extreme Ultraviolet(EUV) source were classified to stationary damage and pulsed damage. We estimated stationary thermal load by using a semi-empirical simulation. As a results, we found that the electrode temperature becomes too hot under the stationary operation. Also, we examined pulsed thermal load by establishing a simplified model based on the Child-Langmuir sheath. The results showed that the calculation over-estimated the sheath potential, which showed the need to develop a self-consistent model which can deal with the plasma sheath boundary.

Keywords

Key Words: EUV Light Source, Plasma Focus, Thermal Damage, Sheaths, High energy density plasma

1 Introduction

Integrated circuits(ICs) are indispensable for our moden society. Performance of ICs basically depends on the scale of the integration, so raising of the accumulation rate is the first priority. ICs are usually processed by photolithography, and the minimum working size depends on wavelength of the light source [1]. Therefore, development of a shorter wavelength light source is important. What expected for the next generation lithography is Extreme Ultraviolet(EUV) light source, which means 13.5 nm wavelength light here, and it is contained in a radiation from a high energy density plasma.

For industrial use, the way of making the high energy density plasma is classified into Laser Produced Plasma(LPP) or Discharge Produced Plasma(DPP). In LPP scheme, a high energy density plasma is produced by irradiating a high intensity laser to the target. LPP is easy to be controled, but the energy conversion efficiency is basically very low. In DPP scheme, a high energy density plasma is produced by a pulsed discharge. DPP has high energy conversion efficiency, but the electrode damage is a serious issue to be solved and is difficult to manage due to the complex nature of the discharge process.

To develop an efficient EUV light source, we have developed a plasma device which has counter-facing plasma focus electrodes. By the research and development of this device so far, we have attained a 100 mJ EUV output per 1 operation [2]. For the next step, we are aiming at repetitive operation at 1 kHz, but there are some problems. One of them is the thermal damage of the electrode because of the load of high current and the electron spattering. Electrode thermal damages can be classified to two types. The first is a stationary damage due to the Joule heating and heat-flow through

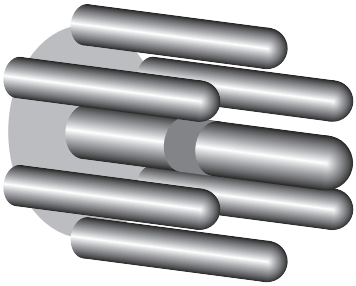

Fig. 1. Configration of one side electrodes in couter-facing discharge plasma focus device.

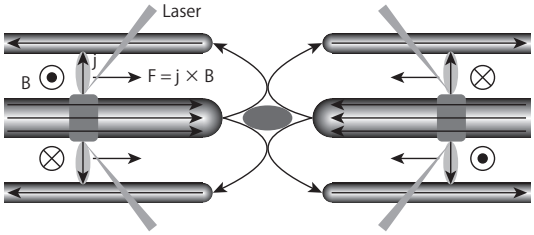

Fig. 2. Schematic of operation of counter-facing plasma focus system.

the sheaths, the second is a pulsed damage due to arc-discharge. To achieve repetitive operation for long periods, these damages should be suppressed under a permissible limit.

The purpose of this research is to evaluate the electrode thermal damages quantitatively and examine the condition in which electrode thermal damages are kept under the permissible limit.

2 Experimental Setup and Method of Evaluation of Electrode Thermal Damages

2.1 Counter-facing Discharge Plasma Focus Device

We have developed a counter-facing discharge device which is composed of a pair of six-channel plasma focus electrodes. Figure 1 shows the focus device composed of a center electrode and six outer electrodes. The plasma source(lithium) is embedded in a groove of the center electrode. Figure 2 schematically shows the operation of the device to make EUV plasma. At first, capacitors between a center electrode and independent six outer electrodes are charged to high voltage(5~7kV). A laser irradiates the plasma source at middle of the center electrodes and makes the plasma. Then, currents start to flow between the center electrode and the outer electrodes through plasma. The plasma is accelerated to the center of the counter-facing electrodes by the Lorentz force. The counter-facing plasma driven by the current sheets collide and thermalize at the center, where it is confined by the Lorentz force. Then, a high energy density EUV plasma is generated.

2.2 Numerical Analysis of Stationary Thermal Load

In the plasma focus device, the current flows with a time constant of μsec and the heat deposition in the electrode diffuses with order of msec. Therefore, the electrode temperature repeats rise and down. But in a time scale longer than the time constant, the electrode temperature can be regarded as having a simply rising character. We call such a heat inflow as a "stationary load" here.

Stationary thermal load raises the electrode temperature, and the temperature distribution can be obtained by solving a thermal diffusion equation. In two-dimensional cylindrical coordinates system, the thermal diffusion equation is given as follows,

$$\frac{\partial T}{\partial t} = a\left(\frac{\partial^2 T}{\partial r^2} + \frac{1}{r}\frac{\partial T}{\partial r} + \frac{\partial^2 T}{\partial z^2}\right) + q(r,z)\,, \qquad (1)$$

where T is the electrode temperature at (r,z), a is thermal diffusivity, $q(r,z)$ is internal heating term [3]. We made a numerical simulation code with two-dimensional cylindrical coordinate system and evaluated the electrode temperature.

2.3 Sheath Modeling for Evaluating Pulsed Thermal Load

When the discharge current is localized at a point of electrode surface, an arc discharge may occur. The arc discharge damages the electrode. We call this damage as a "pulsed thermal load" here.

To evaluate the pulsed thermal load, it is important to understand the sheath dynamics. But there is no es-

Tab. 1. Parameters for thermal calculation.

Parameter	Value
Material of electorode	W(head), Cu(root)
Length of electrode	32.5 mm
Curvature of electrode head	1.5 mm
Charging voltage of capacitor	7 kV
Pulse rate	1 kHz
Sheath heat	270 W
Cooling temperature	200 ℃

Tab. 2. Physical properties of electrode materials.

Parameter	Tungsten	Copper
Melting temperature [K]	3700	1450
Thermal conductivity [W/mK]	173	401
Specific heat [J/gK]	0.138	0.379
Mass density [g/cm^3]	0.138	0.379
Electrical resistivity [nΩm]	52.8	16.8

Tab. 3. Conditions for numerical calculation.

Parameter	Value
Time step Δt	1.0×10^{-5} sec
Division number of z-axis	300
Division number of r-azis	30

tablished model about the sheath dynamics. So we are developing a new sheath dynamics model.

3 Results and Discussion

3.1 Numerical Simulation for Evaluating Stationary Thermal Load

3.1.1 Analysis conditions

Table 1 shows basic parameters of the numerical study. Table 2 shows physical properties of the electrode materials, and Tab. 3 represents the conditions for the numerical calculation.

3.1.2 Time to achieve quasi-steady state

Figure 3 shows temporal evolution of the electrode head temperature. As the figure shows, it takes about 10 sec to achieve the quasi-steady temperature distribution. In other words, we can reach a steady state temperature distribution by the time integration of Eq. (1) for 10 sec.

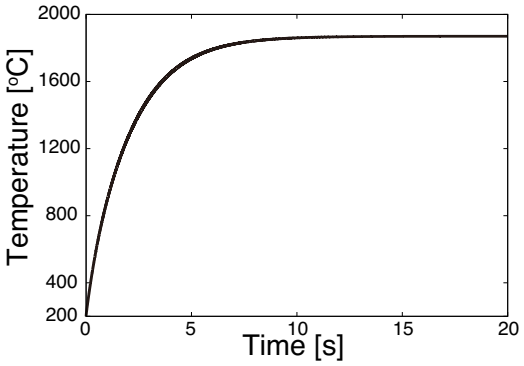

Fig. 3. Evolution of electrode head temperature.

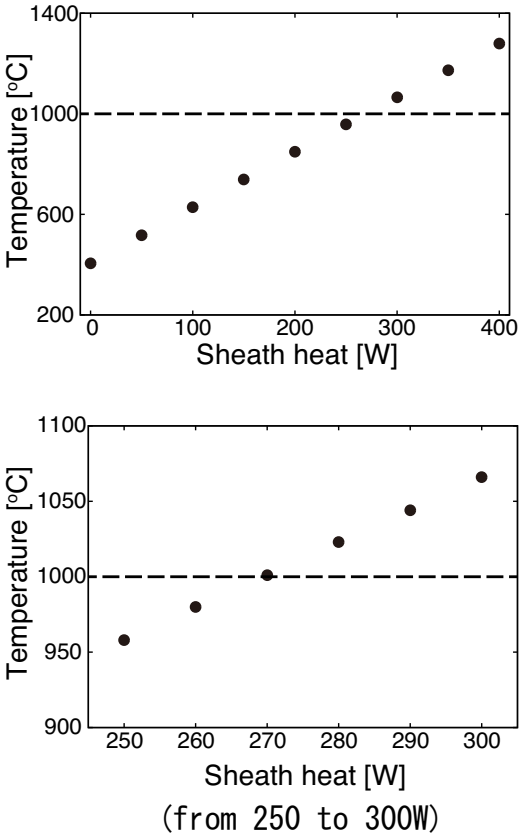

Fig. 4. Temperature change of electrode head as a function of sheath heating power.

3.1.3 Evaluation of sheath heating by parameter survey

It is difficult to evaluate the sheath heating phenomenom with a numerical modeling. So we tried to evaluate the sheath heating semi-empirically, namely by fitting the numerical calculation with the experimental observation. We know that temperature of the elec-

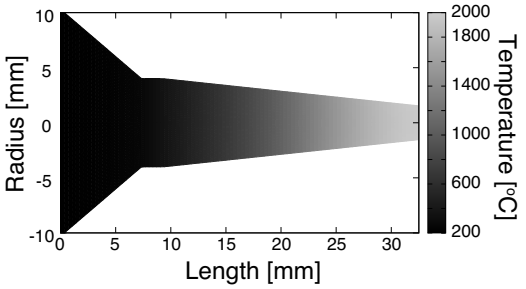

Fig. 5. Typical electrode temperature distribution.

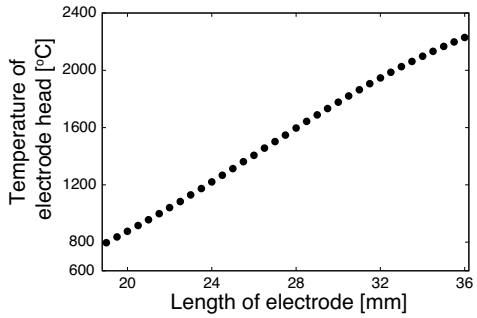

Fig. 6. Temperature change of electrode versus electrode length.

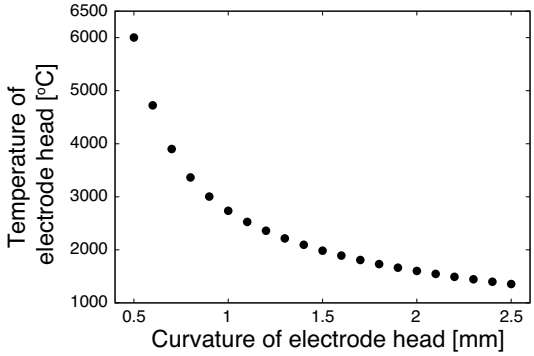

Fig. 7. Temperature change of electrode as a function of electrode head curvature.

trode head reaches around 1000 ℃ when the plasma focus device operated for 1 second at 1 kHz. Figure 4 shows the temperature change of electrode head as a function of sheath heating power ranging from 0 W to 400 W. As Fig. 4 shows, the sheath heating corresponding to the electrode temperature is estimated to be 270 W. After this, we regard the sheath heating as 270 W.

3.1.4 Change of the electrode temperature when the electrode shape is changed

EUV output depends on the electrode configuration [4], and it is expected that the electrode temperature also depends on the electrode shape. So we varied the electrode length form 19.0 mm to 36.0 mm and the electrode head curvature from 0.5 mm to 1.5 mm. Figure 5 shows a typical electrode temperature distribution in the case of condition shown in Tab. 1 . As it shows, we know that the electrode head temperature rises about 2000 ℃.

Figure 6 shows the temperature change of the electrode when the electrode length is changed and Fig. 7 shows the temperature as a function of the electrode head curvature. As these results show, the electrode temperatures decrease as the electrode becomes shorter or the electrode head curvature becomes bigger. The results also show that if we suppose that the temperature limit of tungsten is 1000 ℃, the electrode length has to be shorter than 22 mm or the electrode head curvature has to be bigger than 2.5 mm. But from the point of view of EUV output, this geometry is not optimum, so we have to consider a rational cooling system to optimize the electrode geometry for EUV conversion.

3.1.5 Change of the thermal temperature distribution when the input power is changed

If we increase the input power, EUV output is expected to be increased, but the electrode temperature is also expected to increase. It is important to examine the input power limit, so we made analysis when input power is changed. Experimental results show that when the charge voltage of capacitor is raised, EUV output increases. So we varied the voltage of capacitors from 5 KV to 7 kV. Also, we varied the repetition frequency from 1 kHz to 10 kHz. Figure 8 shows the temperature change of the electrode head versus the charging voltage and Fig. 9 shows the temperature versus repetition frequency. As shown, the electrode head temperature increases as the input power is raised. We are aiming

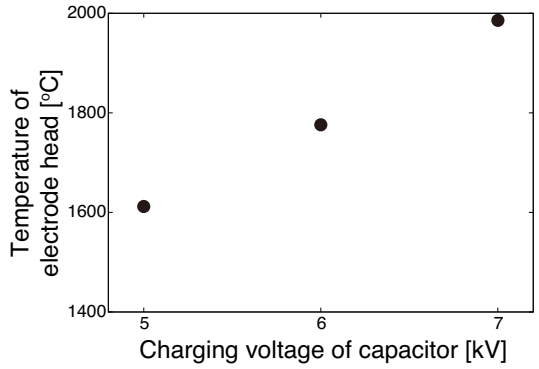

Fig. 8. Temperature change of electrode head versus charging voltage.

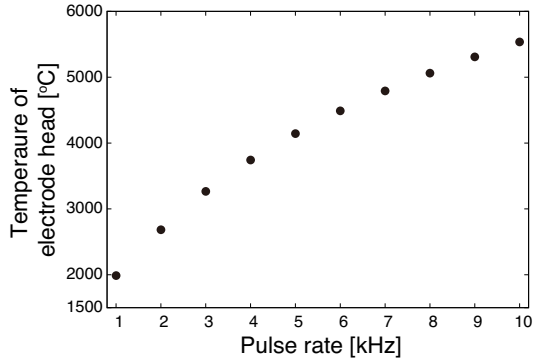

Fig. 9. Temperature change of electrode head versus repetition frequency.

at a continuous operation at 10 kHz, but the head load limits the repetition less than 3 kHz to avoid the melting of tungsten electrode. So we have to improve the energy conversion efficiency.

3.2 Modeling the Sheath Physics for Evaluating Pulsed Heat-inflow

3.2.1 Evaluating the Sheath Potential from the Child-Langmuir Law

Generation of arc spots depend on the sheath potential and width. They can be evaluated from the Child-Langmuir law. The Child-Langmuir law is given by

$$j = \frac{4}{9}\varepsilon_0 \left(\frac{2e}{m_\mathrm{i}}\right)^{1/2} \frac{\phi^{3/2}}{d^2} \ , \qquad (2)$$

where j is the current density, ε_0 is the permittivity of free space, e is the elementary charge, m_i is the mass of ion, ϕ is the sheath potential, d is the sheath width [5]. We can know j because j is primarily determined by the external circuit in case of the discharge plasma device. So ϕ can be calculated using Eq. (2) by assuming d. Generally, the sheath width d is considered to be the order of the Debye length λ_d given by

$$\lambda_d = \left(\frac{\varepsilon_0 k_\mathrm{B} T_\mathrm{e}}{n_\mathrm{e} e^2}\right)^{1/2} \ , \qquad (3)$$

where k_B is the Boltzmann constant, T_e is the electron temperature, n_e is the electron density. The sheath potential ϕ is calculated as shown in Fig. 10 . In the calculation, we assumed $d = 10\lambda_d$, $T_\mathrm{e} = 10\,\mathrm{eV}$, $n_\mathrm{e} = 1.0 \times 10^{14}\,\mathrm{cm}^{-3}$ and $m_\mathrm{i} = 1.15 \times 10^{-26}\,\mathrm{kg(lithium)}$. As shown, the sheath potential was obviously much larger than real one. So we have to develop a self-consistent model which can deal with plasma and sheath dynamics.

4 Conclusions

We estimated stationary temperature distribution of the center electrode by numerical simulations and compared it with experimental observation. We found that time to achieve the quasi-steady state is 10 sec and the sheath heating is ~ 270 W. The results also indicate that the electrode head temperature reaches around 2000 ℃ in typical conditions at a steady operation. If we assume that the electrode limit temperature is 1000 ℃, we have to improve the cooling system and/or increase the energy conversion efficiency.

Also we calculated the sheath potential using the Child-Langmuir law for evaluating the pulsed thermal

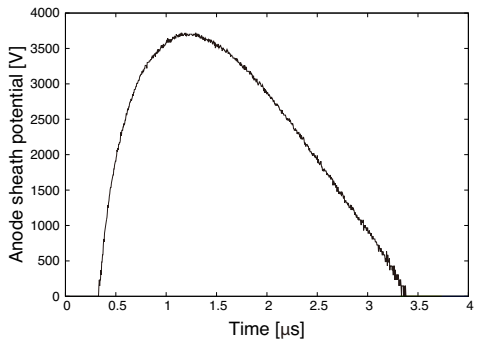

Fig. 10. Calculated sheath potential assuming the Child-Langmuir sheath.

load. The calculation over-estimated the sheath potential, so we have to consider a model which can deal with the plasma and the sheath without contradiction.

References

[1] S. KOBAYASHI, T. KOTANI, and S. KYOH. "Design for Manufactureability Technology to Accelerate Advanced Semiconductor Lithograohy Processes". *TOSHIBA review*, **66**(5):25–28, (2011).

[2] T. Sodekoda, H. Kuwabara, M. Masashi, S. Liu, K. Kanou, K. Kawaguchi, and K. Horioka. "Repetotove operation of counter-facing plasma focus device: toward a practical light source for euv lithography". **9048**:904824–904824–8, (2014).

[3] R. Bird, W. Stewart, and E. Lightfoot. *Transport Phenomena*. Wiley International edition. Wiley, (2007).

[4] K. Kanou, T. Kawasaki, D. Nishii, H. Kuwabara, T. Sodekoda, A. Tokuchi, and K. Horioka. "Quasi-steady operation of counter-facing plasma-focus device for high-average-power radiation source in extreme ultraviolet region". *PROCEEDINGS OF PLASMA CONFERENCE 2014*, (2014).

[5] A. T. Forrester. *Large Ion Beams Fundamentals of Generation and Propagation*. Wiley, (1988).

Pulse-switching characteristics of high-voltage SiC-MOSFETs

Takumi Tomite, Koichi Takaki, Katsuya Okamura*, Ken Takayama* and Kenji Fukuda**

Department of Electrical and Electronic Engineering, Iwate University, Morioka, Japan

**Accelerator Laboratory, High Energy Accelerator Research Organization, Tsukuba, Japan*

***Advanced Power Electronics Research Center, National Institute of Advanced Industrial Science and Technology, Tsukuba, Japan*

ABSTRACT

The pulse-switching characteristics of an implantation epitaxial MOSFET developed by the Tsukuba Power-Electronics Constellations (device A) and commercially available SiC-MOSFET device (device B) were compared with various operating temperatures. In the room temperature region, switching loss of the device A is larger than that of device B. With increasing the device temperature, the switching loss of the device A decreased, whereas that of device B increased. Consequently, the total energy loss of device A is smaller than that of device B at temperature above 120 ºC. The conduction loss of the device A increased with increasing temperature owing to the increase of the on-resistance. The temperature dependency of switching loss is attributed to a change in Miller capacitance and gate threshold voltage.

Keywords

Key Words (MOSFET, Silicon carbide, Pulsed power generator)

1. Introduction

Silicon carbide (SiC), a wide-gap semiconductor material, is expected to play a role in power electronics during the 21st century because of its characteristics. For example, SiC has a dielectric breakdown field strength ten-fold that of Silicon (Si) alone. As a result, SiC can achieve a target applied voltage with a thinner and more concentrated drift layer than Si [1]. This means that extremely low on-voltage devices can be fabricated with SiC because the resistive component of high-voltage power devices depends strongly on the thickness of the drift layer. In addition to this, SiC has many other desirable properties relative to Si, such as triple the thermal conductivity and twice the saturated drift velocity [2, 3].

In previous studies, we have extensively investigated the switching characteristics of a SiC junction field-effect transistor (SiC-JFET) and have obtained excellent results [4]. Additionally, we have developed a custom-built high-power SiC-JFET package [5] and used it to accelerate ion beams in the KEK digital accelerator [6]; in that experiment, an induction acceleration cell was driven by a pulsed power supply based on a SiC-JEFT [7]. We are also interested in SiC metal–oxide–semiconductor field-effect transistors (SiC-MOSFETs), which have been progressing rapidly around the world. These are very attractive to us, because the fact that SiC-MOSFETs are normally off devices with a simple driving circuit system allows various applications to be developed with relative ease.

Recently, an implantation epitaxial MOSFET (IEMOSFET) [8] has been developed during joint research at Tsukuba Power-Electronics Constellations (TPEC) [9]. Figure 1 shows a cross-sectional

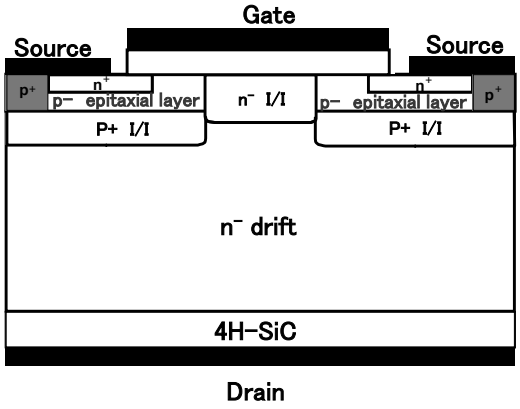

Fig. 1 Cross-sectional schematic of the IEMOSFET.

Table 1 Typical electrical specifications.

Parameter	Device A	Device B	Unit
Blocking voltage	1200	1200	V
Gate-source voltage (Max)	20	22	V
Pulse drain current	30	80	A
On resistance	120-175	80-117	mΩ

schematic of the IEMOSFET [10]. The upper half of the p-well is formed by epitaxial growth without activation annealing, and the smooth surface prevents the gradation of channel mobility that occurs with the conventional double implantation method. The buried channel structure drastically reduces the on-resistance [11].

In this paper, the pulse-switching characteristics of the IEMOSFET and a SiC-MOSFET are compared with various operating temperatures.

2. Experimental Setup

The IEMOSFET developed by TPEC (device A) and a SiC-MOSFET (ROHM, SCH2080KE, Device B) are employed in the evaluation. The typical electrical specifications of these devices are summarized in Table 1.

Figure 2 shows the evaluation circuit for devices. The circuit consists of a DC power source, a charging resistor of 50 kΩ, a load resistor of 50 Ω, a capacitor of 12 μF, a gate drive circuit and a delay generator (Stanford Research Systems, DG645). The settings configured as a drain-source voltage (V_{DS}) of

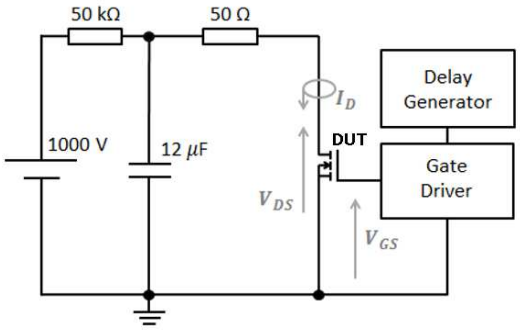

Fig. 2 Evaluation circuit.

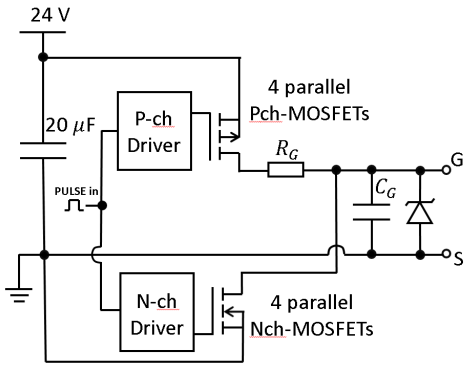

Fig. 3 Gate drive circuit.

1 kV and drain current (I_D) of 20 A. In order to investigate the switching characteristics on operating temperature, the DUT is mounted on a temperature-controlled heat plate (AS ONE, ND-1). The temperature is varied from 20 ºC to 150 ºC.

Figure 3 shows a schematic diagram of the gate drive circuit. The circuit consists of a 24 V DC power source, P-channel MOSFETs (IRF9530), N-channel MOSFETs (IRF530), a gate resistor (Rg), a gate-source capacitor (Cg) and a zener diode (1N5357BRLG, Vz = 20 V). A pulse voltage generated by the delay generator is applied to the gate drive circuits to switch the N-channel and P-channel MOSFETs alternatively. Switching between N-channel and P-channel MOSFETs allows rapid charging and discharging of the gate input capacitance of the DUTs, respectively, which realize fast switching of the DUTs. Resistance of Rg and capacitance of Cg were optimized experimentally in such a way as to decrease the overshoot and ringing of the gate- source voltage.

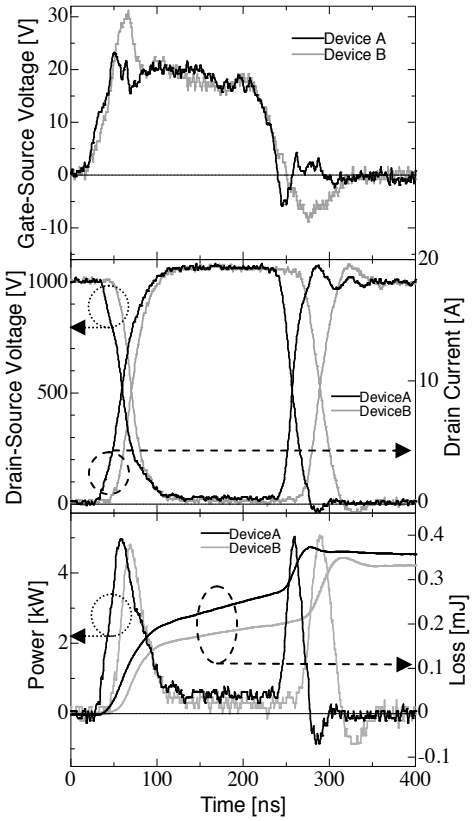

Fig. 4 Waveforms of the gate-source voltage, the drain–source voltage, the drain current, and the total loss of the device A and B.

As a results, Rg of 1.5 Ω and Cg of 0 pF, i.e. without Cg, were chosen for device A and Rg of 1.5 Ω and Cg of 2000 pF were chosen for device B.

3. Results and discussion

Figure 4 shows the waveforms of the gate–source voltage, the drain–source voltage, the drain current, and the energy loss of the both devices at room temperature. The turn-on time of both devices, which is defined as the drain-source voltage fall time from 90% to 10%, were 46 ns and 30 ns, respectively. The turn-off time, which is defined as the drain-source voltage rise time from 10% to 90%, were 20 ns and 26 ns, respectively. The turn-off delay time, which is defined as the intervening time between the 10% fall of the gate-source voltage and the 10% rise of drain-source voltage, of device A was shorter than that of device B.

Table 2 summarizes the turn-on losses, turn-off losses, conduction losses and total energy losses of the device A and B at room temperature.

Table 2 Turn-on losses, turn-off losses, conduction losses and total energy losses of the device A and B at room temperature.

Parameter	Device A	Device B	Unit
Turn-on loss	0.147	0.113	mJ
Conduction loss	0.105	0.091	mJ
Turn-off loss	0.105	0.113	mJ
Total energy loss	0.357	0.317	mJ

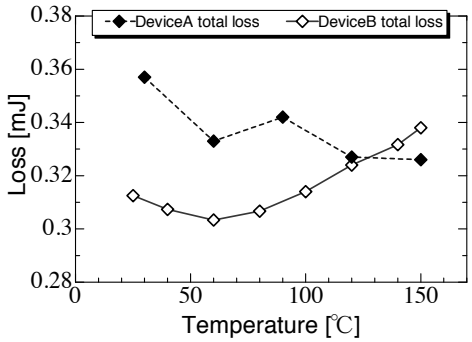

Fig. 5 Total losses of the device A and B as a function of temperature.

losses, conduction losses and total energy losses of the both devices at room temperature, where the conduction period is defined as the time during the drain-source voltage of less than 10%. As shown in table 2, the turn-on loss of device A is larger than that of device B, the reason of which is considered to be caused by longer turn-on time. The difference of the total losses between both devices is mainly due to the difference of the turn-on losses because there isn't much of a difference in the other losses.

Figure 5 shows the total energy losses of device A and B as a function of temperature. The total energy loss of device A decreases with increasing temperature, whereas that of device B increases with temperature, consequently they are reversed above 120 ℃. Figure 6 shows the turn-on, conduction and turn-off losses of the both devices as a function of temperature. The conduction losses of both devices increased with increasing temperature owing to increase of on-resistance. The turn-on losses of both devices decreased with increasing temperature. With increasing temperature, the turn-off loss of device A

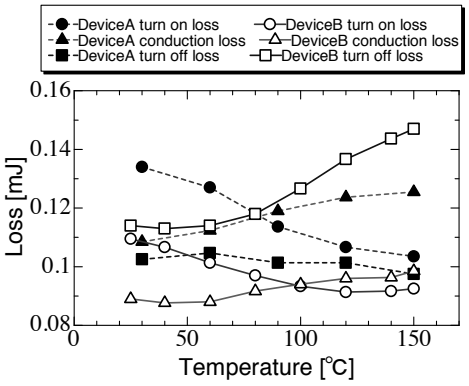

Fig. 6 Turn-on losses, turn-off losses and conduction losses of the device A and B as a function of temperature.

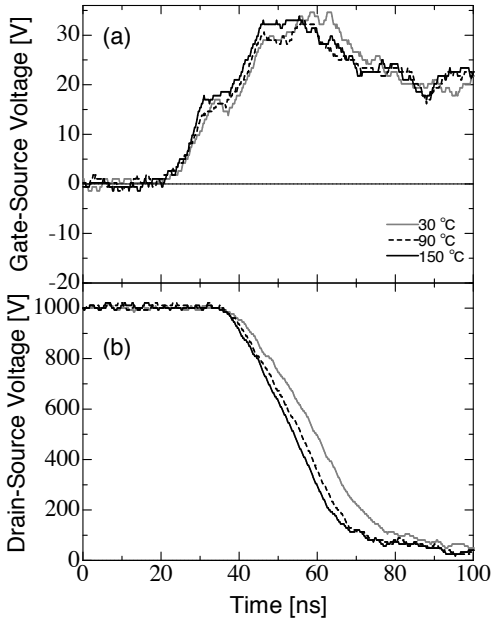

Fig. 7 Waveforms of gate-source voltage and drain-source voltage during the turn-on period in the case of device A for various temperatures.

decreased and that of device B increased.

Figure 7 shows the waveforms of gate-source voltage (a) and drain-source voltage (b) during the turn-on period for various temperatures of device A. The rise time of the gate-source voltage and the turn-on time decreases with increasing temperature. Figure 8 shows the close-up view of the gate-source voltage waveform during the turn-on period in the

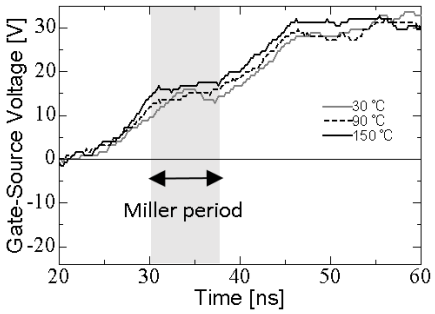

Fig. 8 Close-up view of the gate-source voltage waveform during the turn-on period in the case of the device A.

case of the device A. The gate-source voltage during the Miller period increased with increasing temperature. This result suggests that the Miller capacitance probably decreases with increasing temperature. Therefore, the turn-on loss of device A decreased at increasing temperature, which mainly causes the decrease of the total energy loss.

4. Summary

The pulse switching characteristics of SiC-MOSFETs developed by TPEC and commercialized by ROHM were compared. The switching loss of the IEMOSFET was larger than that of the commercialized device at room temperature. However, the switching loss of the IEMOSFET decreased with increasing temperature due to decrease of turn-on loss. The switching loss of IEMOSFET decreased with increasing temperature, and is lower than that of commercialized device at temperature above 120 ºC.

Acknowledgement

The authors would like to thank Dr. S. Mukaigawa and Dr. K. Takahashi at Iwate University for their valuable comments and discussions. The author would also like to thank Mr. Shida at Iwate University technical staff. Part of this work has been implemented under a joint research project of Tsukuba Power Electronics Constellations (TPEC).

References

[1] M. Bhatnagar et al., “Comparison of 6H-SiC, 3C-SiC, and Si for power devices” IEEE Trans. Electron Devices, **40**, 3, pp. 645–655(1993).

[2] H. Okumura, “Present status and future prospect of wide gap semiconductor high-power devices”, Jpn. J. Appl. Phys., **45**, 10A, pp. 7565–7586 (2006).

[3] K. Shenai et al., “Optimum semiconductors for high-power electronics”, IEEE Trans. Electron Devices, **36**, 9, pp. 1811–1823(1989).

[4] K. Ise et al., “Development of a MHz high voltage switching pulse modulator using a SiC-JFET for an induction synchrotron”, IEEE Trans. Plasma Sci., **39**, 2, pp. 730-736(2011).

[5] K. Okamura et al., “Novel Package of SiC-JFET for a Switching Pulse Supply Operating at 1 MHz for an Induction Synchrotron”, IEEE Trans. Plasma Sci., **40**, 9, pp. 2205-2210(2012).

[6] T. Iwashita et al., “KEK digital accelerator”, Phys. Rev. ST-AB, **14**, 7, 071301(2011).

[7] K. Okamura et al., “Development of a Compact Switching Power Supply for an Induction Synchrotron Utilizing a SiC-JFET”, IEEJ Trans. FM., **134**, 6, pp. 402-409(2014).

[8] https://unit.aist.go.jp/adperc/ci/teams/s-pdt.html #harada

[9] http://www.tia-nano.jp/tpec/index.html

[10] S. Harada et al., “1.8 mΩcm2, 10 A Power MOSFET in 4H-SiC”, conference record of IEDM ’06, pp. 1-4(2006).

[11] S. Harada et al., “High Channel Mobility in Normally-off 4H-SiC Buried Channel MOSFETs”, IEEE Electron Device Lett., **22**, 6, pp. 272-274(2001).

Development of a Negative Ion Source of Clusters for the Tandem Accelerator

Eisuke Baba[1], Jun Hasegawa[1], Katsunori Kawasaki[2], Mitsuo Nakajima[1], Kazuhiko Horioka[1], Yasushi Iwata[3]

[1]*Department of Energy Sciences, Tokyo Institute of Technology*

[2]*Radiation Research and Management Center, Tokyo Institute of Technology*

[3]*Advanced Industrial Science and Technology*

ABSTRACT

With the aim of accelerating giant clusters by a tandem accelerator, we have been developing a negative ion source of C_{60} fullerenes. This paper reports the progress in the development of the components of the cluster negative ion source and the results of preliminary experiments. In a C_{60} sublimation experiment, we confirmed the formation of a neutral beam of C_{60} by heating a ceramic container of C_{60} powder. Furthermore, an electron current density of 20 μA/cm^2 was achieved in the ionization section using thermal electron emission from tungsten filaments, which satisfies the requirement evaluated from the desired performance of the ion source.

Keywords

C_{60}, Cluster, Negative ion source, Tandem accelerator

1. Introduction

An aggregate of several to several million atoms or molecules is called a cluster. A cluster shows different characteristics from either mono-atom or macroscopic material. In addition, it is known that the cluster can have various three-dimensional structures and changes its properties with size. Therefore, the cluster is also called a new phase of material.

When clusters with a kinetic energy of about 100 keV/u or more hit a solid target, they are injected deeply into the target. Because the distance between neighboring atoms in a cluster is almost the same as the lattice distance of solid material, a cluster beam can make much higher energy density in the material than a monoatomic ion beam. Depending on the energy of cluster, the cluster beam can give the materials very high radiation effects because of a stopping power increase by proximity effects. Thus the interaction between high-energy clusters and solid materials has been a very interesting topic, and the cluster beam has been expected to be applied to industrial fields as a novel material reforming tool.

Relatively small clusters composed of 2 to 10 atoms has been accelerated up to about ~ 1 MeV/u by electrostatic accelerators [1-7]. On the other hand, clusters composed of 50 atoms or more such as C_{60} has been accelerated up to 36.2 MeV by a tandem electrostatic accelerator at IPN Orsay in France for the first time [8]. The acceleration of C_{60} has been also carried out in some accelerator facilities in Japan [9,10]. However, the acceleration energy of clusters in these experiment remained less than 10 keV/u. The maximum acceleration voltage of the electrostatic accelerator typically is about 20 MV because of the restriction of high voltage insulation. On the other hand, high-frequency circular accelerators such as cyclotron or synchrotron are not suitable for the acceleration of clusters having extremely small mass-to-charge ratios (q/m).

Takayama *et al*. recently proposed and developed a new type of accelerator called "induction synchrotron" and succeeded in a proof-of-principle experiment [11]. Since it has in principle no limitation on the q/m of accelerated particles, it is suitable for the high-energy acceleration of giant clusters such as C_{60}. Iwata *et al*. recently succeeded in generating giant silicon clusters efficiently [12].

Using the above new technologies for the high-energy acceleration of giant clusters, we plan to perform a preliminary experiment of high-energy acceleration of giant clusters using a tandem electrostatic accelerator. The tandem accelerator needs the injection of negative ions; however, negative ionization techniques for giant clusters have not been established.

The purpose of this study is to develop a negative ion source that can supply negative giant clusters to the tandem accelerator.

2. Negative ionization of cluster

To supply negative cluster ions to tandem accelerators, cesium sputter ion sources have been so far employed. However, the sputtering efficiency of clusters was too low to obtain sufficient amount of cluster beam current [9].

On the other hand, a negative ion production method using sublimation and electron attachment is non-destructive for clusters. This method has been mainly used in the basic studies of clusters, such as the structural analysis of C_{60} [13]. However, it has not been applied to negative ion sources for accelerators yet.

C_{60} has relatively high electron attachment cross sections (- 10^{-18} m^2) for electron energies from zero to 10 eV [13]. From the electron attachment cross section, we can calculate electron attachment probability using Eq. (1).

$$P = \sigma n l \quad . \qquad \cdots (1)$$

Here, σ is cross section, n is electron density, and l is the length of electron attachment region.

We assumed that the desired cluster beam current of the negative ion source was 10 nA. Furthermore, we assumed that the cross section of the beam was 1 cm^2 and all C_{60} clusters produced by sublimation entered the ionization region. Then, we can evaluate the specific lifetime of the beam source from the electron attachment probabilities. Here, the specific lifetime is defined as time duration for which the ion source can continuously supply a 10-nA beam current with a 1-g C_{60} powder initially loaded. The relation between the lifetime and the electron attachment probability are presented in Fig. 1. If the required lifetime is 10^3 - 10^4 s/g, the ionization probability needs to be 10^{-6} - 10^{-7}. The relation between the electron current density and the electron attachment probability is shown in Fig. 2. Here, we assume that the electron energy was 5 eV and the length of the electron attachment section was 10 cm. From this relation the electron current density needs to be 20-200 μA/cm^2 to achieve an ionization probability of 10^{-6} - 10^{-7}.

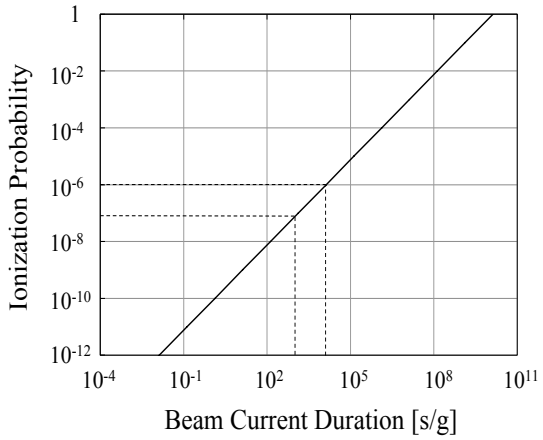

Fig. 1. Beam current duration and ionization probability.

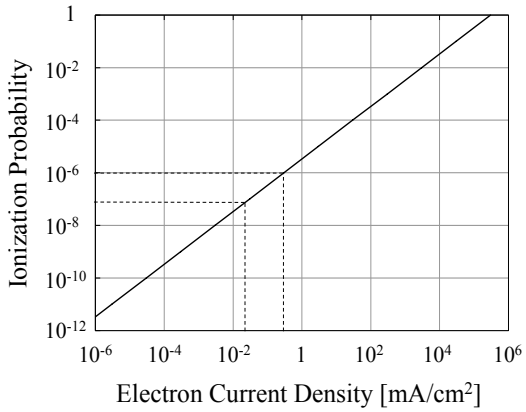

Fig. 2. Dependence on electron density of ionization probability

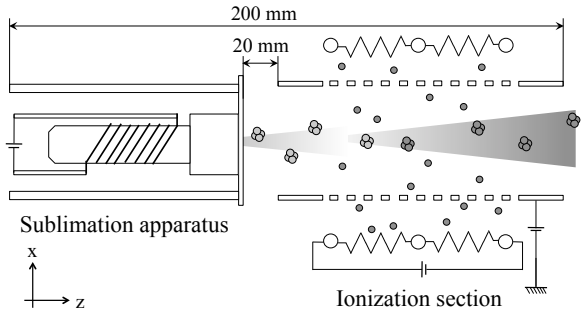

Fig. 3. A schematic of experimental setup.

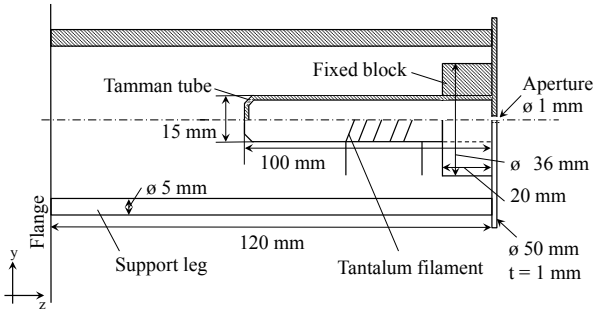

Fig. 4. A cross section of C_{60} sublimation apparatus.

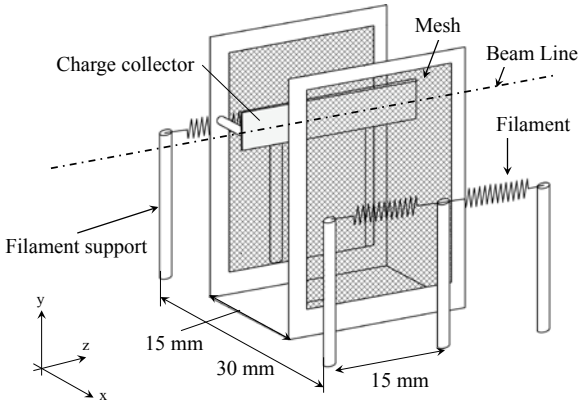

Fig. 5. Layout of ionization section.

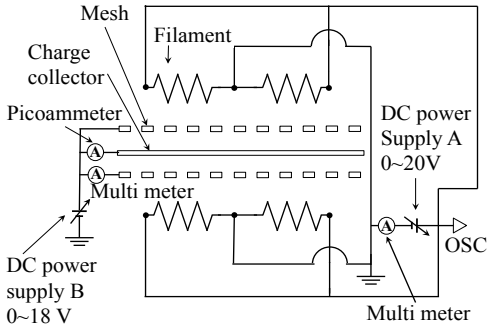

Fig. 6. Circuit diagram of ionization section.

3. Experiment

The experimental device used in this study consisted of a sublimation apparatus and an ionization section. The experimental setup is schematically shown in Fig. 3. A neutral beam of C_{60} generated by the sublimation apparatus was ionized when the beam passes through the ionization section. Then the beam was extracted as a negative ion beam by an extractor located downstream.

The structure of the sublimation apparatus is shown in Fig. 4. We used a tammann tube made of alumina as a container of C_{60}. C_{60} powder was located in the tammann tube. C_{60} is known to be sublimated at about 400 ℃. To heat up the tube, we used tantalum wire (ø 0.3 mm), which was wound around the tammann tube and fixed with a ceramic bound. The wire had a resistance of 1 Ω in total. An aperture (ø 1 mm) was attached to the front of the tammann tube. We used a stabilized DC power supply (30 V, 20 A) to drive the heater.

The structure of the ionization section is illustrated in Fig. 5. Four tungsten filaments were used as thermal electron emitters. Each filament had a resistance of 1.1 Ω. Positively biased grid electrodes made of stainless-steel mesh (12mesh/inch, ø1.4 mm) were placed on the both sides of the beam line (dash-dotted line in Fig.5) to extract electrons from the filaments. The porosity of the mesh was 66 %.

A circuit diagram of the ionization section is shown in Fig. 6. The filaments were connected in parallel to a stabilized DC power supply A (30 V, 20 A). The extraction voltage (up to 18 V) was applied to the mesh electrodes by a stabilized DC power supply B (18 V, 5A).

In the ionization section, as mentioned in Section 2, electron current density obtained in the region where the C_{60} neutral beam pass is important. Therefore, a charge collector was placed in the middle of the mesh electrodes to measure the electron current flowing into the ionization section with a picoammeter. Since the same potential was applied to the collector and the mesh electrodes, there was no electric field in the space between them. In addition, the electron currents flowing into the mesh electrodes were measured at

the same time.

To investigate the spatial distribution of the electron current between the mesh electrodes, we used two kinds of collectors. One was 60 mm in width, 60 mm in height, and 1 mm in thickness so that it could cover the entire area of the mesh electrodes (collector A). The other was 60 mm in width, 10 mm in height, and 1 mm in thickness so that it could cover the region where the neutral beam passed (collector B).

4. Results and Discussion

In the experiment of C_{60} sublimation, an input powder of about 900 W was applied to the heater wire at a maximum. During the experiment the pressure in the chamber increased from 6.0×10^{-4} Pa to 1.2×10^{-2} Pa. Black deposit was observed on the back surface of the aperture plate after the operation for 6 minutes, which indicates that sublimated C_{60} was attached to the wall. Form this result, we confirmed the sublimation of C_{60}. To reduce the loss of C_{60}, it is necessary to improve the structure of the sublimation apparatus so as to maintain all components at the same temperature (~ 400 ºC)

The results of electron current measurement by the collectors A and B are shown in Fig. 7. In both cases (A and B), the electron current increases monotonically with the acceleration voltage (grid voltage). In addition, we evaluated the ratio of the electron current I_a measured by the collector A to the electron current I_b by the collector B, plotting it as a function of the acceleration voltage in Fig. 8. Filled squares and filled triangles are I_b/I_a when the filament input power was 35 W and 56 W, respectively. When the input power was 56 W, I_b/I_a was 54 - 67 %, and when input power is 35 W, I_b/I_a was 6 - 38 %. These results indicate that the spatial distribution of the electron current flowing into the ionization region depended on the input power to the filaments. The voltage applied to the filaments can affect the potential gradient between the filaments and the mesh electrodes, which may be the cause of the change in the electron current distribution.

The results of the electron current measurement by the collector B when the power was over 56 W are

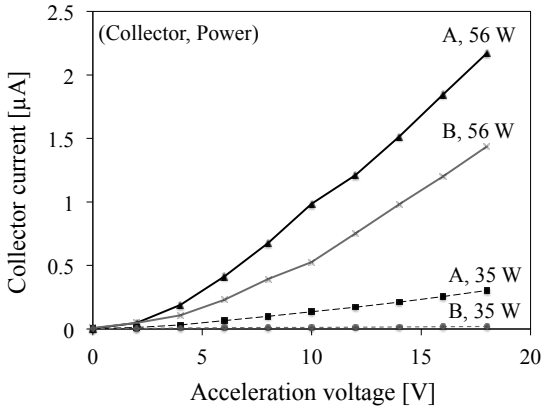

Fig. 7. Dependency of electron current on acceleration voltage.

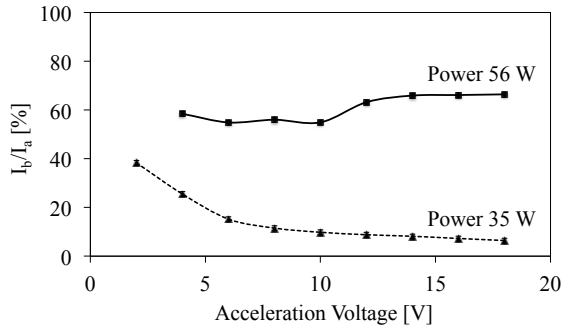

Fig. 8. Dependency of electron current ratio on acceleration voltage.

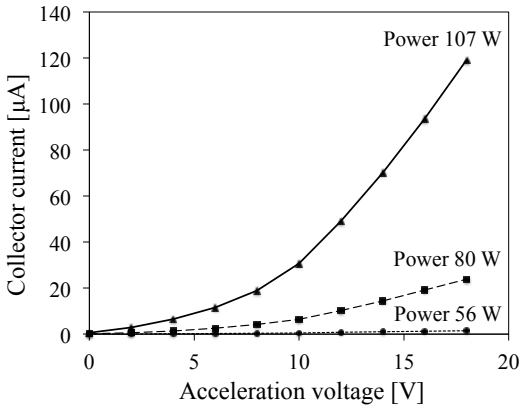

Fig. 9. Dependency of electron current on acceleration voltage.

shown in Fig. 9. The electron current was about 120 μA at a maximum. It was 80 times higher than the value at 56 W. This is probably because the number of thermal electrons emitted from the filament drastically increased with the filament temperature.

The electron use efficiency is plotted as a function

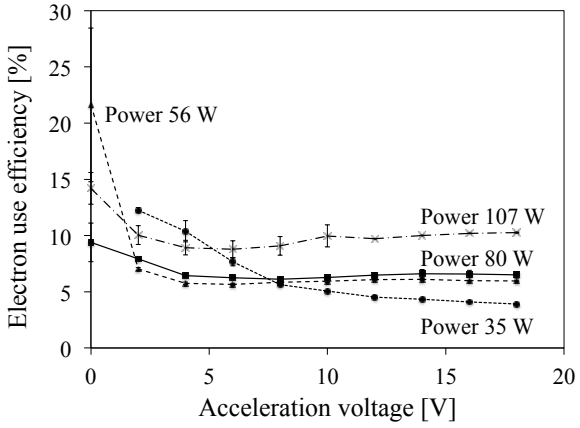

Fig. 10. Dependency of electron use efficiency on acceleration voltage.

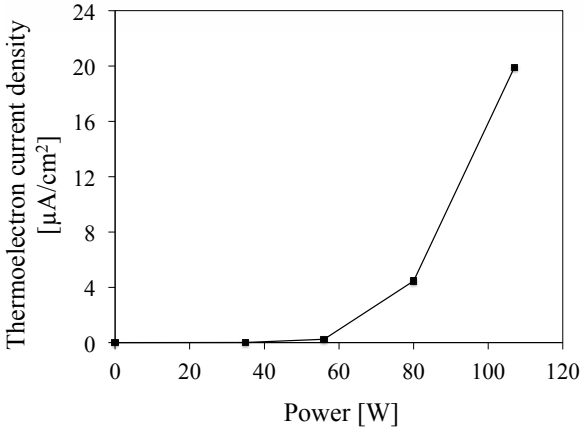

Fig. 11. Dependency of electron current density on filament input power.

of acceleration voltage in Fig. 10. The electron use efficiency was estimated by dividing the electron current measured by the collector B by the sum of the electron currents measured by the collector and the mesh electrodes. When the acceleration voltage was more than 2 V, we found that the efficiency was less than 15 % at any input power. When the acceleration voltage was 0 V, the electron use efficiency was high, compared with those when the acceleration voltage were applied. Also, when the acceleration voltage was more than 8 V, the efficiency increased with increasing input power.

Figure 11 shows the dependency of the electron current density measured by the collector B on the filament input power. The electron current density rapidly increases when the input power exceeds 60 W and it reached about 20 μA/cm^2 at a maximum at 107 W. This current density satisfies our target value. To obtain higher electron current, it is necessary to reduce the distance between the filament and the mesh electrodes and improves the thermal electron emission rate by the Schottky effect. In addition, we are also planning to increase the electron current density by using an oxide thermionic cathode for the electron gun. By guiding thermal electrons emitted from the electron gun by a solenoidal magnetic field, it is expected to suppress the spread of the electrons and drastically increase the electron current density in the ionization section.

5. Summary

For a C_{60} negative ion source for the tandem accelerator, we adopted the sublimation and electron attachment method and carried out preliminary experiments using the sublimation apparatus and the ionization section independently. When heating the C_{60} powder loaded in the tammann tube, we observed an increase in the chamber pressure and black carbon-liken material deposited on the back side of the aperture plate, which indicates the sublimation of C_{60}. When thermal electrons emitted from the filaments were accelerated toward the beam line by the mesh electrodes, we confirmed that an electron current of about 20 μA/cm^2 was obtained at a maximum. This value satisfied our target for the electron current density in the ionization section. In order to achieve more efficient electron attachment, we are planning to make the confinement of electrons in the electron attachment section by a solenoidal magnetic field.

References

[1] D. S. Gemmell, “Determining the stereochemical structures of molecular ions by "Coulomb-explosion" techniques with fast (MeV) molecular ion beams”, Chem. Rev. **80,** pp.301-311 (1980)

[2] M. F Steuer *et al.*, “Diminished stopping power for fast nitrogen and oxygen diclusters in carbon”, Nucl. Instr. and Meth. A **194**, pp.277-279 (1982)

[3] Ch. Tomaschko *et al.*, “Energy loss of MeV

carbon cluster ions in matter", Nucl. Instr. and Meth. B **103**, pp.407-411 (1982)

[4] O. Heber *et. al.*, "Carbon cluster imaging at the Weizmann Institute Coulomb explosion system", Nucl. Instr. and Meth. B **79**, pp.227-230 (1983)

[5] P. Hakansson *et al.*, "Production, acceleration and diagnostics of molecular ions and ionized clusters", Nucl. Instr. and Meth. B **112**, pp.39-47 (1996)

[6] F. Ames *et. al.*, "Acceleration of clusters, collision induced charge exchange at MeV energies and applications for materials science", Nucl. Instr. and Meth. B **112**, pp.64-67 (1996)

[7] D.Shen *et. al*., "Damage production in silicon by MeV Si cluster irradiation" Nucl. Instr. and Meth. B **129**, pp.392-396 (1997)

[8] S. Della-Negra *et al.*, "Acceleration of C_{60}^{n+} molecules to high energy", Nucl. Instr. and Meth B **74**, pp.453-456 (1993).

[9] Y. Saitoh *et al*., "Acceleration of cluster and molecular ions by TIARA 3 MV tandem accelerator", Nucl. Instr. and Meth. A **452**, pp.61-66 (2000).

[10] Y. Saitoh *et al.*, "Transmissions of cluster ions through a tandem accelerator on several stripper gases", Rev. Sci. Instrum. **80**, 106104 (2009).

[11] K. Takayama *et al*., "Experimental Demonstration of the Induction Synchrotron", Phys. Rev. Lett. **98**, 054801 (2007).

[12] Y. Iwata *et al*., "Twenty kilovolts massive ion beam system for well-defined microcluster studies", Nucl. Instr. and Meth. A **427,** pp. 235-241(1999).

[13] S. Matejcik, *et al*., "Formation and decay of C_{60} following free electron capture by C_{60}", Chem. Phys. J. **102**, pp.2516-2521 (1995).

Plume velocity analysis on a spatiotemporally confined cluster source

Y. Ishikawa, A. Takada, J. Hasegawa, Y. Iwata* and K. Horioka

Department of Energy Sciences, Tokyo Institute of Technology

**Electronics and Photonics Research Institute, Advanced Industrial Science and Technology*

Abstract

We have been developing a spatiotemporally confined cluster ion source to supply narrow size-dispersed silicon cluster ions to particle accelerators. The size dispersion of cluster is known to depend strongly on the process of the cluster generation. However, it has not been clarified how the generation process quantatively affects the size dispersion. We observed the light emission of a silicon vapor plume in the cluster generation cavity by a high-speed ICCD camera to clarify the hydrodynamic characteristics of the cluster generation region. The obtained images showed hydrodynamic behaviors of the plume and the existence of multiple light emission peaks, which is not observed in laser ablation processes in vacuum. Additionally, we performed a detailed fitting analysis on the light intensity profile to investigate the behavior of the peaks, and found that the intensity of the peaks was closely related to the light emission of Si atoms, which was acquired by a spectroscopic measurement.

Keywords
Cluster generation, Laser ablation, Plume dynamics, Shock wave

1 Introduction

Recently nanoparticles called micro clusters, which is composed of a number of identical atoms, attracts much attention as beam particles heavier than lead or uranium. The usage of these cluster ions as a beam driver for the inertial confinement fusion has been recently discussed. Generally, as the particles of the beam driver become heavier, the required beam current becomes lower, which is advantageous for the high-current beam driver because space charge effects can be largely reduced.

The high energy acceleration of Fullerene C_{60}, which is the most famous cluster, was demonstrated for the first time at IPN Orsay in France and then have been performed also by some facilities in Japan[1]. In these studies electrostatic accelerators such as tandem accelerators were mainly used to accelerate the cluster ions, and the achievable beam energy was several tens of MeV at the most. To achieve much higher beam energy, circular accelerators need to be employed. A concept of an induction microtron, a circular accelerator which is suitable for the acceleration of exceedingly heavy particles such as cluster ions, was recently proposed by Takayama *et al.*[4], and its design work is under way at KEK. We have been developing a cluster ion source based on a spatiotemporally confined cluster source (SCCS) developed by Iwata *et al*[2]. This cluster source can produce silicon cluster and the number of the constituent atoms

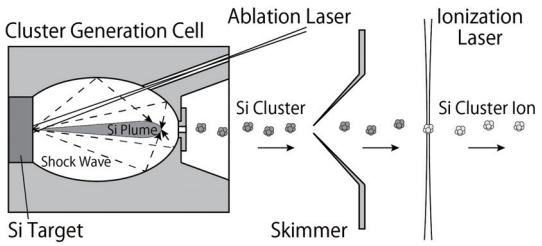

Fig. 1. A schematic of the spatiotemporal confined cluster ion source.

(size) exceeds 100[6]. It was proved that the generated clusters had a considerable narrow size dispersion[6]. Only cluster ions having a specific charged-to-mass ratio can be accelerated in the circular accelerator, so the cluster generation with a narrow size dispersion is a key issue to achieve efficient cluster ion supply to the accelerator.

The principle of the SCCS is schematically illustrated in Fig. 1. A silicon target is placed in a cluster generation cavity having an ellipsoidal shape which is filled with helium gas cooled to the liquid nitrogen temperature. A silicon vapor plume is produced by the laser ablation of the silicon target. The plume induces a shock in the background gas. Since the target surface is located just on the focal point of the ellipsoidal cavity, the induced shock converges on another focal point after reflecting on the cavity wall. When the plume reaches to the focal point, the plume is instantaneously confined by the convergent shock. A rapid cooling of the silicon vapor occurs in a small volume where the silicon vapor and the helium gas are mixed around the contact surface between the plume and the shock. We consider that the substantial cluster growth occurs in this phase and the short duration of the plume confinement (cluster growth) contributes to the narrow size dispersion. The generated clusters are ejected from an exit hole of the cluster generation cavity. The clusters are ionized by a short wavelength laser or an electron beam downstream.

Although the size-dispersion strongly depends on the cluster generation process, i.e. the behavior of the plume and the shock in the cavity, the relationship between the operational conditions (e.g. laser irradiation energy density, helium gas pressure) of the SCCS and the generated cluster properties has not been clarified quantitatively. Thus, we observed the light emission of the silicon plume in the cluster generation cavity by a high-speed imaging camera in order to clarify the hydrodynamic characteristics of the plume. The observed images revealed that the light emission of the plume separated into a few peaks during the expansion, which was particular for laser ablation in background gas. Additionally, we performed a detailed fitting analysis of these peaks to investigate their behaviors and compared it with the result of a spectroscopic analysis[3] of the light emission from the cluster generation cavity.

2 Experimental setup

An experimental configuration used for the high-speed photography is shown in Fig. 2. The ablation laser was a frequency-doubled Nd:YAG laser, whose wavelength, pulse duration (FWHM), and repetition rate are, respectively, 532 nm, 12 ns, and 20 Hz. The laser spot on the silicon target surface was an ellipse shape (4.6 mm × 2.0 mm), and the irradiation energy density was typically 4.1 J/cm^2. The steady rotation of the target prevented the target surface from being unevenly distorted by the laser ablation. A silicon plume produced by the laser ablation was emitted normal to the target surface. An ICCD camera was installed to observe the behavior of the laser ablation plasma normal to the drift direction of the plume. The light emission of the plume passed through an observation window and was converged by a camera lens on a photoelectric surface of the ICCD. The ICCD is sensitive to light in a wavelength range of 350 - 900 nm. The timings between the Q-switch of the Nd:YAG laser, the exposure of the ICCD, and the image capturing by a PC were synchronized by a pulse delay generator. The vacuum chamber was evacuated by a turbo-molecular pump. The degree of vacuum was typically $\sim 10^{-8}$ Torr without helium supply. The helium supply was adjusted by a variable leak valve. The pressures were monitored right behind the variable leak valve and downstream of the turbo-molecular pump to maintain the helium flow rate.

The high-speed imaging of the silicon plume was performed for a single laser shot. We obtained a back-

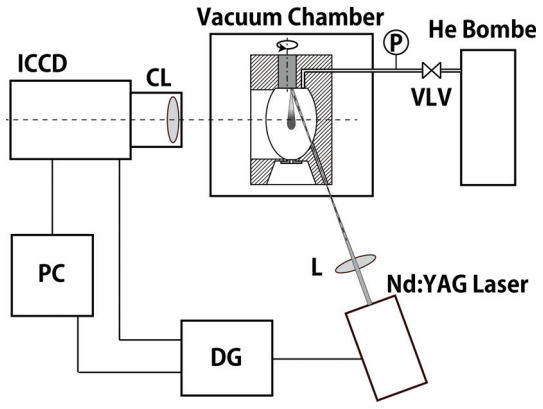

Fig. 2. A schematic of the experimental system used for the high-speed photography. (DG, delay generator; L, lens; CL, camera lens; VLV, variable leak valve; P, pirani gauge).

ground image without laser shot every time we took a plume image. Then, it was subtracted from the plume image to reduce the background noise. The light emission intensity of the ablation plume was attenuated with time, so it was necessary to lengthen the exposure time in order to acquire a sufficient signal intensity for observations with relatively large time delays from the laser irradiation. Exposure times of 0.2 μs, 0.5 μs, and 1.0 μs were used for the observation until 14 μs, 20 μs, and 100 μs, respectively.

3 Results and discussion

The high-speed framing images of the silicon plume until 100 μs after the laser irradiation are shown in Fig. 3. They were obtained with an exposure time of 1.0 μs, and the time origin corresponds to a rise time of the Q-switch trigger. These images showed that the hydrodynamic behavior of the plume differed from that in vacuum and the interaction between the plume and the background gas affected the light emission from the plume. Two characteristic emission peaks appeared at 2.0 μs, and the one of these peaks near the target was rapidly attenuated after 7.0 μs. While the forward peak near the plume front proceeded and arrived at the exit hole of the cluster generation cavity at $\sim$20 μs. After stagnation near the exit hole until 25 μs, the forward peak was reflected and went back toward the target. We found that the forward peak made a round trip in the cluster generation cavity until 100 μs.

In order to investigate the plume behavior more precisely, we made distance-intensity profiles, which

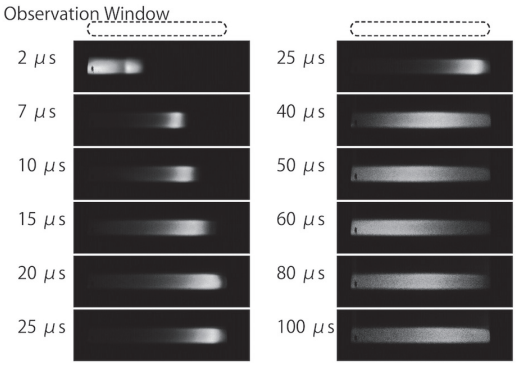

Fig. 3. Plume images in the cluster generation cavity acquired by the observation until 100 μs. The contrast of each image was normalized by the maximum intensity. The exposure time was 1.0 μs.

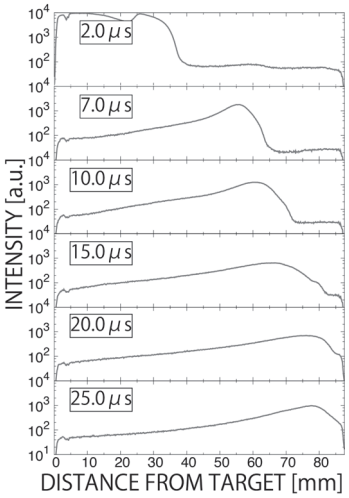

Fig. 4. Profiles of the emission intensity, which were acquired by plotting the longitudinal mean intensity of Fig. 3 against the distance from the target. The origin of the transverse axis is the position of the target, and the maximum position (87.6 mm) is the edge of the observation window.

were obtained by plotting the longitudinal mean intensity of the images of Fig. 3 against the distance from the target. Two peaks arising right after the ablation and the stagnation of the plume near the exit hole also were observed in this profile. The position where the emission intensity became maximum in Fig. 4 was plotted against the time from the laser irradiation in Fig. 5. Note that the stagnation of the maximum intensity peak occurred between 20 μs and 25 μs at 78 mm from the target surface, which corresponds to the focal point of the ellipsoidal cavity. This fact indicates that the plume confinement by the convergent shock actually occurred. As for the plume behavior until 20 μs, the maximum intensity

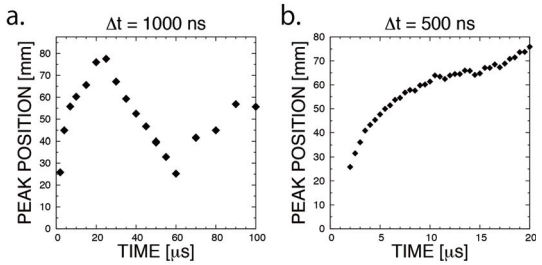

Fig. 5. The time variation of the maximum intensity peak position. Left: the exposure time $\Delta t = 1.0\,\mu$s, right: $\Delta t = 0.5\,\mu$s

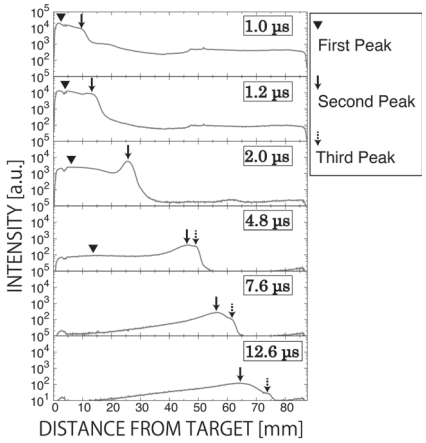

Fig. 6. Profiles of the emission intensity for the measurement with an exposure time of 0.2 μs. It is found that the peak near the plume front separated into two peaks: Second Peak marked by a continuous arrow and Third Peak marked by a dotted arrow.

peak moved to the exit hole decelerating until 15 μs, but it appeared to be accelerated again between 15 μs and 20 μs. This interesting behavior could be confirmed in the more detailed observation with an exposure time of 0.5 μs as shown in Fig. 5. We consider that the reacceleration of the maximum intensity peak was due to the contact of the shock reflected by the ellipsoidal wall of the cavity with the rear end of the plume. The confinement and reaccelerating of the plume by the reflected shock was predicted also in a three-dimensional numerical fluid simulation[5].

Observations until 14 μs with a short exposure time of 0.2 μs were conducted to analyze the detailed behavior of the plume just after the ablation. Figure 6 shows profiles acquired by the same procedures as Fig. 4. The peaks indicated with a solid triangle, a solid arrow, and a dotted arrow in the figure were named "First Peak", "Second Peak" and "Third Peak", respectively. First and Second Peaks were appeared just after the ablation. The emission intensity of First Peak was higher than that of Second Peak just after the ablation, but attenuated more rapidly. In the case of laser ablation under vacuum, an emission peak like First Peak appeared, but Second Peak does not appear. Since Second Peak located near the plume front, we consider that Second Peak was formed by atoms and ions with relatively large velocities in the plume when they were prevented from expanding by the background gas. Second Peak separated and Third Peak appeared after 4.8 μs.

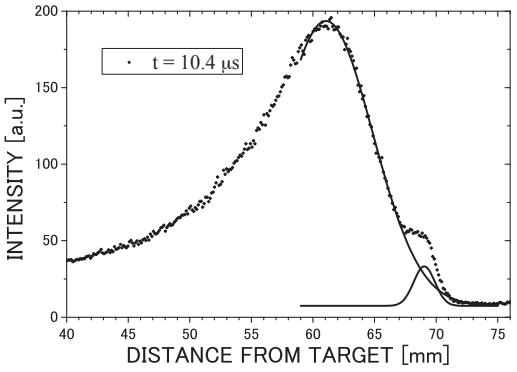

Fig. 7. The separation by the fitting of Second Peak and Third Peak. If the fitting scope was restricted to a region near the plume front, the fitting corresponded well.

In order to analyze the detailed behavior of Second Peak and Third Peak, the profile near the plume front was separated into two Gaussian peaks by fitting as shown in Fig. 7. Fig. 8 shows the result of the fitting analysis. According to the time variation of the peak position, the velocities of both two peaks were reduced, and the distance between two peaks broadened proportionally to the time after laser irradiation. The width of Second Peak broadened monotonically, while the width of Third Peak stayed almost constant. The broadening of the Second Peak width could be

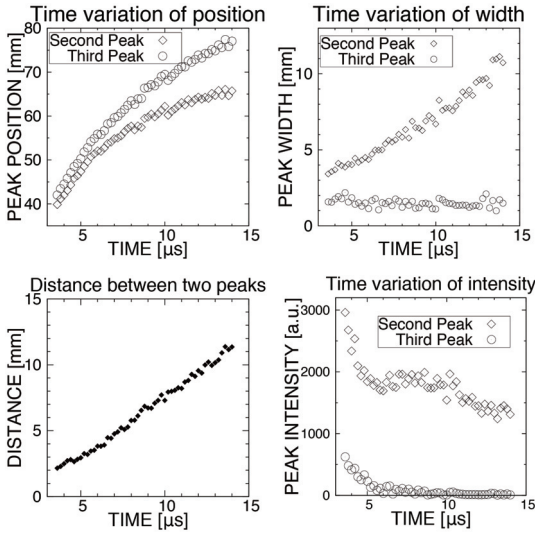

Fig. 8. Peak position, distance, peak intensity and peak width of Second Peak and Third Peak defined by fitting using two gaussians.

due to the expansion of the plume. As shown in Fig. 8 the peak intensities of Second Peak and Third peak decreases with time in different ways from each other. Although the Third Peak intensity decreased exponentially with time while the Second Peak intensity stayed almost constant from 6.0 μs to 10 μs. The separation between the Second Peak and Third Peak occurred after 3.6 μs, components forming these two peaks already existed overlapping with each other even before the separation because the Third Peak intensity was probably higher before 3.6 μs. The time variation of the Second Peak intensity showed a characteristic tendency and seemed to have a strong correlation with the result of spectroscopic analyses for light emission from the cluster generation cavity [3]. The time variations of the Second Peak intensity and the emission intensity from silicon atoms are shown in Fig. 9. We found that the intensities of both of them became moderate between 5 μs and 10 μs and then started increasing after 10 μs. The whole optical emission from the plume was attributed to the lights from silicon atoms and ions. Second Peak could be mainly composed of the silicon atoms because the time variation of Second Peak coincided well with that of the emission from the silicon atoms.

Third Peak might be induced to the mixing between the plume and the helium background gas, because Third Peak existed near the plume front. The cluster growth occurs when the silicon vapor are cooled by the background gas, so the behavior of Third Peak could be related to cluster generation.

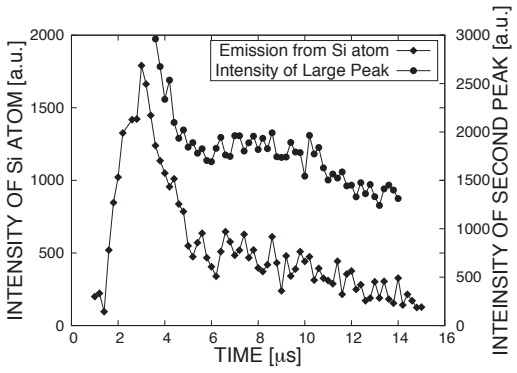

Fig. 9. A comparison between the time variation of the Second Peak intensity and that of the emission intensity from Si atoms. The attenuation of both became moderate between 5 μs and 10 μs.

4 Conclusion

In order to clarify the behavior of a laser ablation plume in the cluster generation cavity with the ellipsoidal shape filled with the helium background gas, we observed the emission of the plume using a high-speed imaging camera.

Three characteristic peaks appeared in the expansion process of the ablation plume. Two peaks appeared at first: one near the target (First Peak) and another near the plume front (Second Peak). Second Peak is known to be particular for the laser ablation in gas. After 3.6 μs from laser irradiation, the Second Peak separate into fast and slow components: Third Peak and Second Peak. The broadening of the distance between these two peaks and the correlation between the time variations of the Second Peak intensity and the emission intensity from silicon atoms was observed.

Phenomena indicating the interaction between the plume and the shock was also observed near the ellipsoidal focal point. The maximum intensity peak was decelerated by the background gas until 15 μs, but reaccelerated between 15 μs and 20 μs. The stagnation near the ellipsoidal focal point indicates the confinement of the plume by the convergent shock.

References

[1] H. Dammak, A. Dunlop, D. Lesueur, A. Brunelle, S.Della-Negra, and Y.LeBeye. *Phys. Rev. Lett.*, 74(7):1135, 1995.

[2] Y. Iwata, K. Tomita, T. Utida, and H. Matsuhata. *Cryst. Growth Des.*, 15(5):2110–2128, 2015.

[3] T. Takada, Y. Ishikawa, J. Hasegawa, Y. Iwata, and K. Horioka. *NIFS-proc.*, this volume, 2015.

[4] K. Takayama, T. Adachi, M. Wake, and K. Okumura. *Phys. Rev. ST-AB*, 18:050101, 2015.

[5] M. Yaga, T. Takiya, and Y. Iwata. *Shock Waves*, 14:403–411, 2005.

[6] Y.Iwata, M. Kishida, M. Muto, S. Yu, T. Sawada, A. Fukuda, T.Takiya, A. Komura, and K. Nakajima. *Chem. Phys. Lett.*, 358:36–42, 2002.

Time-resolved spectroscopic analysis of a spatiotemporally confined cluster source

A. Takada[A] , Y. Ishikawa[A] , J. Hasegawa[A] , Y. Iwata[B] and K. Horioka[A]

[A] *Department of Energy Sciences, Tokyo Institute of Technology*

[B] *National Institute of Advanced Industrial Science and Technology*

Abstract

We have been developing a cluster ion source that can supply giant silicon clusters (SiN, N $\sim$ 100) to an induction microtron. This article reports the results of a time-resolved spectroscopic analysis for light emissions from the cluster production cavity of a Spatiotemporally Confined Cluster Source (SCCS), which will be adopted as the giant cluster ion source. The observation of spectral lines of silicon atoms and ions in a laser-ablated plume revealed that there were strong correlations among light emissions from these two species. This result indicates that light emissions from a mixing area of the silicon vapor plume and background helium gas were mainly due to silicon neutral atoms.

Keyword

silicon cluster, cluster source, cluster growth, giant cluster, spectroscopic analysis, laser ablation

1. Introduction

Iwata *et al.* recently succeeded in developing a novel technique to produce silicon clusters with a narrow size distribution[1]. This new cluster source is called the Spatiotemporally Confined Cluster Source (SCCS). Figure 1 shows the operation principle of the SCCS. The ellipsoidal cavity, where clusters are formed, is filled with helium gas cooled with liquid nitrogen. A silicon solid target is placed at one of the focal points of the cavity. When a pulsed laser irradiates the target surface, a silicon ablation plume is generated and then it starts to expand into the background helium gas. At the same time, a shock wave driven by the plume travels in the cavity and concentrates in the other focal point after reflecting at the inner wall of the cavity. The plume is considered to be confined locally and instantaneously by the shock wave at this moment. Previous numerical simulations indicated that a mixing area of the silicon plume and helium gas was formed through this process[2]. We consider that silicon clusters having a narrow size distribution are formed in this region. Additionally, the direct observation of silicon clusters deposited on a graphen substrate has revealed that uniformly-sized silicon clusters have 3D-lattice arrangement[3].

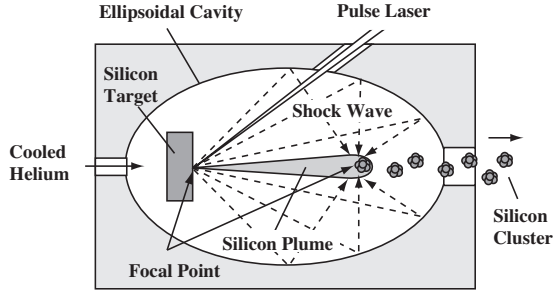

Figure 1: Principle of cluster generation with a SCCS.

While the generation of silicon clusters was confirmed, the relationships between the cluster growth process and cluster properties such as size, structure, electronic state have been unexplored. Thus, the detailed investigation of the cluster growth process is needed. In this article, we report the results of time-resolved spectroscopic observation of light emissions from silicon neutral atoms and ions, and helium neutral atoms confined in the ellipsoidal cavity and discuss their dependencies on the operating conditions of the SCCS.

2. Experimental Setup

A schematic view of the experimental device is shown in Fig. 2. The ellipsoidal cavity has a laser entrance small aperture (ϕ1.6 mm), a cluster beam exit aperture (ϕ3.2 mm) and a rectangular observation window. Clusters are produced by irradiating a frequency-doubled Nd:YAG laser at a repetition

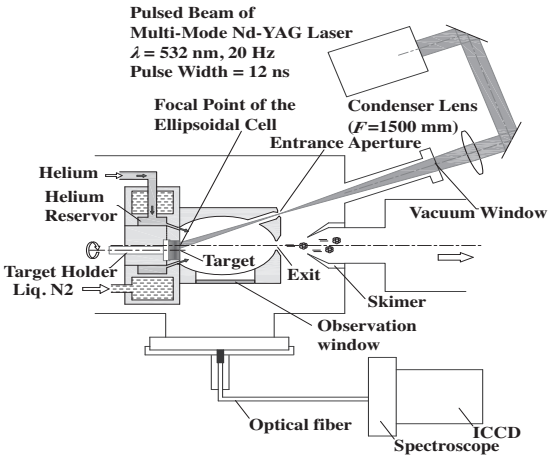

Figure 2: An experimental setup for spectroscopic analysis of SCCS.

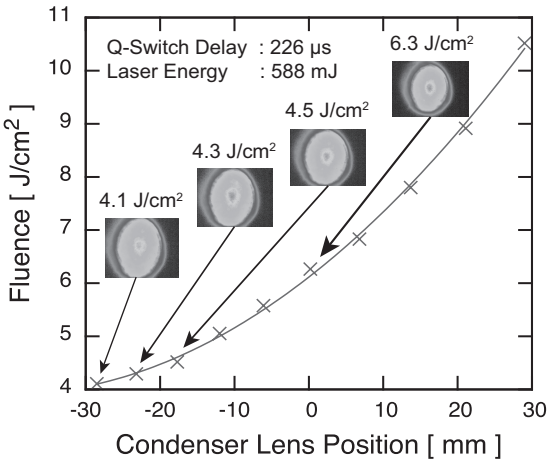

Figure 3: Dependency of laser fluence on condenser lens position. Images show laser intensity profiles under four different condenser lens positions.

rate of 20 Hz onto a silicon target located on the focal point of the cavity. Light emissions from the cavity were observed with a spectroscope and an ICCD camera through the observation window and an optical fiberbundle with a diameter of about 1 mm.

In the present study, we used two different spectroscopes. One of them was a wide-range type (JOBINYVON,CP140/104), which can cover a wavelength range from 300 to 800 nm in a single observation with a resolution of 4.05 nm. The other one (McPHERSON, 2035) was a high resolution type having a wavelength resolution of 0.12 nm. We employed the former to get entire pictures and the latter to investigate specificspectra lines. In advance of the experiment, we obtained spectral data of a mercury lamp to calibrate the wavelength axis of the spectroscopes. The wave length resolutions mentioned above were determined from the FWHM of spectral lines from mercury atoms. The laser pulses with an energy of 588 mJ and a duration of 12 ns was focused with a 1500-mm-focal-length condenser lens on the target as shown in Fig. 2. By changing the condenser lens position, we changed the laser spot size to perform the experiment under various laser fluences. Figure 3 plots the laser fluence as a function of the condenser lens position. In the spectroscopic measurement, we used four different laser irradiation conditions with fluences from 4.1 to 6.3 J/cm^2. The laser power densities corresponding to these laser fluences were $3.4-5.2\times10^8$ W/cm^2. These values are slightly above the threshold of the laser ablation, so we expect to suppress the production of multi-charged ions[4]. Images in Fig. 3 were taken with a beam profiler (OPHIR, PX-50). We adjusted the laser optics to minimize the asymmetry of the laser intensity profiles. The laser fluences were estimated by substituting laser pulse energies measured with a calorimeter (OPHIR, F100A-HE-SH) by laser spot areas, which were assumed to be equal to ellipse areas calculated from the lengths of major and minor axes of the intensity profiles.

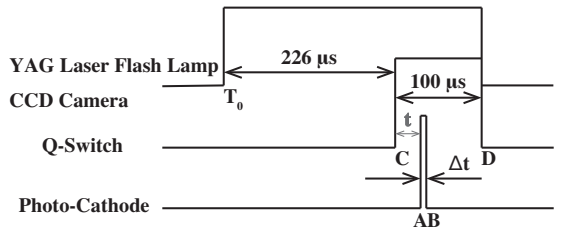

Figure 4: A timing chart of the laser and ICCD camera.

Figure 4 shows a timing chart of the laser and ICCD camera. We performed the spectroscopic measurement with changing the delay time t, which means time from triggering the laser Q-switch to applying a gate voltage to the photocathode of the ICCD. The exposure time of the ICCD was typically $\Delta t = 500$ ns. When taking a spectrum, we accumulated 500 shots to ensure enough statistical accuracy of the data.

3. Results and Discussion

A typical spectrum taken with the wide-range spectroscope is shown in Fig. 5. We found that light emissions from Si^+ were dominant. Figure 6 shows the spectral line profiles around 390 nm at $t = 1-2.5$ μs. One can see that these profiles clearly consist of at least two line spectra from Si (390.6 nm) and Si^+ (386.5 nm). Light emissions from neutral silicon atoms were observed but its intensity was lower than that of Si^+ ions in the early stage of the plume expansion ($t \leq 1$ μs). The peak

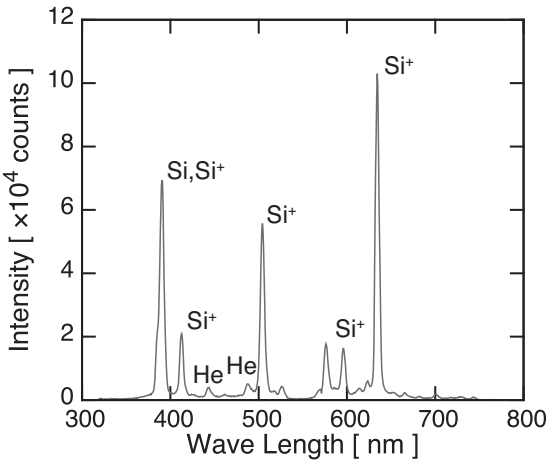

Figure 5: A typical spectrum of light emission from the SCCS cavity 2 μs after laser irradiation.

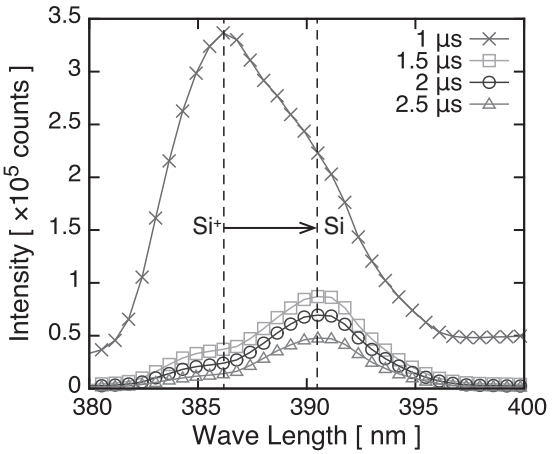

Figure 6: Peak shift of the combined spectrum.

position of the spectral line profile obviously changed after 1.5 μs. This shift means that the spectral line intensity of silicon atoms largely exceeded that of Si^+ ions in this wavelength region. Thus, we can regard that this spectral line was mostly attributed to the line emission from Si atoms after 1.5 μs.

Based on this assumption, we investigated relative intensity of two spectral lines at wavelengths of about 390.6 nm and 504.1 nm. At each of time, we defined the total spectral intensity integrated over wavelengths from 300 to 800 nm as I_0, and spectral intensity of a specific line as I_λ, here λ denotes wavelength in nanometer. We analyzed the time evolution of relative intensities $I_{390.6}/I_0$ and $I_{504.1}/I_0$, which are shown in Fig. 7 and 8, respectively. The figures clearly show that there exists a strong correlation between these two line intensities, that is, emissions intensity of Si atoms increases when that of Si^+ ions decrease, and vice versa. In addition, one can see that light emissions from silicon neutral atoms were suppressed and that from Si ions were enhanced when the laser fluence was relatively high (6.3 J/cm^2). This trend is consistent with a well known fact that the ionization degree of an ablation plasma increases in proportion to the irradiation power density of the laser. Our results also show that lower laser fluence is better to generate neutral silicon atoms. Of course, if the laser fluence is too low, the laser ablation cannot supply enough amount of silicon atoms for cluster formation. Thus, there should be an appropriate laser fluence from the viewpoint of efficient production of clusters.

Finally, we compare the results of these spectroscopic analysis with framing images of ablation plume behavior in the ellipsoidal cavity. The latter was taken with an ICCD camera[5]. A typical image of the ablation plume is also shown in Fig. 9. In this image, the target position is indicated by a dashed line. The visible light emission from an ablation plume traveling perpendicularly to the target surface (from left to right in the image) was recored 2 μs after laser irradiation with an exposure time of 500 ns. We can recognize that the head of the plume shined more brightly than others. While at the same time, the spectrum in this figure shows that the intensity of the silicon atom spectral line (λ =390.6 nm) was the highest of all. This indicates that emissions from silicon atom mainly contribute to the bright spot at the head of the plume. We investigated the spectral line at a wavelength of about 390 nm more in detail with the high-resolution spectroscope. We could separate a spectral line of silicon atoms (λ=390.6 nm) from those of ions (λ=386.5 nm and 388.7 nm) as shown in Fig. 9. The intensity of silicon atomic line was found to be much higher than the other silicon ionic lines, which strongly supports our assumption that the emission from silicon atoms dominates the spectral line observed at 390.6 nm in Fig. 9 at the early stage of the plume expansion ($t \leq 2 \sim 3\mu$s). Figure 10 compares the time evolution of the emission int-

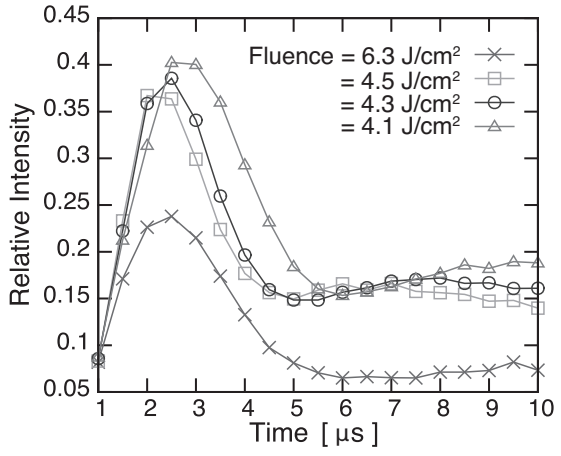

Figure 7: Time evolutions of relative intensities of spectral lines around 390.6 nm under various laser fluences.

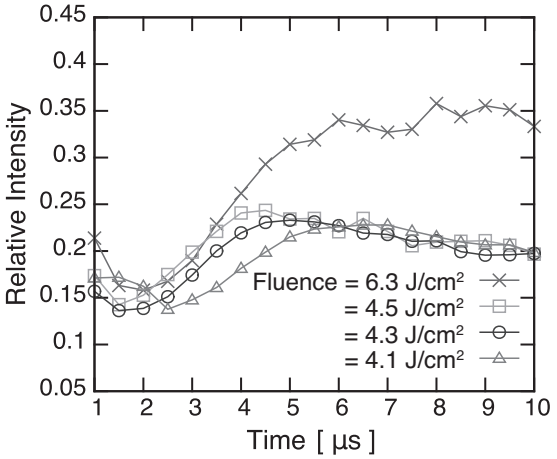

Figure 8: Time evolutions of relative intensities of spectral lines around 504.1 nm under various laser fluences.

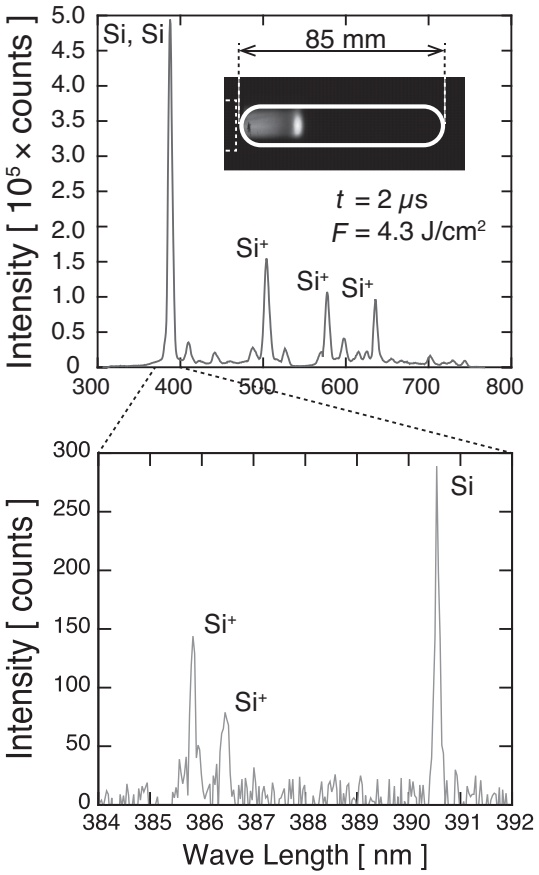

Figure 9: Comparison at plume behavior with emission spectra observed with a wide-range spectroscope and high-resolution one.

ensity of silicon atoms with that of the total emission of the plume observed with the ICCD camera [5]. The time evolutions of these two kinds of emissions were almost coincide with each other.

This result also indicates that the head of the plume mainly consisted of silicon atoms. In the head of the plume, where mixing of silicon vapor and helium gas probably occurred, so we think that the cooling of the silicon vapor by the cold helium gas could enhance the recombination of silicon ions and electrons in this area. The hypothesis that emissions from that area are primarily due to silicon atoms is consistent with our prediction that clusters are mainly produced in the mixing area. To examine correlations between the emission spectrum of the plume and a cluster generation in more detail, we plan to use a high sensitivity spectrometer.

4. Conclusion

We performed a time-resolved spectroscopy analysis for light emissions from the ellipsoidal cavity of the SCCS. We found that the generation of silicon ions could be suppressed by carefully choos

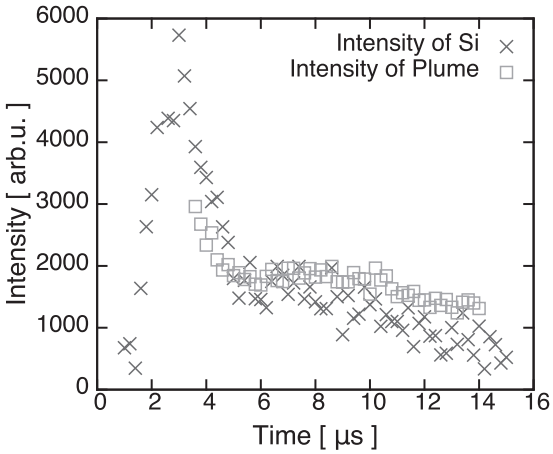

Figure 10: Comparison of time evolution between the total emissions intensity of the silicon vapor plume observed with an ICCD camera with silicon atoms.

ing the laser fluence, and there was an inverse correlation between light emissions from silicon neutral atoms and ions. Moreover, by comparing the spectroscopy analysis with the observation of the ablation plume behavior in the ellipsoidal cavity, we revealed that light emissions from the head of the plume where clusters might be mainly produced by interactions with helium gas primarily came from silicon neutral atoms.

References

[1] Y. Iwata, M. Kishida, M. Muto, S. Yu, T. Sawada, A.Fukuda, T. Takiya, A. Komura, K. Nakajima, " Narrow Size-distributed Silicon Cluster Beam Generated Using a Spatiotemporal Confined Cluster Source", Chemical Physics Letters, 358, 36-42 (2002).

[2] M. Yaga, T. Takiya, Y. Iwata, " Numerical study of unsteady compressible flow driven by supersonic jet injected into elliptical cell with small exit hole" , Shock Waves 14, 403-411(2005).

[3] Y. Iwata, K. Tomita, T. Uchida, H. Matsuhata, "Crystallographic Coalescence of Crystalline Silicon Clusters into Superlattice Structures", Cryst. Growth Des. 2015, 15, 2119-2128.

[4] P. Mulser, D. Bauer, " High Power Laser-Matter Interaction", STMP 238, Springer, Berlin Heidelberg, 361-363 (2010).

[5] Y. Ishikawa, A. Takada, J. Hasegawa, Y. Iwata, K. Horioka, " Plume velocity analysis on a spatiotemporally confined cluster source", NIFS-Proc. (this volume).

Characteristics and Biological Applications of Atmospheric-pressure Non-thermal Plasma Jets

Norimitsu Takamura[1*, a)], Douyan Wang[1], Takao Namihira[1, b)] and Hidenori Akiyama[1]

[*1] *Institute of Pulsed Power Science, Kumamoto University*

ABSTRACT

Atmospheric-pressure non-thermal plasma jets (APPJs) have been widely studied and used in particular for biological and medical applications since they can be touched by a bare hand and can produce highly reactive chemical species. On the other hand, in biological and medical research fields, the "Protein transduction method" was required to improve their transduction efficiency into cells. In our previous study, therefore, we demonstrated that a certain type of proteins was successfully delivered into human cells by irradiating an APPJ for 30 seconds in comparison with no plasma treated cells. In this study, as basic research for improving the efficiency of our new protein transduction method using APPJs, at first, we focused on the kind of dielectric material and generated two types of APPJs by using a glass- or an alumina- tube. And then, we investigated their emission spectra. Secondly, we developed a "Dry plasma jet (DPJ)", generated using only dry helium gas, and a "Mist plasma jet (MPJ)", generated using dry helium gas mixed with water mist, by using an alumina tube and investigated their emission spectra. Finally, we checked the effects of irradiating DPJ and MPJ on HeLa cells by determining their viability. The experimental results suggest that MPJ generated using an alumina tube has a good potential for improving the efficiency of our new protein transduction method.

Keywords

Atmospheric-pressure plasma jet, protein transduction, dielectric material, dry plasma jet, mist plasma jet

1. Introduction

Atmospheric-pressure non-thermal plasma jets (APPJs) have been widely studied and used in particular for biological and medical applications such as disinfection, sterilization, cell growth, and cancer treatment [1-4]. In these studies, most of APPJs were generated by flowing helium (He) or argon (Ar) gas through a dielectric cylindrical tube wrapped with a coaxial high voltage (H.V.) electrode and a ground (GND) electrode connected to a AC or pulsed high voltage (H.V.) power supply in the output range of several kV and kHz (see Fig. 1). One of the main features of APPJs is able to be touched by a bare hand without any feeling of electrical shock or warmth. Furthermore, APPJs have unique capability of generating high-energy electrons, ions, ultraviolet light, and free radicals such as reactive oxygen species (ROS) and reactive nitrogen species (RNS) (see Fig. 2). Especially, OH radicals produced by APPJs are well-known as a most important factor to cause cell stimulation.

On the other hand, a technology, which enabling introduction of polymers into cells, has concurrently advanced with the development of molecular biology. Particularly, induced pluripotent stem (iPS) cells have attracted attention in the field of regenerative medicine. It is well known that there are two main types of the way to create iPS cells. One way is the "Gene transfection method" and the other is the

a) Present affiliation of: Norimitsu Takamura.
Department of Electrical Engineering, Faculty of Engineering, Fukuoka University
8-19-1 Nanakuma, Jonan-ku, Fukuoka 814-0190, Japan
b) Correspondence to: Takao Namihira.
E-mail: namihira@cs.kumamoto-u.ac.jp
Institute of Pulsed Power Science, Kumamoto University
2-39-1 Kurokami, Chuo-ku, Kumamoto 860-8555, Japan

"Protein transduction method" [5-6]. The former is generally accomplished by introducing genes into cells using retroviral virus vectors. However, most of the methods producing iPS cells developed to date still involve the use of genetic materials and the consequent potential for unexpected genetic modifications or malignant alterations by exogenous sequences in the target cells [7]. In contrast, the latter is accomplished by introducing appropriate proteins functioning in remodeling chromatin structure directly into target cells [8], thus avoiding unexpected genetic modifications or malignant alterations. However, a problem exists that transduction of proteins into cells is often inefficient.

In our previous study, therefore, we demonstrated that green fluorescent proteins fused to protein transduction domain (PTD-GFPs) were successfully delivered into human cultured cells (HeLa cells) by irradiating an APPJ for 30 seconds in comparison

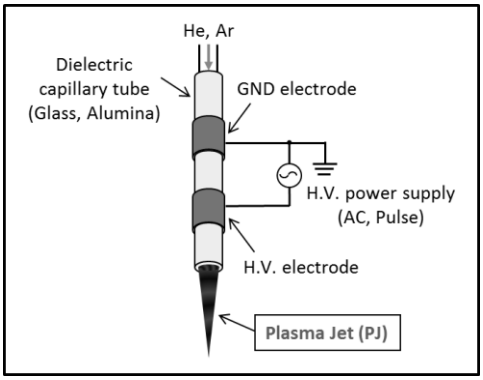

Fig. 1. Schematic of typical APPJ.

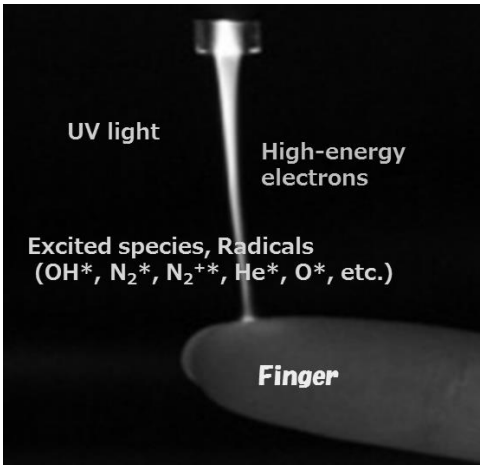

Fig. 2. Image of typical APPJ.

with no plasma treated cells [9]. Additionally, we developed a "Mist plasma jet (MPJ)", generated using dry helium gas mixed with water mist, as alternatives to the traditional method using only dry helium gas, known as the "Dry plasma jet (DPJ)" in order to increase OH and H_2O_2 production amount for causing cell stimulation [10].

In this study, as basic research for improving the efficiency of our new protein transduction method using APPJs, at first, we focused on the kind of dielectric material and generated two types of APPJs by using a glass- or an alumina- tube. And then, we investigated their emission spectra. Secondly, we developed DPJ and MPJ by using an alumina tube and investigated their emission spectra. Finally, we checked the effects of irradiating DPJ and MPJ on human cells by determining their viability. In this paper, we report about the above experimental results.

2. Experimental Setup

2.1 Emission spectroscopic measurements of APPJs generated using different dielectric tubes

Fig. 3 shows the schematic diagram of experimental setup for emission spectroscopic measurements of APPJs generated using different dielectric tubes. In this study, a glass tube (TE-32 Glass, Iwaki, Japan; inner diameter: 3 mm, outer diameter: 6 mm) and an alumina tube (SSA-S, AGC TECHNO GLASS, Japan; inner diameter: 3 mm, outer diameter: 5 mm) ware used as dielectric cylindrical tubes. The relative permittivities (ε_r) of the glass- and the alumina- tubes were 4.8 and 8.5, and the condenser capacities (C) of the both tubes were 8.87 pF and 21.31 pF, respectively.

A dry helium gas cylinder, a mass flow controller (8500MC, KOFLOC, Japan), and the glass or the alumina tube were connected using gas plumbing tubes. The helium gas flow rate was controlled to 3.0 L/min by the mass flow controller. A pair of coaxial copper electrodes surrounded the both tubes with the 10 mm width and the 30 mm separation. The electrodes were connected to a H.V. power supply (LHV-13AC, Logy Electric, Japan). The output

voltage and the operating frequency of the power supply were fixed at 10 kV and 10 kHz, respectively.

The applied voltage and the discharge current between the electrodes were measured using a high voltage probe (P6015A, Tektronix, USA) and a current transformer (Pearson current monitor; Model 2878, Pearson Electronics, USA). A digital oscilloscope (TDS3054B, Tektronix, USA) recorded the signals from the voltage probe and the current transformer.

For observation and comparison of the APPJs' emission spectra, a digital delay generator (DG535, Stanford Research System, USA), an ICCD camera with high speed gate (C8484-05, Hamamatsu Photonics, Japan) coupled to a multichannel spectrograph (C5094, Hamamatsu Photonics, Japan), and a personal computer installed an image analyzing software (U9317, Hamamatsu Photonics, Japan) were used.

2.2 Emission spectroscopic measurements of DPJ and MPJ

Fig. 4 shows the schematic diagram of DPJ and MPJ generation systems. DPJ was generated using only dry helium gas by directly connected a dry helium gas cylinder, a mass flow controller (8500MC, KOFLOC, Japan), and an alumina tube (SSA-S, AGC TECHNO GLASS, Japan). Conversely, MPJ was generated using helium gas to which pure water mist was added by installing an atomizing device between the mass flow controller and the alumina tube. The helium gas flow rate was controlled to 3.0 L/min by the mass flow controller. A pair of coaxial copper electrodes surrounded the alumina tube with the 10 mm width and the 30 mm separation. The electrodes were connected to a H.V. power supply (PHF-2K, HAIDEN KENKYUUSYO, Japan). The output voltage and the operating frequency of the power supply were fixed at 10 kV and 10 kHz, respectively.

Fig. 5 shows the schematic diagram of experimental setup for emission spectroscopic measurements of DPJ and MPJ. For observation and comparison of DPJ and MPJ emission spectra, a plano-convex lens (SLSQ-100-200P, SIGMA KOKI, Japan), an optimal fiber, and a multichannel spectrometry device (PMA-12 C10027-01, Hamamatsu photonics, Japan) were used.

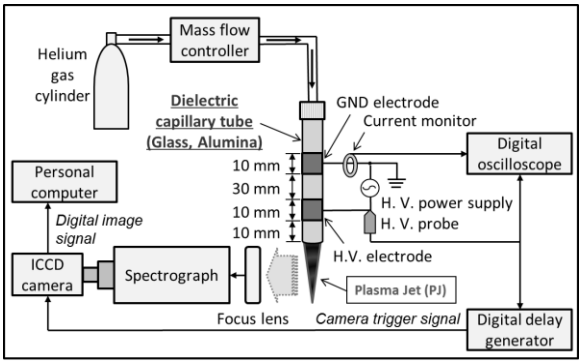

Fig. 3. Schematic diagram of experimental setup for emission spectroscopic measurements of APPJs generated using different dielectric tubes [11].

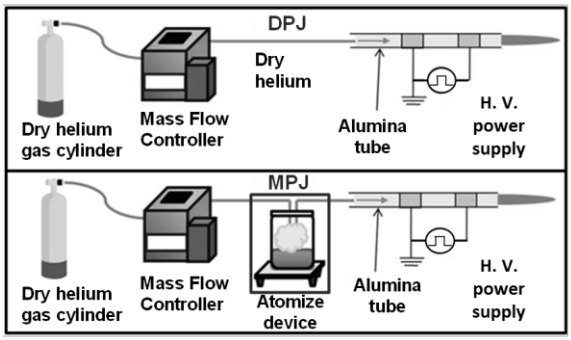

Fig. 4. Schematic diagram of DPJ and MPJ generation systems [12].

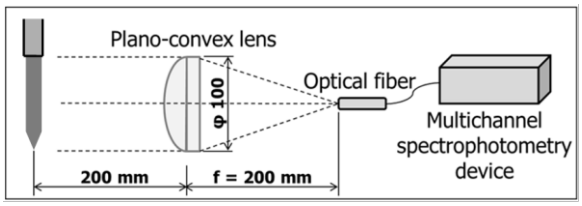

Fig. 5. Schematic diagram of experimental setup for emission spectroscopic measurements of DPJ and MPJ [12].

2.3 Effects of DPJ and MPJ on Human cells

Fig. 6 shows the schematic diagram of experimental setup for irradiating DPJ and MPJ on Human cells. DPJ and MPJ were generated at the same conditions shown in section 2.2 (see Fig. 4).

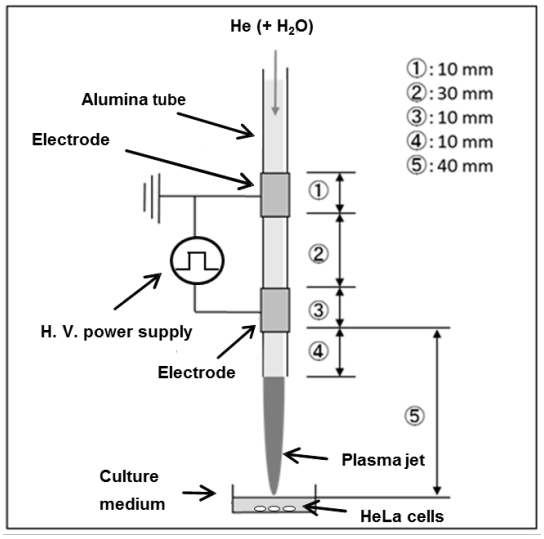

Fig. 6. Schematic diagram of experimental setup for irradiating DPJ and MPJ on human cells [12].

This study utilized human cancer (HeLa) cells. The HeLa cells were cultivated for 24 hours in an incubator at 37 ˚C with 5% of CO_2. Irradiation time of DPJ and MPJ to the HeLa cells was fixed for 5 min. After 24 hours from the DPJ and MPJ irradiation, dead cell nuclei were stained by Propidium Iodide (PI) in order to determine the cell viability. After that, the dead cells were observed by a type fluorescence microscope (ECLIPSE TE2000-s, Nikon, Japan) and a flow cytometry (PERFLOW Sort 4c TSK, AS ONE, Japan). The amount of cell culture medium was fixed to 2.0 mL per cell culture dish.

3. Results and Discussion

3.1 Emission spectroscopic measurements of APPJs generated using different dielectric tubes

Fig. 7 shows typical images of APPJs, generated using the glass- and the alumina tubes, taken by ICCD camera. From Fig. 7 (a) and (b), the APPJ generated using the alumina tube is little longer than the APPJ generated using the glass tube.

Fig. 8 shows the emission spectra of APPJs generated using the glass- and the alumina- tubes From Fig. 8 (a) and (b), it is clear that the emission intensity of the APPJ generated using the alumina tube is much higher than that of the APPJ generated using the glass tube, which means that the production

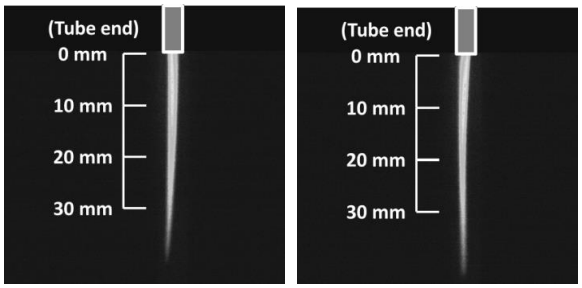

(a) Glass tube (b) Alumina tube

Fig. 7. Typical images of APPJs taken by ICCD camera [11].

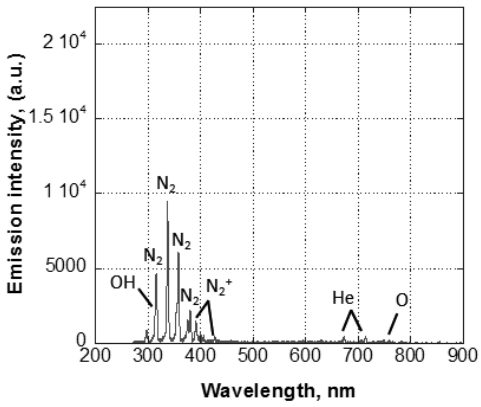

(a) Glass tube

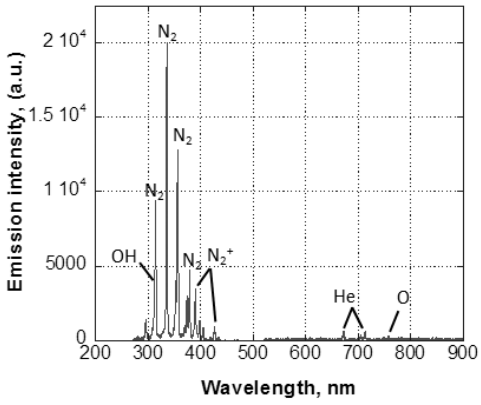

(b) Alumina tube

Fig. 8. Emission spectra of APPJs generated using the glass- and the alumina- tubes (whole of emission region) [11].

amount of reactive chemical species, such as OH* (309 nm), N_2* (Second Positive System: SPS; 315.9, 337.1, 375.5, and 380.5 nm), and N_2^+* (First Negative System: FNS; 395.1 and 487.8 nm), were clearly increased by using the alumina tube.

These results suggest that an APPJ generated using a dielectric tube having higher relative permittivity and/or higher condenser capacity might be able to strongly affect to cause cell stimulation, which means that it might have a good potential for improving the efficiency of our new protein transduction method.

3.2 Emission spectroscopic measurements of DPJ and MPJ

Fig. 9 shows the emission spectra of DPJ and MPJ. As can be seen from Fig. 9 (a) and (b), the emission intensity of OH* (309 nm) decreased with increasing the amount of H_2O. Moreover, MPJ was seen to result in a lower emission intensity of O* (777 nm) than DPJ. These results might be due to following formulas [12].

$$e + H_2O \rightarrow H + OH + e \quad (1)$$

$$O(^1D) + H_2O \rightarrow 2OH \quad (2)$$

$$OH + OH \rightarrow H_2O_2 + (M) \quad (3)$$

From formula (1), much OH* and ground state OH might be produced in MPJ; however, in this experiment, it could not measure ground state OH because it has no illuminant. In addition, from formula (2), O* (777 nm) of MPJ might decreased by an instant reaction between O and H_2O. Furthermore, from formula (3), the production amount of H_2O_2 might increase with increasing the amount of H_2O.

3.3 Effects of DPJ and MPJ on Human cells

Fig. 10 and Fig. 11 show the microscopic images and the flow cytometry images of HeLa cells after 24 hours from DPJ and MPJ irradiation. While about 70% of cells died by irradiating DPJ, almost all cells died by irradiating MPJ. This assumed the increased amount of OH*, ground state OH, and H_2O_2 production caused by adding pure water mist (H_2O) to the plasma source, helium gas.

These results suggest that MPJ can strongly affect to cause cell stimulation, which means that it might have a good potential for improving the efficiency of our new protein transduction method.

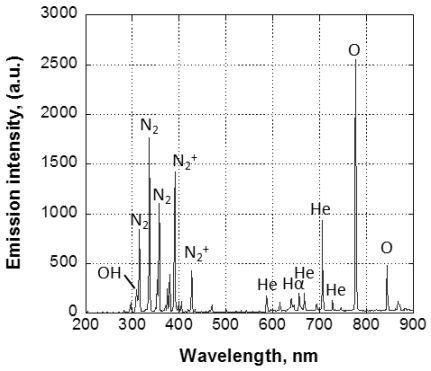

(a) DPJ

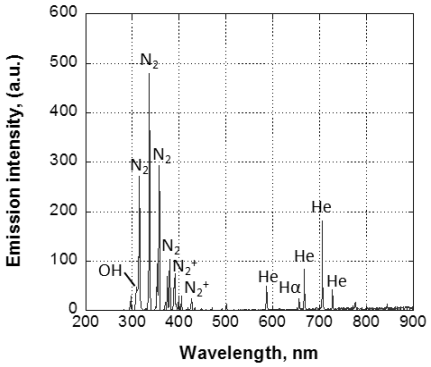

(b) MPJ

Fig. 9. Emission spectra of DPJ and MPJ (whole of emission region) [12].

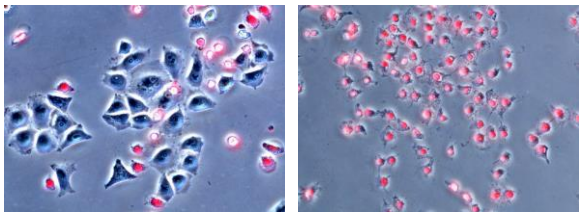

(a) DPJ (b) MPJ

Fig. 10. Microscopic images of HeLa cells after 24 hours from DPJ and MPJ irradiation [12].

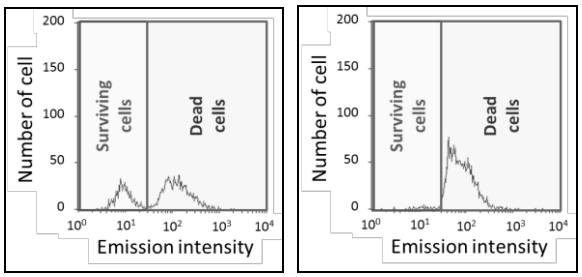

(a) DPJ (b) MPJ

Fig. 11. Flow cytometry images of HeLa cells after 24 hours from DPJ and MPJ irradiation [12].

4. Conclusions

In this study, as basic research for improving the efficiency of our new protein transduction method using APPJs, at first, we focused on the kind of dielectric material and generated two types of APPJs by using a glass- or an alumina- tube. And then, we investigated their emission spectra. Secondly, we developed DPJ and MPJ by using an alumina tube and investigated their emission spectra. Finally, we checked the effects of irradiating DPJ and MPJ on HeLa cells by determining their viability.

The experimental results suggest that MPJ generated using an alumina tube has a good potential for improving the efficiency of our new protein transduction method

Interaction between APPJs, cell culture medium and cells, mechanism of protein transduction using APPJs are required explain the details in the future works.

References

[1] R. ONO, "Plasma Medicine", *IEEJ Journal*, 133, 5, pp.290-293 (2013) [in Japanese].

[2] K. KITANO et al., "Mechanism of Plasma Disinfection by Plasma Jet and its Applications: Physics, Chemistry, Molecular Biology in Effective Sterilization with the Reduced pH Method", *J. Inst. Electrostat. Jpn.*, 37, 3, pp.112-116 (2013) [in Japanese].

[3] C. TSUTSUI et al., "Tissue and Cell Activation Using Micro-Spot Atmospheric Pressure Plasma Source", *J. Inst. Electrostat. Jpn.*, 35, 1, pp.20-24 (2011) [in Japanese].

[4] D. SHIBAHARA et al., "Sterilization of *Escherichia coli* by Small Size Argon Plasma Jet", *J. Inst. Electrostat. Jpn.*, 34, 1, pp.2-7 (2010) [in Japanese].

[5] K. TASHIRO et al., "Efficient Adipocyte and Osteoblast Differentiation from Mouse Induced Pluripotent Stem Cells by Adenoviral Transduction", *Stem Cells*, 27, 8, pp.1802-1811 (2009).

[6] H. ZAEHRES et al., "Induced Pluripotent Stem Cells", *Methods in Enzymology*, 476, pp.309-325 (2010).

[7] M. I. LAI et al., "Advancements in Reprogramming Strategies for the Generation of Induced Pluripotent Stem Cells", *J. Assist. Reprod. Genet.*, 28, 4, pp.291-301 (2011).

[8] R. BERTOLOTTI, "Translational Perspectives Transient Epigenetic Gene Therapy: Hazard-free Cell Reprogramming Approach and Rising Arm of a Universal Stem Cell Gene Therapy Platform", *Gene Therapy and Regulation*, 4, 1, pp.11-39 (2009).

[9] N. TAKAMURA et al., "Protein Transduction into Eukaryotic Cells Using Non-thermal Plasma", *Int. J. Plasma Environmental Sci. Tech.*, 6, 1, pp.59-62 (2012).

[10] N. TAKAMURA et al., "Generation of Atmospheric-pressure Mist Plasma Jet and its Characteristics", *J. Inst. Electrostat. Jpn.*, 38, 1, pp.22-27 (2015) [in Japanese].

[11] N. TAKAMURA et al., "Emission Spectroscopic Measurements of Atmospheric-pressure Non-thermal Plasma Jets Generated Using Glass- and Alumina- Tubes", *J. Inst. Electrostat. Jpn.*, 39, 1, pp.9-14 (2015) [in Japanese].

[12] K. UMEDA et al., "Generation of Atmospheric-pressure Dry- and Mist- Plasma Jets and Their Effects on Human Cells", *Proc. 5th Euro-Asian Pulsed Power Conf.*, 4pp (2014)

Study on the Laser Triggered Pinch Discharge for High Power EUV Source

Lim Soowon, Seiya Kitajima, Takashi Kamohara, Hidenori Akiyama, Sunao Katsuki

Kumamoto University

ABSTRACT

This Paper reports a physical limitation of high-rep-rate operation and extreme ultraviolet (EUV) emission intensity depend on current rise time of laser triggered pinch discharge (LTD) plasma source for high power EUV radiation. The post-discharge phenomena of the EUV source were observed tin droplet distribution and visible light emission of the LTD plasma using both of the schlieren method and high-speed camera, respectively. The schlieren images show development of tin droplets between the electrodes after a discharge. The visible light images show that a subsequent laser pulse evaporates not only the cathode surface but also the droplets which are generated by the previous discharge. As a result, the large amount of vaporized tin droplet discourages a strong Z-pinch which is essential for the high-power EUV radiation. We investigated the EUV emission intensity by changing the current rise time. The current rise time (20~80 % of the peak value) was changed from 30 ns to 55 ns. The experimental results show that faster rise time represents stronger EUV yields despite of its lower energy.

Keywords

Key Words : EUV, Laser trigger, discharge plasma, post discharge, droplet, rise-time

1. Introduction

Extreme ultraviolet (EUV) is taken as extending from wavelengths in vacuum of about 5 nm to 40 nm with corresponding photon energies from about 30 eV to about 250 eV. It is a region of the electromagnetic spectrum where there are a large number of atomic resonances, leading to absorption of radiation in very short distances, typically measured in nanometers or micrometers, in all materials. These resonances provide mechanisms for both elemental and chemical identification. Moreover, because the wavelengths are relatively short, it makes possible both to see smaller structures as in microscopy, and to write smaller patterns as in lithography [1].

Extreme ultraviolet lithography (EUVL) is the leading technology considered for printing circuits at the 32 nm node and below [2, 3]. In order to support high volume manufacturing of the EUVL, surrounding technologies such as actinic mask inspection and source are being developed [4]. For the actinic mask inspection applications, more than 30 W brightness of the in-band (13.5 nm +/- 1 %) EUV beam after debris mitigation and spectral purifying filter is needed. Furthermore, more than 1 hour of 10 ms integrated energy stability (within 1 %) and 14 days of continuous operation without any maintenance are required to satisfy the requirements [5].

Laser triggered discharge (LTD) plasma source is regarded as a promising candidate for actinic mask inspection applications since it can provide not only sufficient radiance but also power. The LTD plasma source was originally developed for lithography application and still used in a beta-level scanner showing stable performance and high reliability [4].

We previously investigated the electrical recovery and EUV emission recovery between two sequential LTD plasmas [6]. We found that the recovery time of EUV emission limit the minimum time interval

during high-rep-rate operation. This paper describes post-discharge phenomena by using both of the schlieren method and high-speed camera to explain the EUV emission recovery process. Furthermore, we investigated a dependence of the EUV intensity on the current rise time.

2. Experimental Setup

Figure 1 shows a schematic diagram of the LTD plasma source. A tin rod cathode is 8 mm in diameter. An anode is of half-conical shaped stainless steel with a bottom diameter of 6 mm and with a 2 mm diameter vertical hole in the center. The anode is connected to a ground through a coaxial birdcage. The gap distance between the electrodes is 5 mm. the electrodes were in a vacuum chamber of below 1.0 x 10^{-5} Torr. The Z-pinch plasma was driven by a low inductance circuit for high-peak current. A capacitor bank is 34 nF and charged up to -21.7 kV.

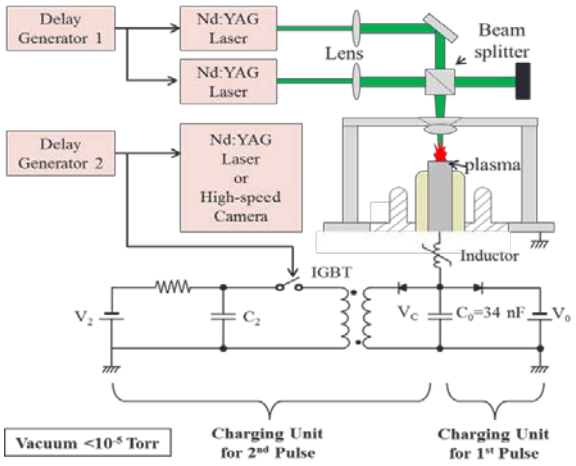

Fig. 1 Schematic diagram of LTD plasma source for schlieren and high speed camera experiments

Two Nd:YAG lasers were utilized to trigger the discharge between the electrodes individually (for first discharge, 532 nm, 12 mJ, Continuum Minilite; for second discharge, 532 nm, 12 mJ, New Wave Research Polaris II). The trigger lasers have 4-ns-long pulse width and 10^{10} W/cm^2 intensity according to the specifications. These lasers focused on a spot of the charged cathode surface through the hollow anode to produce a localized dense tin vapor. Since the produced vapor has reasonably good axial symmetry to the normal direction with respect to the target surface, the plasma can be compressed quickly and efficiently in comparison with conventional gas-fed Z-pinches [7].

The schlieren system comprises a 532 nm narrow bandpass filter, a 500 mm focal lens, a neutral density filter, a digital single-lens reflex camera, a horizontal knife-edge and a Nd:YAG laser(532 nm, 0.36 mJ, Continuum Minilite) as a light source. The schlieren method is based on a beam deflection, while the interferometry accounts for phase difference. The adjustment of the knife-edge plays a significant role in the quality of the schlieren image recorded because contrast of the images, camera saturation and loss of information will be affected. In this experiment, large cutoff was used to see the droplet distribution clearly. The high-speed camera (Stanford Scientific Research Quick E) is utilized instead of the laser for the schlieren method to observe early stage light emission of the plasma.

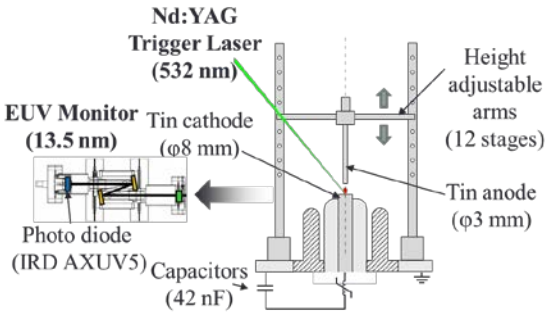

Fig. 2 Schematic diagram of LTD plasma source for different current rise time experiment

Figure 2 show a schematic diagram of the LTD plasma source for the different current rise time experiment. The coaxial birdcage in previous experiments was changed to a coaxial birdcage with height adjustable arms. The gap distance is 3 mm. The anode is tin rod of 3 mm in diameter. The current rise time (20~80 % of the peak value) was changed from 30 ns to 55 ns by changing the arms height. 42 nF capacitor bank was charged up to certain voltage to keep the peak current at 10 kA. The EUV intensity was monitored by a EUV monitoring system. The

monitoring system is consists of a photodiode (IRD AXUV5), a spectrum band pass filter (2 % at 13.5 nm) which is comprised of two silicone/molybdenum multilayer mirrors and a zirconium filter.

3. Results and Discussion

3.1 Developments of droplets of single LTD plasma

Time-resolved images of the schlieren photograph which show development of droplet after a discharge is shown in figure 3. The photographs were taken at various delay times from 200 μs to 5 ms. The droplets of larger than sub-micron are visible in this experiment because 532 nm laser was used as a light source. The droplets appear around 200 μs and are scattered near the cathode. At 400 μs, droplets are distributed throughout the entire electrodes gap. The density of the droplets was decreased after the 400 μs. The droplets last for more than 5 ms. However, it is worth noting that droplets smaller than these droplets, and thus invisible in this experiment, might have similar dispersion characteristics at faster velocities.

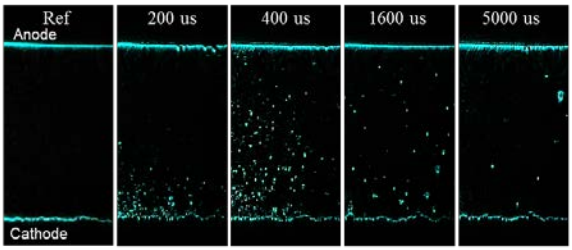

Fig. 3 Distribution of droplets after a discharge taken at different delay time

3.2 Effect of the droplets on the subsequent trigger laser irradiation

Figure 4 shows the visible light emissions from the laser ablation plasma. The pictures were taken at 20 ns after the trigger laser irradiation. Exposure time is 50 ns. Figure 4-(a) shows a typical visible light emission of the laser ablation plasma when the trigger laser was irradiated on the charged cathode surface. The typical ablation plasma has a shape of a candle light. The light emission by the subsequent trigger irradiation after the previous discharge is shown in figure 4-(b). In the figure 4-(b), light emission area and brightness are bigger and higher than the typical case. Furthermore, small spots are observed along the trigger laser axis. This experimental result suggests the subsequent trigger laser evaporate not only the irradiated cathode surface but also the droplets produced by the discharge previously. The large amount of vaporized tin droplet discourages a strong Z-pinch which is essential for the high-power EUV radiation. Consequently, the droplet limits the minimum time interval in high-rep-rate operation of the LTD plasma source.

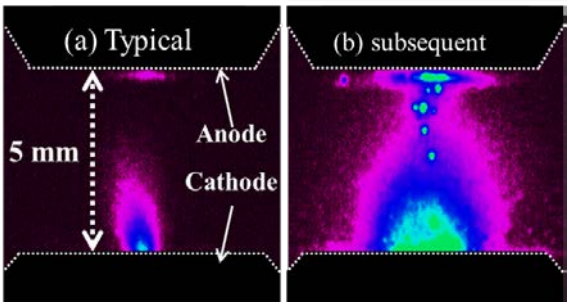

Fig. 4 Visible light emission from the plasma produced by the trigger laser

3.3 Effect of a current pulse rise time on the EUV intensity

Scattering of the droplet is an unavoidable consequence of using a plasma to generate photons. Bulgakova and Blugakov give an excellent theoretical and experimental treatment of this subject [8]. Although the literature describes the mechanism of liquid droplet ejection by pulsed laser ablation of solids, that theory may be applicable to the LTD plasma source. For the LTD plasma, not only the laser irradiation but also ion bombardment, heat conduction, radiation from the Z-pinch plasma and ohmic heating by discharge current can be heat sources. It is reasonable that if the discharge energy becomes lower, the amount of droplet will be lower. In this experiment, the discharge energy was varied by changing the total circuit inductance as shown in figure 2.

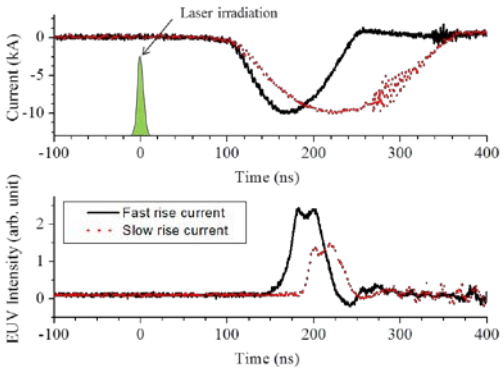

(a) Typical waveforms

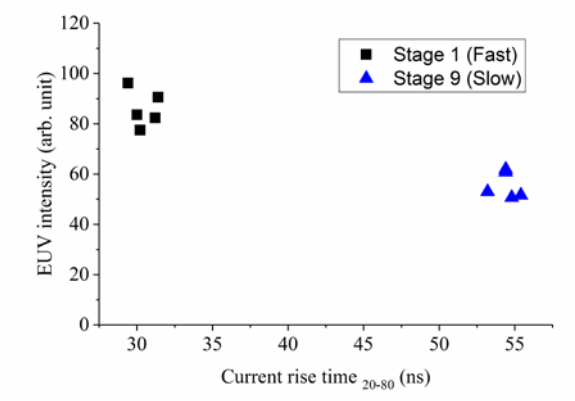

(b) Dependence of current rise time and EUV emission intensity

Fig. 5 Effect of current rise time on EUV yield for LTD plasma source

A typical current waveform and EUV intensity are shown in figure 5-(a). The rise times were changed from 30 ns to 55 ns while maintaining the peak current at 10 kA. The charged energy of capacitor of faster and slower rise time were 2.9 J and 10.2 J, respectively. The time integrated EUV intensity of the fast rise time case is 54.8 % stronger than slow rise time case in spite of the lower energy (Figure 5-(b)). The lower energy indicates lower energy consumption between the electrodes and consequently better for high repetition rate operation.

4. Conclusions

In this paper, the physical limitation of high-rep-rate operation of the LTD plasma source and the dependence of the EUV intensity and the current rise time were discussed. The droplets generated by previous discharge were vaporized by the subsequent trigger laser and consequently discourages the occurrence of a strong Z-pinch. The fast rise time has a great advantage regarding to the heat load and the droplet generation because of its low total energy consumption between the electrodes. Further study such as on a relationship between the vapor and current rise time should be conducted to understand the laser triggered pinch plasma physics and to improve the performance of the EUV sources.

References

[1] David Attwood, “Soft X-rays and Extreme Ultraviolet Radiation: Principles and Applications”, Cambridge University Press, Chapter 1. (1999)

[2] V. Banine and R. Moors, “Extreme Ultraviolet Sources for Lithography Applications Proc. SPIE 4343, 203-214 (2001)

[3] V. Bakshi, “EUV Sources for Lithography”, SPIE Press, Chapter 1. (2005)

[4] Y. Teramoto et al., “High-radiance LDP source for mask-inspection application”, *Proc. Of SPIE*, Vol. 9422, 94220F-1 (2015)

[5] Stephen F. Horne, “Metrology Source Requirements for Actinic Mask Blank Inspection”, *Proc. Of 2014 International Workshop on EUV and Soft X-Ray Sources*, Ireland, November 3-6 (2014)

[6] P. Lu et al., “Electrical Recovery after Laser-Assisted Discharge for Highly Repetitive Plasma EUV Source”, *IEEE Trans. Plasma Sci.*, Vol. 39, No. 9 (2011)

[7] P. Lu et al., “Dynamic Characteristics of Laser-Assisted Discharge Plasmas for Extreme Ultraviolet Light Sources”, *Japanese Journal of Applied Physics*, 49, 096202 (2010)

[8] N. M. Bulgakova, A. V. Bulgakov, “Pulsed Laser Ablation of Solids: Transition from Normal Vaporization to Phase Explosion”, *Appl. Phys. A* 73, 199 (2001)

Treatment of Larvae and Spawn of Zooplankton Simultaneously by Pulsed Power Injection into Water

Genki Nakao[1], Daisuke Kuwata[1], and Go Imada[1,2]

[1] *Department of Information & Electronics Engineering, Niigata Institute of Technology, Japan*

[2] *Extreme Energy Density Research Institute, Nagaoka University of Technology, Japan*

ABSTRACT

Enhancement of inactivation of larvae and spawn of zooplankton in ballast water is experimentally proved in pulsed power method. A large number of micro bubbles are successfully produced by applying the pulsed power (1.25 kV, 0.29 kA, 3.6 μs) to the water. Shock waves generated by collapse of the bubbles and/or instantaneous heating of the water due to the pulsed power injection may inactivate the larvae and spawn of the zooplankton. Artemia larvae and spawn are added to the water in s treatment chamber as the zooplankton and its egg. We found that 89 % of the larvae and 98 % of spawn are inactivated by firing 400 and 200 shots of the pulsed power injection, respectively.

Keyword

Pulsed power, Zooplankton, Ballast water, Micro bubble

1. Introduction

Ballast water is necessary to stabilize ship's hulls during navigation. The total amount of ballast water reaches 3 to 5 billion tons a year, which is transferred internationally. Japan exports approximately 0.3 billion tons of the ballast water a year and imports 0.017 billion. The ballast water includes bacilli, microbes, spawn and larvae of marine organisms, which are undesirably discharged at a port of call. To prevent the migration of these organisms and conserve the marine environment, a international convention for the control and management of ships ballast water and sediments was adopted by the International Maritime Organization in 2004 [1]. It obligates the ships to manage their ballast water by using devices not later than 2006. Many methods for treatment of the ballast water have been studied; such as chemical, heat, sonic, magnetic, biological, radioactive and electrical treatments [2-4], however, more methods and techniques are required to develop the feasible devices.

In this study, we propose a new technique on the treatment of the larvae and spawn of zooplankton in the ballast water [5], which uses pulsed-power method [6]. Micro bubbles are produced by applying the pulsed power to the water. Shock wave generated by collapse of the bubbles and/or instantaneous heating of the water between the pulsed power electrodes may affect the life of the larvae of zooplankton and its spawn.

The purpose of this study is to investigate the properties of simultaneously treatment of the larvae and spawn of zooplankton.

2. Experimental setup

Figure 1 shows the experimental setup. It consists of a pulsed power supply, a gap switch and a water vessel with electrode. The pulsed power supply, pulse forming network,PFN (4000 pF−10 μH × 8 stages, charged energy: 3.6 J), generates a rectangular pulsed power with 13 kV, 0.3 kA and 4 μs into short-circuited load (see Fig. 2). This pulse is applied to the electrode through the rotary gap switch, where the pulse repetition rate is 0.33 pps (pulse per second). The water vessel is made of clear

* imada@iee.niit.ac.jp

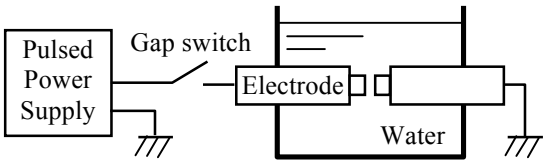

Fig. 1. Experimental setup.

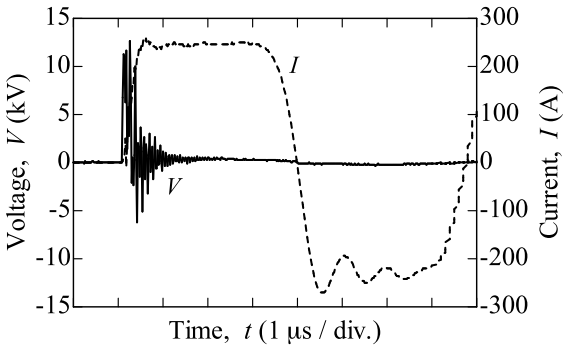

Fig. 2. Typical voltage and current of pulsed power supply into short-circuited load.

(a) Larva

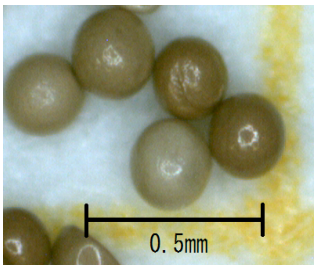

(b) Spawn

Fig. 3. Example of Artemia.

acrylic-resin sheet with the inner dimensions of 40×40×40 mm^3 and is filled with tap water (21 °C, 310 μS/cm, pH 7.1). The electrode, made of copper covered with acrylic-resin pipe, is located at 15 mm above the bottom of the vessel. Its gap diameter and distance are 2.4 and 0.3 mm, respectively. If all of the stored energy in the pulsed power supply is consumed to heat the water in the vessel, the water

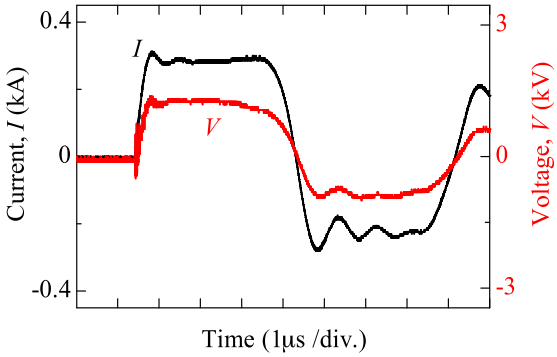

Fig. 4. Voltage and current at electrode.

temperature rises to 21.03 °C.

Artemia larvae and spawn are added to the water as the zooplankton and its spawn (see Fig. 3). The Artemia is a species of brine shrimp, which can live in 25-% salt water and its spawn have frozen and dry resistance [7]. The larvae of Artemia immediately after the incubation are used in this experiment. These are observed using a microscope. We assume that the larvae which stop moving in a minute are inactivated ones because of pulsed power injection. We also assume that the spawn which does not incubate within 26 hours in a salt water are inactivated ones because of pulsed power injection. The inactivation rate η for the larvae or spawn is defined as

$$\eta = \frac{\text{Number of inactivated larva or eggs}}{\text{Total number of larva or eggs}}. \quad (1)$$

3. Results and Discussion

3.1 Properties of pulsed power

Figure 4 shows the voltage and current at the electrode in the tap water. The pulsed power of 1.25 kV in voltage, 0.29 kA in current and 3.6 μs (FWHM) in pulse width of the current is applied to the water. It is found from Fig. 4 that the plateau of voltage is confirmed during 3.4 μs, where the power and the injected energy into the water at the period of the first positive pulse are estimated to be 0.36 MW and 1 J (3×10^{-7} kWh), respectively. Approximate one-third of the stored energy of the capacitor in the PFN is deposited into the water during the first positive pulse.

3.2 Bubble production by pulsed power injection into water

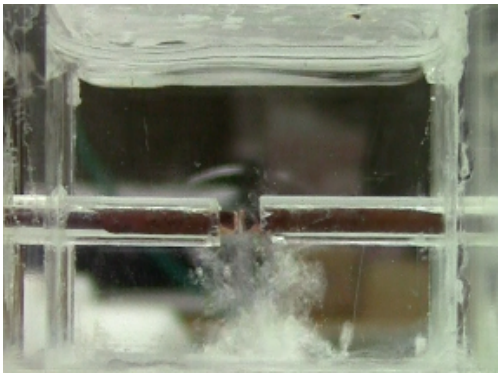

(a) Immediately after pulsed-power applying

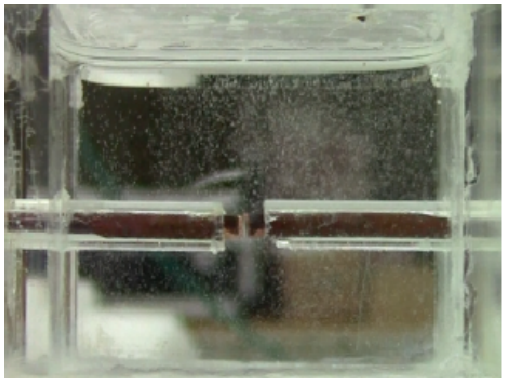

(b) Just before second pulse of pulsed-power applying

Fig. 5. Production and expansion of bubbles by pulsed-power injection into water.

Figure 5 shows the photographs of the bubbles produced by the pulsed power injection into the water. It is taken immediately after the pulsed-power applying and just before the second pulse of pulsed-power applying with the exposure time of 40 ms. Here, the time interval between the first and second pulse is 3 s. The expansion of bubbles into the water is seen as white fog around the electrode. The number density of bubble is estimated to be 10-20 bubbles/mm^2. The extent area of bubbles in the water is also estimated to be 300-500 mm^2. It is found from Fig. 5(b) that the babbles are widespread into the water just before the second pulsed-power applying.

3.3 Treatment of larvae and spawn of Artemia

Figure 6 shows the inactivation rate of the larvae of artemia in control experiment. Few larvae are inactivated in the fresh tap water within 45 minutes.

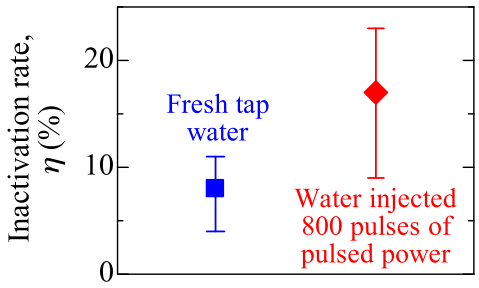

Fig. 6. Inactivation rate of larvae in control experiment.

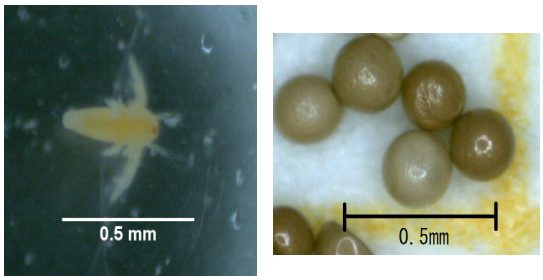

(a) Before pulsed power injection into water

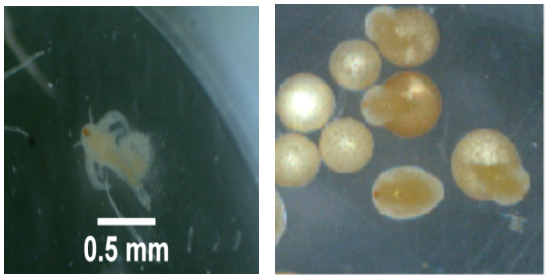

(b) After pulsed power injection into water

Fig. 7. Larvae and spawn before and after treatment.

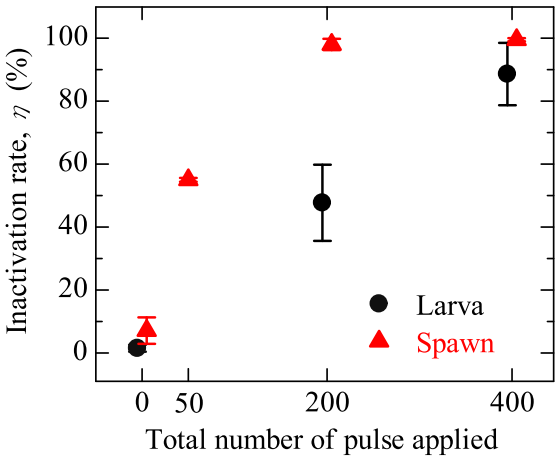

Fig. 8. Inactivation rate of larvae and spawn of Artemia as a function of number of pulsed power applied.

Some larvae are inactivated in the water which is injected 800 pulses of pulsed power within 45 minutes.

Figure 7 shows the larvae and the spawn before and after the pulsed-power injection into the water. Before the injection, the larvae swim the water actively and the spawn have a smooth texture. After the injection, on the other hand, the larvae lost his/her movement and the spawn are discolored and broken.

Figure 8 shows the inactivation rate of the larvae and the spawn of Artemia as a function of number of pulsed power applied into the water. Here, 250 larvae are discharged into the water and 250 spawn are contained in the water vessel. The pulsed power is continuously applied with 3 s in the time interval. We found that 89 % of the larvae and 98 % of spawn are successfully inactivated by firing 400 and 200 shots of the pulsed power injection, respectively. It is difficult to inactivate the larvae because the larvae swim the water freely. Since almost all the spawn collect in the bottom of the water vessel, the shock wave generated by the instantaneous heating of the water and the electric discharge between the electrodes may not affect the inactivation of spawn. It is found from Figs. 4 and 8 that the net energy efficiency for inactivation reaches 1.1 million larvae a kWh and 2.6 million spawn a kWh.

4. Conclusions

A large number of bubbles are produced by applying the pulsed power into the water. Simultaneously treatment of the larvae and spawn of zooplankton is successfully demonstrated by the pulsed-power injection into the water with a small amount of electric energy. Elucidation of the inactivation mechanism of the zooplankton is the subject for a future study.

Acknowledgement

The authors would like to thank Y. Tahara of Niigata Insitute of Technology for their help in the experiment for treatment of spawn.

This work was partly supported by JSPS KAKENHI Grant Number 26289079 and Uchida energy science foundation.

References

[1] GloBallast, http://globallast.imo.org/ (2011).

[2] M. Takahashi, K. Chiba and P. Li : “Free-Radical Generation from Collapsing Microbubbles in the Absence of a Dynamic Stimulus”, J. Phys. Chem. B, Vol. 111, pp. 1343-1347 (2007).

[3] S. Sawant, A. Anil, V. Krishnamurthy, C. Gaonkar, J. Kolwalker, L. Khandeparker, D. Desai, A. Mahulkar, V. Rande and A. Pandit : “Effect of Hydrodynamic Cavitation on Zooplankton: A Tool for Disinfection”, Biochem. Eng. J., Vol. 42, pp. 320-328 (2008).

[4] T. Sakugawa, N. Aoki, H. Akiyama, K. Ishibashi, M. Watanabe, A. Kouda and K. Suematu : “A Method of Cyanobacteria Treatment Using Underwater Pulsed Streamer-Like Discharge”, IEEE Trans. Plasma. Sci., Vol. 42, No. 3, pp. 794-798 (2014).

[5] Kouhei Satoh, Masayuki Onda, Shin-ichi Sakai, and Go Imada: “Treatment of Zooplankton in Water by Pulsed Power − An Effect of $NaHCO_3$ Additive for Micro Bubble Production −”, NIFS-PROC-90, 88-92 (2012).

[6] I. V. Lisitsyn et al., "Streamer Discharge Reactor for Water Treatment by Pulsed Power", *Rev. Sci. Instrum.*, **70**, 8, pp.3457-3462 (1999).

[7] G. Stappen, G. Merchie, J. Dhont, P. Lavens, P. Baert, T. Bosteels, P. Sorgeloos: “ARTEMIA” in Manual on the production and use of live food for aquaculture ed. by P. Lavens, FAO Fisheries Tech. Paper, No. 361, pp. 79-251 (1996).

Energy evaluation of Pulsed Heavy Ion Beam produced by Bipolar Pulse Accelerator

K. Okajima, K. Sugiura, H. Ohashi and H. Ito

Department of Electrical and Electronic Engineering, University of Toyama,
3190 Gofuku, Toyama 930-8555, Japan

ABSTRACT

We demonstrated evaluation experiments of a prototype bipolar pulse accelerator (BPA) which produces an intense pulsed ion beam with higher purity than the conventional ion diode. The BPA achieves the high purity in principle by the two step acceleration with a bipolar pulsed voltage. With the bipolar pulse with the voltage of ± 110 kV and pulse duration of about 70 ns, the ions from the gas puff nitrogen plasma source were successfully accelerated with the energy of the corresponding applied negative voltage of the bipolar pulse as the first step acceleration. The pulsed ion beam with current density of 70 A/cm^2 was obtained at 48 mm downstream from the grounded anode surface with the appropriate time delay operation of the plasma source and the bipolar pulse generator.

Keywords

Pulsed ion beam, Bipolar pulse accelerator, Pulse power technology

1. Introduction

Pulsed ion beam (PIB) technology has been developed primarily for nuclear fusion and high energy density physics research [1,2]. Recently, however, these PIBs with an ion energy of several 100 keV, a high ion current density of several 100 A/cm^2 and a short pulse duration of < 1 μs has been widely used for surface modification of material properties by the methods of ion implantation, ion plasma coating deposition and high energy ion beam impact [3-5]. Compared with the traditional ion implantation method, the PIB irradiation onto materials enables the accumulation of energy in very short time into the near surface region while it maintains a low substrate temperature. The annealing by PIB is expected to be a novel annealing technique for the next generation semiconductor materials such as silicon carbide (SiC). In the case of SiC, a high temperature annealing is normally done by using a traditional thermal method, which requires temperatures as high as 1500–1700ºC to recover the crystal damage and activate the dopants after the implantation. The conventional method at such a high temperature causes several disadvantages such as the redistribution of implanted dopants and increasing of surface roughness. Therefore, PIB has received extensive attention as a tool for a new ion implantation technique named “pulsed ion beam implantation” that can complete both the ion implantation and the annealing simultaneously.

To meet the requirements of research and industrial application, a number of PIB sources have been developed so far for different applications of PIBs [6-8]. The producible ion species, however, is limited to the material of electrode (anode), since the anode plasma is produced by a high-voltage flashover and an electron bombardment to the anode surface. In addition, the purity of the PIB is usually deteriorated by absorbed matter on the anode surface and residual gases in the diode chamber. Therefore, the conventional pulsed ion diode is not suitable for the application to the ion implantation. We have developed a new type of the magnetically insulated ion diode (MID) with an ion source of a gas puff

plasma gun and were successful in generating the high-purity pulsed nitrogen ion beam with an ion current density of 54 A/cm^2, a pulse duration of 90 ns and purity of the nitrogen beam of 94% [9]. In order to improve the purity of the intense pulsed ion beam, we have proposed a new type of pulsed ion beam accelerator named "bipolar pulse accelerator (BPA)" and developed a prototype of the accelerator and a bipolar pulse generator as the power supply of the BPA [10,11]. The bipolar pulse generator consists of a Marx generator and a pulse forming line (PFL) with a rail-gap switch on its end. The BPA utilizes a MID with an ion source of a coaxial gas puff plasma gun. In this paper, the evaluation of the characteristics of pulsed ion beam accelerated by the BPA and its energy are presented.

2. Principle of bipolar pulse accelerator

Figure 1 shows the conceptual diagram of the BPA. A conventional PIB diode is also shown for comparison. As shown in Fig. 1 (a), proposed ion accelerator is an electrostatic two-stage accelerator that consists of a grounded ion source, a drift tube and a grounded cathode. In the system, a bipolar pulse of voltage $\pm V_0$, duration τ_p each is applied to the drift tube. At first, the negative voltage pulse of duration τ_p is applied to the drift tube and ions on the grounded ion source are accelerated toward the drift tube. If τ_p is adjusted to the time of flight delay of the ions to pass the drift tube, the pulse is reversed and the positive voltage of duration τ_p is applied to the drift tube when top of the ion beam reaches the 2nd gap. As a result, the ions are again accelerated in the 2nd gap toward the grounded cathode. As seen in Fig. 1 (b), in the conventional PIB diode, the ion source is placed on the anode where high voltage pulse is applied, while in the proposed ion diode, BPA, the ion source is on the grounded anode which extremely enhances the accessibility to the anode.

Figure 2 illustrates the principle of the improvement of the purity of the ion beam. Let us now consider the acceleration of ions in the case that the ion beam produced in the ion source consists of N^+ ion and impurity of H^+ ion. Each ion of N^+ and H^+

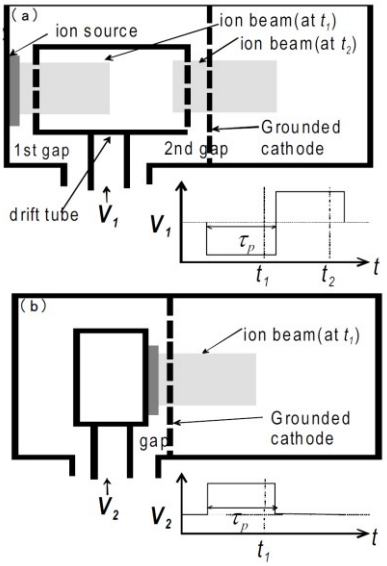

Fig. 1 Conceptual drawing of (a) BPA and (b) conventional PIB accelerator.

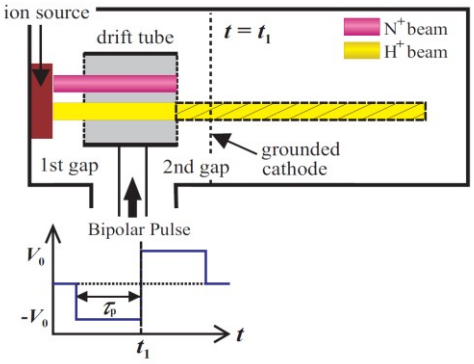

Fig. 2 Principle of the improvement of the purity of the ion beam.

is accelerated in the 1st gap toward the drift tube when the negative voltage is applied. As seen in Fig. 2, the length of H^+ beam is much longer than that of N^+ beam due to the difference of the velocity. We assume that the length of the drift tube is designed to be same as the beam length of N^+ beam with a beam pulse duration τ_p at an acceleration voltage V_0. With $V_0 = 200$ kV and $\tau_p = 70$ ns, for example, the flight length of N^+ beam is estimated to be 11.6 cm while that of H^+ beam is 43.3 cm. When the polarity of applied voltage is reversed and the positive voltage is applied to the drift tube ($t = t_1$), N^+ ions in the drift tube is accelerated again with acceleration voltage V_0 in the 2nd gap. In contrast, 73% of the H^+ ions passed

through the drift tube and decelerated in the 2nd gap by the negative voltage component of the bipolar pulse. Only the rest H+ ions could be accelerated in the 2nd gap by positive component of the bipolar pulse, and then the BPA produces an ion beam with the higher purity than that with a conventional ion diode.

3. Experimental Setup

Figure 3 shows the schematic configuration of the BPA in the present experiment. The system consists of a bipolar pulse generator and an accelerator. The bipolar pulse generator consists of a Marx generator and a PFL. The designed output of the bipolar pulse generator is the negative and positive pulses of voltage ± 200 kV with pulse duration of 70 ns each. In the present system, the double coaxial type PFL is employed for the formation of the bipolar pulse. The line consists of three coaxial cylinders with a rail-gap switch connected between the intermediate and outer conductors at the end of the line. The characteristic impedance of the line between the inner and intermediate conductors and one between the intermediate and outer conductors are 6.7 Ω and 7.6 Ω, respectively. The PFL is filled with the deionized water as a dielectric and charged positively by the low inductance Marx generator with maximum output voltage of 300 kV through the intermediate conductor. The rail-gap switch is filled with pure SF_6 gas and the pressure is adjusted to control the optimum trigger timing for each experimental condition.

The bipolar pulse voltage (V_0) and charging voltage of the PFL (V_{PFL}) are measured by the resistive voltage divider and capacitive voltage divider placed near the rail-gap switch, respectively. The values of V_0 and V_{PFL} are calculated by the ratio factor of the two voltage dividers (K = 1840 and 48500, respectively). The Rogowski coil with the coefficient of 7 kA/V is used for the measurement of the bipolar pulse current.

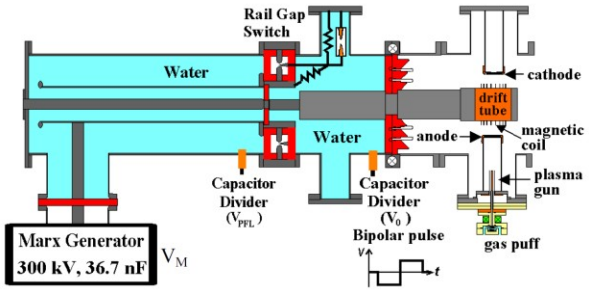

Fig. 3 Schematic configuration of bipolar pulse accelerator.

Figure 4 shows in detail the acceleration gap design of the BPA which consists of a grounded anode, a drift tube, a grounded cathode and a magnetically insulated acceleration gap (MIG). The drift tube is connected to a high voltage terminal of a high voltage pulsed power generator. A double coaxial type bipolar pulse generator was used [11], which generate an output pulse of the negative and positive pulses of voltage ± 200 kV with pulse duration of 70 ns each. The anode and the cathode are the copper electrodes of 78 mm in diameter with the thickness of 5 mm. The electrodes are uniformly drilled with 4 mm$^{\phi}$ apertures giving the transmission efficiency of 58%. In order to produce insulating magnetic fields in both acceleration gaps for suppression of the electron flow, a magnetic field coil of grating structure is used, which produces a uniform magnetic field in direction transverse to the acceleration gap. The magnetic coil of the MIG is installed on the rectangular drift tube. The uniform magnetic field with strength of 0.3–0.4 T is produced in the acceleration gap, of which length d_{A-K} = 10 mm, by a capacitor bank with capacitance of 480 μF and charging voltage of 4 kV. At peak of the magnetic field, the bipolar pulse voltage supplied from bipolar pulse generator is applied to the drift tube. To obtain

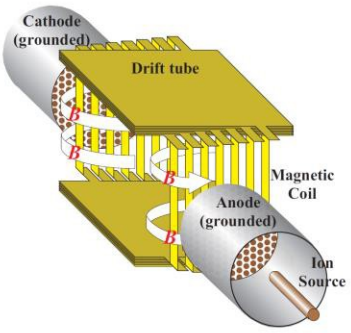

Fig. 4 Conceptual drawing of magnetically insulated gap of bipolar pulse accelerator.

higher transmission efficiency of the ion beam, right and left sides of the coil have a grating structure with 8-blades as shown in Fig. 4. Each of the blades (10 mm^W × 118 mm^L × 1 mm^T) is connected in series and works as an 8-turn coil. Since high voltage pulse is applied to the drift tube, the pulsed current produced by the capacitor bank is applied to the coil through an inductively isolated current feeder (IC). The IC is a helically winded coaxial cable and the outer conductor of the IC is connecting the grounded vacuum chamber and the drift tube with inductance of 12.4 μH.

A gas puff plasma gun was used as the ion source and installed in the anode. Figure 5 shows the detail of the gas puff plasma gun used in the experiment. The plasma gun is composed of a coaxial plasma gun and a high-speed gas puff valve. The plasma gun has a pair of coaxial electrodes, i.e. an inner electrode of 80 mm length with 6 mm outer diameter and an outer electrode of 18 mm inner diameter. The inner electrode has six gas nozzles of 1 mm^{ϕ}. The gas puff valve consists of a nylon vessel pre-filled with N_2 gas, an aluminum valve and a drive coil. By applying a pulse current to the driver coil, a pulsed strong magnetic field is produced and then the magnetic pressure pushes the aluminum valve to open the valve. As a result, the gas expands with a supersonic velocity and is injected into the plasma gun through the nozzles on the inner electrode of the plasma gun. The source plasma is produced by discharging the capacitor bank of the plasma gun with a delay time of τ_{PG} around 260–320 μs, since it takes about a hundred μs to open the valve and several tens μs for N_2 gas to reach the gas nozzle on the inner electrode of the plasma gun. To apply pulsed currents to the gas puff coil and the plasma gun, capacitor banks of 5 μF and 1.5 μF were used, respectively. Each capacitor bank is usually charged up to 6 kV and 15 kV, respectively.

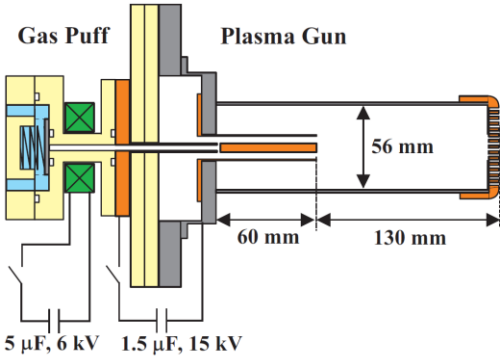

Fig. 5 Cross-sectional view of the gas puff plasma gun.

4. Results and Discussion

In order to confirm the acceleration of ions in the 1st gap, the bipolar pulse was applied to the drift tube. Figure 6 shows the set-up of beam acceleration experiment to measure the ion beam accelerated in the 1st gap by the first pulse of the bipolar pulse. The beam ion collector (BIC) was installed inside the drift tube to observe the ion current density. Since high voltage pulse is applied to the drift tube, the inductively isolated coaxial cable of same structure as IC was used to transport the BIC signal. The bipolar pulse generator was operated at 70% of the full charge condition of the PFL. Insulating magnetic field with strength of 0.3–0.4 T was applied to the acceleration gap. The plasma gun was operated at the condition of $\tau_{PG} \approx 290$ μs and the Marx generator was fired at τ_{PG} = 8–20 μs after the rise of the discharge current of the plasma gun.

Figure 7 shows the typical waveforms of the charging voltage of the PFL (V_{PFL}), the output voltage (V_0) and the ion current density (J_i) accelerated in the 1st gap. They were obtained at the condition of τ_{PM} = 15.6 μs. J_i was measured at 48 mm downstream from the grounded anode surface. As seen in the Fig. 7, the first pulse of V_0 rises at t = 230 ns and has averaged peak voltage of -96 kV and a pulse duration of 70 ns. The ion beam with a current density of J_i = 24 A/cm^2 and a pulse duration of 80 ns (FWHM) was obtained at around 42 ns after the peak of the negative voltage pulse. Considering the delay time of the flight, the peak current density corresponds to nitrogen ions (N^+, N^{2+}) which were accelerated

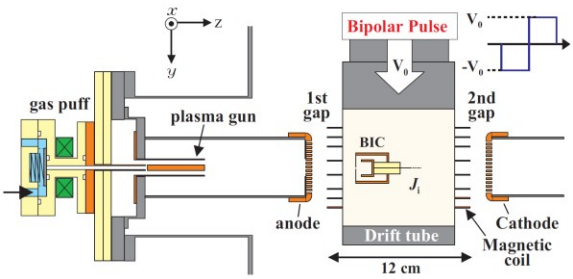

Fig. 6 Experimental setup of BPA.

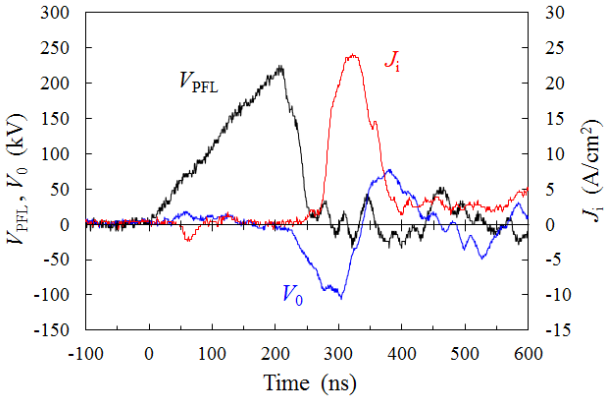

Fig. 7 Typical waveforms of charging voltage of PFL(V_{PFL}), output voltage (V_0) and ion current density (J_i).

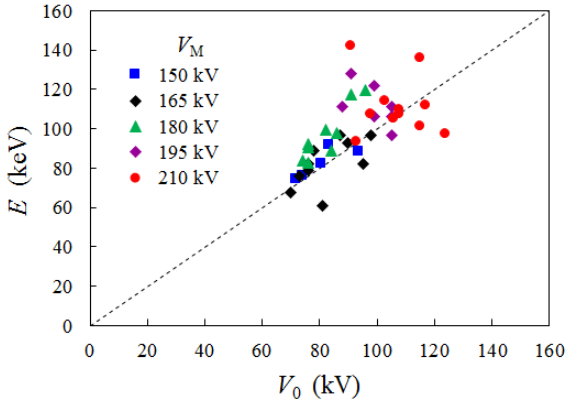

Fig. 8 Dependence of accelerated ion energy on applied negative pulse voltage assuming nitrogen ions.

around the peak of the negative pulse. In the case of Fig. 7, the estimated energy of the nitrogen ion was about 95 keV while the acceleration voltage was 96 kV. Figure 8 shows estimated ion energies at the peaks of J_i as a function of V_0 supposing nitrogen ions are main components of the ion beam. Even though Marx charging voltage (V_M) was varied, the relation between the accelerated ion energy and V_0 is basically on the N^+ proportional line. Therefore, the singly-charged nitrogen ion was the dominant component of accelerated ion beam.

Figure 9 shows the dependence of the peak value of J_i on τ_{PM} for several V_M. As seen in the Fig. 9, each V_M result has a peak at different τ_{PM}, i.e. $\tau_{PM} \approx 12$, 13 and 15 μs for $V_M = 150$, 180 and 210 kV, respectively. There seem to be appropriate τ_{PM} for each V_M. The maximum current density of 70 A/cm^2 was obtained with $V_M = 210$ kV and $\tau_{PM} = 14.4$ μs.

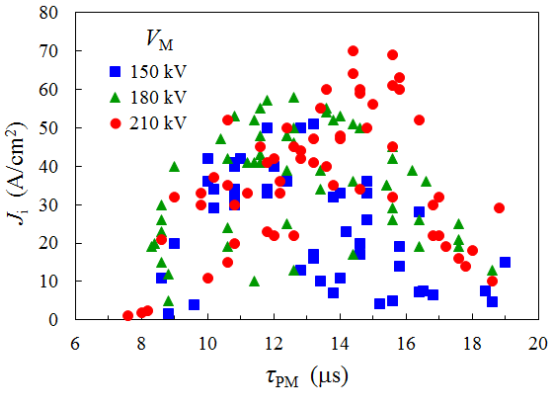

Fig. 9 Dependence of the peak values of ion current density (J_i) on the delay time (τ_{PM}).

5. Conclusions

We have developed a prototype of the BPA to perform experiments for the proof of principle. When the bipolar pulse was applied to the drift tube, the ions were successfully accelerated in 1st acceleration gap by the negative voltage component of a bipolar pulse. To confirm the principle of the BPA in more detail, we are planning to evaluate the ion species and the energy spectrum of the accelerated ions.

Acknowledgement

This work was supported in part by JSPS KAKENHI Grant Number 24540534.

References

[1] S. Humphries Jr., Nucl. Fusion, **20**, pp.1549–1612, (1980).

[2] J. P. VanDevender and D. L. Cook, Science, **232**, pp.831-836, (1986).

[3] K. Yatsui *et al.*, Phys. Plasma, **1**, pp.1730–1737, (1994).

[4] D. J. Rej *et al.*, J. Vac. Sci. Technol., **15**, pp.1089–1097, (1997).

[5] H. Akamatsu, T. Ikeda, K. Azuma, E. Fujiwara and M. Yatsuzuka, Suf. Coat. Technol., **136**, p.269 (2001).

[6] Y. Hashimoto, M. Sato, M. Yatsuzuka and S. Nobuhara, Jpn. J. Appl. Phys., **31**, 1922 (1992).

[7] D. J. Rej, R. R. Bartsch, H. A. Davis, R. J. Faehl, J. B. Greenly and W. J. Waganaar, Rev. Sci. Instrum., **64**, 2753 (1993).

[8] X. P. Zhu, M. K. Lei and T. C. Ma, Rev. Sci.

Instrum., **73**, 1728 (2002).
[9] H. Ito, H. Miyake and K. Masugata, Rev. Sci. Instrum., **79**, 103502 (2008).
[10] K. Masugata, Y. Shimizu, Y. Fujioka, I. Kitamura, H. Tanoue and K. Arai, Nucl. Instrum. & Methods in Phys. Res. A, **535**, 614 (2004).
[11] H. Ito, K. Igawa, I. Kitamura and K. Masugata, Rev. Sci. Instrum., **78**, 013502 (2007).

Sub-Terahertz radiation from DARC with laser created filament

Takeharu Hommyo, Yusuke Hyuga, Takamitsu Otsuka and Noboru Yugami

Department of Engineering, Utsunomiya University
7-1-2 Yoto, Utsunomiya, Tochi 321-8585 JAPAN

ABSTRACT

We present the results on generating sub-terahertz radiation by using the dc to ac radiation converter. A relativistic ionization front which is created by the laser filament of loose focus of Ti:sapphire laser pass through a capacitor array of period d= 0.5 cm with a gas pressure between 1 and 200 Pa. The maximum frequency of the generated emission is determined to be in the range of 0.1 to 0.3 THz by several diodes.

Keywords

Laser created plasma, sub-Terahertz wave, DARC

1. Introduction

Generation of the electromagnetic wave by laser-plasma interaction is one of the most attractive topics in order to realize powerfull radiation sources with tunable frequency. Not only the theoretical works but also experimental ones have been studied for plasma application of a short, tunable radiation sources. As the recent interests, the generation of terahertz radiation has been extensively investigated in experiments of the laser-plasma interaction and formation of filaments by intense laser propagating in air or gas. The THz radiation has a lot of potential applications in imaging, biological sensing, surface investigation, and condensed matter studies, and so on[1,2]. High power radiation sources are required for these applications, however the power of conventional THz sources, e.g. the photo-conductive (PC) antenna or the device based on optical rectification phenomena excited by the femtosecond laser pulse, is limited still in a range of μW–mW.

In the last two decades the radiation generation studies by the interaction between a plasma and electromagnetic wave has been experimentally and theoretically investigated for plasma applications of short and tunable radiation source[3-17]. Mori *et. al* have shown that the frequency up-shift occurs by the interaction between a periodic electrostatic field and an ionization front. In the laboratory frame, the generated wave in the plasma behind the ionization front is directly observed as the EM wave radiation pulse[18]. The observed frequency, however, is upshifed from zero-frequency, that is, this scheme can directly convert the DC field energy to the EM wave radiation. Therefore, this scheme was referred to as a dc to ac radiation converter (DARC source). This means a direct electromagnetic wave generation from the static electric field and this mechanism is expected to be efficient and to generate tunable in frequency. The DARC has following advantages: short emission pulse, tunable in frequency, high output power and compact. Lai *et. al*. have reported this phenomenon using a high-power short-pulse glass laser system and observed emitted radiation in the microwave region[19]. Muggli *et. al*. have also reported the higher frequency radiation(85 GHz) generation by the DARC combining the rectangular waveguide[20]. Moreover, a superluminous front, which has a velocity that exceeds the speed of light, may be created by sweeping the gas-filled periodic electrostatic field with an ionizing laser beam from one side of the field[21].

2. DARC Theory

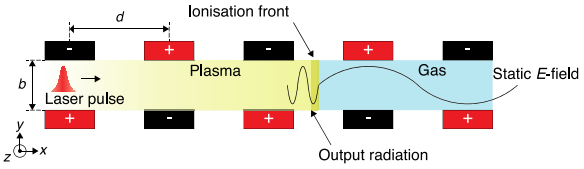

Fig. 1 Schematic of a dc to ac radiation converter (DARC).

The DARC structure is shown in Fig. 1. Alternately biased capacitor array produces a periodic electrostatic field of the form $E \approx E_0 \sin(k_0 x)$ in a gap (b), where $k_0 = \pi/d$ and d is the spacing between adjacent capacitor plates. The maximum electric field E_0 is given by V_0/b, where V_0 is the applied voltage to the capacitor. The laser for creation of ionization front propagate between the gaps in the x direction with the laser group velocity $v=c(1-\omega_p^2/\omega_L^2)^{1/2}$,where $\omega_p = \sqrt{4\pi ne^2/m}$ is the plasma frequency at the plasma density of n_0 and ω_L is the laser frequency.

In the DARC scheme, the frequency of the transmitted radiation ω is evaluated using the dispersion relation for an electromagnetic wave in the plasma and the phase continuity condition between the periodic electrostatic field and the emission at an ionization front in the laboratory frame. The dispersion relation of the emission in a plasma is $\omega^2 = \omega_p^2 + c^2k^2$, while the phase continuity equation for fields at the ionization front is $\omega + kv_f = k_0 v_f$. The frequency of the emission is then given as

$$\boldsymbol{\omega \approx \frac{k_0 v_f}{2} + \frac{\omega_p^2}{2k_0 v_f}}. \qquad (1)$$

The minimum frequency of the emission ω is ω_p, when $\omega_p = k_0 v_f \approx k_0 c$ and the emission frequency ω strongly depends on the plasma density. For example, the plasma density $n = 10^{16}$ cm^{-3} is required for the generation of radiation frequency of 1 THz.

The theory also gives theoretical output power of the radiation by considering the situation when the electrostatic field (it can be seen as a EM wave in front frame) transmitting into the ionization front boundary. Transmission and reflection coefficients must be considered. However, in this case the relativistic front can be assumed as $v_f \simeq c$. Therefore the transmission coefficient of the transmitted wave approaches unity. In other words, the applied electric field will completely convert to the amplitude of the output radiation and finally the output power is approximately represented by using engineering formula,

$$P_{out} = 1.33 v_g A V_0^2 / c b^2 \qquad (2)$$

where v_g is the group velocity of the radiation ($v_g = c(1-\omega_p^2/\omega_L^2)^{1/2}$) in the plasma, and A is the area of the ionization front.

3. Experimental Setup

Figure 2 shows the schematic of experimental setup. A Ti:sapphire chirped-pulse-amplification (CPA) laser system which delivers 800 nm, 40 mJ and 120 fs (full width at half maximum: FWHM) at 10 Hz repetition rate is used to create the ionization front. The polarization of the laser pulse is perpendicular to static electric field (z direction in fig. 1). The structure consists of 5 pairs of capacitors (2 periods). The spacing between capacitors (d) is 2 mm and the gap between the electrodes (b) is 1 mm. The laser light is focused at the entrance of capacitor array with a focal diameter of 100 μ m. The capacitors were biased with a pulsed power supply up to 5.0 kV with the duration of 200 ns (FWHM), which is limited by the static breakdown threshold of the gas. The maximum electric field E_0 at each of the gaps is estimated to be 50 kV/cm.

The plasma density is measured with a pump-probe Michelson's interferometer. The image was detected by a charge-coupled device (CCD) camera. When no laser was irradiated, i.e. without the probe beam, the CCD camera detected the visible

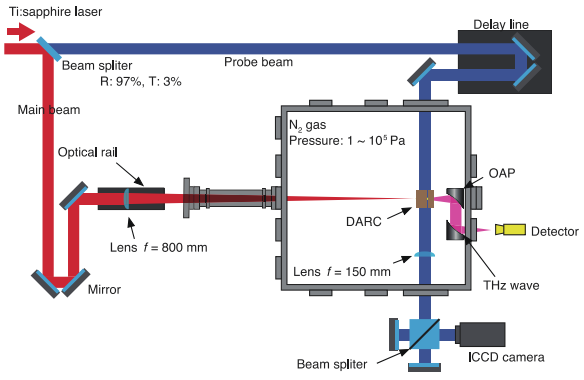

Fig. 2 Schematic of the experimental setup

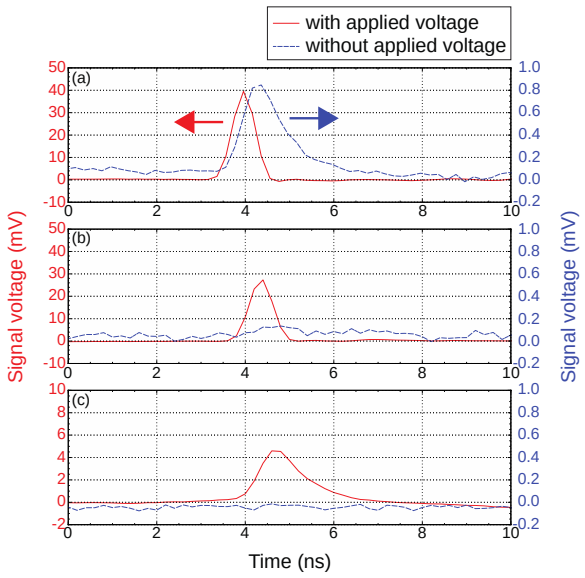

Fig. 3 Detected signals of output radiation by the Y-band (a), G-band (b) and F-band (c) crystal detectors. Solid lines (left axis) and dashed (right axis) lines show temporal waveform of the radiation with and without the applied voltage, respectively.

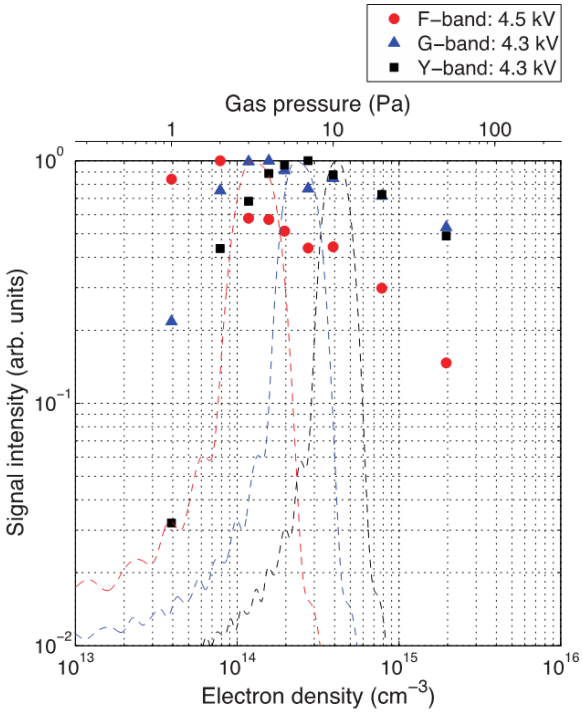

Fig. 4 Electron density dependences of signal intensity for different detectors. Dotted curves show estimated values.

light emission from the ionized gas and allowing to estimate the length of the plasma.

The emission from the DARC structure is collected by two f/3 off-axis parabola (OAP) mirrors with a focal length of 152.4 mm. The first OAP has a hole for the laser transmission and the emission from the DARC was partially reflected. At the focal point of the second OAP, we use three different crystal detectors which had responses at F band (0.09-0.14 THz), G band (0.14-0.22 THz) and Y band (0.22-0.33 THz). These detectors are connected to a 750 MHz bandwidth oscilloscope to detect the power of emission. All detectors are calibrated and connected with a waveguide and a horn antenna at a directivity of ±7° to efficiently detect the emission. The polarization of the radiation can be measured by rotating the microwave horn antenna.

4. Results and Discussion

Solid and dashed dashed lines in figure 3(a)–(c) show temporal waveforms of the output radiation detected by the crystal detectors with and without the applied voltage, respectively. Polarization of the detector is set to be parallel to the static electric field (y direction in fig.1). It is expected that the pulse width is much shorter than detected signal limited by the detection system such as RC time constant of the detector and the scope. Without the applied voltage, no significant signals were observed except for radiation which comes from laser produced plasma itself[22,23].

To verify the DARC mechanism, we measured signals by changing the polarizations of the detectors to perpendicular to the electrostatic field (z direction in fig.1). In this case, there was no detectable signal regardless of the applied voltage value. Thus, it is clear that the ionization front gives rise to modulation of the electrostatic field in the DARC.

Figure 4 shows the observed signal intensity of the diodes by changing the gas pressure from 1 to 100 Pa. The electron density and gas pressure are correlated by results obtained by using the interferometer. The frequency of the output radiation increases with the increase of the plasma

density as the theory predicted.

The observed signals of each detector has broad in the electron density. The spectral broadening $\Delta\omega$ of the output radiation depends on the number of the period of the electrostatic field N, where N = 2 in this experiment, and it can be evaluated as $\Delta\omega = \omega_0/2$, where ω_0 is the central frequency of the output radiation. Therefore the power spectrum can be assumed as $I(\omega) \simeq [\sin[(\omega_0 - \omega)T]/(\omega_0 - \omega)]^2$. So that, intensity measured in the experiments can be estimated by integrating $I(\omega)$ over the detection range of each detector. The dashed curves in figure 4 show the theoretical estimation by using the above assumption. The estimated peaks and behaviors are slightly different to the experimental results. In the experiment, plasma is generated by laser pulse with spatial profile of TEM_{00} mode. Therefore, plasma density distribution of the ionization front is not homogenous in the radial direction of the beam. This inhomogeneity distribution of the density might affect the experimental results. The discrepancy between experimental and theoretical values will be investigated with particle-in-cell simulation.

Figure 5 shows the maximum signal voltage as a function of the applied voltage. The dependence is measured under the condition of

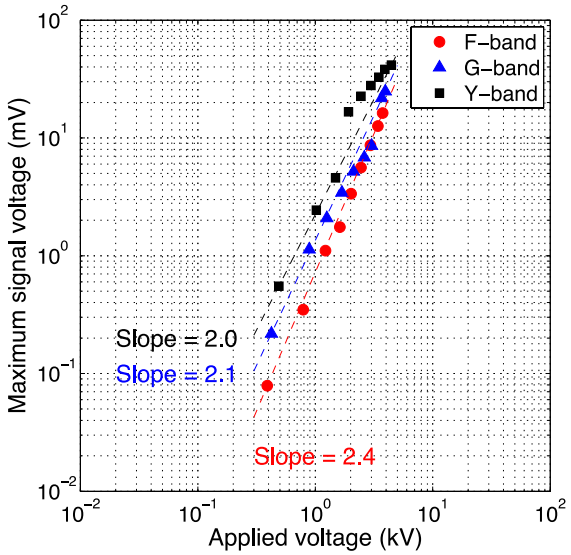

Fig. 5 Maximum signal voltage versus applied voltage. Dashed lines shows best fit for experimental results for each of the detectors.

electron density of $2 - 4 \times 10^{14}\,\mathrm{cm}^{-3}$. The maximum signal voltages increase with the increasing applied voltage. Dashed lines in figure 5 show the best fits for the observed signal intensity of each detector in the experiment, and the signal intensity of the radiation depended on almost the square of the applied voltage, agreeing well with the theoretical prediction with Eq. (2).

The theoretical output power can be simply calculated by Eq. (2)[19], and it is estimated to be 220 W with our experimental condition. However, calculated output power of the experimental results is about 20 W. As stated above, to archive the high power radiation output, it is important to design the DARC including a waveguide structure[20,24]. In this experiment, however, the design does not include such waveguide structure. Thus, there is a large impedance mismatch at the exit of the DARC. To optimize the output power from the DARC, the waveguide structure and the improvement of the impedance matching at the exit of the structure will be required.

5. Conclusions

In conclusion, sub-THz radiation from the DARC is investigated by using laser induced plasma. The measured dependence between the output frequency and the gas pressure, i.e. electron density, well agrees with the theoretical prediction. The maximum frequency range observed is up to Y band (0.22 - 0.33 THz), which is the highest frequency reported using the DARC (to our knowledge). Theoretically, higher frequency can also be obtained with higher electron density. Such experiments are in preparation with a new single shot THz measurement system. At the moment, the output power is not high enough for applications. However, by optimizing the parameters, such a frequency tunable and non- damage threshold radiation source (plasma photonic device: PPD) has potential to be significantly useful tool.

References

[1] B. Ferguson and X.-C. Zhang, Nature Mater. **1**, 26 (2002).
[2] M. Tonouchi, Nature Photon. **1**, 97 (2007).
[3] D. H. Auston, K. P. Cheung, J. A. Valdmanis, and D. A. Kleinman, Phys. Rev. Lett. **53**, 1555 (1984).
[4] D . H. Auston, K. P. Cheung, and P. R. Smith, Appl. Phys. Lett. **45**, 284 (1984).
[5] B. B. Hu, X.-C. Zhang, D. H. Auston, and P. R. Smith, Appl. Phys. Lett. **56**, 506 (1990).
[6] G. M. H. Knippels, X. Yan, A. M. MacLeod, W. A. Gillespie, M. Yasumoto, D. Opts, and A. F. G. van der Meer, Phys. Rev. Lett. **83**, 1578 (1999).
[7] D. J. Cook and R. M. Hochstrasser, Opt. Lett. **25**, 1210 (2000).
[8] K. Y. Kim, J. H. Glownia, A. J. Taylor and G. Rodriguez, Opt. Express **15**, 4577 (2007).
[9] K. Y. Kim, A. J. Taylor, J. H. Glownia and G. Rodriguez, Nature Photon. **2**, 605 (2008).
[10] A. V. Balakin, A. V. Borodin, I. A. Kotelnikov, and A. P. Shkurinov, J. Opt. Soc. Am. B 27, 16 (2010).
[11] Ch. Fattinger and D. Grischkowsky, Appl. Phys. Lett. **54**, 490 (1989).
[12] P. U. Jepsen, R. H. Jacobsen, and S. R. Keiding, J. Opt. Soc. Am. B **13**, 42424 (1996).
[13] M. Tani, S. Matsuura, K. Sakai, and S. Nakashima, Appl. Opt. **36**, 7853 (1997).
[14] Y. C. Shen, P. C. Upadhya, E. H. Linfield, H. E. Beere, A. G. Davies, Appl. Phys. Lett. **83**, 3117 (2003).
[15] S. C. Wilks, J. M. Dawson, and W. B. Mori, Phys. Rev. Lett. **61**, 337 (1988).
[16] M. Lampe, E. Ott, Phys. Fluids **21**, 42 (1978).
[17] W. B. Mori, Phys. Rev. A **44**, 5118 (1991).
[18] W. B. Mori, T. Katsouleas, J. M. Dawson, and C. Lai, Phys.Rev. Lett. **74**, 542 (1995).
[19] C. H. Lai, R. Liou, T. C. Katsouleas, P. Muggil, R. Brogle, C.Joshi, and W. B. Mori, Phys. Rev. Lett. **77**, 4764 (1996).
[20] P. Muggil, R.Liou, J. Hoffman, T. Katsouleas, and C. Joshi, Appl. Phys. Lett. **72**, 19 (1998).
[21] N. Yugami, T. Niiyama, T. Higashiguchi, and K. Takahashi, J. J. Appl. Phys. **44**, 1304 (2005).
[22] N. Yugami, K. Ninomiya, K. Kobayashi, and H. Noda, J. J. Appl. Phys. **45**, 1051 (2006).
[23] C. D'Amico, A. Houard, M. Franco, B. Prade, A. Mysyrowicz, A. Couairon, and V. T. Tikhonchuk, Phys. Rev. Lett. **98**, 235002 (2007).
[24] P. Muggil, R.Liou, C. H. Lai, J. Hoffman, T. C. Katsouleas, and C. Joshi, Phys. Plasma 5, 2112 (1998).

Experimental Study on a narrow band Intense Free Electron Maser using an Intense Relativistic Electron beam with a Bragg Resonator

Takahiro Yamaguchi, Takuma Asami, Momoko Katsuoka, Ryusuke Kiyomoto, Dai Takagi, Yukihiro Soga, Keiichi Kamada

Graduate School of Science and Technology, Kanazawa University, Kanazawa, Ishikawa, 920-1192, Japan

ABSTRACT

An intense mildly relativistic electron beam with energy of around 800 keV, current of 400 A and pulse duration of 150 ns was injected into the cylindrical tube immersed in an axial guide magnetic field. A helical wiggler magnetic field was also applied. The microwave with frequency of 40, 45 GHz was observed with the helical magnetic field. The frequency was increased as the beam energy was increased. Cold tests of two Bragg resonators were carried out again and the advantage of a hybrid Bragg resonator on the frequency selectivity was reconfirmed.

Keywords

electron beam, microwave source, Bragg resonator, FEM, IREB

1. Introduction

An intense relativistic electron beam (IREB) with energy of ~ 1 MeV, current of over 1 kA and output power of over 1 GW with duration of ~ 100 ns is a convenient energy source of an intense free electron maser (FEM). The radiated frequency of the FEM increases as the beam energy increases and the periodic length of the structure for FEM can be desined longer because of the relativistic effect. High current density yields its strong self electric field and it makes the energy spectrum of the beam wide. Experiments were reported about the intense FEM [1-5].

We proposed two types of Bragg resonators to improve the frequency selectivity of a FEM using an IREB. A normal Bragg resonator uses two traditional Bragg reflectors at the entrance and exit sides. A hybrid Bragg resonator utilizes a traditional Bragg reflector at the entrance and an advanced Bragg reflector[6,7] at the exit. While the corrugation period of a traditional Bragg reflector is designed a half of the wavelength of the reflection wave, that of an advanced Bragg reflector is nearly equal to it. A hybrid Bragg resonator is expected to show higher frequency selectivity than a normal one.

2. Experimental Apparatus

Figure 1 shows the schematics of experimental setup. An intense relativistic electron beam was injected through an annular anode into the drift tube with diameter of 17 mm. The energy and current of the IREB were around 800 keV and 400 A, respectively. The diameter of the IREB was 8 mm. A solenoid coil applied an axial magnet field (Bg) with strength of up to 1T. A helical wiggler coil [2] located inside the solenoid coils provided a periodic radial magnetic field (Bh) up

to 0.18 T.

The IREB was diverged to the wall at the exit of the axial magnetic field. In Fig. 1, the helical coil is not depicted exactly. The period of the wiggler coil is 54.4 mm. The helical wiggler field is applied gradually at the entrance not to diverge the IREB. The calculated orbit of a single electron with energy of 800 keV in the guide and the helical magnetic fields were shown in Fig. 2. In the calculation, the axial and helical magnetic fields were considered in the momentum equation. The self-electric filed of the beam electrons was not taken into account. When the helical magnetic field increased gradually at the entrance, the orbit of an electron in the helical magnetic field was periodical. The orbit showed more complicated and larger radial motion without gradual increase of the helical field.

Though the Bragg reflectors were not used with the IREB in this paper, the location of the Bragg reflectors is the entrance and exit sides of the helical wiggler coil.

A damage pattern on a brass plate was used to observe the deformation of the beam cross-section along the axis of the beam.

A Faraday cup with diameter of 17 mm was utilized to detect the beam current. The total beam current was not decreased through the magnetic fields.

The radiated microwave was detected by a horn just behind an acrylic window with depth of 10 mm. A 100 m dispersive line used to observe the overall radiated frequency. Though the accurate frequency could not determined with width of 150 ns of the signal at the entrance, it is useful to observe the total radiation spectrum. The expected radiation frequency was around 40 GHz in this experiment. The more accurate frequency spectrum over 35 GHz was measured by a reflection grating system as shown in Fig. 3. Four detectors were used in a shot. The resolution of each detector was about 1 GHz. The radiated microwave in each shot showed good reproducibility.

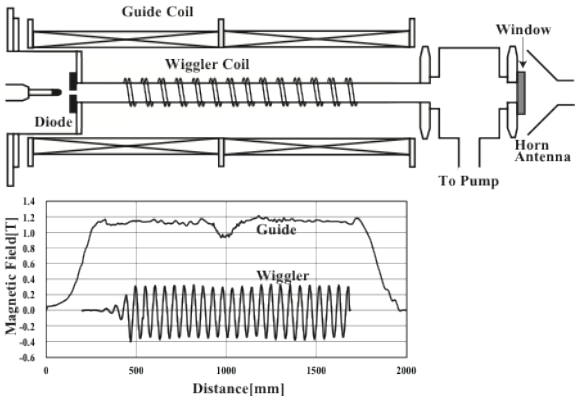

Fig. 1 Schematics of the experiment.

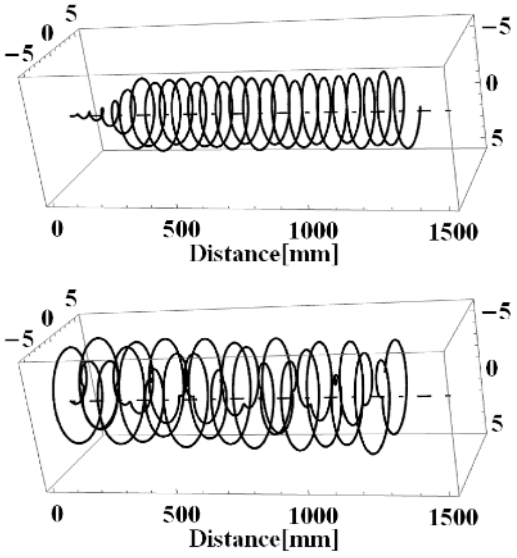

Fig.2 The orbit of an electron in the guide and helical magnetic field. Upper: the strength of the helical magnetic field was increased gradually. Lower: the helical magnetic field was applied without gradual increase of its strength.

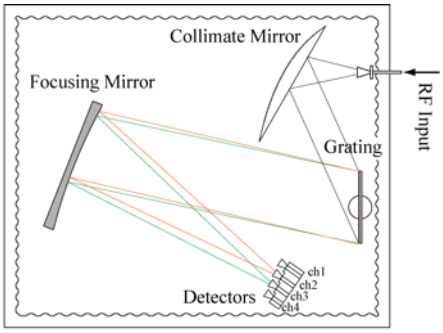

Fig. 3. Schematics of the reflection grating system. The resolution of detectors is 1 GHz.

3. Experimental Results and Discussions

The cold tests of both Bragg reflectors were carried out in collaboration with Reserch Center for Development of Far-Infrared Region, Fukui University (FIR-FU). The vector network analyzer (ABmm MVNA 8-350 GHz) of FIR-FU was used to observe the transmission spectrum of both reflectors. While the frequency of 39.6±0.5 GHz was reflected with the traditional Bragg reflector, that of 39.85±0.05 GHz was reflected with the advanced Bragg reflector as shown in Fig. 4. These results showed good agreement with the previous results using E8354C (Agilent Technology) [7]. About the reflected frequencies of 39.6 and 39.85 GHz, the TE_{11} mode was kept at the reflection from the simulation [7]. About the reflected frequency of 41-42.5 GHz of the traditional Bragg reflector, it was suggested by the simulation that the TE_{11} mode was converted into TM_{11} mode.

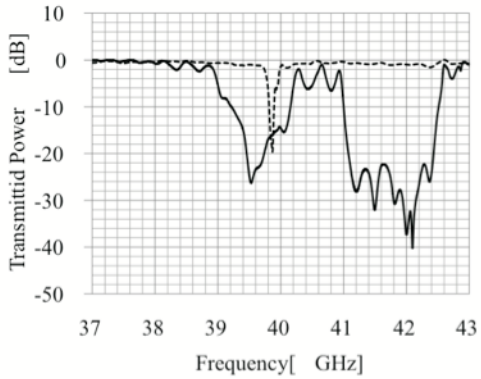

Fig. 4. Transmition spectra of a traditional (solid line) and an advanced (dotted line) Bragg reflectors. The reflected frequency of 39.6±0.5 GHz was observed by the traditional Bragg reflector, and that of 39.85±0.05 GHz by the advanced Bragg reflector.

We could not utilize the Bragg reflector in the FEM experiments because of a malfunction of the IREB source.

The typical waveforms of the diode voltage and the beam current were shown in Fig. 5. The damage pattern showed a circular cross-section with diameter nearly equal to the annular anode. The damage pattern detected at 1200 mm downstream side from anode are also shown in Fig. 5. The beam propagated along the guide magnetic field line of force with almost the same diameter of

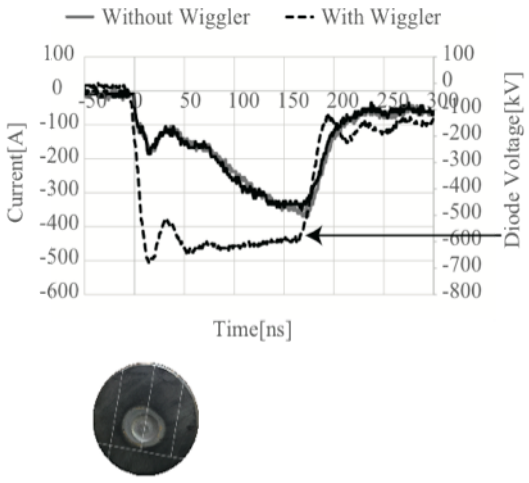

Fig. 5. Waveforms of diode voltage and the Faraday cup with and without the wiggler field (upper) and the damage pattern without the wiggler field (lower). The radius of the beam was nearly the same along the 1200 mm propagation.

the anode with/without wiggler magnetic field. The beam current was a little decreased with the guide magnetic field of less than 0.32 T. It was suspected that a part of the beam was diverged to the wall.

A 100 m dispersive line to observe the overall frequency spectrum of the radiation was utilized. The waveforms of the microwave detected at the entrance and the exit of the dispersive line were detected, where the diode voltage was about 820 keV. The calculated frequency in Fig. 6 is not accurate because the correspondence between the signals detected at the entrance and the exit cannot be clear. The signal with frequency around 40 GHz was observed only with the wiggler field. The signals around 20-30 GHz were suspected to be the interaction between the beam cyclotron mode and the waveguide mode.

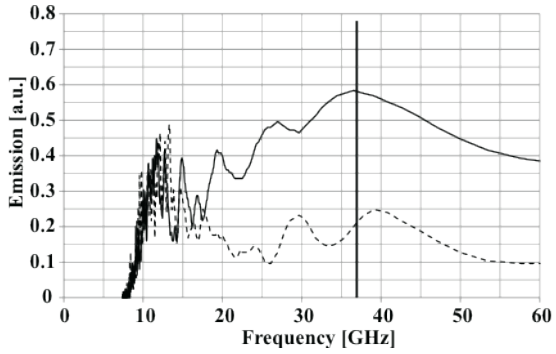

Fig. 6. Calculated frequency spectrum by the 100 m dispersive line with(solid line) and without(dotted line) the wiggler field.

The diffraction grating was used to observe the radiation with frequency of around 40 GHz. The waveforms of radiated microwave with the beam energy of 780 keV is shown in Fig. 7. The radiation was observed with frequency of around 40.5-43.0 GHz. The calculated frequency from the dispersion relation between the beam mode passing through the wiggler magnetic field and the TE_{11} waveguide mode was 40 GHz. The observed microwave frequency was nearly equal to the calculated one. No signal was observed without the helical wiggler field. And the radiated frequencies were not changed by the strength of the guide magnetic field. The output power of the radiated microwave was roughly estimated to be less than 1 MW. More improvements on the alignment of axes of the beam and the magnetic fields were expected to increase the microwave output power.

The signals of the diffraction grating with the beam energy of 820 keV is shown in Fig. 8. In this case the calculated frequency was 45 GHz. The radiated microwave with frequency of 44.5-46

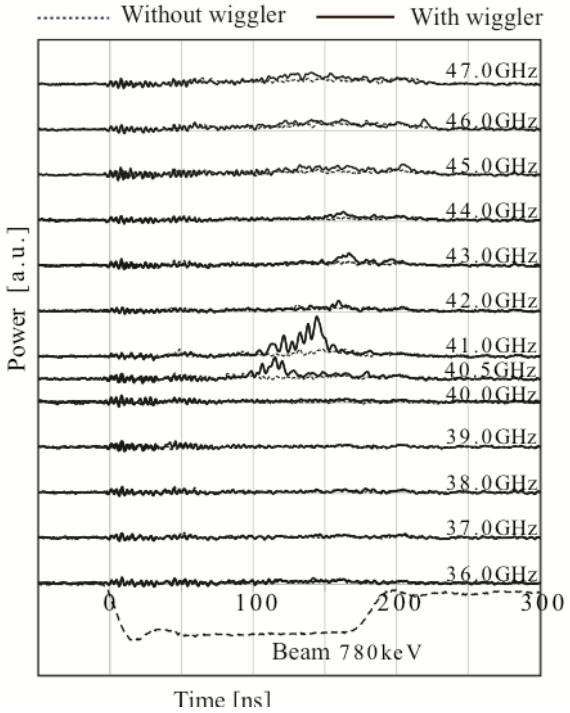

Fig.7. The signals with diffraction grating with (solid line) and without (dotted line) wiggler field where the diode voltage was 780 keV. The frequency of 40.5-43 GHz was observed only with the helical wiggler field.

GHz was observed. It also showed good agreements between the calculated and the

observed frequency. The frequency was increased by the increase of the beam energy as expected in the FEM operation. However, in this case, the microwave with lower output power was observed when the helical wiggler field was not applied. We suspected that the radiation without wiggler field was originated from the interaction between the beam cyclotron mode and TM waveguide mode.

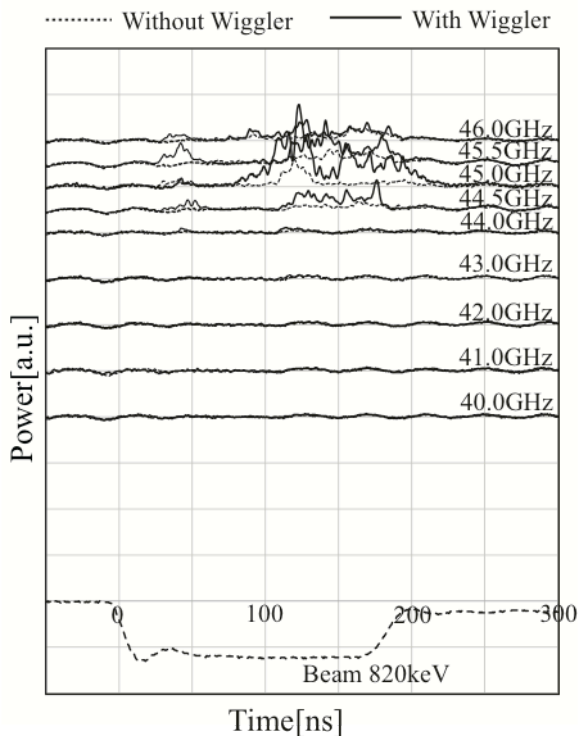

Fig.8. The signals with diffraction grating with (solid line) and without (dotted line) wiggler field where the diode voltage was 820 keV. The frequency of 44.5-46 GHz was observed.

4. Conclusions

The radiation with frequency of 40 GHz was observed only when the wiggler magnetic field was applied in the experiments with the diffraction grating.

The Bragg resonators were designed for 40 GHz and they worked as expected. We can start the experiments to show the effect of a normal and a hybrid Bragg resonators.

References

[1] A. Kasugai, K. Sakamoto, K. Takahashi, K. Kajiwara and N. Kobayashi, Nuclear Fusion, Vol. 48, Issue 5, pp. 054009 (2008).

[2] G. G. Denisov, M. G. Reznikov, Radiophysics and Quantum Electronics, vol. 25, No 5, pp. 407-413, (1982).

[3] R. B. Mccowan, Int. J. Electronics, Vol.65, No.3, pp. 463-475, (1988).

[4] I. Boscolo, Appl. Phys. B57, pp. 217-225, (1993)

[5] T. S. Chu, F. V. Hartemann, B. G. Danly, and R. J. Temkin, Phys. Rev. Lett., 72, 2391-2394 (1994)

[6] N. S. Ginzburg, A. M. Malkin, N. Yu. Peskov, A. S. Sergeev, A. K. Kaminsky, S. N. Sedykh, E. A. Perelshtein, A. P. Sergeev, A. V. Elzhov, Phys. Rev. ST-AB, vol. 8, 040705, (2005).

[7] K.Kamada, Y. Soga, S. Odawara, K. Misawa, M. Yoshida, N. S. Ginzburg , Plasma Fusion Res. 8, 2406154 (2013).

Effect of Cathode Materials on Output Characteristics of High Power Microwave by Virtual Cathode Oscillator

S. Shinokawa, R. Shinoda, H. Ohashi and H. Ito

Dep. of Electrical and Electronic Engineering, University of Toyama,
3190 Gofuku, Toyama 930-8555, Japan

ABSTRACT

The virtual cathode oscillator (vircator) is one of the most attractive high-power microwave sources. The most fundamental issues in the virtual cathode oscillator are conversion efficiency improvement and oscillation frequency control. The cathode material plays an important role in the output power and frequency of microwaves emitted from the vircator. We present the experimental studies on the effect of cathode materials on the output characteristics of the vircator. The pulse power system was utilized to generate a high-power microwave in an axial virtual cathode oscillator. Experiments were conducted using three different cathode materials (aluminum, graphite and polymer velvet) for various anode cathode gap distances. In addition, a time-dependent frequency analysis is applied to the output signal of the vircator to investigate the time evolution of the emitted frequency spectrum for various AK gaps.

Keywords

High-power microwave, virtual cathode oscillator, axial vircator, pulse power technology

1. Introduction

Radiation sources of the high-power microwave are being developed for applications in plasma heating, particle acceleration, high-power radar, and many other industrial and military fields [1,2]. A number of high-power microwave sources have been developed, such as Virtual Cathode Oscillator, Magnetron, Klystron, Gyrotron and so on. The vircator has remarkably attracted attention over other kinds of high-power microwave sources. The vircator has the attribute of high-power capability, wide frequency tuning ability, and conceptual simplicity [3]. It is possible to generate high-power microwaves ranging from a few tens of megawatts up to a few gigawatts. However, the vircator has difficult problems in low efficiency of beam-to-microwave power conversion and wide frequency bandwidth [3]. The many researchers have been making research efforts and experimental studies to improve the conversion efficiency and oscillation frequency control [4-8]. Despite these efforts, the best microwave efficiency is still not higher than 10%.

The cathode material is found to play an important role in the output characteristics of the vircator. We performed the experiments on the generation of microwaves from an axial vircator for various anode-cathode (AK) gaps using three kinds of aluminum, graphite and polymer velvet as a cathode material. This paper reports the experimental results on the effect of cathode materials on the output frequency of the vircator. In addition, time-dependent frequency analysis (TFA) [9,10] was carried out for the obtained microwave radiation.

2. Principle of Vircator

The vircator consists of cathode and meshed anode as shown in Fig. 1. When a high pulsed negative voltage is applied to a cathode, electrons are emitted from the surface of the cathode. The electron beam has passed through the anode. When the injected electron beam current exceeds the space charge limited current in the region behind the anode, a

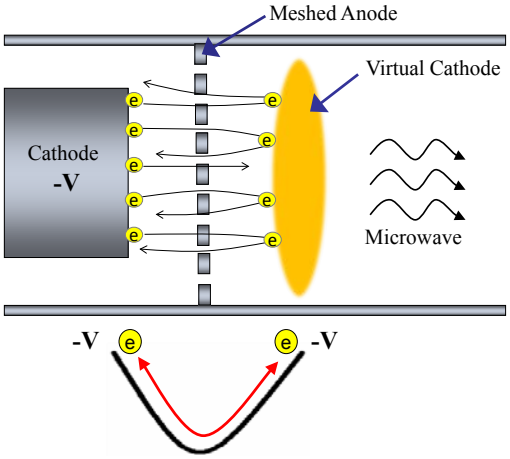

Fig.1 Schematic view for virtual cathode oscillator.

virtual cathode, which is an unstable region of negative potential, is formed at the same distance as AK gap. Most of the electrons in the beam lose their kinetic energy and are then reflected back toward the anode. The mechanism of microwave generation in the vircator can generally be explained by two dynamical mechanisms [2, 11]. The first is electron reflection in the potential well formed between the real cathode and virtual cathode. The reflection frequency is approximately given by

$$f_e = \frac{v_e}{4d_{AK}} \approx \frac{c\sqrt{\gamma^2 - 1}}{4d_{AK}\gamma}$$

where v_e is the velocity of the electrons, d_{AK} is the distance between the anode and the cathode, and c is the velocity of light. The relativistic factor γ is given by

$$\gamma = \frac{1}{\sqrt{1-(v_e/c)^2}} = 1 + \frac{eV_0}{m_e c^2}$$

The second is an oscillation of the virtual cathode in time and space. The oscillation frequency is given by

$$f_{vc} = \frac{5}{4\pi}\omega_p = \frac{5}{4\pi}\sqrt{\frac{e^2 n_b}{\varepsilon_0 m_e \gamma}}^{1/2}$$

$$= \frac{5}{4\pi}\sqrt{\frac{e^2}{\gamma\varepsilon_0 m_e}}\sqrt{\frac{1}{e\beta c}\left(\frac{4\varepsilon_0}{9}\left(\frac{2e}{m_e}\right)^{1/2}\frac{V_0^{3/2}}{d_{AK}^2}\right)}^{1/2}$$

where ω_p is the electron plasma frequency, n_b is electron beam density derived by the space charge limited current, e and m_e are the electron charge and mass, respectively, ε_0 is the vacuum permittivity, V_0 is the applied voltage across the AK gap, and $\beta = v/c$. These two oscillation frequencies are fundamentally determined by the geometric structure, the applied voltage and the electron beam parameter.

3. Experimental Arrangement

Figure 2 shows a schematic configuration of the pulse power system for studies on generation of the high-power microwave from the axial vircator. The system consists of a high-voltage generator, a single pulse forming line (PFL), a gas SF_6 spark gap and a pulse transmission line. The high-voltage generator is an eight-stage bipolar Marx generator with the maximum output of 800 kV and the stored energy of 5 kJ. The PFL is filled with the deionized water as a dielectric. The designed parameters of the PFL are characteristic impedance of 3 Ω, and electrical length of 50 ns. In this experiment, the pulsed power system was operated in negative-output mode and the charging voltage of Marx generator was set to 24 kV.

Figure 3 shows the schematic structure of the axial vircator and the microwave measurement setup. The

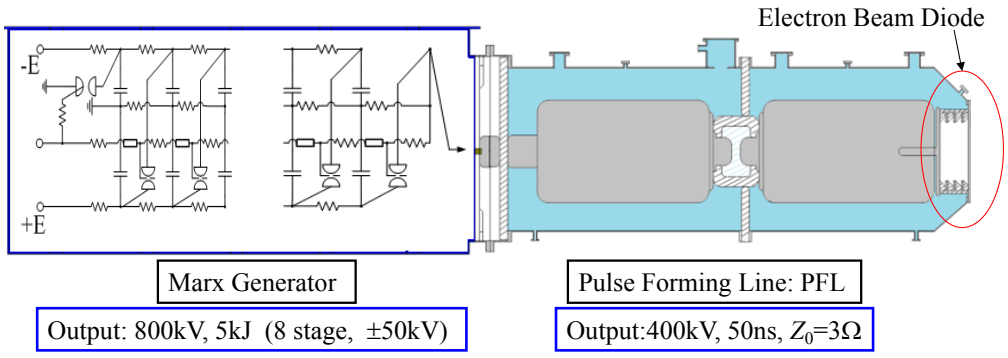

Fig.2 Schematic diagram of Pulsed Power system

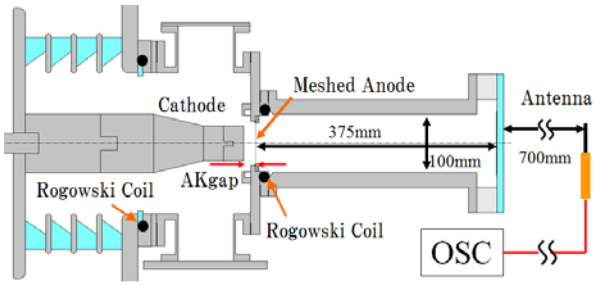

Fig. 3 Schematic structure of axial vircator and microwave measurement setup.

high-voltage pulse generated from the pulsed power system is applied to the cathode of the electron beam diode. A vacuum explosive electron emission diode was used to generate an intense relativistic electron beam. The diode consists of a planar disk cathode of 60 mm in diameter and a stainless-steel mesh anode with a transparency of ~65%. An aluminum, a graphite and a polymer velvet were tested as a cathode material. Here, the velvet cathode used the aluminum disk covered with a piece of polymer velvet. The AK gap d_{AK} was in the range of 4-12 mm and changed with the step of 2 mm. The diode region and output waveguide are maintained at a base pressure of 5.5×10^{-3} Pa. A resistive $CuSO_4$ voltage divider was used to measure the output voltage (V_{PFL}) of the pulsed power system and placed at the edge of PFL. The diode voltage (V_d) applied to the cathode is calculated by the inductive correction, since the inductance of the transmission line from the resistive divider to the cathode is ~100 nH. The diode current (I_d) and the beam current (I_b) passed through the anode were monitored by Rogowski coil at the upstream and downstream of the anode.

The output microwave from the vircator traveled along a circular waveguide of 100 mm in diameter and 375 mm in length and is emitted into free space through an acrylic window. All microwave measurements were carried out with the receiving antenna placed at a distance of 0.7 m away from the vircator window. The temporal waveform of the output microwave was obtained by using a crystal diode and recorded by a digital oscilloscope with a bandwidth of 200 MHz and a sampling rate of 2 GS/s, together with the beam parameters (voltage and current). In order to carry out Fourier transforms and TFA, the signal from the antenna was also recorded by a high-speed digital oscilloscope with a sampling rate of 40 GS/s through a coaxial RF cable.

4. Experimental Results

Figure 4 shows the typical waveforms of diode voltage V_d, diode current I_d, beam current I_b and microwave at d_{AK}=4 mm for three different cathode materials. As shown in Fig.4, the microwave is emitted at the rise time of V_d. It can be seen that as compared with each cathode material, the rise time of

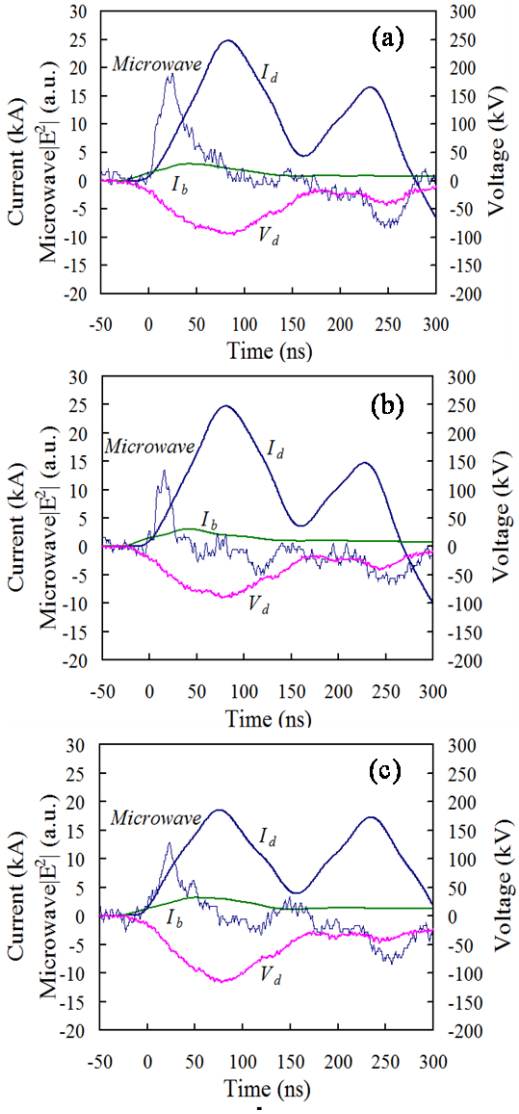

Fig.4 Typical waveforms of diode voltage V_d, diode current I_d, beam current I_b and microwave at d_{AK}=4 mm for (a) aluminum cathode, (b) graphite cathode and (c) velvet cathode.

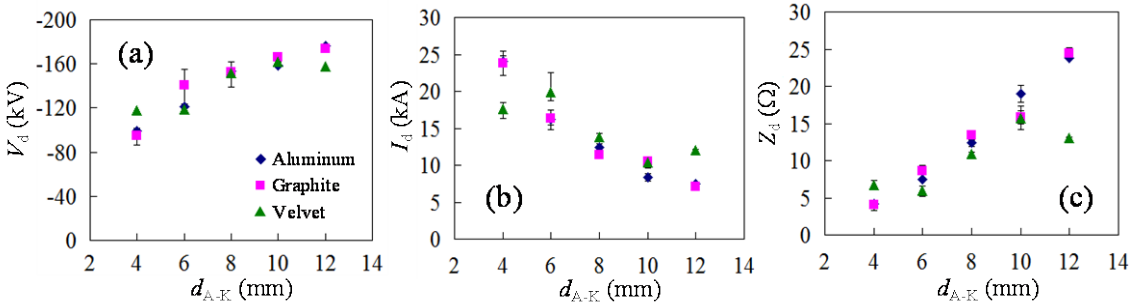

Fig.5 Dependence of V_d, I_d, and characteristic impedance $Z_d=V_d/I_d$ of diode on cathode materials for various AK gap distances.

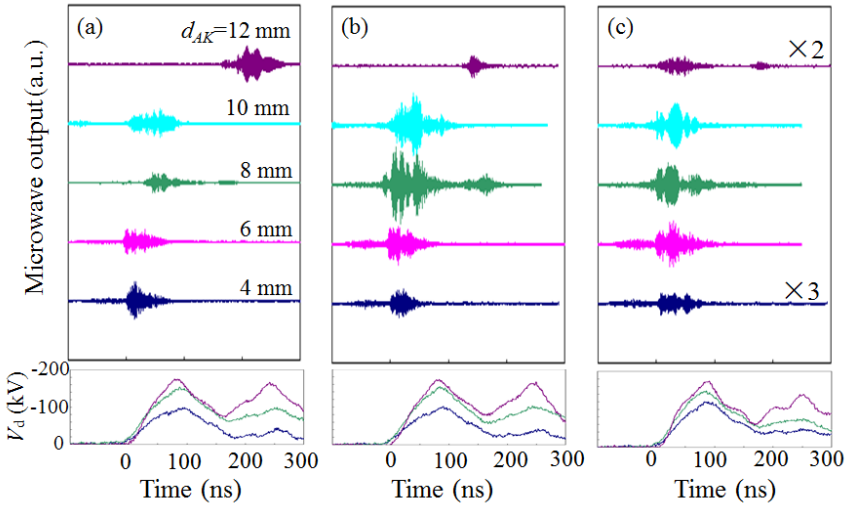

Fig.6 Microwave output signal at various AK gap distances for (a) aluminum cathode, (b) graphite cathode and (c) velvet cathode.

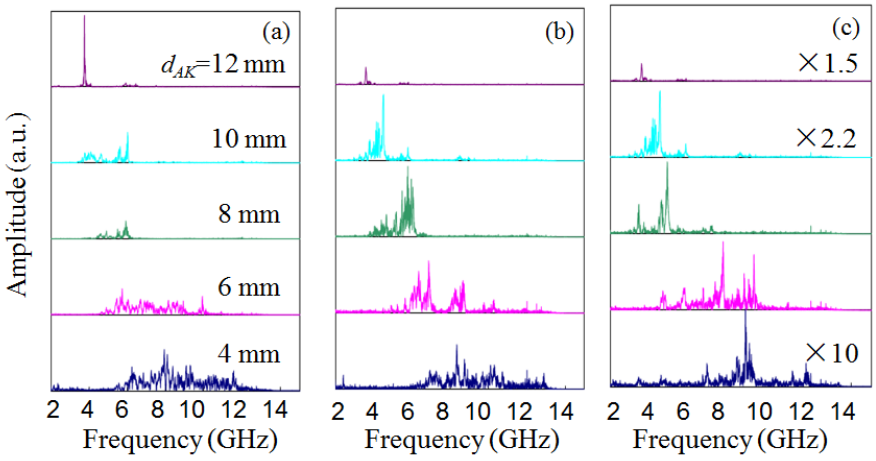

Fig.7 Fast Fourier Transform of microwave signal for the shots shown in Fig.6.

the diode current for the velvet cathode is earlier than those for other two materials. Figure 5 shows the dependence of V_d, I_d, and the characteristic impedance $Z_d=V_d/I_d$ of the diode on the cathode materials for various AK gap distances. Each data point is an average of 4 shots. The characteristic of

the diode seems to be almost same for three cathode materials.

Figure 6 shows the microwave output signal recorded by the high-speed digital oscilloscope for three cathode materials at various AK gap distances. The waveform of V_d is shown as the reference. For both aluminum and graphite cathodes, the output microwave appears at a later time with the increase of the AK gap distance, whereas for the velvet cathode, the output microwave appears at a same time. This is considered that the turn on time for the velvet cathode is lower than for other two cathodes. Figure 7 shows the Fast Fourier Transform of the microwave signal for the shots shown in Fig.6. One can see that as the AK gap distance increases, the main frequency of the microwave shifts to the lower side and the spectrum tends to become narrower. Figure 8 shows the TFA result for the aluminum cathode at various AK gap distances, where a time-window width of 12.8 ns (512 data points) was shifted by the step of 0.25 ns. In Fig. 8, the horizontal axis represents the center of the time window, and the spectrum intensity obtained within each window is represented by the blackness variation in the vertical direction. It can be seen in Fig. 8 that the output frequency increases with time for lower AK-gap distances. At the AK gap

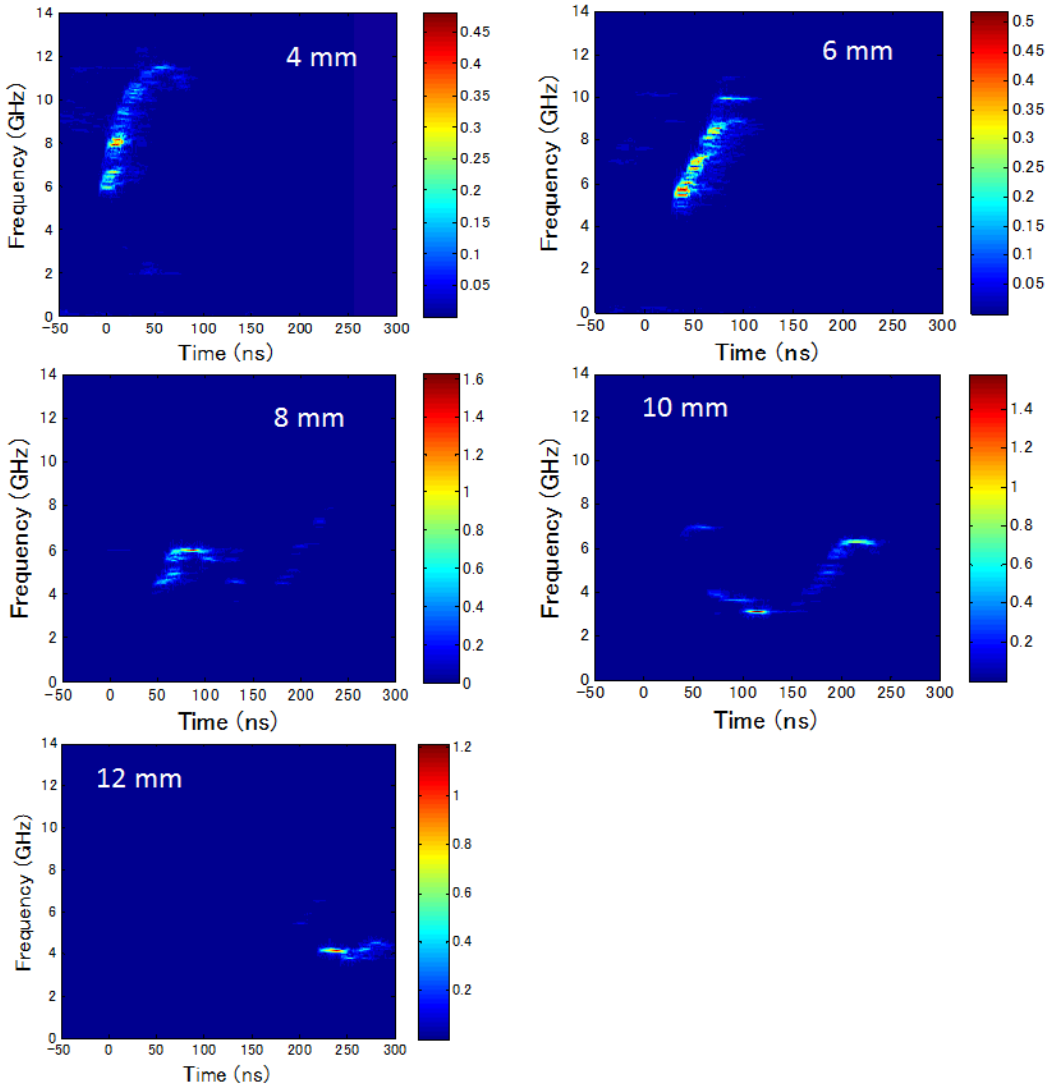

Fig.8 Time evolution of microwave frequency spectrum measured for aluminum cathode at various AK gap distances.

distance of d_{AK}=4 mm, the frequency increases from ~6 to ~12 GHz during the period of 0-50 ns. This phenomenon shows fairly good agreement with the result that the microwave radiation for lower AK gap distances has the broad spectrum. It is thought that this frequency shift is due to the fact that the diode voltage (electron beam energy) increases more rapidly with time during the generation of the microwave. On the other hand, at the AK gap distance of d_{AK}=12 mm, the microwave with the constant frequency of ~4 GHz is emitted during the period of 200–300 ns.

5. Conclusions

The effect of cathode materials on the output frequency of microwaves emitted from the axial vircator has been studied for various AK gap distances. The diode current rises earlier for velvet cathode due to its lower turn on time. The influence of cathode materials on the power of microwaves is investigated in future.

In addition, the time-dependent frequency analysis shows that the output frequency varies drastically with time for lower AK gap distances, while for higher AK gap distances, the output frequency is almost constant during the pulse duration of the output microwave. It was found from this result that a flat-top voltage and a relatively stable gap provide a possibility of generating a constant microwave frequency.

References

[1] R. J. Barker and E. Schamiloglu, Eds., "High-Power Microwave Sources and Technologies", New York: Wiley-IEEE Press (2001).

[2] J. Benford, J. Swegle, and E. Schamiloglu, "High Power Microwaves" 2nd ed., New York: Taylor & Francis (2007).

[3] D. J. Sullivan, J. E. Walsh, and E. A. Coutsias, "Virtual cathode oscillator (vircator) theory," in High Power Microwave Sources, V. Granastein and I. Alexeff, Eds. Norwood, MA: Artech House, p. 441 (1987).

[4] B. V. Alyokhin, A. E. Dubinov, V. D. Selemir, O. A. Shamro, K. V. Shibalko, N. V. Stepanov, and V. E. Vatrunin, IEEE Trans. Plasma Sci., vol.22, pp.945–959 (1994).

[5] E. H. Choi, M. C. Choi, Y. Jung, M. W. Chong, J. J. Ko, Y. Seo, G. Cho, and H. S. Uhm, IEEE Trans. Plasma Sci., vol.28, pp.2128–2134 (2000).

[6] W. Jeon, J. E. Lim, M. W. Moon, K. B. Jung, W. B. Park, H. M. Shin, Y. Seo, and E. H. Choi, IEEE Trans. Plasma Sci., vol.34, pp.937-944 (2006).

[7] D. Biswas and R. Kumar, IEEE Trans. Plasma Sci., vol.35, pp.369-378 (2007).

[8] R. Menon, A. Roy, S. K. Singh, S. Mitra, V. Sharma, S. Kumar, A. Sharma, K. V. Nagesh, K. C. Mittal, and D. P. Chakravarthy, J. Appl. Phys. vol.107, p.093301 (2010).

[9] C. W. Peters, R. L. Jaynes, Y. Y. Lau, R. M. Gilgenbach, W. J. Williams, J. M. Hochman, W. E. Cohen, J. I. Rintamaki, D. E. Vollers, and T. A. Spencer, Phys. Rev. E, vol.58, pp.6880-6883 (1998).

[10] W. Jiang, IEEE Trans. Plasma Sci., vol.38, pp.1325-1328 (2010).

[11] H. Sze, J. Benford, W. Woo, and B. Harteneck, Phys. Fluids, vol.29, pp.3873-3880 (1986).

Study on Uniformity of Laser Ablation Plasma Flow Guided by an Axial Magnetic Field

K. Hiraide, S. Kanamaru, J. Hasegawa, M. Nakajima, K. Horioka

Department of Energy Sciences, Tokyo Institute of Technology

ABSTRACT

The transverse uniformity of a laser-ablation plasma flow transported through an axial guiding magnetic field was investigated. The transverse profiles of the plasma ion flux were measured by a Faraday cup and compared with simulation results based on the collective focusing model. We found that the plasma ion current density increased with increasing axial magnetic field. We also confirmed that when the guiding magnetic field existed, the transverse profile of the plasma ion flux was slightly modulated in contrast to the uniform profile obtained without the field.

Keywords

heavy ion beam inertial fusion, high-current ion source, laser-ablation plasma, magnetic guiding

1. Introduction

To implode and ignite a fuel target of Heavy Ion Fusion (HIF), we need to develop a driver accelerator that can produce extremely intense heavy ion beams of 10^{11} - 10^{12} W. A HIF driver design based on induction accelerators requires ion sources to supply ion beams of 50 A in total during 20 μs. Generally, it is almost impossible to transport such a high current ion beam in the low-energy section of the driver accelerator because of the space charge limit. So in a typical driver design, 0.5-A heavy ion beams are extracted from a hundred of ion sources independently, and then gradually merged into several ion beams after acceleration. Normalized emittance must be less than 1.0 πmm-mrad at the ion sources, which is determined from a required beam emittance at final beam focusing in the fusion reactor and prospective emittance growth in the driver accelerator [1].

Recently, Kwan *et al*. proposed to use a multi-beamlet extracting method for HIF ion sources. This method can downsize the ion sources and enable us to employ various plasma sources [2].

One of the candidates for the plasma source is laser-ablation plasma. Since the laser-ablation plasma intrinsically has high density and high drift velocity, it has the potential to supply a high brightness ion beam to the HIF driver. Generally, the pulse width of laser is very short compared to the beam pulse width required by the accelerators. To expand the pulse width of the laser-ablation plasma, a drift chamber is usually employed for the laser ion source. Since the laser-ablation plasma expands from a small laser spot without collisions among ions, it becomes a laminar flow after traveling through the long drift chamber. This feature is very advantageous for extracting low-emittance ion beams.

On the other hand, the plasma ion current decreases rapidly with increasing drift distance because of the three-dimensional expansion of the plasma. To overcome this problem, it had been demonstrated that the plasma ion current was controlled by a magnetic field along the plasma propagating direction [3]. Okamura *et al*. observed that the decrease in the plasma current density was suppressed by a solenoidal magnetic field of a few hundred gauss [4]. And also, the calculated trajectories of plasma particles by using the collective focusing model [5] showed that the guiding magnetic field leads to efficient transport of the laser-ablation

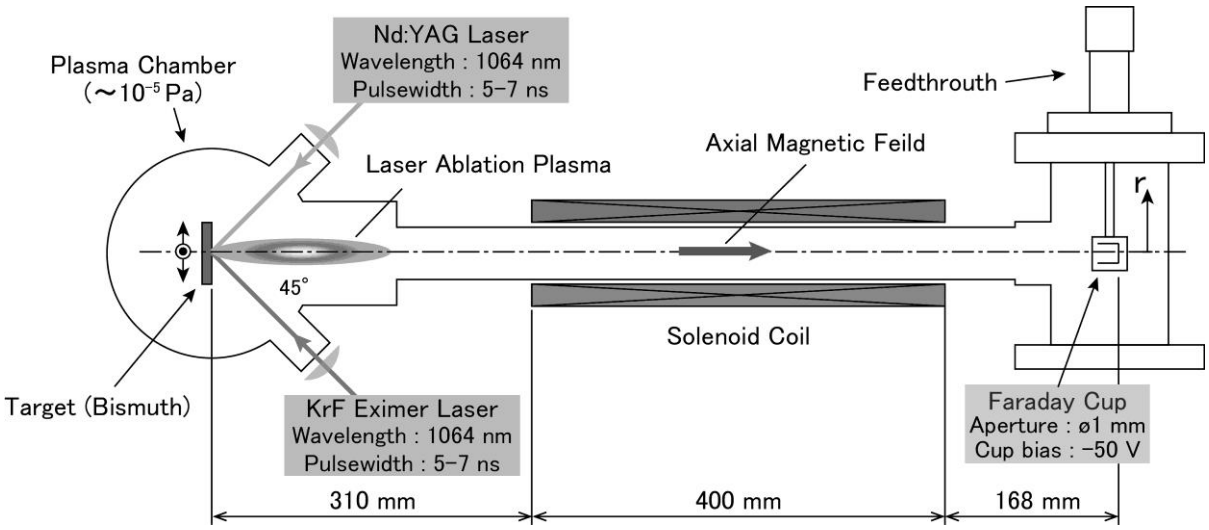

Fig. 1. An experimental setup for measuring transverse distribution of plasma ion current density.

plasma. On the other hand, the gyro motion of the plasma ions in the magnetic field may increase the momentum spread particularly in the transverse direction. Therefore, there are concerns about the transverse uniformity of the plasma ion flux and the momentum distributions. In particular, the latter may cause the emittance increase of extracted ion beams.

The purpose of this study is to examine the influence of guiding magnetic field on the transverse distribution of particle flux of laser-ablation plasma. This article presents the results of measurement of transverse distribution of plasma ion current and simulation results based on the collective focusing model.

2. Experimental Setup

An experimental setup for the plasma ion flux measurement is shown in Fig. 1. The experimental apparatus was composed of a plasma production chamber, a drift chamber, a solenoid coil, a Nd:YAG laser, a KrF eximer laser, and a Faraday cup. The plasma production chamber is evacuated to about 10^{-5} Pa by a turbo-molecular pump (260 L/s) and an oil-sealed rotary pump (30 L/min). To produce an ablation plasma, we used the Nd:YAG laser (wavelength: 1064 nm, pulse width (FWHM): 6 ns, maximum pulse energy: 650 mJ) or the KrF eximer laser（wavelength: 248 nm, pulse width (FWHM): 30 ns, maximum pulse energy: 300 mJ）. The laser was focused with a plano-convex lens through an optical window onto a plane target with an incident angle of 45 degrees. The target was mounted on an automatic XY-axis stage to change the position of the target without breaking vacuum. We changed the laser irradiation position on the target every 10-20 shots to prevent the irreproducibility of the produced plasma due to target surface deformation by successive laser irradiation at the same position. A solenoid coil of 400 mm long was located 310 mm downstream from the target. It applied a guiding magnetic field of 0.6 T at a maximum to the expanding plasma in the drift chamber. The solenoid coil was excited by a pulse current of 700 A peak from a RLC circuit. The time constant of the pulse current was 7.5×10^{-4} s , which was much longer than the plasma expansion time in the drift chamber (≤100 μs). Therefore, the excited magnetic field could be considered constant for the laser-ablation plasma.

To measure the transverse distribution of the plasma ion current after the plasma was transported though the solenoid magnetic field, a Faraday cup was located 878 mm downstream from the target. The charge collection cup was set in a grounded metal cage that had a ø1 mm aperture on the front surface and biased to -50 V typically. The cage was attached to a linear motion feedthrough having a stroke of 20 mm. We measured the plasma ion current by changing the position of the Faraday cup perpendicularly to the central axis of the drift

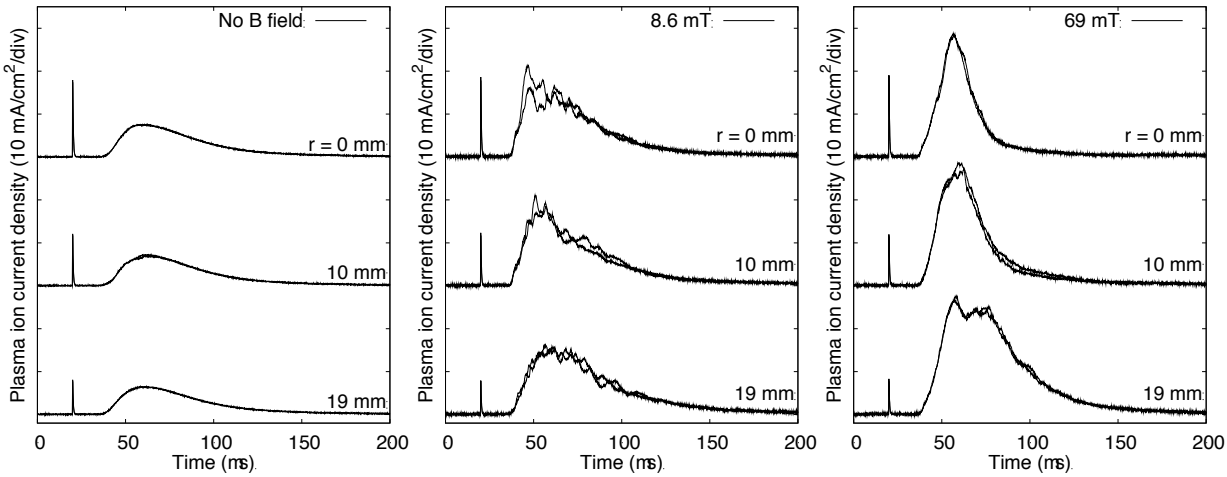

Fig. 2. Typical waveforms of plasma ion current (left: B_z = 0 mT, middle: B_z = 8.6 mT, right: B_z = 69 mT) .

chamber. We used a plate of bismuth as the laser target. The laser intensity on the target was 3×10^8 W/cm^2 with the Nd:YAG laser, and 2×10^8 W/cm^2 with the KrF eximer laser. The solenoid magnetic field was changed in a range of 0 - 69 mT. Whenever changing the target position, we irradiated the target several times before data taking to minimize the influence of impurity attached on the target surface.

3. Results and Discussion

Figure 2 shows the typical waveforms of plasma ion current. The waveform reproducibility was high without guiding magnetic field. When a magnetic field of 8.6 mT was applied, small fluctuations appeared on the waveform and the reproducibility of the waveform was degraded. However, the ion current density was two times greater than without magnetic field. Under a magnetic field of 69 mT, the ion current density increased significantly. The small fluctuation disappeared and the reproducibility was improved compared with the cases of 8.6 mT. And also, with 69 mT, the width of the current waveform increased with the increasing distance from the central axis.

The transverse distributions of the total ion charge are shown in Fig. 3. Here, the total charge was calculated by integrating the ion current waveform observed at each radial position. Each data point is an average of 5 shots. The error bar shows the standard deviation. The above figure shows the result obtained with the Nd:YAG laser, the below shows the result with the KrF eximer laser. The transverse distribution of the ion current density was nearly uniform without the guiding field. The ion current density increased with guiding magnetic field at every position

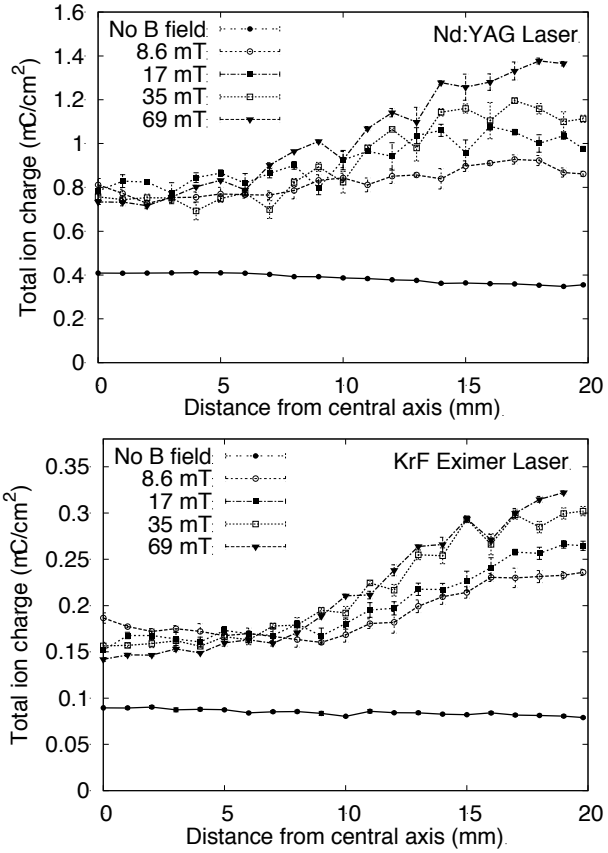

Fig. 3. Transverse distributions of ion current density (upper: Nd:YAG laser, lower: KrF eximer laser).

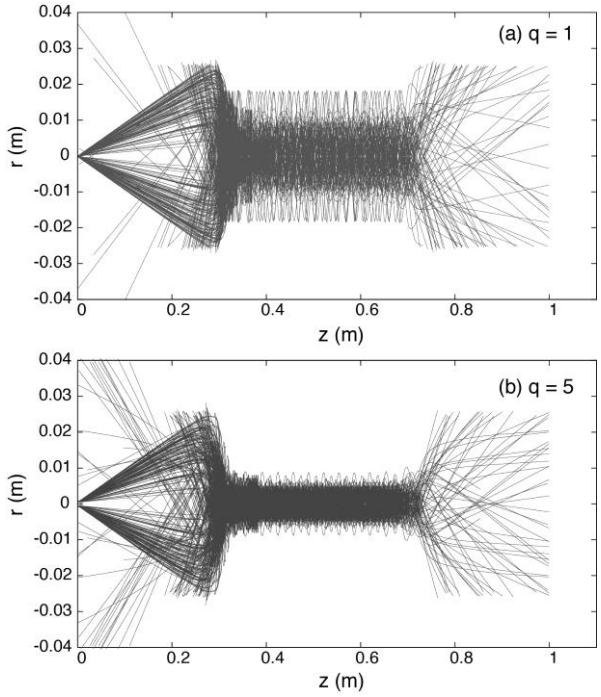

Fig. 4. Calculated trajectories of Bi plasma ions in a solenoid coil; (a) Bi^{+}, (b) Bi^{5+}.

compared to that without the field. In addition, the ion current density increased with the increasing distance from the central axis. With increasing applied magnetic field, this tendency became more obvious. The ion current densities obtained by the Nd:YAG laser were higher than those with the KrF eximer laser.

Figure 4 shows the results of numerical simulation on plasma particle trajectories in the guiding magnetic field. We used the collective focusing model in this simulation. The solenoid magnetic field was calculated by the Poisson-Superfish code. Figure 4 (a) and (b) show the trajectories of Bi^{+} and Bi^{5+}, respectively.

As shown in Fig. 4, even ions emitted from the target with large divergence angles were gathered around the entrance of the solenoid coil (L = 350 mm, here L is the distance from the target) by the guiding effect of the applied magnetic field. The guiding effect depended on the ion charge state and became more obvious for Bi^{5+}. Moreover, it can be seen that the envelope radius of the plasma particles in the solenoid coil was considerably smaller in the higher charge-state case. On the other hand, the guiding effect for the Bi^{+} ions was weak. Since the envelope radius was comparable to the inner radius of the drift chamber, ions might hit the wall chamber, resulting in the loss of the ions. The plasma expanded quickly after passing through the solenoid coil, and the transverse momentum spread of the plasma particles was very large compared to that in the case of no guiding field. Most of the particles traveled apart from the central axis regardless of the charge state. These simulation results seem to agree with the result of the experiment.

4. Conclusions

In this study, we measured the transverse ion current density distribution of laser ablation plasma guided by an axial magnetic field along the plasma drift direction, and compared the experimental results with simulation results by the collective focusing model. The ion current density increased in the presence of the guiding magnetic field. This result supports that the magnetic field is very effective to suppress ion current reduction. We also found that the enhancement of the ion current density was more significant at relatively large distances from the central axis of the axial magnetic field.

References

[1] J.W. Kwan *et al*., Nucl. Instrum Methods A **464**, 397 (2001).

[2] D.P. Grote *et al*., Phys. Rev. Special Topics Accel. Beams. **6**, 014202 (2003).

[3] L. G. Gray *et al*., J. Appl. Phys., **53**, 6628 (1982).

[4] M. Okamura *et al*., Rev Sci Instrum., **81**, 02A510 (2010).

[5] S. Robertson, Phys. Rev. Lett. **48**, 149 (1982).

Formation Process of Two-step Shock Wave driven by Laser Detonation

Kenta Kawaguchi, Ken Yonezawa, Mitsuo Nakajima,
Jun Hasegawa, Tohru Kawamura, and Kazuhiko Horioka
Department of Energy Sciences, Tokyo Institute of Technology, Yokohama 226-8502, Japan

ABSTRACT

We observed a two-step shock wave by irradiating a TEA CO_2 laser to a conical brass target in atmospheric condition. We showed that the propagation of shock front was enhanced by the presence of the metal target. The results indicated that there is an abrupt acceleration mechanism of the energy deposition region. We also showed that a streamer-like structure appears at the initial phase of the laser breakdown. Based on the results, we performed an electric measurement to study the plasma interaction with the metal target. The result clearly showed that electrons emit from the target. All of the results indicated that an interplay among the laser absorption, the breakdown plasma, and the metal plays an important role for the formation process of LSD.

Keywords

Laser induced plasma, Breakdown, Shockwave, Laser supported detonation

1. Introduction

Detonation is a hybrid wave in which shockwave and a heating fluid area propagate together [1],[2]. When a detonation is triggered in a combustible gas, the heating fluid area drives a shockwave, at the same time, the shock heated region enhances the combustion and vice versa.

LSD (Laser-supported detonation) is driven by a high power laser. In the case of LSD, the heating fluid area is made of high energy density plasma. The laser absorbing rate enhances at the shock heated region that strengthen the shock wave. Therefore the LSD usually has a complicated structure, in which laser induced highly non-equilibrium plasma and the radiation transport induces highly transient hydro-dynamical motion [3].

The LSD is one of the effective mechanism of the thrust for a laser propulsion [4],[5]. In the system, a projectile emits a fast ablation plasma generated by an ablation and/or LSD behind the projectile to obtain a high specific impulse. Also, that can be powered and controlled remotely. For example in 1920s, K. E. Tsiolkovsky discussed a propulsion system of spacecraft which receives thrust power from a ground based electromagnetic waves. It was the first idea of the beamed propulsion system [6].

The study on the laser propulsion started just after a laser device was invented in 1960s. A memorable idea was proposed by A.Kantrowits in which he discussed the capability of a laser launching system of spacecraft from the earth using a rocket model based on laser ablation pressure [7]. He also pointed out the advantage of laser propulsion; higher specific impulse because of no needs of fuel and oxidizer.

The pressure induced by laser ablation was thought to be the most effective mechanism for propulsion at an early stage of study on the laser propulsion system. However, as the study advanced, it was found that ablation itself plays a minor role in terms of the propulsion [8]. Nowadays it became clear that, instead of ablation, LSD or LSC (Laser-supported combustion) caused by the laser and chemical reaction are more effective for generating the thrust. The aircraft obtains the thrust by the shock-induced high-pressure gradient of LSD behind the aircraft [9].

The “Light Craft” invented by LN. Myrabo et al is famous for the demonstration of laser propulsion [10]. They succeeded in launching a projectile with about

50 g weight to 120 meters high under gravity by using a 10kW CO_2 laser.

The phenomena; LSD itself was already found in 1960's [11]. Fluid dynamic phenomenon driven by the LSD and its structure are already known in simple condition such as gas atmosphere. However, for a more complex situation such as existence of a metal target, detailed models are still in discussion.

For generating a LSD, laser power density should be more than a threshold value. When we generated a LSD close to a metal in an atmosphere, we observed decrease of threshold and increase of shock speed [12]. Propagation velocity of LSD didn't vary so much according to the size of target. So the metal target was considered to exert only an effect that decreases the threshold energy [1]. As is well known, shockwave propagates integrally with laser absorption area in LSD. However the effect of the metal target is still under discussion [13,14].

In this paper, we show recent study on the LSD where we focused a transversely excited atmospheric (TEA) CO_2 laser close to a top of metal (Brass) cone and observed the LSD phenomena. We could see two-step spheroidal shock wave using the Schlieren method.

We also observed, using a fast framing camera, a streamer like light emission after about 10 ns from the laser irradiation. We considered it may mean that high-speed electrons play some roles for the formation of the structure. It may be relevant to the LSD evolution mechanism peculiar to the existence of metal target. In addition to these imaging experiments, we conducted electric measurements to make clear the role of the metal target for LSD.

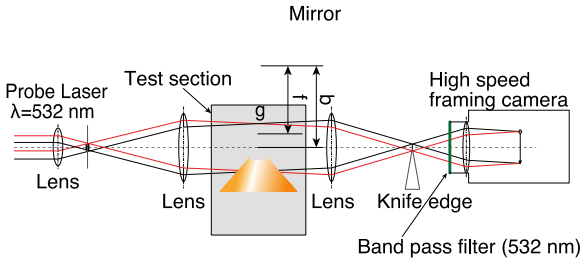

Fig. 1. A schematic diagram of experimental arrangement and schlieren optics.

2. Experimental Setup

We have carried out the following three measurements to investigate the effect of metal on the LSD evolution. .

First, we observed the shock evolution with- and without- metal target by taking Schlieren images [14]. Figure 1 shows a schematic diagram of the experimental arrangement for the shock wave observations. In this figure, f is focal length of a ZnSe lens and b is a distance between the lens and a conical brass target. A TEA CO2 laser (Ushio-Unimark 400) whose wavelength λ is 10,600 nm, was used for forming and driving LSDs. The laser which has 20 × 30 mm^2 cross-section was focused 4 mm above the top of a conical target made of brass (b = 67.5 mm) using the ZnSe lens (f = 63.5 mm). So the F-value of laser optics was 2.3, and the beam waist was estimated to be about 0.031 mm.

We measured the temporal profile of the TEA CO2 laser by using a pyroelectric detector (QS3-H) and the total laser energy with a joule detector (PHD50). We conducted the experiments by focusing the laser with Q = 0.7-2.5 J under atmospheric air conditions.

The laser power profile is shown in Fig. 2. We took shockwave images by using a Schlieren optical system and a fast framing camera (NAC-Ultra Neo). We used a semiconductor laser (λ = 532 nm) for the probe light for the Schlieren image. We placed a band pass filter (532nm) in front of the fast framing camera lens to avoid the stray light from the laser breakdown plasma.

Second, we removed the Schlieren optical system and the band pass filter, and observed the evolution of laser-induced plasma using the fast framing camera.

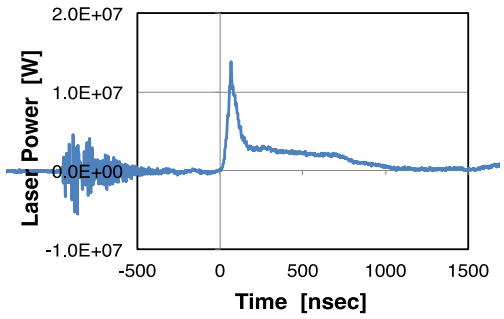

Fig. 2. Temporal profile of TEA CO_2 laser power.

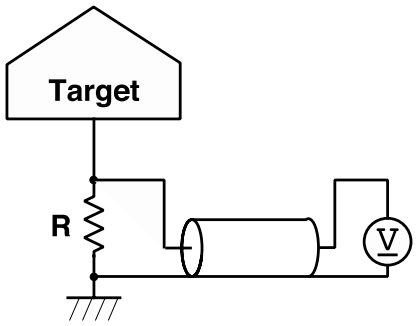

Fig. 3. Set-up for electric measurements.

We also carried out an electrical measurement to see the role of metal target on the LSD evolution, in which we connected the target to the ground through a resister R (=500 kΩ) as shown in Fig.3. If electrons emit from the target during laser irradiation, the target potential should shift to plus.

In order to avoid the switching noise of the TEA laser, we observed the voltage signal through a BNC cable with high impedance (1MΩ) mode. Although the signal does not have time resolution, time integration of the signal reflects total charge emitted from the metal target. The capacitance of the cable C was estimated to be about 600pF. Thus, when the interaction between the laser plasma and the metal target induce an electron emission, the target potential is expected to decay according to the time constant of the circuit in Fig.3.

3. Results and Discussion

3.1 Two-step spheroidal shockwave

The TEA CO2 laser was focused by the ZnSe lens (f = 63.5 mm and b = 67.5 mm) and irradiated the brass target with Q = 2.0 J. Thus the laser irradiated the top of target with an over-focused optical geometry.

Figure 4 shows a typical Schlieren image around the target at 1150-1550 nsec from the laser irradiation. As shown, the shock boundary discontinuously evolved to the upstream. Namely, when we induced breakdown plasma with brass target, we observed the two-step spheroidal shockwave.

We took Schilieren images with and without the metal target as a function of time from the laser injection and estimated the front speed. The results are shown in Fig.5, where red squares denote the shock speed with metal and blue ones for without metal. As shown in the figure, the velocity of shock front was estimated to be 7000 m/s (with metal target) and 3000 m/s (without target) for 600 ns after the laser injection and that decreased about 2000 m/s after 1200 nsec.

In case of a pulsed laser breakdown, the plasma induces a shock wave usually spherically propagating from the laser focusing point. In the case of TEA-CO2 laser irradiation without metal target, we always observed spheroidal shock wave. The spheroidal shockwave is an outcome of the drift of energy deposition region, namely it is the evidence of an interplay between the laser energy deposition and the shock heated region, thus the occurrence of LSD.

However the Schlieren image shown in Fig.4 clearly shows a discontinuous structure composed of two-spheroidal shockwave. The structure should be caused by a discontinuous jump of the energy deposition region. That is, the energy deposition region moved faster than the hydro-dynamical speed. The high-speed front speed (7000 m/s) is also supporting this supposition.

The observation in this study is different a bit from the conventional understanding of the laser detonation mechanism in which a spheroidal shockwave is induced by a continuously moving laser absorption region.

When we assume calorimetrically perfect condition in the shock heated region, we can analytically estimate the shock front pressure using the Rankine – Hugoniot relation [15], as follows,

$$p_s = \frac{\rho_0 V_s^2}{\gamma_m + 1} \qquad (1)$$

where p_s is the pressure in the shock heated region, Vs is the shock velocity, ρ_0 is the density of the atmospheric air, γ_m is the specific heat ratio.

When we substitute V_s from the data given in Fig.5, ρ_0 = 1.25 kg/m^3 for the atmospheric air and γ_m = 1.67, the pressure p_s can be estimated to be about 25 MPa.

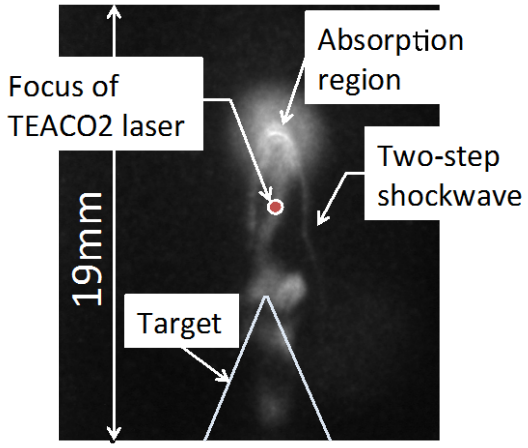

Fig. 4. Schlieren image of two-step shock wave measured at 1150-1550 nsec after laser irradiation with methal target.

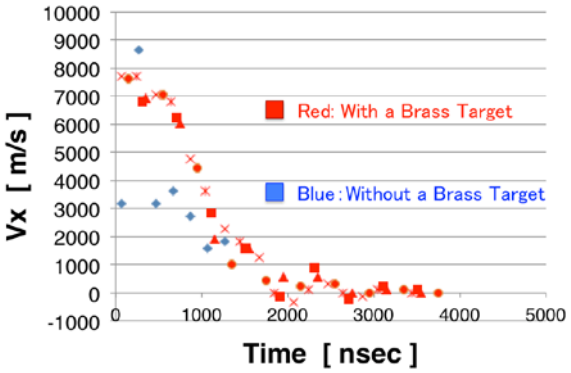

Fig. 5. Shock front speed in LSD (with and without brass target).

3.2 Precursor of LSD

We irradiated the brass target with TEA CO2 laser by ZnSe lens (f = 127 mm). Then we observed visible light emission from the irradiation region in the early stage of the LSD with the fast framing camera. In these experiments, ambient gas was He, Q was 2.5 J and b = 127 mm.

Typical results are shown in Fig.6 (2 atm He) and Fig.7 (1 atm He). As shown in these images, when the laser irradiated the metal target, we could observe the streamer like structures along the laser paths. This streamer-like structure evolved toward the laser

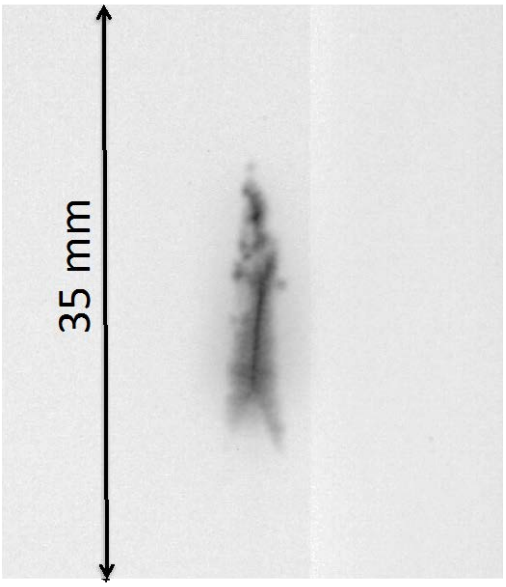

Fig.6 Visible image of laser interaction region at 20-40 ns after laser irradiation in 2 atm He.

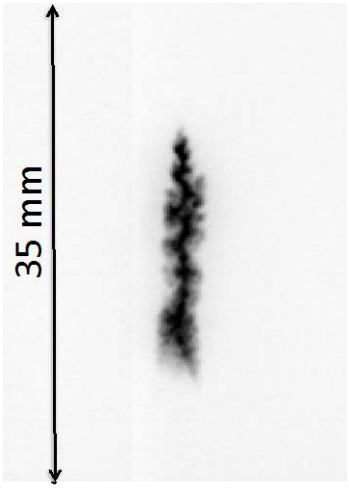

Fig. 7. Visible image at 50-60 ns after laser irradiation in 1 atm He.

and the image decayed after a few tens of nsec from the laser irradiation. These results motivated us to investigate the charge flow through the metal target.

3.3. Electron emission from the metal target

We measured the target voltage after the laser irradiation using the circuit shown in Fig.3. We used a

coaxial cable 6m in length. As was discussed in the previous section, the time constant of the circuit τ was estimated to be $RC \sim 300$ μs.

In this experiment, we irradiated the target with Q=2.0 J, f = 95.8 mm and b = 97.5 mm. A typical signal of the voltage profile of the metal target is shown in Fig.8. As shown, the voltage shifted plus by the laser irradiation which means that electrons are emitted from or ions are injected to the target. When we think about the time scale of the streamer like image, the signal seems to correspond to the electron emission.

As expected, the signal decayed with the time constant τ. Obviously the time scale of LSD phenomena is much smaller than that of the signal. Then we cannot know the temporal profile of charge flow. Instead we can know the total charge flow through the metal target from the time integration of the signal. We calculated the net number of electrons which emitted from the target using the following equation,

$$N_e = \frac{1}{e}\int \frac{V}{R}\,dt \qquad (2)$$

where e is elementary charge and N_e is the net number of the electrons.

We show the estimated N_e as a function of laser energy in Fig.9. As shown N_e increased with the laser energy. In the experiments, we used optical window made of polyathethal. We checked effect of the window material on the signal accompanied by the LSD formation. We figured out that the signal is caused by the pile-up of negative charge on the window (insulator) surface.

This result clearly shows that an electric phenomena plays some roles in the formation of LSD in the presence of metal target. The electron density n_e in the laser breakdown region is estimated to be around that corresponding the cutoff frequency of CO2 laser. The electrons emitted from the metal target should increase the electron density, i.e., that extends the energy deposition region along the laser path. That may cause rapid acceleration of the laser absorption regime to the upstream. If the accelerated speed is

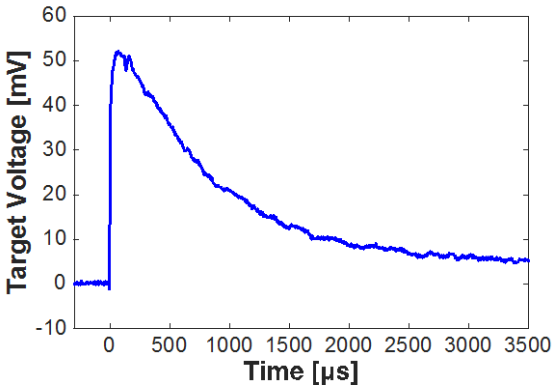

Fig. 8. Potential variation of metal target after laser breakdown.

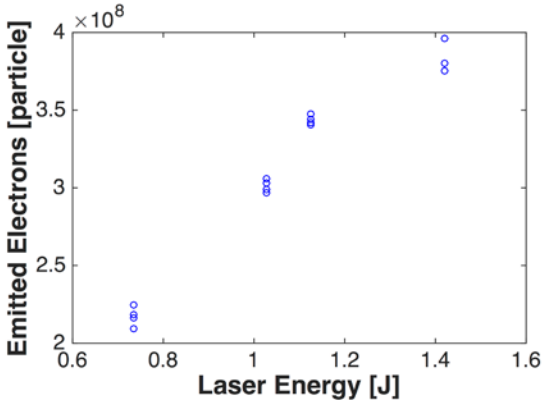

Fig. 9. Number of net electrons from the target versus laser energy.

larger than the shock speed, it should induce discontinuous shock wave.

The results obtained in this study shows that an interplay among the laser energy deposition, the plasma evolution, and the electrical phenomena around metal surface is significant for the formation and the evolution processes of LSD.

4. Concluding Remarks

A two-step spheroidal shock wave was observed as a result of irradiation of TEA CO2 laser to a conical brass target in atmosphere. The results indicated that

there is an acceleration mechanism of the laser absorption area. As conventional models of LSD cannot explain the mechanism, we took fast imaging photos and made charge flow measurements.

The fast framing images in the initial phase of plasma formation showed a streamer like structure. The electrical measurements indicated an electrical phenomena in which electrons emitted from the target.

All of the results obtained in this study showed that in the formation process of LSD with metal target, electric phenomenon plays an important role for the formation and the evolution of discontinuous detonation wave.

We need to know more about the initial phase of the plasma evolution. In particular, current measurements with time resolution at the laser breakdown phase is of primary concern. In the very initial phase of laser plasma breakdown, the interaction between the highly transient plasma and the metal wall may form a potential difference [16]. In the process, most of the current should flow back to a localized metal surface. In the model, the emission and the back flow are just departed by the plasma scale length. That also requests us to develop a diagnostics for the electron flow with much higher spatial resolution.

5. Acknowledgement

We would like to express our appreciation to Mr. S.Someya and Mr. S.Matsumura of NAC Image Technology for the help with fast framing photography.

References

[1] T.Endo, J.Kasahara, A.Matsuo, et.al., AIAA J. **Vol.42**, p.1921 (2004).

[2] K. Terao ”Irreversible Phenomena Ignitions, Combustion and Detonation Waves”, Springer, (2007).

[3] H. Shiraishi, Journal of the Japan Society for Aeronautical and Space Sciences, **47** (549), pp.383-388, (1999).

[4] C. Phipps, M. Birkan, W. Bohn, et. al., Review: Laser-Ablation Propulsion”, JOURNAL OF PROPULSION AND POWER, **Vol.26**, No.4 pp.609-637 (2010).

[5] A. Saso, Review of Laser Engineering, **Vol.34**, Np.6 pp.404-407 (2006).

[6] K. E. Tsiolkovsky: “Spaceship”, Edited Machine Translation prepared by Translation Division, Foreign Technology Division, WP-AFB, Ohio, pp.307 (1966).

[7] A. Kantrowitz, ”Propulsion to Orbit by Ground-Based Lasers”, Aeronaut. Astronaut., **Vol.10**, pp.74-76 (1972).

[8] A.V. Pakhomov, “Basic Study of Laser Ablation for Laser Propulsion”, Review of Laser Engineering, **Vol.34**, No.6, pp.429-434 (2006).

[9] A. Sasoh, “High-speed Plasma Flows and Detonation Waves in Laser Propulsion”, J. Plasma Fusion Res., **83**(5): 472-476, (2007).

[10] LN. Myrabo: “Brief History of the Lightcraft Technology Demonstrator (LTD) Project”, AIP Conference Proceedings, **Vol.664**, No.1, pp.49-60 (2003).

[11] S. A. Ramsden and P. Savic: “A Radiative Detonation Model for the Development of a Laser-Induced Spark in Air”, NATURE, **Vol.203**, No.4951, pp.1217-1219 (1964).

[12] K. Yonezawa, K. Kawaguchi et.al., “Effects of Solid Target on the Formation of Laser Supported Detonation Waves”, to be appear in NIFS-Proc.

[13] K.Kawaguchi, K.Yonezawa, M.Nakajima, K.Horioka, “Two-Step Spheroidal Shock Wave Driven by TEA-CO2 Laser”, Plasma Fusion Res., 10, 008 (2015).

[14] H. W. Liepmann and A. Roshko: “*Elements of Gasdynamics*”, Dover Publications, (1957).

[15] Y. B. Zeldovich and Y. P. Raizer, *“Physics of Shock Waves and High-temperature Hydrodynamic Phenomena”*, Dover, New York, (2002).

[16] F.Schwirzke,”Unipolar arc model”, J. Nucl. Mater. **Vol.128**, p.609 (1984).

Simulating Beam Parameter using Malmberg–Penning Trap Device for Longitudinal Pulse Compression in Heavy Ion Inertial Fusion

Takashi Kikuchi, Tomohiro Sato, Y. Park*, Y. Soga*,
K. Takahashi, T. Sasaki, Nob. Harada

Nagaoka University of Technology
**Kanazawa University*

ABSTRACT

A simulating beam parameter is considered in a compact beam simulator constructed with a Malmberg–Penning trap device for heavy ion inertial fusion. The Malmberg–Penning trap device is expected as an experimental device to simulate longitudinal pulse compression in a driver system for heavy ion inertial fusion. Tune depression is estimated with Brillouin density limit, rigid–rotor Vlasov equilibrium, and a model considering with radial distribution of charge density. As a result, it is considered that these estimations are not suitable for the space charge strength of the condition in the device.

Keywords

Tune Depression, Malmberg–Penning Trap, Heavy Ion Inertial Fusion, Compact Simulator, Space–Charge–Dominated Beam, Beam Physics

1 Introduction

In inertial confinement fusion driven by intense heavy–ion–beam irradiation, so–called heavy ion inertial fusion (HIF), beam physics and dynamics should be cleared well for effective target pellet implosion [1]. Especially, the extreme longitudinal pulse compression scheme is required in the final stage of energy driver in HIF accelerator system [2–4].

Theoretically, it is predicted that the beam parameters passage through a risky regime to increase the emittance [5, 6]. For this reason, the emittance growth should be estimated to design the heavy ion accelerator for HIF system during the longitudinal pulse compression.

A Malmberg–Penning trap device [7, 8] is expected as an experimental device to simulate the longitudinal pulse compression for HIF driver system [9]. In the Malmberg–Penning trap device, the magnetic flux density B_z applied in the axial z direction confines the charged particle in radial r direction, and the electrostatic potential applied at both the ends of axial direction reflects the charged particle. Electron devices scaled by the parameters of the heavy ion beam in HIF driver system were useful experimental device due to the compact size [10–12]. Not only the experimental work, but also the numerical approach was carried out [13], and the electron dynamics is simulated during the pulse compression manipulation [13].

In this study, the simulating beam parameter is estimated by using theoretical approach. One of most unique properties is "space–charge–dominated beam" for the HIF driver system. The simulating beam parameter in the Malmberg–Penning trap device as a compact simulator is indicated from the viewpoint of the space charge strength of the beam.

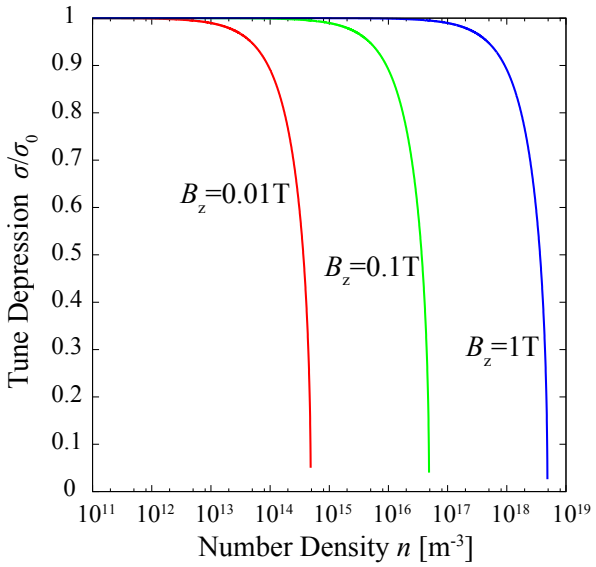

Figure 1: Tune depression estimated by Brillouin density limit.

2 Simulating Beam Parameter

To simulate the beam dynamics in HIF driver system, there are some indexes such as space charge wave velocity, generalized perveance, compression ratio, aspect ratio of bunch size, beam velocity divided by speed of light, and so on.

A tune depression is one of indexes to estimate the space–charge strength of the charged particle beams. The tune depression σ/σ_0 is explained by the ratio of the undepressed tune σ to the undepressed tune σ_0 [14–16]. For $\sigma/\sigma_0 \to 1$, the beam is in weak space–charge strength, so–called *emittance–dominated beam*. On the other hand, the beam is in strong space–charge strength, so–called *space–charge–dominated beam*, for $\sigma/\sigma_0 \to 0$.

3 Estimation of Tune depression with Brillouin density limit

Figure 1 shows the tune depression estimated by the Brillouin density limit [17]. The tune depression is estimated by [17]

$$\sigma/\sigma_0 = \sqrt{1 - \frac{\tilde{n}}{n_{\rm lim}}} \qquad (1)$$

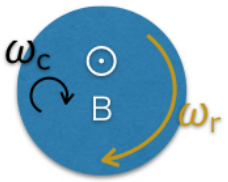

Figure 2: Rotation angular frequency $\omega_{\rm r}$ in rigid-rotor Vlasov equilibrium and cyclotron frequency $\omega_{\rm c}$.

where $\tilde{n}$ is the average density and $n_{\rm lim}$ is the density evaluated by the Brillouin density limit. In the case of electron, the limiting density is estimated as $n_{\rm lim} = 4.86 \times 10^4 B_{\rm z}^2$ cm^{-3}, where $B_{\rm z}$ is in unit of Gauss.

As shown in Fig. 1, when the number density is assumed in $10^{11} \sim 10^{12}$ m^{-3} with the solenoidal strength $B_{\rm z} = 0.01 \sim 1$ T according to the experimental condition [9], and the tune depression $\sigma/\sigma_0 \sim 1$ is expected.

As mentioned in Ref. [17], this estimation is "*based on the KV model and is not very accurate for low–density plasma.*" For this reason, it is expected that the evaluation result in this assumption is not suitable for the parameters in this experimental setup.

4 Estimation of Tune depression with Rigid-Rotor Vlasov equilibrium

The tune depression is also described by using a dimensionless parameter Δ. The dimensionless parameter indicates the ratio of applied focusing strength to the space–charge defocusing strength [18]. In the case of Malmberg–Penning trap configuration, the dimensionless parameter Δ is written by [18]

$$\Delta = \frac{2\left(\omega_{\rm r}\,\omega_{\rm c} - \omega_{\rm r}^2\right)}{\omega_{\rm p}^2} - 1 \qquad (2)$$

where $\omega_{\rm r}$ is the rotation angular frequency in the assumption of rigid rotation, $\omega_{\rm c}$ is the cyclotron frequency, and $\omega_{\rm p}$ is the plasma frequency, respectively. Figure 2 shows the relation between the rotation angular frequency and the cyclotron frequency. For the assumption of the thermal equilibrium distribution, the dimensionless parameter

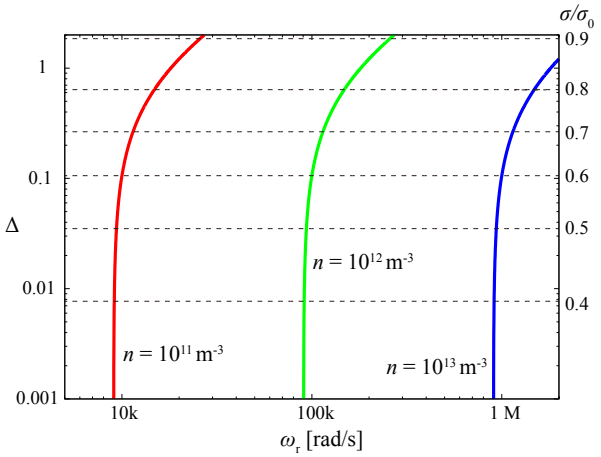

Figure 3: Tune depression σ/σ_0 and dimensionless paratmeter Δ as a function of rotation angular frequency ω_r for T =1 eV and B_z =0.1 T.

Δ is related by the tune depression as shown in Table V in Ref. [19], e.g., $\sigma/\sigma_0 = 0.9$ for $\Delta = 1.851$ and $\sigma/\sigma_0 = 0.1$ for $\Delta = 4.975 \times 10^{-12}$.

Figure 3 shows the tune depression estimated with the above dimensionless parameter. The temperature is assumed by 1 eV. As shown in Fig.3, the tune depression is controlled in the range of $\sigma/\sigma_0 = 1 \sim 0$ for number density $n = 10^{11} \sim 10^{12}$ m^{-3} with the several–10 krad/s of the rotation angular frequency.

5 Estimation of Tune depression considering with radial distribution of charge density

The frequency of rigid rotation of the plasma column ω_r, the cyclotron frequency ω_c, (electron) plasma frequency ω_p are defined by

$$\omega_\mathrm{r} = \frac{E_\mathrm{r}}{rB_\mathrm{z}} \tag{3}$$

$$\omega_\mathrm{c} = \frac{eB_\mathrm{z}}{m_\mathrm{e}} \tag{4}$$

$$\omega_\mathrm{p}^2 = \frac{n_0\, e^2}{m_\mathrm{e}\, \varepsilon_0}. \tag{5}$$

Here B_z is the magnetic flux density in axial (z) direction, e is the elementary charge, m_e is the electron mass, n_0 is the number density at uniform inside the beam, ε_0 is the permittivity of free space, and the electric field in radial (r) direction is

$$E_\mathrm{r} = \frac{e}{\varepsilon_0}\frac{1}{r}\int_0^r n(r)\, r\, dr = \frac{n_0\, e}{\varepsilon_0\, r}\int_0^r \tilde{n}(r)\, r\, dr \tag{6}$$

where $n(r) = n_0\, \tilde{n}(r)$.

Substituting Eqs.(3), (4), (5), and (6) into Eq.(2),

$$\Delta = 2\left(1 - \frac{m_\mathrm{e}\, n_0}{\varepsilon_0\, B_\mathrm{z}^2}\frac{\tilde{E}_\mathrm{r}}{r}\right)\frac{\tilde{E}_\mathrm{r}}{r} - 1 \tag{7}$$

where

$$\frac{\tilde{E}_\mathrm{r}}{r} = \frac{1}{r^2}\int_0^r \tilde{n}(r)\, r\, dr \tag{8}$$

depends on the density profile inside the beam. From Eq.(7), the dependence of Δ is written with

$$\Delta \propto 1 - \frac{n_0}{B_\mathrm{z}^2}. \tag{9}$$

As a result, it is found that the condition for dense and weak strength of applied magnetic flux density creates the space–charge–dominated state.

If the distribution is flat top for strong space-charge-dominated state (tune depression $\sigma/\sigma_0 = 0$, temperature $T \to 0$), the number density of the beam is described with

$$\tilde{n}(r) = \begin{cases} 1 & (r < a_0) \\ 0 & (otherwise) \end{cases} \tag{10}$$

where a_0 is the zero-temperature beam radius [14]. Substituting Eq.(10) into Eq.(8), $\tilde{E}_\mathrm{r}/r$ inside the beam is given by

$$\frac{\tilde{E}_\mathrm{r}}{r} = \frac{1}{2} = 0.5. \tag{11}$$

If the distribution becomes Gaussian for weak space-charge-dominated state (= emittance-dominated limit) ($\sigma/\sigma_0 = 1$, $T \to \infty$), the number density of the beam is assumed with

$$\tilde{n}(r) = \frac{n(0)}{n_0}\exp\left(-\frac{r^2}{\tilde{r}_0^2}\right) \tag{12}$$

where $\tilde{r}_0 = a_0/\sqrt{2}$. Substituting Eq.(12) into Eq.(8),

$$\frac{\tilde{E}_\mathrm{r}}{r} = 1 - \frac{1}{e} \simeq 0.632... \tag{13}$$

for $r = \tilde{r}_0$ (beam edge radius of equivalent rms beam). Here $n(0)/n_0 = 2$ for $T \to \infty$ [14].

Figure 4 shows the Δ using Eq.(7) as a function of number density and magnetic flux density for

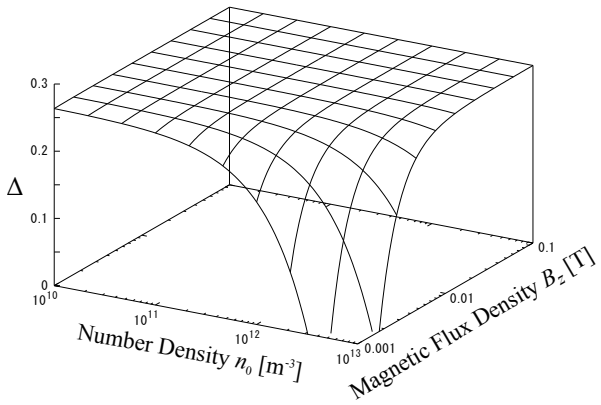

Figure 4: Dimensionless paratmeter Δ as a function of number density and magnetic flux density for $\tilde{E}_{\rm r}/r = 0.632$.

$\tilde{E}_{\rm r}/r = 0.632$ (i.e., at beam edge radius of equivalent rms beam for Gaussian distribution).

For this reason, the range of $\tilde{E}_{\rm r}/r$ is written by

$$\frac{1}{2} < \frac{\tilde{E}_{\rm r}}{r} < 1 - \frac{1}{e} \tag{14}$$

or

$$0.5 < \frac{\tilde{E}_{\rm r}}{r} < 0.632 \tag{15}$$

If in case of low density ($n_0 \to 0$) and/or extreme strong magnetic flux ($B_{\rm z} \to \infty$) condition, the maximum value of Δ is given by

$$\Delta \simeq 2\frac{\tilde{E}_{\rm r}}{r} - 1 \simeq 0.264... \tag{16}$$

for $\tilde{E}_{\rm r}/r = 0.632$. From Ref. [19], the dimensionless parameter $\Delta = 0.264$ corresponds to the tune depression $\sigma/\sigma_0 = 0.7$. Also, as shown in Fig.4, the tune depression is always below 0.7.

6 Conclusion

The simulating beam parameter was studied in the compact beam simulator constructed with the Malmberg–Penning trap device for HIF system. The tune depression was estimated with the Brillouin density limit, the rigid–rotor Vlasov equilibrium, and the model considering with the radial distribution of charge density.

The estimation of tune depression based on the Brillouin limit implied the quite weak in the space charge condition in the experimental device.

The estimation of tune depression based on the rigid–rotor Vlasov equilibrium indicated from weak to strong space charge condition. However, the assumption of the rigid–rotor model is a little bit odd, because of the rotation is driven by $\mathbf{E} \times \mathbf{B}$ drift, and the electrical field $\mathbf{E}$ depends on the charge density distribution in the radial direction. The rigid–rotor equilibrium fixes the linear electric field distribution.

The estimation of tune depression considering with the radial distribution of charge density was derived, and indicated that the tune depression becomes always below 0.7, theoretically.

As a result, it is considered that the above estimations are not suitable for the space charge strength of the condition in the device.

References

[1] S. ATZENI and J. MEYER-TER-VEHN, *The Physics of Inertial Fusion: Beam Plasma Interaction, Hydrodynamics, Hot Dense Matter* (Oxford Univ., N.Y., 2004).

[2] D. D.-M. HO and S. T. BRANDON, *Nucl. Instrum. Methods Phys. Res.*, **A278**, pp.182-185 (1989).

[3] M.J.L. DE HOON, E.P. LEE, J.J. BARNARD and A. FRIEDMAN, *Phys. Plasmas*, **10**, pp.855-861 (2003).

[4] T. KIKUCHI, K. HORIOKA, M. NAKAJIMA and S. KAWATA, *Nucl. Instrum. Methods Phys. Res.*, **A577**, pp.103-109 (2007).

[5] T. KIKUCHI and K. HORIOKA, *Phys. Plasmas*, **16**, 050703 (2009).

[6] T. KIKUCHI and K. HORIOKA, *IEEJ Trans. FM*, **135**, pp.161-162 (2015).

[7] Y. SOGA, Y. KIWAMOTO and N. HASHIZUME, *Phys. Plasmas*, **13**, 052105 (2006).

[8] Y. SOGA, T. MIMURA, Y. KATO and Y. PARK, *Plasma Fusion Res.*, **8**, 2401034 (2013).

[9] Y. PARK, Y. SOGA, Y. MIHARA, M. TAKEDA and K. KAMADA, *NIFS-PROC*, **93**, pp.84-87 (2013).

[10] P.G. O'SHEA, M. REISER, R.A. KISHEK, S. BERNAL, H. LI, M. PRUESSNER, V. YUN, Y. CUI, W. ZHANG, Y. ZOU, T. GODLOVE, D. KEHNE, P. HALDEMANN and I. HABER, *Nucl. Instrum. Methods Phys. Res.*, **A464**, pp.646-652 (2001).

[11] A. NAKAYAMA, Y. SAKAI, Y. MIYAZAKI, T. KIKUCHI, M. NAKAJIMA and K. HORIOKA, *EPJ Web Conf.*, **59**, 09005 (2013).

[12] Y. SAKAI, M. NAKAJIMA, J. HASEGAWA, T. KIKUCHI and K. HORIOKA, *Nucl. Instrum. Methods Phys. Res.* **A733**, pp.70-74 (2014).

[13] T. SATO, Y. PARK, Y. SOGA, K. TAKAHASHI, T. SASAKI, T. KIKUCHI and Nob. HARADA, *Plasma Conference 2014*, 20PA-025 (2014).

[14] M. REISER, *Theory and Design of Charged Particle Beams* (Wiley, New York, 1994).

[15] R.C. DAVIDSON and H. QIN, *Physics of Intense Charged Particle Beams in High Energy Accelerators* (Imperial College Press, 2001).

[16] T.P. WANGLER, *RF Linear Accelerators* (Wiley-VCH, 2008).

[17] H. OKAMOTO and H. TANAKA, *Nuclear Instrum. Methods Phys. Res.*, **A437**, 178 (1999).

[18] E.A. STARTSEV and S.M. LUND, *Phys. Plasmas*, **15**, 043101 (2008).

[19] S.M. LUND, T. KIKUCHI, R.C. DAVIDSON, *Phys. Rev. STAB*, **12**, 114801 (2009).

Experimental study on the axial compression of a pure electron plasma simulating space-charge-dominated beam

Youngsoo Park, Yukihiro Soga, and Takashi Kikuchi*

Graduate School of Natural Science and Technology, Kanazawa University, Kakuma-machi, Kanazawa, Ishikawa, 920-1192, Japan

**Nagaoka University of Technology, Nagaoka, 940-2188, Japan*

ABSTRACT

An axial temperature and radial density distribution of a pure electron plasma have been measured before and after the compression in the longitudinal direction under a strong and weak magnetic fields. The time evolution of the temperature can be interpreted as that of beam emittance during the longitudinal pulse compression of charged-particle beam. Tune depression can be controlled by a density of the electrons and a magnetic field strength of the trap. The increase ratio of the axial temperature during the compression under the weak magnetic field is almost 1.7 times larger than that under the strong magnetic field. On the other hand, the radial density distribution remains unchanged as the initial condition in both cases.

Keywords

Non-neutral plasma, Heavy ion fusion, Pulse compression, Space-charge-dominated beam

1. Introduction

Heavy ion beam has been studied as a candidate for the energy driver of an inertial fusion device[1]. In order to assure a large amount of the current for an efficient implosion of a target, an abrupt compression in the propagating direction of the heavy ion beam is required[2-4]. The sudden increase of the current density generates a high space charge effect which causes an increase of the beam emittance. The increase of the beam emittance will prevent the efficient fusion reaction. A method for controlling the increase of beam emittance after the dramatic compression has to be studied. However, the study on the ion beam will cost a great expense because a production of ion beam with a high energy requires a large accelerator complex.

A pure electron plasma is a suitable material for the study on charged particle beam. The equivalence has been confirmed of a pure electron plasma in a Malmberg-Penning trap and the charged particle beam in the center-of-mass frame under a proper scale transformation[5]. A pure electron plasma with the temperature less than 1 eV has the large self-electric potential compared with the kinetic energy. The compression in the longitudinal direction of a heavy ion beam could be simulated by the compression in the axial direction of the pure electron plasma with low temperature. The observed energy in the axial direction of the pure electron plasma during the compression could be related to the beam emittance of the ion beam during the pulse compression.

The preliminary experiment using a pure electron plasma showed a considerable increase of the average energy and temperature in the axial direction after the compression in the axial direction[6]. In this study, we observed the time evolution of the energy and temperature of a pure electron plasma in the axial direction during the axial compression as a function of the strength of the axial magnetic field which governs the space-charge effect in terms of charged particle beam.

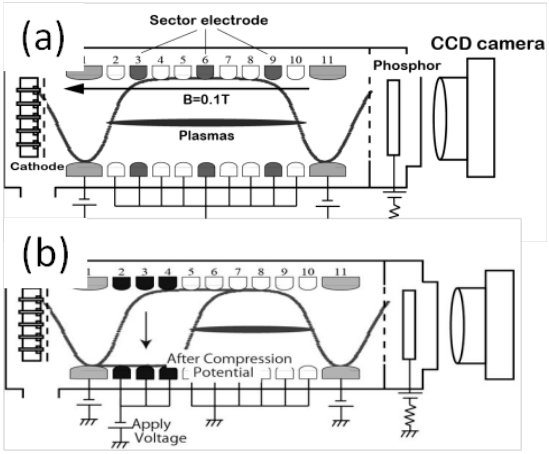

Fig. 1 Schematic configuration of the electron trap(a). Electrons are compressed in the axial direction by changing the electric potential(b).

2. Experimental Setup

The schematic configuration of the compression experiment device is shown in Fig.1(a). The device is composed of an electron source, ring electrodes with 60 mm in a diameter, and a phosphor screen in a cylindrical vessel. The basic scheme of an electron confinement consists of the homogeneous magnetic field B = 0.1 T along the z-axis and the saddle shaped axisymmetric potential with negative barriers at both ends[7].

Electrons are provided from an array of small electron emitters placed in the weaker field region through the left barrier, while the confining potential at the plug cylinder is raised to ground in a variable short time. Electrons are disconnected from the sources on the recovery of the potential barrier. After arbitrary time, the barrier potential is grounded, and electrons exit the trap region along the magnetic filed lines. Measurements of the density profile are made by dumping the whole electrons through the end cylinder on the other side of the cathodes onto a phosphor screen. The luminosity distribution on the screen is detected with a CCD camera. A linear relationship has been confirmed between the total electron number and the luminosity integrated over the screen.

A method of the plasma compression is schematicall shown in Fig.1(b). The axial compression is achieved by applying negative voltage to five ring electrodes where the electrons originally exists. In this experiment, an electron column is compressed from 0.120 m to 0.030 m in the axial length.

We use an electron plasma of cylinder in shape with an equilibrium state as an initial profile for the compression experiment. Figure 2 shows the initial density of the electron plasma in a cross section(a) and in the radial direction(b). The cylindrical electron plasma is produced by mixing and relaxation of about 500 strings of electrons which accumulate in the trap through multiple injection-hold-mixing cycles.

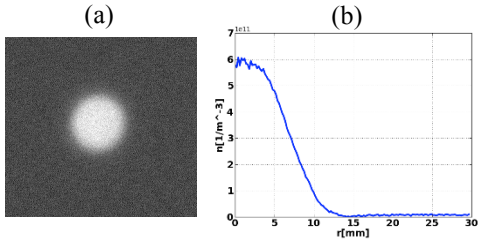

Fig. 2 CCD Image(a) and the radial profile(b) of the initial electron density distribution under a magnetic field 0.1 T.

A longitudinal kinetic energy distribution of plasmas is measured by the energy selection method using variable potential at end electrodes[8]. The electrons are dumped by a lowered, but non-zero, confinement potential. Electrons with sufficient energy can escape from the potential barrier. By repeating the procedure with various barrier potentials, a number of electrons Q as a function of the energy E can be measured. The measured $Q(E)$ is expressed by the longitudinal energy distribution function $f(E)$ as follows.

$$Q(E) = Q_0 \int_E^{\infty} dE \frac{f(E)}{\sqrt{E}}$$

Here Q_0 represents the total number of electrons. By differentiating $Q(E)$, we can obtain the energy distribution $f(E)$.

$$f(E) = -\sqrt{E} \frac{d}{dE} \frac{Q(E)}{Q_0}$$

A longitudinal temperature can be determined by the high energy tail of the distribution function $f(E)$, assuming that the $f(E)$ forms a Maxwell

distribution. The temperature can be related to a beam emittance.

3. Results and Discussion

Figure 3(a) shows the radial profile of the initial density and the axial temperature of an electron plasma under the magnetic field of 0.1 T. A Gaussian distribution for the initial density at the axial temperature of 0.13 eV can be generated as the initial condition. The axial compression of the electron plasma was achieved until the axial electron distribution becomes the one forth of the original length. After the compression, the axial temperature on the axis increases to 0.40 eV probably due to a space charge effect. On the periphery of the plasma at r > 11 mm, the abrupt increase and oscillation of the radial temperature was obtained due to a large dispersion of the observed data for extremely small number of electrons.

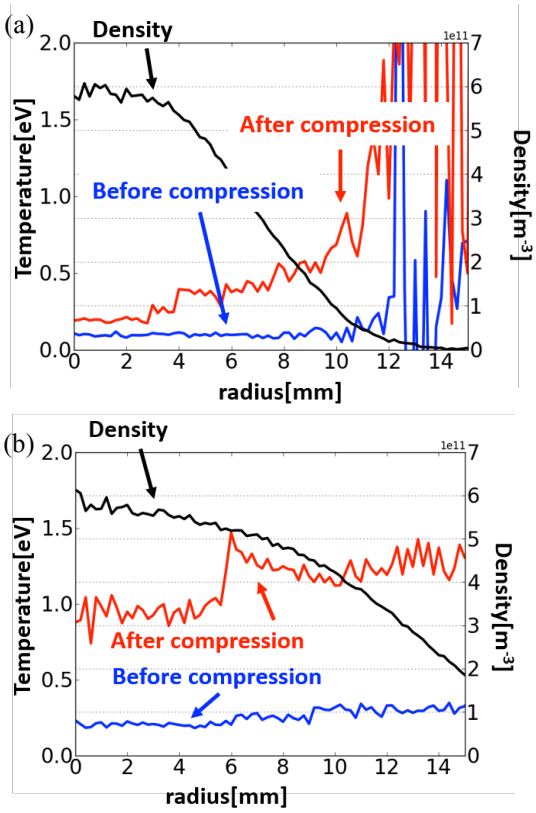

Fig. 3 Radial distribution of the density profile and the axial temperature under the strong magnetic field B = 0.1 T(a) and the weak magnetic field B = 0.02 T(b).

Under the weaker magnetic field of 0.02 T, the initial density and the axial temperature profiles are shown in Fig. 3(b). The initial density profile expands radially compared to that under the strong B filed in Fig. 3(a) because the electron plasma has a large Debye length for the higher axial temperature 0.23 eV on the axis. After the compression, the axial temperature was raised to more than 1 eV. The increase ratio of the axial temperature during the compression under the weak magnetic field is almost 1.7 times larger than that under the strong magnetic field.

A space charge effect in charged particle beam can be characterized by tune depression η, which means a ratio between a bare tune and a depressed tune of the beam. According to the theoretical study by Okamoto[5], the tune depression could be related to an electron plasma density as follows.

$$\eta = \frac{\sigma}{\sigma_0} = \sqrt{1 - \frac{n}{n_{\mathrm{lim}}}}$$

Here, σ_0 is bare tune, σ is depressed tune, n_{lim} is the Brillouin density limit, and n is the electron plasma density, and the Kapchinsky-Vladimirsky model is assumed. A low tune depression can be realized for the high density electron plasma. An electron plasma at Brillouin density corresponds to a space charge dominated beam with a tune depression $\eta = 0$.

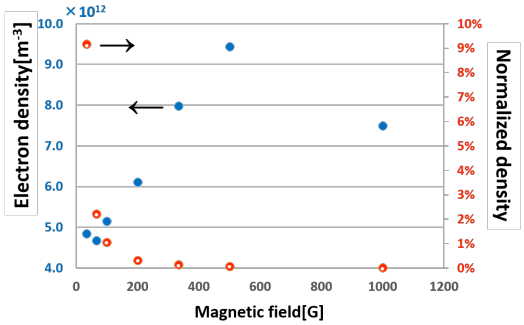

Fig. 4 On-axis electron densities and the normalized densities by the Brillouin density limit are plotted as a function of a magnetic field strength.

Figure 4 shows electron densities and the densities normalized by Brillouin density limit which we can generate in our trap as a function of a

magnetic field strength. Because a Brillouin density limit is proportional to the square of a magnetic filed strength, a high normalized density can be produced under the weaker magnetic field. However, the achieved normalized density in the experiment is at most 0.09.

In a framework of such a low density electron plasma, a tune depression has to be reevaluated by taking into account the radial dependence of a density profile like a typical Gaussian distribution. Here, we adopt the dimensionless parameter Δ as the index of space charge effect for a low density electron plasma[9]. The dimensionless parameter Δ represents the ratio between self field strength and confinement effect by external field[10].

$$\Delta = \frac{2\omega_r(\omega_c - \omega_r)}{\omega_p^2} - 1$$

Here ω_p is a plasma frequency, ω_c is a cyclotron frequency, and ω_r is a macroscopic azimuthal rotation frequency. The dimensionless parameters Δ in the experiment are plotted in Fig.5.

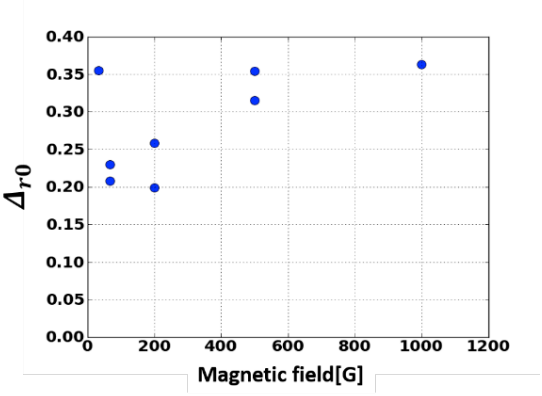

Fig. 5 Dimensionless parameters Δ are plotted as a function of a magnetic field.

The minimum Δ of 0.20 is obtained with a magnetic field 0.02 T which corresponds to the data shown in Fig.3(b). Although the increase of the temperature during the axial compression was observed at the minimum Δ, a production of electrons with higher density under a weaker magnetic field around $\Delta \ll 1$ is expected in order to investigate space charge dominated beam.

4. Conclusions

Considerable increase of the axial temperature of a pure electron plasma with a weak magnetic field in a Malmberg-Penning trap was observed during the longitudinal compression. The increase ratio of the axial temperature during the compression under the weak magnetic field is almost 1.7 times larger than that under the strong magnetic field.

References

[1] S. Atzeni and J. Meyer-ter-vehn, The Physics of Inertial Fusion: Beam Plasma Interac- tion, Hydrodynamics, Hot Dense Matter (Oxford Univ., N.Y., 2004).

[2] D. D.-M. Ho and S. T. Brandon, Nucl. Instrum. Methods Phys. Res., A**278**, pp.182-185 (1989).

[3] M.J.L. De Hoon, E.P. Lee, J.J. Barnard and A. Friedman, Phys. Plasmas, **10**, pp.855- 861 (2003).

[4] T. Kikuchi, K. Horioka, M. Nakajima and S. Kawata, Nucl. Instrum. Methods Phys. Res., A**577**, pp.103-109 (2007).

[5] H. Okamoto, H. Tanaka, Nucl. Instr. Meth. Phys. Res. A **437**, pp.178-187(1999).

[6] Y. Park, Y. Soga et al., "Measurement of energy distribution in a pulse-compressed pure electron plasma", NIFS-PROC Series in print.

[7] Y. Soga, T. Mimura, Y. Kato and Y. Park, Plasma Fusion Res. **8**, 2401034 (2013).

[8] D. L. Eggleston, C. F. Driscoll et al., Phys. Fluids B **4** 3432 (1992).

[9] T. Kikuchi, T. Sato, Y. Park, Y. Soga et al., "Simulating beam parameter using Malmberg-Penning trap device for longitudinal pulse compression in heavy ion inertial fusion", NIFS PROC in print.

[10] Steven M. Lund, T. Kikuchi, and Ronald C. Davidon, Phys. Rev. Accel. Beams **12**, 114801 (2009).

Design Works of Intense Electron Gun for Miniaturized Beam Bunching Simulator

Yoshiki Shou, Yasuo Sakai, Mitsuo Nakajima, Jun Hasegawa and Kazuhiko Horioka

Department of Energy Sciences, Tokyo Institute of Technology,
Nagatsuta 4259, Midori-ku, Yokohama, 226-8502, Japan

ABSTRACT

We developed a beam trace simulation program to increase the current level of electron gun from mA to 100 mA level in our bunching device. To confirm the validity of the program, we applied this program to a test problem. The results indicated that we should improve this program so as to take the space charge effect into consideration. We started design works using this program to develop a bright electron injector based on the Pierce geometry. An analytical scaling indicated that the upgrade of beam current level extends the parameter of the bunching device to a fully space charge dominated region.

Keywords

Space charge, Intense beam, Longitudinal compression, Electron gun

1. Introduction

Heavy ion beams (HIBs) are expected to be potential drivers for high-energy density science and heavy ion inertial fusion (HIB-ICF) [1]. HIBs have advantages of capability of repetitive operation and controllability of the energy deposition to the solid target. For the fusion driver, we need to enhance the beam power up-to a 10^{15} W level. To achieve the power enhancement, longitudinal compression of beam bunch is a crucial issue.

Figure 1 shows a schematic illustration of the principle of the longitudinal drift compression, in which the beam is modulated to have a velocity tilt along the bunch length. The modulation voltage applies the velocity tilt so as to focus the beam bunch at a focal point.

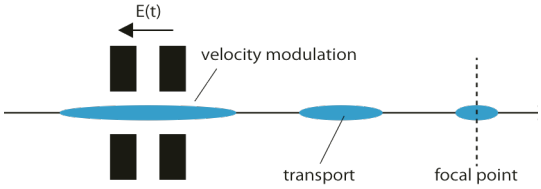

Fig. 1. Principle of longitudinal compression.

However, the space charge field is expected to deteriorate the compression process. In particular, at the final phase of the compression process, collective effects induced by the space charge field may dominate the beam behavior [2].

To investigate the beam dynamics, we constructed a miniaturized bunching simulator using electron beams (e-beams) instead of HIBs. We could make scale down experiments using the e-beam simulator for longitudinal compression of HIBs at a low voltage and low current condition owing to the small inertia and the large specific charge of electrons. We have been trying to investigate the space charge effects on the beam behavior by measurements of the current waveforms and the compression ratios.

Table 1 shows comparisons of beam parameters between a Pb beam at a condition of the HIB-ICF and the electron beams in our device. As shown in Tab. 1, we can discuss the beam dynamics of HIBs by using the e-beams of mA-kV level at a similar condition of heavy ions,

Tab. 1. Typical beam parameters for HIB and e-beams. V_{ex}, I_b, $\beta = v/c$, and K_L indicate the beam extracting voltage, the current, the particle speed, and the longitudinal perveance respectively.

Beam species	q/m [C/kg]	V_{ex} [V]	I_b [A]	β	K_L [mm]
Pb	4.67×10^5	$1\text{-}10 \times 10^9$	$0.1\text{-}10 \times 10^3$	0.1-0.3	0.038-38
Electron	1.75×10^{11}	$2.7\text{-}27 \times 10^3$	$0.3\text{-}30 \times 10^{-3}$	0.1-0.3	0.038-38

concerning the β, and the perveance K_L.

Up to now, we used an electron gun with ~ 1 mA level to investigate the beam dynamics in the bunching simulator. From now on, we are planning to upgrade the electron gun to a 100 mA level to discuss the beam dynamics in a wider parameter region where the beam collective effects dominate the beam behaviors.

In this paper, we show our ongoing study on the research and development of the new high current and low emittance electron gun.

2. Compact Beam Simulator Based on E-beams

Figure 2 shows a schematic diagram of the longitudinal compression experiment using the bunching simulator. Our device consists of a hot cathode electron gun, an induction voltage modulator, a solenoidal transport line, and current monitors.

Experimental procedure is as follows. First, we inject a continuous e-beam with 2.8 keV energy into the induction modulator. Next, we apply a time varying voltage to the modulation gap that cuts out a beam bunch and applies a velocity gradient from the beam head to the tail. Then, this velocity modulated beam drifts through the solenoidal transport line and shortens during the transport to the destination. Finally, we measure the compressed beam bunch by the current monitors as a current waveform.

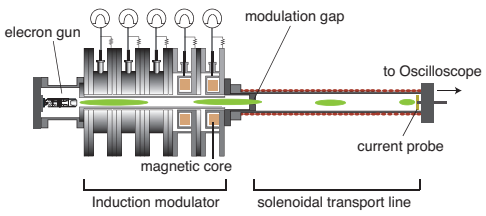

Fig. 2. Schematic diagram of beam simulator.

We apply the following voltage for the beam modulation to compress all of the beam bunch at a focusing point L away from the modulator.

$$V(t) = \frac{m_e}{2q_e} \frac{1}{\left(\sqrt{\frac{m_e}{2q_eV_0}} + \frac{T-t}{L}\right)^2} - V_0 \quad (1),$$

where q_e, m_e is the charge and the mass of electron respectively. V_0 is the extracting voltage of the electron beam.

In this experiments, we generate this ideal voltage by the stacked induction modulator (induction adder). The induction modulator is consisted of 5 units (See Fig. 1). Each unit makes a sinusoidal voltage waveform that is independently controllable. By superimposing their voltages, we can make the modulation voltage.

Figure 3 shows typical voltage waveforms of this device. As shown in Fig. 3, we could confirm that this waveform almost matches the ideal waveform.

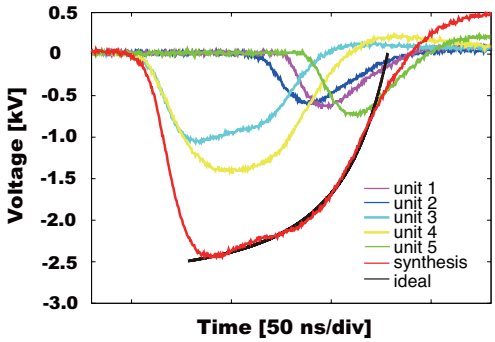

Fig. 3. Typical voltage waveforms of induction units and the modulation gap.

2.1 Typical experimental results

We can measure the beam parameters such as the initial beam current, the compressed beam current and the pulse duration (FWHM) with this device. Figure 4 is the typical current waveforms measured by this device which show the initial (gray line) and the modulated beam (black line) currents. In this case, the initial beam was estimated to be 84 μA, the peak of compressed beam was estimated to be 1.6×10^3 μA, and compression ratio was estimated to be about 20. Here we defined the compression ratio as the peak current divided by the initial current. Furthermore, we can estimate that the pulse duration is compressed from 100 ns to 3.2 ns in this case.

2.2 Space charge effect on the compression experiment

In a previous research [3], we confirmed that both the compression ratio and the pulse duration depend on the initial current.

Figure 5 shows the current waveforms at focusing point as a function of initial beam levels. As shown in Fig. 5, the compression ratio decreased from about 32 for I_0 = 83 μA to about 18 for I_0 = 748 μA. Meanwhile the pulse duration increased from 2.0 ns to 2.8 ns. From these results, we could know that the space charge affects the beam behaviors in this experimental condition.

3. Design works of an electron gun to upgrade the current level

Up to now, the initial beam current available with our device, that is, the current of electron gun was up-to ~ 1 mA. However, the HIB-ICF needs beam operations at much more large perveance level in the final stage of accelerator. This motivated us to upgrade the current level of our bunching simulator to ~ 100 mA level.

Thus, to design and develop an electron gun that can be operated at ~ 100 mA level with low emittance is the purpose of this study. Finally, using this electron gun, we discuss the beam

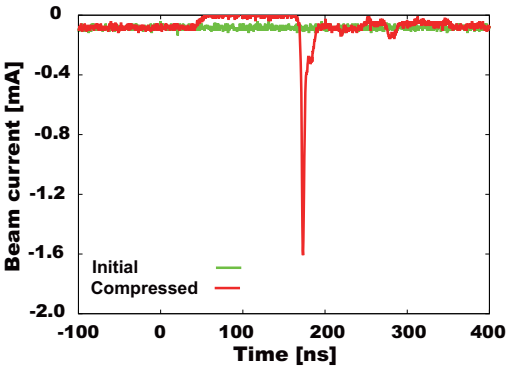

Fig. 4. Typical current waveforms.

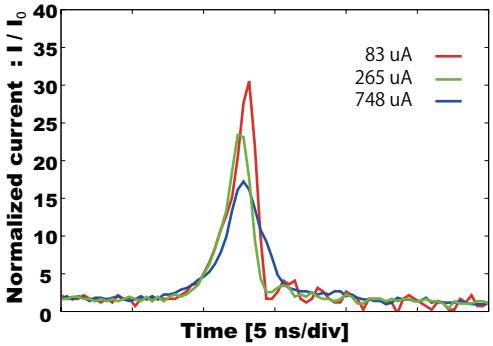

Fig. 5. Typical normalized current waveform.

dynamics in the space charge dominated region.

3.1 A hot cathode electron gun

We are planning to develop a hot cathode electron gun. The hot cathode electron gun generates an e-beam by heating the cathode to emit electrons and accelerate them through a gap. The thermal emission process is expected to be reliable and stable. To develop this type of electron guns, we use a hot cathode "Standard Series Barium Tungsten Dispenser Cathodes" made by Heat Wave Labs, Inc.

Needless to say, but the electron gun which we are planning to develop must be operated at low emittance. In longitudinal direction, the beam envelope equation is written by Eq. (2) as follows [4].

$$\frac{d^2 Z_b}{ds^2} + \kappa Z_b - \frac{K_L}{Z_b^2} - \frac{\epsilon^2}{Z_b^3} = 0 \quad (2),$$

where $2Z_b$ is the bunch length, κ is the longitudinal focusing force, K_L is the

longitudinal beam perveance and ε is the longitudinal emittance.

To realize the beam operation at a space charge dominated region, the third term representing the influence of space-charge effect must be larger than the fourth term representing the longitudinal emittance. This criterion is expressed in the following expression,

$$\frac{K_L Z_b}{\epsilon^2} = \frac{3egI_b\tau_b}{40\pi\varepsilon_0 k_b T_L} > 1 \quad (3),$$

where e is the elementary charge, g is a geometry factor, I_b is the initial beam current, τ_b is the initial beam pulse length, ε_0 is the permittivity in vacuum and $k_b T_L$ is the longitudinal beam temperature [5].

So, we have to conduct e-beams fulfilling Eq. (3) to investigate the influence of space charge effect to the bunching process.

3.2 Method of electrons orbital calculation

We are planning to use a simulation program which estimates the electrons trace and make the design works of the electrode geometry for the high current and low emittance electron gun.

The method of electrons trace calculation is as follows. POISSON/SUPERFISH [6] is a collection of programs for calculating static magnetic and electric fields and radio-frequency electromagnetic fields in either 2-D Cartesian coordinate or axially symmetric cylindrical coordinate. Using this program, we evaluated the static electric field in the acceleration gap of electron gun using 2-D Cartesian coordinate. When we apply an electric potential to the electrodes, we can get the field distribution. Next, we substitute this value for E_y and E_z in the equation of motion (4).

$$\ddot{y} = \frac{q}{m}E_y, \ddot{z} = \frac{q}{m}E_z \quad (4)$$

Finally, by solving the Eq. (4), we can derive a solution for y and z, that is, electrons trace. We search an optimum shape of the electrode so as to the electrons trace is parallel and the beam diameter is small at the 100 mA level.

4. Results and Discussion

4.1 Test of program and conclusion

It's necessary to examine whether the simulation code can be applied to the design of the electron gun. Thus, we tested this program for the electron gun geometry in Ref. 7.

The performance of this electron gun was estimated as follows. The current was delivered as a beam of ~ 1 mm in diameter, with <50 mrad angular divergence and it typically has a current more than 1 mA at 100 eV.

Furthermore, it was established as the early stage condition of the trace calculation as follows. The initial positions of electron were set as the 10 points (z, y) = (9.0×10^{-3}, -2.0×10^{-3})~(9.0×10^{-3}, 2.0×10^{-3}).

The result of the field distribution and the traces are shown in Fig. 6.

4.2 Comparison with test problem

As shown in Fig. 6, the beam diameter was 4 mm at downstream. This value is larger than that of electron gun's diameter described in Ref. 7. When we consider the space charge effect, the

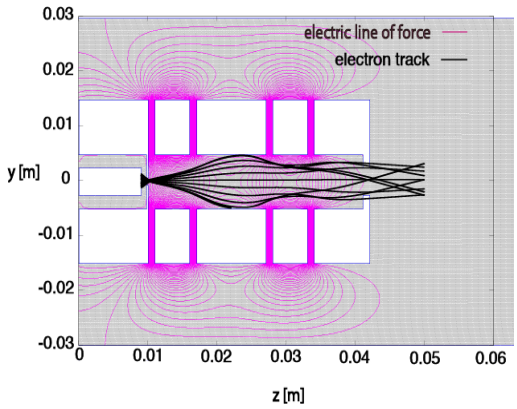

Fig. 6. An example of electron trace obtained for the test problem.

actual electrons trace becomes parallel at the over-focus point at z = 0.01 m (See Fig. 6). This indicates that we should take the influence of the space charge effect into account for the trace calculation. We are going to use the beam envelope equation [8] shown below instead of the Eq. (4) to upgrade the program. The envelope equation is shown as,

$$\frac{d^2r}{d^2z} = -\frac{\phi' r'}{2\phi} - \left[\frac{\phi''}{4\phi}\right] r + \frac{\varepsilon^2}{r^3} + \frac{K}{r} \quad (5),$$

where r, z, φ, ε, and K is the envelope radius of beam, longitudinal coordinate, the electric potential at center (r = 0), the transverse emittance, and the generalized perveance respectively.

4.3 Pierce electrode

Considering the space charge effect of injector, we decided to make an electron gun with Pierce geometry. The analytic derivation of the Pierce geometry [9] gives a solution for a space-charge-dominated injector. The procedure predicts the shapes of accelerating electrodes to produce a laminar beam with uniform current density.

Pierce and Wehnelt invented the Pierce Gun, which generated a parallel and stationary electron current with the diode structure. As has been discussed, a typical geometry is represented by a straight line oriented at 67.5° with respect to the z axis as shown in Fig. 7.

From now on, we are going to make the design works based on this type of electrode geometry.

5. Concluding Remarks

A miniaturized bunching simulator based on a miniature e-beam accelerator was established at our laboratory to investigate the beam dynamics of longitudinal compression. To extend the parameter region into a stronger space charge dominated region, we need to make higher brightness e-beams.

We are developing a simulation program for

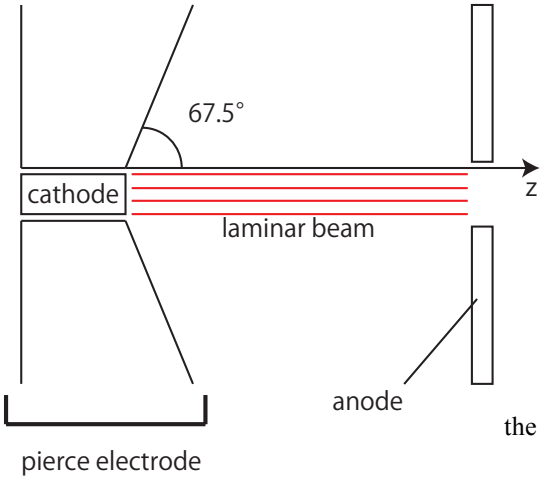

Fig. 7. Electron beam extraction based on Pierce geometry.

beam trace in the electron gun, because the beam brightness is determined entirely by the electrode geometry. The preliminary result of program test indicated that we should consider self-consistently the space charge effect at the extraction electrode in the injector. Therefore, we are making efforts to improve the program of electron trace using the beam envelope equation. We also decide to make the design works of electron gun based on the Pierce geometry.

References

[1] K. Horioka et al., "Activities on Heavy Ion Inertial Fusion and Beam-driven High Energy Density Science in Japan", Nucl. Instr. Meth, **A-606**, pp.1-5 (2009).

[2] M. Reiser, "Theory and Design of Charged Particle Beams", John Wiley and Sons. INC (1994).

[3] Y. Sakai et al., "Precise Control of Stacked Induction Modulator", NIFS-Proceedings (to be appeared).

[4] David Neuffer, "Longitudinal Motion in High Current Ion Beams - A Self-Consistent Phase Space Distribution with an Envelope Equation" IEEE Transactions on Nuclear Science, **NS-26**, 3, pp.3031-3033 (1979).

[5] T. Kikuchi et al., “Beam dynamics analysis in pulse compression using electron beam compact simulator for Heavy Ion Fusion”, EPJ Web of Conferences, **59**, 09004 (2013).
[6] John L. Warren et al., “Reference Manual for the POISSON/SUPERFISH Group of Codes”, No. LA-UR-87-126, Los Alamos National Laboratory, NM (United States) (1987).
[7] Peter W. Erdman and Edward C. Zipf, “Low voltage, high current electron gun”, Review of Scientific Instruments, **53**, pp.225-227 (1982).
[8] Stanley Humphries, Jr. “Charged Particle Beams”, John Wiley and Sons. INC (1990).
[9] J. R. Pierce, “Theory and design of Electron Beams”, Van Nostrand, Princeton, NJ (1949).